IEKP-KA/2003-12

Suche nach sichtbaren und unsichtbaren Higgszerfällen mit dem DELPHI Detektor bei LEP2

Marcel Stanitzki

Zur Erlangung des akademischen Grades eines
DOKTORS DER NATURWISSENSCHAFTEN
von der Fakultät für Physik der
Universität Karlsruhe(TH)

genehmigte

DISSERTATION

Tag der mündlichen Prüfung: 09.05.2003

Referent: Prof. Dr. W. de Boer, Institut für Experimentelle Kernphysik

Korreferent: Prof. Dr. G. Quast, Institut für Experimentelle Kernphysik

Deutsche Zusammenfassung

In dieser Arbeit werden Suchen nach Higgszerfällen vorgestellt, die im Standardmodell entweder stark unterdrückt sind oder überhaupt nicht vorkommen. Man kann diese Zerfallskanäle grob in zwei Klassen einteilen, in sichtbare Zerfälle und unsichtbare Zerfälle. Sichtbare Zerfälle sind entweder Zerfälle in hadronische (Quarks oder Gluonen) oder massive bosonische Endzustände (W- oder Z-Bosonen). Unsichtbare Zerfälle sind zum Beispiel Zerfälle in zwei neutrale supersymmetrische Teilchen, Neutralinos $\tilde{\chi}_1^0$ genannt, die fast nie mit Materie wechselwirken und deswegen den Detektor spurlos durchqueren. Es wurde versucht, solche Zerfälle in dem Hochenergie-Datensatz von 188.6 - 209 GeV Schwerpunktsenergie des DELPHI[1]-Detektors nachzuweisen. Die gesamte verwendete Datenmenge dieses Datensatzes beträgt 592 pb^{-1}. In dieser Zusammenfassung wird zuerst ein kurzer Abriß über die Eigenschaften des Higgs-Bosons gegeben, bevor dann die einzelnen Analysen kurz beschrieben werden.

1.1 Die Eigenschaften des Higgs-Bosons

Das Standardmodell der Teilchenphysik liefert eine hervorragende Beschreibung der Teilchen und ihrer Wechselwirkungen bis zur elektroschwachen Energieskala $\mathcal{O}(100\ \mathrm{GeV})$. Das Standardmodell ist durch Messungen am SPS[2], LEP[3] und Tevatron[4] eindeutig bestätigt worden, allerdings fehlt bis heute der Nachweis eines seiner wichtigsten Bestandteile, das Higgs-Boson.

Alle Austauschteilchen des Standardmodells sind zunächst masselos, was für Gluonen und Photonen auch in Einklang mit den experimentellen Ergebnissen steht. Allerdings weiß man aus Messungen, dass dies für die W- und Z-Bosonen der schwachen Wechselwirkung nicht zutrifft, denn W und Z sind massive Teilchen. Im Standardmodell wird der Higgs-Mechanismus dazu verwendet, um den Eichbosonen der schwachen Wechselwirkung Masse zu verleihen und dabei das Standardmodell mathematisch konsistent zu halten. Dies geschieht mit Hilfe einer spontanen Symmetriebrechung. Von solch einer spontanen Symmetriebrechung wird immer dann gesprochen, wenn dem Grundzustand eine kontinuierliche Symmetrie der Lagrange-Funktion fehlt. Durch den Higgs-

[1] **DE**tector with **L**epton, **P**hoton and **H**adron **I**dentification
[2] **S**uper **P**roton **S**ynchrotron: $p\bar{p}$ Beschleuniger am CERN, Genf
[3] **L**arge **E**lectron **P**ositron collider: e^+e^- Beschleuniger am CERN, Genf
[4] $p\bar{p}$ Beschleuniger am Fermilab, Chicago

Mechanismus entsteht dabei noch ein zusätzliches Teilchen, das skalare Higgs-Boson. Um den ebenfalls masselosen Fermionen Masse zu verleihen, werden die sogenannten Yukawa-Kopplungen zwischen dem Higgs-Feld und den Fermionen eingeführt. Obwohl das Standardmodell detaillierte Aussagen über Produktion und Zerfall des Higgs-Bosons macht, bleibt seine Masse ein freier Parameter. Bei LEP wird das Higgs-Boson dominant über den Higgs-Strahlungs-Prozess $e^+e^- \to HZ$ erzeugt und zerfällt in dem mit LEP kinematisch zugänglichen Bereich hauptsächlich in ein Paar von b-Quarks. Nach dem Higgs-Boson wird intensiv gesucht, die Ausschlussgrenze für die Higgsmasse durch direkte Suchen liegt bei einer Masse von 114.4 GeV/c^2 [LEP03]. In den Anpassungen der elektroschwachen Präzisionsdaten an das Standardmodell wird eine Higgsmasse kleiner als 193 GeV/c^2 [LEP02] bevorzugt.

Nachdem das Higgs-Boson bis jetzt nicht gefunden wurde, gibt es zwei Möglichkeiten, entweder es ist schwerer als 114.4 GeV/c^2 oder der Higgs-Mechanismus im Standardmodell ist anders realisiert. Im Standardmodell wird das Higgs-Feld als ein Dublett komplexer Felder eingeführt; es spricht allerdings wenig dagegen, zwei Dubletts oder mehr zu verwenden, solange die experimentellen Ergebnisse damit beschrieben werden können. In dieser Arbeit wurde die zweite Möglichkeit untersucht. Insbesondere die minimale supersymmetrische Erweiterung des Standardmodells (MSSM) sowie das allgemeine 2-Higgs-Dublett-Modell (2HDM) wurden betrachtet. Beide Modelle verwenden zwei Higgs-Dubletts für die Symmetriebrechung. Supersymmetrie postuliert, daß zu jedem Teilchen ein supersymmetrisches Partnerteilchen mit bis auf den Spin genau gleichen Eigenschaften existiert, der Superpartner. Supersymmetrischen Modelle verdoppeln also die Teilchenzahl im Standardmodell. Allerdings muß die Supersymmetrie gebrochen sein, da man bis heute keinen Superpartner gefunden hat. Bei einer ungebrochene Supersymmetrie hätten z.B. die Superpartner der Elektronen die gleiche Masse wie die Elektronen. Man hat allerdings solche Teilchen nie gefunden. Für den Higgs-Sektor im MSSM gibt es zwei wichtige Neuerungen: Erstens, es gibt im MSSM 5 physikalische Higgs-Bosonen, wobei das leichteste neutrale Higgs-Boson h dem Standardmodell-Higgs-Boson am ähnlichsten ist. Im MSSM gibt es auch eine Massengrenze für h: Es soll leichter als 135 GeV/c^2 sein [Hei99]. Zweitens, es ändern sich die Verzweigungsverhältnisse beim Higgszerfall. Die Higgs-Kopplungen des Standardmodells werden durch Terme modifiziert, die von den Higgs-Parametern α und β abhängen. Durch entsprechende Wahl von α und β können so z.B. die Zerfälle in ein b-Quarkpaar unterdrückt und dafür Zerfälle in up-type Quarks wie c- oder t-Quark dominant werden. Zusätzlich kann das Higgs-Boson auch in die Superpartner zerfallen, wobei der Zerfall in Neutralinos $\tilde{\chi}_1^0$ als leichtestes Teilchen des MSSM am interessantesten ist. Vom Neutralino nimmt man an, daß es stabil ist und fast nicht mit Materie wechselwirkt. Es kann also spurlos aus dem Detektor entweichen, man spricht hier von unsichtbaren Zerfällen.

Im 2HDM, daß ebenfalls 5 Higgs-Bosonen vorhersagt, gibt es wieder Modifikationen der Higgs-Kopplungen durch die Parameter α und β, so daß die Unterdrückung von Zerfällen in b-Quarks ebenfalls möglich ist. Im 2HDM gibt es auch die Möglichkeit, dass die Kopplungen von h an Fermionen komplett un-

terdrückt und somit nur Zerfälle in Bosonen möglich sind. Man spricht dann von fermiophobischen oder bosonischen Higgszerfällen. Im Gegensatz zum MSSM, wo die Higgsmassen in fester Beziehung zueinander stehen, sind die Higgsmassen im 2HDM freie Parameter. Mehr Details zu diesen Modellen finden sich in den Kapiteln 1 bis 3.

1.2 LEP und DELPHI

Die verwendeten Daten wurden mit dem DELPHI-Detektor am LEP aufgezeichnet. LEP ist der größte je gebaute e^+e^--Beschleuniger mit einem Umfang von fast 27 km und einer maximalen Schwerpunktsenergie von 208.8 GeV. Die Datennahme bei LEP fand von August 1989 bis November 2000 statt und läßt sich in zwei Perioden einteilen. Die LEP1-Phase dauerte von 1989 bis 1995 mit einer Schwerpunktsenergie von 91 GeV, was der Z-Boson-Resonanz entspricht. Wichtigster Bestandteil des LEP1-Programms war die exakte Vermessung der Eigenschaften des Z-Bosons. In der LEP2-Phase von 1995 bis 2002 wurde die Schwerpunktsenergie stufenweise von 161 bis 209 GeV erhöht, hier lag der Hauptaugenmerk vor allem auf dem Studium von W- und Z-Paarproduktion sowie der Suche nach dem Higgs-Boson.

Der DELPHI-Detektor, einer der 4 LEP-Detektoren, ist ein typischer symmetrischer 4π-Detektor, mit einem Zentralbereich und zwei Endkappen (siehe Abbildung 1). Der Zentralbereich besteht aus einem System von Spurkam-

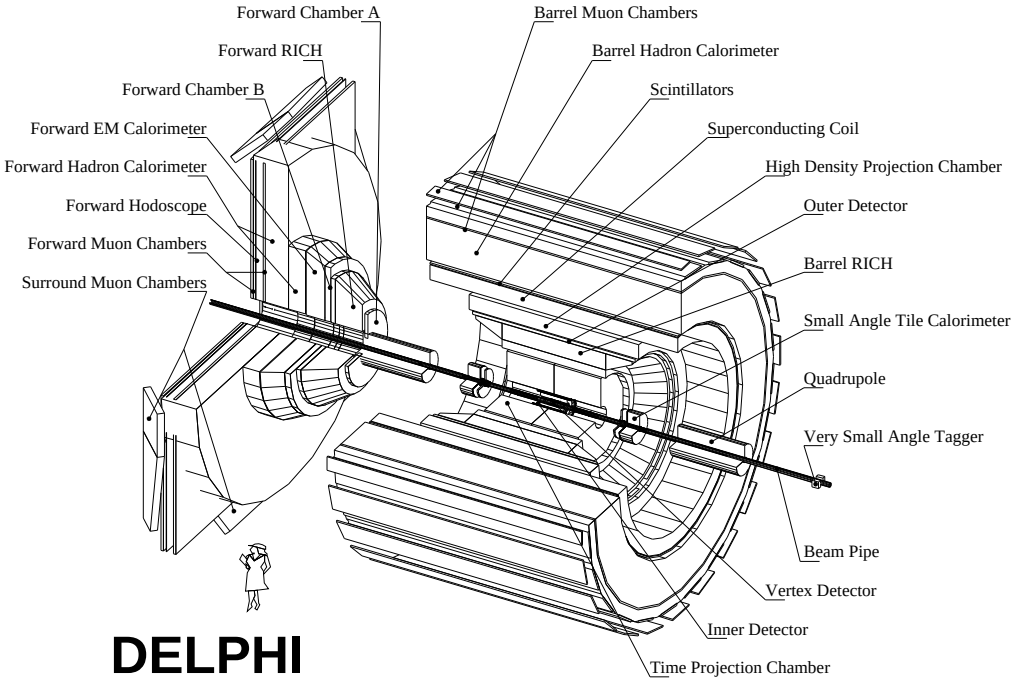

Abbildung 1: Der DELPHI-Detektor

mern, Kalorimetern und Detektoren zur Teilchenidentifikation. Das Spursystem besteht im Wesentlichen aus einem Siliziumstreifendetektor und einer TPC[5]-Driftkammer. Das System zur Energiemessung besteht aus einem elektromagnetischen und einem Hadronkalorimeter. Zur Teilchenidentifikation besitzt DELPHI einen Cherenkov-Detektor sowie Myonkammern. Die Endkappen sind ähnlich aufgebaut, allerdings besteht das Spursystem dort nur aus zwei Drahtkammern.

1.3 Suche nach unsichtbaren Higgszerfällen

Die Motivation für diese Analyse kommt aus dem möglichen Zerfall in zwei Neutralinos $\tilde{\chi}_1^0$, wobei die Analyse generell nach unsichtbaren Zerfällen sucht, ohne sich auf ein Modell zu konzentrieren. In dieser Analyse wird nach Ereignissen mit fehlender Energie gesucht, die aus dem unsichtbaren Higgszerfall herrührt. Die gesuchte Signatur ist in Abbildung 2 gezeigt, dabei stammen die beiden Jets aus dem hadronischen Zerfall des Z-Bosons. Mögliche Untergrundprozesse aus dem Standardmodell sind hauptsächlich $q\bar{q}\gamma$-Ereignisse, bei denen das Photon entlang des Strahlrohrs abgestrahlt wird, sowie aus sogenannten 4-Fermion Prozessen wie $e^+e^- \to W^+W^-$ und vor allem $e^+e^- \to ZZ \to q\bar{q}\nu\bar{\nu}$.

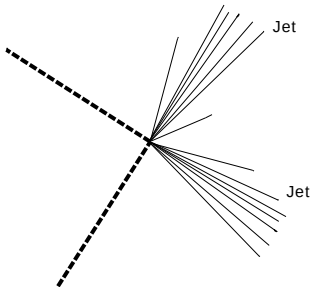

Abbildung 2: Die gesuchte Ereignistopologie für den Prozess $e^+e^- \to HZ$ ($H \to$ unsichtbar)($Z \to q\bar{q}$). Die gepunkteten Linien symbolisieren die unsichtbaren Teilchen.

Um einen großen Higgsmassenbereich (40-120 GeV/c^2) abzudecken, wurde die Analyse in zwei Massenbereiche geteilt, die jeweils für leichte oder schwere Higgs-Bosonen optimiert sind. Nach einer gemeinsamen Vorselektion zur Unterdrückung von Photon-Photon-Ereignissen und hadronischen 2-Fermion-Ereignissen wählt die letzte Stufe der Vorselektion Ereignisse mit zwei Jets und fehlender Energie aus, dabei hängt die Menge der fehlenden Energie von der untersuchten Higgsmasse ab. Danach wird eine Diskriminanz-Analyse angewandt, um eine hohe Trennungseffizienz zwischen Signal und Untergrund zu erreichen. Am Ende der Analyse wird dann ein Schnitt auf die Diskriminanzvariable durchgeführt.

[5] **T**ime **P**rojection **C**hamber

Da kein Hinweis auf ein Signal gefunden wurde, ist eine Ausschlussgrenze mit 95% Vertrauensintervall für ein Higgs-Boson, das zu 100% in unsichtbare Endzustände zerfällt, berechnet worden. Dieser Suchkanal wurde dazu mit den Ergebnissen der Suchen nach unsichtbaren Higgszerfällen mit einem leptonischen Z-Zerfall kombiniert. Da diese Kanäle allerdings nur 9% des gesamten Verzweigungsverhältnisses abdecken, ist ihr Beitrag klein im Vergleich zum dominierenden Kanal mit einen hadronischen Z-Zerfall (69.9% Verzweigungsverhältnis). Die so erhaltenen Massenausschlussgrenze mit 95% Vertrauensintervall beträgt 112.1 GeV/c^2. Daneben wurde auch die erwartete Ausschlussgrenze berechnet, die ein Maß für die Sensitivität der Analyse ist, sie beträgt 110.5 GeV/c^2. Einen allgemeineren Ausschluß erhält man, indem man eine Ausschlussgrenze für den Wirkungsquerschnitt des Prozesses $e^+e^- \rightarrow HZ(H \rightarrow \text{unsichtbar})(Z \rightarrow alles)$ in Abhängigkeit von der Higgsmasse berechnet. Dieser Ausschluss ist in Abbildung 3a gezeigt. Man kann

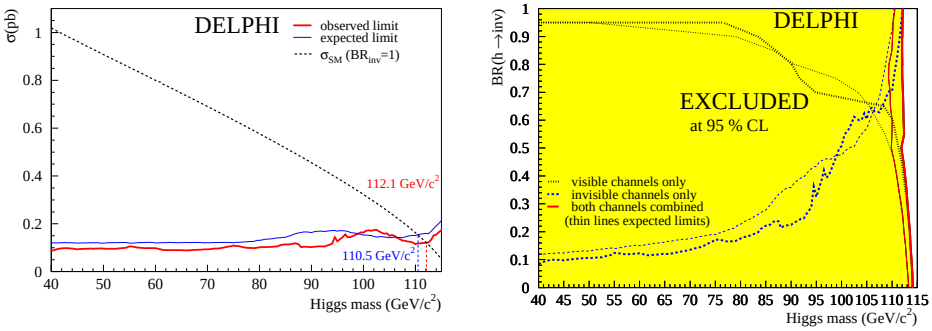

(a) **(b)**

Abbildung 3: Die Ausschlussgrenze für den Wirkungsquerschnitt $e^+e^- \rightarrow HZ(H \rightarrow \text{unsichtbar})(Z \rightarrow \text{alles})$ (a) und der ausgeschlossene Massenbereich für ein beliebiges Verzweigungsverhältnis in unsichtbare Endzustände (b).

auch die Ergebnisse der Suche nach unsichtbaren Zerfällen mit den Ergebnissen der Standardmodell-Higgs-Suchen kombinieren, unter der Annahme, dass das Higgs nur teilweise unsichtbar und teilweise in Standardmodell-Endzustände zerfällt. Dazu wurden die Ergebnisse der DELPHI-Standardmodell-Higgssuchen [DEL98, DEL00, DEL02b, DEL03a] verwendet. Man erhält eine Massengrenze von 111.8 GeV/c^2, unabhängig vom Verzweigungsverhältnis in unsichtbare Endzustände. Der ausgeschlossene Massenbereich in der Ebene Higgsmasse-Verzweigungsverhältnis ist in Abbildung 3b gezeigt.

1.4 Suche nach hadronischen Higgszerfällen

Die Motivation für die Suche nach hadronischen Higgszerfällen ist, eine Analyse zu haben, die nicht von der Identifikation von b-Quarks im Ereignis abhängt,

wie bei den Standardmodell-Higgs-Suchen. Mit solch einer Suche ist man sensitiv auf einen hadronischen Higgszerfall, unabhängig von der Quarksorte. Die erwartete Ereignistopologie ist in Abbildung 4 gezeigt. Die Signaltopologie ist der

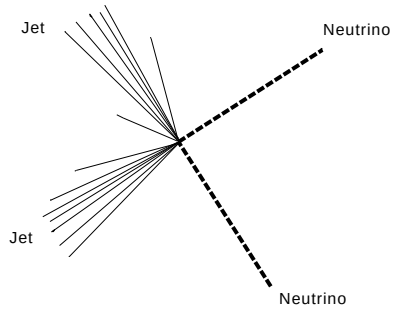

Abbildung 4: Die gesuchte Ereignistopologie für den Prozess $e^+e^- \rightarrow HZ(H \rightarrow$ hadronisch$)(Z \rightarrow \nu\bar{\nu})$.

eines unsichtbaren Higgszerfalls sehr ähnlich, allerdings stammt diesmal die fehlende Energie vom Zerfall des Z-Bosons in zwei Neutrinos. Die Standardmodell-Untergrundprozesse sind die gleichen wie bei der Suche nach unsichtbaren Higgszerfällen. Der abgedeckte Higgsmassen-Bereich beträgt hier 40 bis 115 GeV/c^2. Um eine gute Signaleffizienz im gesamten untersuchten Massenbereich zu erzielen, wurden hier drei Massenfenster verwendet, von 40 bis 67.5 GeV/c^2, von 70 bis 87.5 GeV/c^2 und von 90 bis 115 GeV/c^2. Die ersten beiden Stufen der Vorselektion sind identisch mit der Vorselektion für die Suchen nach unsichtbaren Higgszerfällen. Die letzte Stufe der Vorselektion ist allerdings modifiziert, um der leicht geänderten Ereignistopologie Rechnung zu tragen. Während bei den unsichtbaren Zerfällen ausgenutzt wird, daß die sichtbare Masse kompatibel mit der Z-Boson-Masse ist, geht man bei den hadronischen Suchen davon aus, daß die unsichtbare Masse mit der Z-Masse kompatibel ist. Für die drei verschiedenen Massenbereiche wurden auch kinematische Unterschiede in dieser Selektion berücksichtigt.

Um bei der Analyse keinen Zerfallstyp wie z.B. leichte Quarks, c-Quarks, b-Quarks oder Gluonen zu bevorzugen, wurden zum Training der Diskriminanzanalyse ein generischer hadronischer Higgszerfall konstruiert, bei dem keiner der vier Zerfallstypen bevorzugt wird. Die dann erhaltenen Ergebnisse sind so gültig für ein hadronisch zerfallendes Higgs, unabhängig davon, in welchen Typ es zerfällt. Am Ende der Analyse wurde keine Evidenz für hadronische Higgszerfälle gefunden. Deshalb wurde auch hier eine Massenausschlussgrenze mit 95% Vertrauensintervall berechnet. Im Gegensatz zu der Suche nach unsichtbaren Higgszerfällen, bei dem der Kanal $e^+e^- \rightarrow HZ$ ($H \rightarrow$ unsichtbar$)(Z \rightarrow q\bar{q})$ der wichtigste Kanal ist und die Ausschlussgrenze dominiert, muß hier zur Berechnung einen Massenausschlussgrenze die Ergebnisse mit den DELPHI-Ergebnissen [DEL03b] für die anderen Kanäle ($e^+e^- \rightarrow HZ$ ($H \rightarrow$ hadronisch$)(Z \rightarrow q\bar{q})$ und $e^+e^- \rightarrow HZ$ ($H \rightarrow$ hadronisch$)(Z \rightarrow l^+l^-)$) kombiniert werden. Diese Kanäle haben ein Verzweigungsverhältnis von 69% bzw. 6%, während der Kanal $e^+e^- \rightarrow HZ(H \rightarrow$ hadronisch$)(Z \rightarrow \nu\bar{\nu})$

nur 21% des Verzweigungsverhältnisses abdeckt. Nach der Kombination erhält man als beobachtete Massenausschlussgrenze für ein zu 100% hadronisch zerfallendes Higgs-Boson 110.6 GeV/c^2 mit 95% Vertrauensintervall. Die erwartete Massenausschlussgrenze liegt bei 108.0 GeV/c^2. Auch in diesem Kanal wurden die Ergebnisse benutzt, um einen Ausschluss auf den Wirkungsquerschnitt $e^+e^- \to HZ(H \to \text{unsichtbar})(Z \to \text{alles})$ zu setzen. Das Ergebnis ist in Abbildung 5a zu sehen. Zusätzlich wurde noch der Ausschluss als Funktion des Unterdrückungsfaktors ξ berechnet. Der Unterdrückungsfaktor ξ ist definiert als:

$$\xi = \frac{\sigma_{ausgeschlossen}}{\sigma_{SM}(e^+e^- \to HZ)}$$

Das Ergebnis des Ausschlusses mit 95% Vertrauensintervall ist in Abbildung 4b gezeigt.

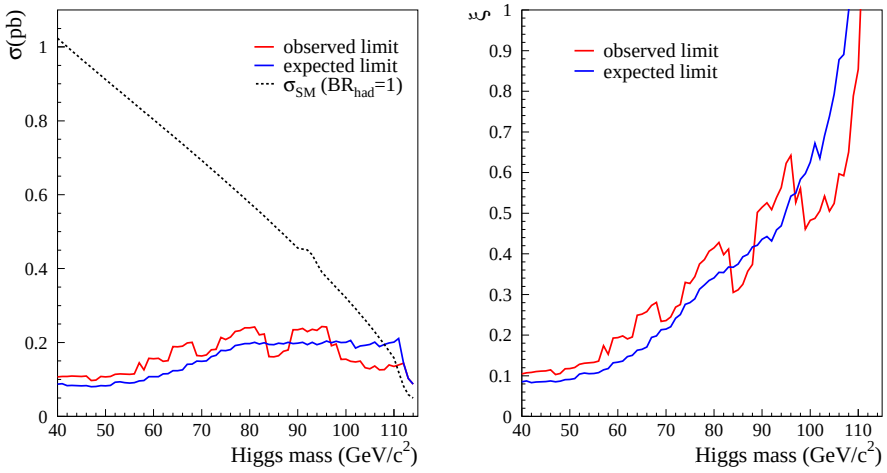

(a) **(b)**

Abbildung 5: Der ausgeschlossene Wirkungsquerschnitt für den Prozess $e^+e^- \to HZ(H \to \text{hadronisch})(Z \to \text{alles})$ in (a). Der ausgeschlossene Unterdrückungsfaktor ξ ist in (b) gezeigt.

1.5 Suche nach bosonischen Higgszerfällen

Die Suche nach bosonischen Higgszerfällen der Form $H \to WW^* \to f\bar{f}'f\bar{f}'$ wird vor allem durch fermiophobische Szenarien in 2-Higgs-Dublett-Modellen motiviert, in denen die Kopplungen des leichten neutralen Higgs-Bosons an die Fermionen unterdrückt ist. In diesen Modellen sind dann die bosonischen Zerfälle in $\gamma\gamma$ oder WW^* die Hauptzerfallskanäle, wobei der Kanal $H \to WW^*$ bei Higgsmassen über 100 GeV/c^2 der dominante Kanal ist. Für Higgsmassen kleiner als 161 GeV/c^2 können nicht zwei reelle W-Bosonen produziert werden,

so dass mindestens eines der beiden W-Bosonen virtuell ist. Eine Schwierigkeit dieses Kanals ist die große Anzahl an möglichen Endzuständen. Die Ursache hierfür ist, daß die W-Bosonen als Zerfallsprodukte des Higgs-Bosons wieder in je zwei Fermionen zerfallen. Der in dieser Arbeit analysierte Kanal $e^+e^- \to HZ$ $(H \to WW^* \to q\bar{q}'q\bar{q}')(Z \to q\bar{q})$ hat einen Anteil von 32% am gesamten Verzweigungsverhältnis. Die erwartete Ereignistopologie ist in Abbildung 6 gezeigt. Die Signatur in dieser Analyse ist sehr unterschiedlich im Ver-

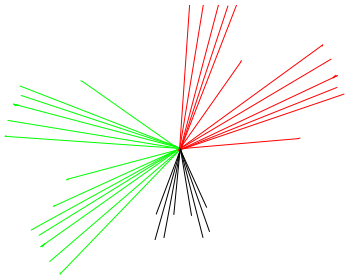

Abbildung 6: Die gesuchte Ereignistopologie für den Prozess $e^+e^- \to HZ$ $(H \to WW^* \to q\bar{q}'q\bar{q}')(Z \to q\bar{q})$

gleich zu den beiden vorherigen Analysen, denn in diesen Ereignissen gibt es keine fehlende Energie. Man erwartet Multijet-Ereignisse mit sechs einzelnen Jets, wobei man von zwei der sechs Jets annimmt, daß sie etwas niederenergetischer sind, da sie vom Zerfalls des virtuellen W-Bosons herrühren. Die möglichen Standardmodelluntergründe sind $q\bar{q}$-Prozesse mit Abstrahlung mehrerer Gluonen sowie voll hadronisch zerfallende 4-Fermion Prozesse wie $e^+e^- \to W^+W^-$ oder $e^+e^- \to ZZ$, bei denen entweder Gluonen abgestrahlt werden oder deren Ereignisform auch eine Jetrekonstruktion mit sechs Jets zuläßt.

In dieser Analyse wird eine zweistufige Vorselektion verwendet. In der ersten Stufe werden hadronische Ereignisse mit mehreren (> 3) Jets und einer sichtbaren Energie nahe der Schwerpunktsenergie selektiert. In einer zweiten Stufe werden Ereignisse selektiert, bei denen eine Jetrekonstruktion mit sechs Jets möglich ist und die auch die erwartete Ereignisform des Signals aufweisen. Zur guten Trennung zwischen Signal und Untergrund wird hier ein neuronales Netzwerk zur Ereignisklassifikation verwendet. Am Ende dieser Analyse ist auch hier keine Evidenz für ein Signal vorhanden.

Auch in diesem Kanal wird eine Massenausschlussgrenze mit 95% Vertrauensintervall berechnet, unter der Annahme eines Zerfalls von 100% in WW^*. Dazu wurden die Ergebnisse dieser Analyse mit den Ergebnissen der Analysen in den Kanälen $H \to WW^* \to q\bar{q}'l\nu_l q\bar{q}$ [Reh03] und $H \to WW^* \to q\bar{q}'q\bar{q}'\nu\bar{\nu}$ [Dal03] kombiniert. Diese beiden Kanäle tragen mit 20% beziehungsweise 9% zum gesamten Verzweigungsverhältnis bei. Nach der Kombination aller Kanäle kann keine beobachtete Massenausschlussgrenze gesetzt werden, die erwarte Massenausschlussgrenze liegt bei 101.7 GeV/c^2. Das Fehlen einer beobachteten Massengrenze wird durch einen leichten Überschuß signifikanter Kandidaten im Kanal $H \to WW^* \to q\bar{q}'l\nu_l q\bar{q}$ [Reh03] verursacht. Zusätzlich wurde auch die

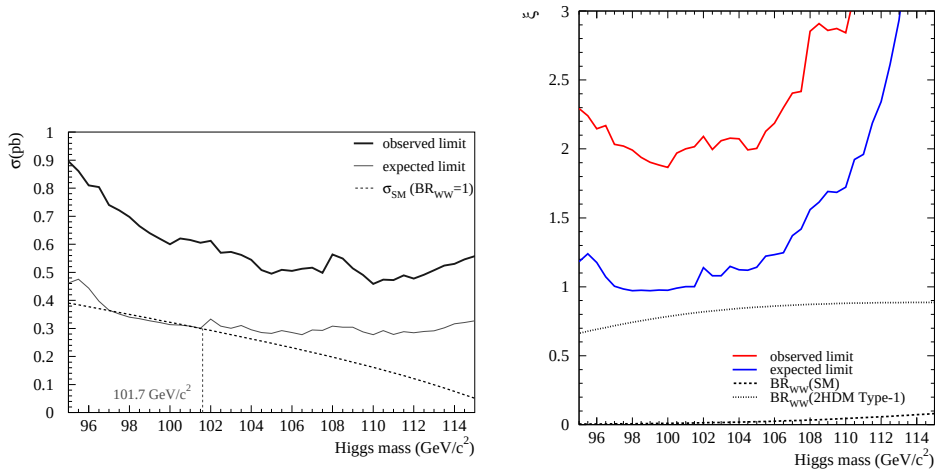

(a) **(b)**

Abbildung 7: Der ausgeschlossen Wirkungsquerschnitt für den Prozess $e^+e^- \to HZ$ $(H \to WW^* \to f\bar{f}'f\bar{f}')(Z \to \text{alles})$ in Abhängigkeit von der Higgsmasse (a) und der ausgeschlossene Unterdrückungsfaktor ξ für $H \to WW^* \to f\bar{f}'f\bar{f}'$ in Abhängigkeit von der Higgsmasse (b). Zusätzlich gezeigt sind die vorhergesagte Verzweigungsverhältnisse für $H \to WW^* \to f\bar{f}'f\bar{f}'$ im Standardmodell und im fermiophobischen Modell.

allgemeinere Ausschlussgrenze mit 95% Vertrauensintervall auf den Wirkungsquerschnittes für den Prozess $e^+e^- \to HZ$ $(H \to WW^* \to f\bar{f}'f\bar{f}')(Z \to \text{alles})$ berechnet. Das Ergebnis ist in Abbildung 7a zu sehen. In Abbildung 7b ist das ausgeschlossene Verzweigungsverhältnis in WW^* zu sehen, unter der Voraussetzung, dass der Standardmodell-Wirkungsquerschnitt gilt. Zusätzlich eingezeichnet sind die erwarteten Verzweigungsverhältnisse im Standardmodell und in einem fermiophobischen Modell. Deutlich sichtbar ist, dass die Analyse auf WW^*-Zerfälle im Standardmodell nicht sensitiv wäre. In beiden Abbildungen ist der Effekt des leichten Überschusses signifikanter Kandidaten deutlich sichtbar.

1.6 Zusammenfassung

In dieser Arbeit wurden Suchen nach sichtbaren und unsichtbaren Higgszerfällen in den Daten des DELPHI-Detektors durchgeführt. Kein Hinweis auf ein Signal wurde gefunden. Deswegen wurden Massenausschlußgrenzen mit 95% Vertrauensintervall berechnet, die in Tabelle 1 zusammengefasst sind.

Die Suche nach dem Higgs-Boson wird fortgesetzt werden und wenn es existiert, dann wird es höchstwahrscheinlich mit dem LHC[6] gefunden werden. Um

[6] **L**arge **H**adron **C**ollider

Kanal	Massenausschlussgrenze (in GeV/c^2)	
	beobachtet	erwartet
$H \rightarrow$ unsichtbar	112.1	110.5
$H \rightarrow$ sichtbar+unsichtbar	111.8	109.3
$H \rightarrow$ hadronisch	110.6	108.0
$H \rightarrow WW^*$	-	101.7

Tabelle 1: Massenausschlußgrenzen der verschiedenen Analysen mit 95% Vertrauensintervall.

die genaue Natur des Higgs-Boson zu bestimmen, wird ein Linearbeschleuniger wie TESLA[7] notwendig sein. Erst mit einer solchen Maschine lassen sich die Masse, Verzweigungsverhältnisse und Kopplungen präzise genug vermessen, um solche Fragen zu beantworten.

[7] **T**era Electron Volt **E**nergy **S**uperconducting **L**inear **A**ccelerator

IEKP-KA/2003-12

Searches for visible and invisible Higgs decays with the DELPHI detector at LEP2

Marcel Stanitzki

Zur Erlangung des akademischen Grades eines
DOKTORS DER NATURWISSENSCHAFTEN
von der Fakultät für Physik der
Universität Karlsruhe(TH)

genehmigte

DISSERTATION

Tag der mündlichen Prüfung: 09.05.2003

Referent: Prof. Dr. W. de Boer, Institut für Experimentelle Kernphysik

Korreferent: Prof. Dr. G. Quast, Institut für Experimentelle Kernphysik

Contents

List of Figures

List of Tables

Introduction

I was able to see further, because I was
standing on the shoulders of giants
(Sir Isaac Newton)

Since almost 30 years, the Standard Model of particle physics has been very successful in describing the particles and interactions, which are accessible at present colliders. At the time of its birth, the Standard Model predicted the existence of heavy gauge bosons as mediators of the weak interaction, which is for example responsible for the nuclear β decay. In order to obtain a theoretically consistent model, a new mechanism of spontaneous symmetry breaking had to be used, the so-called Higgs mechanism. This mechanism made it possible to have a gauge invariant theory with massive bosons, which is not possible without it. Additionally the Higgs mechanism also gives mass to the before massless fermions via the Yukawa couplings.

The consistency of the Standard Model was proven with the discovery of these massive gauge bosons $W^{\pm}$ and Z with the SPS[8] collider at CERN[9] in 1983 [UA183a, UA183b, UA185]. At this time the number of fermion families was still an open question until the four experiments at the LEP[10] collider at CERN finally established the existence of exactly three Standard Model fermion families in 1990. At that time two out of twelve fermions had not been observed directly. The mass of the heaviest quark, the top quark, has been predicted with remarkable accuracy using the LEP precision data and was then found by the CDF[11] experiment at the Fermilab Tevatron collider in 1994 [CDF95]. The last missing fermion, the τ neutrino has then been experimentally established in 2000 by the DONUT[12] [DON01] experiment. At present all but one particle predicted by the Standard Model have been experimentally observed. But the particle related to the key ingredient of the Standard Model, the Higgs boson, has not been observed yet. The mass of the Higgs boson is one of the free parameters in the Standard Model which can not be predicted by theory. The only constraints for its mass come from experimental results, either direct searches for a Higgs boson or fits to the Standard Model using the available precision data. This constrains the mass of a Standard Model Higgs boson

[8] **S**uper **P**roton **S**ynchrotron
[9] **C**onseil **E**uropènne pour la **R**echerche **N**uclèaire
[10] **L**arge **E**lectron **P**ositron collider
[11] **C**ollider **D**etector at **F**ermilab
[12] **D**irect **O**bservation of the ν_τ

between 114.4 GeV/c^2 [LEP03] and 193 GeV/c^2 [LEP02]. The Standard Model predicts, that the Higgs boson decays predominantly in the heaviest particle pairs accessible. The direct searches at LEP therefore focus on the decay into a pair of b quarks or τ leptons which are the dominant decay modes for the mass range accessible at LEP ($\approx$ 5 - 115 GeV/c^2).

The Standard Model, albeit its huge success in describing all kind of particle interactions up to present energy scales, is not considered to be the ultimate theory in particle physics. Especially in the Higgs sector many extensions can be made, which can lead to modified Higgs couplings or completely new decay modes. Well known extensions to the Standard Model are the Minimal Supersymmetric Standard Model (MSSM), the Two Higgs Doublet Model (2HDM) and Majoron models. All these models predict decay possibilities of the Higgs boson, to which the present searches for Standard Model Higgs bosons at LEP would be insensitive to, like a Higgs decay into particles that do not interact with the detector (*invisible decay*) or visible decay modes like a hadronic decay of the Higgs without the preference of a b quark decay (*flavourblind decay*) and the decay into heavy gauge bosons (*fermiophobic decay*).

In this thesis, such decays have been searched for in data taken with the DELPHI[13] detector, which is one of the four LEP detectors. The data analysed in this thesis were taken between 1998 and 2000 at centre-of-mass energies between 189 and 209 GeV/c^2. In November 2000 the data taking at LEP ended and the detector was dismantled.

This thesis is organised as follows: In the first chapter a short summary of the Standard Model is given, while in chapter 2 the three extensions to the Standard Model relevant for this thesis are briefly introduced. In chapter 3 the phenomenological consequences of these models for the Higgs production and decay in e^+e^- collisions at LEP are explained. The main focus in this chapter lies on the Higgs-Strahlung production process, in which the Higgs boson is accompanied by a Z gauge boson. This process is the main production process in the Standard Model and plays also an important role in all extended models considered in this thesis.

The LEP collider, the DELPHI detector and the DELPHI data acquisition are described in chapter 4. As the production of a Higgs boson produced at LEP is not a background-free process, one needs a reliable description of the background due to Standard Model processes. This is obtained using Monte Carlo event generators, which are described in chapter 5. The tools to reconstruct the events recorded by DELPHI are also introduced there. The possible Higgs signal is very small compared to the background coming from Standard Model processes, so advanced methods like Iterative Discriminant Analyses or Neural Networks were used in order to effectively separate between the Standard Model background and a possible Higgs signal. These methods are also introduced in this chapter. At the end of each search without clear evidence for a signal, one would like to set an exclusion limit on the Higgs mass. This is done using the statistical method of confidence level limits, which is also explained

[13] **DE**tector with **L**epton, **P**hoton and **H**adron **I**dentification

in this chapter.

The main goal of the three analyses conducted in the framework of this thesis is to exclude a signature and not a specific model. By giving general cross-section limits, any model or scenarios can than be tested using its predicted cross section. The analyses in this thesis can be separated into two groups, the final states with two jets and missing energy and the multi-jet final states.

In chapter 6 the search for a Higgs boson decaying into invisible final states and the Z boson decaying into two quarks is described. The signature observed in the detector is two jets originating from the Z and missing energy from the invisible Higgs decays. The results are used to exclude such scenarios in the MSSM or in Majoron models.

The second search presented in chapter 7 is closely related to the search for an invisible Higgs decay, but in this case the Higgs decays into two quarks, which form the two jets and the Z decays into two neutrinos, which are then responsible for the missing energy. In order not to focus on a specific hadronic decay mode, a general hadronic Higgs boson signal has been constructed combining different hadronic decay modes like decays into light quarks, heavy quarks and gluons. Using this, a very general limit on a hadronic decay and additionally limits on the light quark, heavy quark and gluon modes can be set.

The third search presented in chapter 8 is quite different from the two searches described before. In this case a multi-jet final state is searched for due to Higgs decaying into a pair of W bosons which subsequent decay into four quarks. The accompanying Z boson is also decaying into two quarks. This leads to a 6 jet signature in the detector. The coupling of the Higgs to the W boson is more fundamental than the couplings to the fermions, since the generation of mass for the W bosons is the main reason for the Higgs mechanism. So its existence is a key ingredient to Standard Model and Standard Model like scenarios. The results obtained in this analysis were then used to set limits on the cross-section for such a process and to exclude fermiophobic scenarios in the framework of a general 2HDM.

Chapter 1

The Standard Model

The theoretical foundation of particle physics is quantum field theory. All interactions and particles known in particle physics today are described using the means of quantum field theory. The knowledge of particle physics is then put together in a theoretical model, called the Standard Model. In this chapter an introduction to the theoretical foundations of the Standard Model is given and the basic interactions and particles included in the Standard Model are described.

In physics, one separates between two kinds of fundamental particles: the fermions with half integer spins and the bosons with an integer spin. The fermions are the constituents of matter, while the bosons mediate the forces between them. The fermions can be grouped into so-called generations. Each of the three generations contains two quarks and two leptons. All the atoms and nuclei one observes in nature are built up only from members of the first generation. The heavier quarks and charged leptons of the second and third generation can all decay into the lighter particles of the first generation and are therefore unstable. Tab. 1.1 gives an overview of all Standard Model fermions. Since neutrinos are considered massless in the Standard Model, only left-handed neutrinos are included.

Bosons of various kinds are the mediators of the four fundamental interactions: the electromagnetic, the weak, the strong and the gravitational interaction. The Standard Model includes a description of the first three, while gravitation is usually described in Einstein's General Relativity, although General Relativity does not include a graviton. The graviton is introduced in quantum gravity, in analogy to the other three interactions. Since gravity is weak on the scale accessible in particle accelerators, gravity effects are neglected in the Standard Model. Another big difference between gravity and the other three interactions is the spin of the mediator. The graviton as the mediator of gravity has spin 2, while all other mediators have spin 1. A summary about the properties of the Standard Model bosons is shown in Tab. 1.2.

Before coming to the Standard Model in detail, an introduction to the fundamental gauge principle is given.

1	2	3	Q	I_3	Y
$\begin{pmatrix} \nu_e \\ e \end{pmatrix}_L$	$\begin{pmatrix} \nu_\mu \\ \mu \end{pmatrix}_L$	$\begin{pmatrix} \nu_\tau \\ \tau \end{pmatrix}_L$	$\begin{pmatrix} 0 \\ -1 \end{pmatrix}$	$\begin{pmatrix} +\frac{1}{2} \\ -\frac{1}{2} \end{pmatrix}$	-1
$(e)_R$	$(\mu)_R$	$(\tau)_R$	-1	0	-2
$\begin{pmatrix} u \\ d' \end{pmatrix}_L$	$\begin{pmatrix} c \\ s' \end{pmatrix}_L$	$\begin{pmatrix} t \\ b' \end{pmatrix}_L$	$\begin{pmatrix} +\frac{2}{3} \\ -\frac{1}{3} \end{pmatrix}$	$\begin{pmatrix} +\frac{1}{2} \\ -\frac{1}{2} \end{pmatrix}$	$+\frac{1}{3}$
$(u)_R$	$(c)_R$	$(t)_R$	$+\frac{2}{3}$	0	$+\frac{4}{3}$
$(d)_R$	$(s)_R$	$(b)_R$	$-\frac{1}{3}$	0	$-\frac{2}{3}$

Table 1.1: The three generations of Standard Model fermions. Shown are the electric charge Q, the third component of the weak isospin I_3 and the weak hypercharge Y. The indices L and R indicate the chirality of the particles.

1.1 The gauge principle

To study the effect of gauge invariance, one studies the influence of phase transformations on a wave function $\psi(x)$ [Sch95]. There are two kinds of such transformations, the global phase transformation with the phase α

$$\psi'(x) = e^{i\alpha}\psi(x) \tag{1.1}$$

and the local phase transformation with the phase $\chi(x)$

$$\psi'(x) = e^{iq\chi(x)}\psi(x) \tag{1.2}$$

where q represents the electrical charge. The global transformation leaves the structure of the equation untouched. Applying a local phase transformation and putting it into the Dirac equation

$$(i\gamma^\mu\partial_\mu - m)\psi(x) = 0 \tag{1.3}$$

one yields

$$(i\gamma^\mu\partial_\mu - m)\psi'(x) = -q\gamma^\mu\partial_\mu\chi(x)\psi'(x)$$

The transformed equation does not describe a particle in a vacuum anymore but in an electromagnetic field. Demanding local gauge invariance can not be fulfilled in a vacuum. One needs an additional vector field, which is also transformed.

$$\psi'(x) \quad = e^{iq\chi(x)}\psi(x) \tag{1.4}$$

$$A'_\mu \quad = A_\mu - \partial_\mu\chi(x) \tag{1.5}$$

Boson	Interaction	Amount	Spin	Mass	el. charge
Photon γ	electromag.	1	1	0 $< 2 \cdot 10^{-16}$ eV	0
$W^{\pm}$	weak	2	1	80.394 ± 0.019 80.449 ± 0.034	± 1
Z^0	weak	1	1	$M_W / \cos(\theta_w)$ 91.188 ± 0.002	0
Gluons g	strong	8	1	0 $\mathcal{O}$(MeV)	0
Graviton G	gravitational	1	2	? ?	0

Table 1.2: The bosons of the four fundamental interactions. For the masses of the bosons both the theoretical expected (upper value) and the experimental measured values from the Particle Data Book [Hag02] (lower value) are given. For the theoretical value of the W mass, the result of the fit from the Electroweak Working Group [LEP02] is given.

In order to couple the charged particle wave function and the electromagnetic field, one introduces the covariant derivative

$$D_\mu = \partial_\mu + iqA_\mu \tag{1.6}$$

into the Dirac equation.

$$(i\gamma^\mu D_\mu - m)\psi(x) = 0 \Rightarrow (i\gamma^\mu \partial_\mu - m)\psi(x) = q\gamma^\mu A_\mu(x)\psi(x) \tag{1.7}$$

The local phase transformations considered above belong mathematically to the $U(1)$ group. This means, that the transformations are unitary ($UU^\dagger = 1$) and one-dimensional. $U(1)$ groups are moreover abelian, so their generators commutate. One can also demand local gauge invariance for the $SU(N)$ groups, which play an important role in the Standard Model. The $SU(N)$ groups fulfil the condition $\det U = 1$. The local phase transformations for the $SU(2)$ group have the following form:

$$\psi'(x) = e^{i\frac{g}{2}\vec{\tau}\cdot\vec{\beta}(x)}\psi(x) \tag{1.8}$$

$$\vec{W}'_\mu(x) = \vec{W}_\mu(x) - \partial_\mu\vec{\beta}(x) - g(\vec{\beta}(x) \times \vec{W}_\mu(x)) \tag{1.9}$$

$\vec{\tau}$ stands for the Pauli-Matrices and $\vec{W}_\mu(x)$ stands for the vector fields. The covariant derivative for $SU(2)$ is:

$$D_\mu = \partial_\mu + i\frac{g}{2}\vec{\tau}\cdot\vec{W}_\mu \tag{1.10}$$

The only difference to the $U(1)$ group is the term $g(\vec{\beta}(x)\times\vec{W}_\mu(x))$, which results from the nonabelian character of the $SU(2)$. The covariant derivative of $SU(3)$ and more general representations can be found for example in [Gri87, Sch95].

All the vector fields considered up to now are massless. If one takes the following equation for a photon:

$$\Box A^\nu - \partial^\nu \partial_\mu A^\mu = j^\nu \tag{1.11}$$

it is invariant under $U(1)$ transformations. If one takes the equation for a massive vector field W,

$$(\Box + M^2)W^\nu - \partial^\nu \partial_\mu W^\mu = j^\nu \tag{1.12}$$

one immediately obtains, that this equation is not gauge invariant.
This results in a general rule:

Local gauge invariance is not possible for massive vector fields

This has severe consequences for the structure of the Standard Model, since one knows from experiment, that both W and Z bosons are massive.

1.2 The Standard Model

One refers to the Standard Model as the combination of Quantum Chromodynamics (QCD), the theory of the strong interactions, and the electroweak interactions, which results of the unification of Quantum Electrodynamics (QED) and the theory of the weak interaction. One writes the Group of the Standard Model as

$$S = SU(3)_C \otimes SU(2)_L \otimes U(1)_Y \tag{1.13}$$

In this section a short summary about the two main components of the Standard Model is given. After that, one of the central mechanisms of the Standard Model, the Higgs mechanism, is described in detail.

1.2.1 Quantum Chromodynamics

Quantum Chromodynamics describe the interactions between the quarks and gluons. The static quark model came up in the sixties of the 20th century, when Gell-Mann [GM62, GM64] and Zweig[Zwe64] discovered that all known mesons and baryons (the so-called hadrons) could be described using quark multiplets of three quarks (u, d and s). The baryons like the proton were described as qqq-states, while the mesons like the pion were described as $q\bar{q}$ states. The existence of quarks was proven some years later, after electron-proton scattering showed a proton substructure. The quark model was finally accepted with the discovery of the J/ψ meson in 1974 [Aub74], which represents a $c\bar{c}$ bound state.

The quark model still had one problem. It violated the Pauli principle in the case of baryons consisting of three quarks with the same flavour, e.g. Δ^{++} (uuu), Δ^- (ddd) or Ω^- (sss). In order to conserve the Pauli principle, a new quantum number, the colour charge was introduced. There are three colour charges: red, green and blue. In order to explain why all observed particles

are colourless, a simple rule is introduced. Mesons are made up of a colour-anticolour ($red\ \overline{red}$ ..) $q\bar{q}$ state and are therefore colourless, while baryons consist out of a red-green-blue qqq-state which adds up to white, which also means colourless. This rule also explains why there are no qq or $qqqq$ states or why free quarks do not exist in nature. In order to describe the three colour charges, the $SU(3)_{Colour}$ group is introduced.

The covariant derivative and the local phase transformation of the vector fields are:

$$D^{\mu} = \partial^{\mu} + i\frac{g_S}{2}\lambda_j G_j^{\mu} \tag{1.14}$$

$$G_j'^{\mu} = G_j^{\mu} - \partial^{\mu}\beta_j - g_S f_{jkl}\beta_k G_l^{\mu} \tag{1.15}$$

The β_j are the eight angles of the transformation, g_S is the coupling constant, the λ_j are the eight Gell-Mann-Matrices and the G_l^{μ} are the eight gluon fields. The eight fields result from demanding $\det U = 1$.

The bosons of the $SU(3)_{Colour}$, the gluons, are also carrying colour charge and can therefore interact with themselves. This is the physical manifestation of the nonabelian character of the $SU(3)_{Colour}$. The three fundamental vertices of QCD are shown in Fig. 1.1. The self interaction is also the reason for the quark

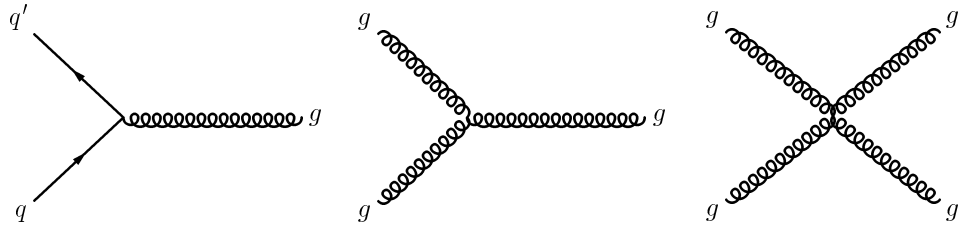

Figure 1.1: The three fundamental QCD vertices: quark-quark-gluon-interaction (a), the 3-gluon-interaction (b) and the 4-gluon-interaction (c).

confinement and the asymptotic freedom. The coupling constant of QCD,

$$\alpha_S = \frac{g_S^2}{4\pi} \tag{1.16}$$

is not constant, but is strongly depending upon the momentum transfer Q^2. for $Q^2 \to \infty$, which means small distances, α_S approaches 0. This has the effect that quarks behave like free particles if Q^2 is large. This behaviour is called asymptotic freedom. For small Q^2, which means large distances, the quarks are enclosed within the hadrons. This effect, which cannot be described by usual perturbation theory, is called confinement.

1.2.2 Electroweak interactions

The theory of electroweak interactions was first introduced by Glashow, Weinberg and Salam [Gla61, Wei67, Sva68]. Using this theory, it was possible to have an uniform description of the electromagnetic and weak interactions for the first time. In order to describe the weak interactions, one has to consider the experimental results:

- The violation of parity conservation by the weak interaction. Left handed particles are preferred by the weak interaction. This was shown for the first time in the famous Wu experiment [Wu57].
- The weak interaction has a very short range.
- There are neutral and charged weak interactions. The charged currents are known for quite some time now (e.g. β decay), the neutral currents have been discovered in the begin of the seventies at CERN.

In order to meet these requirements by the experiments, the fermions are put together in doublets and singlets, as shown in Tab. 1.1. The index L indicates, that the doublets are left-handed and the index R indicates that the singlets are right-handed. The singlets do not take part in charged weak interactions. The chirality is introduced by the following projection operators:

$$P_L = \frac{1-\gamma^5}{2} \tag{1.17}$$

$$P_R = \frac{1+\gamma^5}{2} \tag{1.18}$$

The electromagnetic interaction on the other hand does not separate between left- and right-handed particles. This has to be taken into account for the gauge transformations. The gauge transformations are members of the $SU(2)_L \otimes U(1)_Y$ group. As the goal is an unified electroweak theory, one must not use $U(1)_{Charge}$, but has to introduce a new quantity hypercharge Y

$$Q = I_3 + \frac{Y}{2} \tag{1.19}$$

using the Gell-Mann-Nishijima relation. Y is then constructed of the charge Q and the third component of the weak isospin I_3. By using the charge Q only, the electric charge of the charged leptons and the neutrinos has to be the same and neutral weak currents would be completely left-handed. One obtains for the $SU(2)_L$ transformations:

$$\begin{pmatrix} \nu_e \\ e \end{pmatrix}'_L = e^{i\frac{g}{2}\vec{\tau}\cdot\vec{\beta}(x)} \begin{pmatrix} \nu_e \\ e \end{pmatrix}_L \tag{1.20}$$

$$e'_R = e_R \tag{1.21}$$

with the coupling constant g, the three Pauli-matrices τ_i and and the three transformation angles of the $SU(2)$, $\beta_i(x)$. The $U(1)_Y$ transformations are :

$$\begin{pmatrix} \nu_e \\ e \end{pmatrix}'_L = e^{i\frac{g'}{2}Y_L\cdot\chi(x)} \begin{pmatrix} \nu_e \\ e \end{pmatrix}_L \tag{1.22}$$

$$e'_R = e^{i\frac{g'}{2}Y_R\cdot\chi(x)} e_R \tag{1.23}$$

the coupling constant here is g′ and $Y_{(L,R)}$ is the newly introduced quantity hypercharge, which has different values for left- and right-handed particles. Using this, one can write the covariant derivate as:

$$D^\mu = \partial^\mu + g\vec{T}\cdot\vec{W}^\mu + i\frac{g'}{2}YB^\mu \tag{1.24}$$

For $\vec{T}$ one has to consider two cases:

$$\vec{T} = \frac{1}{2}\vec{\tau} \ (\text{left} - \text{handed}) \tag{1.25}$$

$$\vec{T} = 0 \ (\text{right} - \text{handed}) \tag{1.26}$$

The electroweak theory introduces four vector fields, the three W^μ fields and the B^μ field. All the fields are still massless in order to be locally gauge invariant. The Lagrangian of the electroweak interaction has four components:

$$\mathcal{L} = \mathcal{L}_{Gauge} + \mathcal{L}_{Fermion} + \mathcal{L}_{Higgs} + \mathcal{L}_{Yukawa} \tag{1.27}$$

The last two parts will be discussed in detail in section 1.2.3. For the Lagrangian of the gauge field $\mathcal{L}_{Gauge}$:

$$\mathcal{L}_{Gauge} = -\frac{1}{4}F^i_{\mu\nu}F^{i\mu\nu} - \frac{1}{4}f_{\mu\nu}f^{\mu\nu} \tag{1.28}$$

The $F^i_{\mu\nu}$ and $f_{\mu\nu}$ are the field tensors of the $SU(2)_L$ and the $U(1)_Y$:

$$F^i_{\mu\nu} = \partial_\mu W^i_\nu - \partial_\nu W^i_\mu - g\epsilon_{ijk}W^j_\mu W^k_\nu \tag{1.29}$$

$$f_{\mu\nu} = \partial_\mu B_\nu - \partial_\nu B_\mu \tag{1.30}$$

The Lagrangian of the fermions $\mathcal{L}_{Fermion}$ has the following form:

$$\mathcal{L}_{Fermion} = \sum_{\psi_L}\bar{\psi}_L i\gamma^\mu D_\mu\psi_L + \sum_{\psi_R}\bar{\psi}_R i\gamma^\mu D_\mu\psi_R \tag{1.31}$$

Up to now all fields and particles are massless, which results from demanding local gauge invariance. Another reason for demanding local gauge invariance is - as has been shown in the beginning of the seventies by t'Hooft [tH72] that abelian and nonabelian gauge theories can be renormalised[1]. The intermediate gauge bosons of the weak interaction on the other hand are massive and heavy, which can be deduced by the short range of weak interactions. Demanding both local gauge invariance and massive vector bosons seems to be impossible. With the help of spontaneous symmetry breaking by the Higgs mechanism, one can fulfil both requirements.

[1] For their contributions in this field, the Nobel price for physics 1999 has been awarded to G. t'Hooft and M. Veltman

1.2.3 The Higgs mechanism

The Higgs mechanism [Hig64] has been introduced by Weinberg into the theory of electroweak interactions. Originally it was a relativistic extension of the Ginzburg-Landau-Model [Gin50] of superconductivity. The Higgs mechanism *hides* local gauge invariance [Qui99] in order to give mass to electroweak gauge bosons. It introduces a potential V with a complex scalar field Φ

$$V(\Phi) = \mu^2 \Phi^\dagger \Phi + \lambda^2 (\Phi^\dagger \Phi)^2 \tag{1.32}$$

This potential only contains even terms in order to preserve the symmetry with respect to the $\Phi = 0$ axis. Terms of higher order like $(\Phi^\dagger \Phi)^4$ are not included either, because they would lead to renormalisation problems. The contributions of those terms to the potential close to 0 would be negligible anyway [Kaz99]. For $\mu^2 < 0$ the Higgs potential has minima at:

$$|\Phi| = \frac{v}{\sqrt{2}} \quad , v = \frac{\mu}{\lambda} \tag{1.33}$$

For Φ one chooses in the Standard Model a doublet with respect to the weak

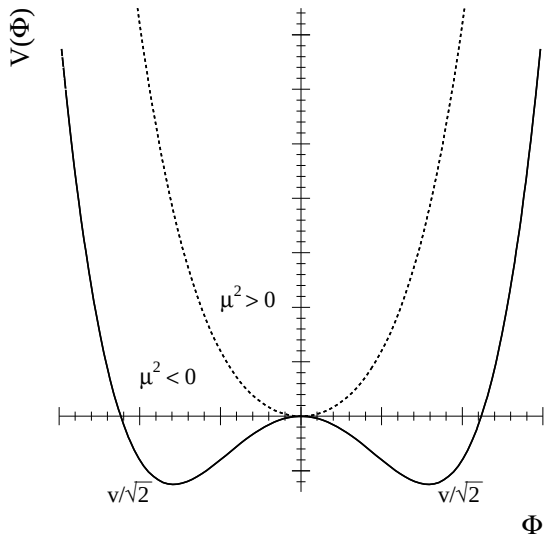

Figure 1.2: The Higgs potential $V(\Phi(x))$ for $\mu^2 > 0$ and $\mu^2 < 0$. For $\mu^2 > 0$ the symmetry is unbroken and only 0 exists as a trivial minimum. For $\mu^2 < 0$ the symmetry is broken and nontrivial minima exist. The Higgs potential has now the well known mexican hat shape.

isospin (I=1/2, Y=1):

$$\Phi = \begin{pmatrix} \Phi^+ \\ \Phi^0 \end{pmatrix} \tag{1.34}$$

The coupling to the gauge boson fields is achieved by using the covariant derivative. The Lagrangian is written:

$$\mathcal{L}_{Higgs} = (D^{\mu}\Phi)^{\dagger}(D_{\mu}\Phi) - V(\Phi) \tag{1.35}$$

This Lagrangian is gauge invariant under $SU(2)$ and $U(1)$ transformations. One now assumes, that the vacuum expectation value of the neutral Higgs field Φ^0 is not equal 0, while the vacuum expectation value of the charged Higgs field Φ^+ is 0. This is necessary in order to keep $U(1)$ symmetry unbroken and therefore avoid massive photons. This constraint leads to a minimum:

$$\Phi_0 = \frac{1}{\sqrt{2}} \begin{pmatrix} 0 \\ v \end{pmatrix} \tag{1.36}$$

If one considers now excitations around the groundstate, gauge invariance allows to choose:

$$\Phi(x) = \frac{1}{\sqrt{2}} \begin{pmatrix} 0 \\ v + \eta(x) \end{pmatrix} \tag{1.37}$$

The mass of the gauge bosons

Putting this potential into the Lagrangian $\mathcal{L}_{Higgs} + \mathcal{L}_{Gauge}$ and using the identities

$$W^{\mu\pm} = \frac{1}{\sqrt{2}}(W_1^{\mu} \pm iW_2^{\mu}) \tag{1.38}$$

$$\begin{pmatrix} A^{\mu} \\ Z^{\mu} \end{pmatrix} = \begin{pmatrix} \cos\theta_W & \sin\theta_W \\ -\sin\theta_W & \cos\theta_W \end{pmatrix} \begin{pmatrix} B^{\mu} \\ W_3^{\mu} \end{pmatrix} \tag{1.39}$$

one obtains

$$\mathcal{L} = \left[\frac{1}{2}(\partial^{\mu})(\partial_{\mu}) - \mu^2\eta^2\right] - \frac{1}{4}F^i_{\mu\nu}F^{i\mu\nu} - \frac{1}{4}f_{\mu\nu}f^{\mu\nu} + \frac{1}{2}\cdot\frac{g^2v^2}{4}\left(\left|W_{\mu}^{+}\right|^2 + \left|W_{\mu}^{-}\right|^2\right) + \frac{1}{2}\cdot\frac{g^2v^2}{4\cos^2\theta_W}\left|Z_{\mu}\right|^2 \tag{1.40}$$

θ_W is the so-called Weinberg or weak mixing angle, which is defined by the relation:

$$\cos\theta_W = \frac{g}{\sqrt{g^2 + g'^2}} \tag{1.41}$$

The gauge bosons of the weak interactions have obtained mass through the spontaneous symmetry breaking by the Higgs mechanism, while the photon is still massless as required. The mass of the charged W boson is

$$M_W = \frac{gv}{2} \tag{1.42}$$

The mass of the neutral Z boson is connected to the mass of the W boson

$$M_Z = \frac{gv}{2\cos\theta_W} = \frac{M_W}{\cos\theta_W} \tag{1.43}$$

In the term for A^μ there does not occur any mass term:

$$A^\mu = \frac{1}{\sqrt{g^2 + g'^2}}(gB^\mu + g'W^{3\mu}) \tag{1.44}$$

The vacuum expectation value v can not be directly calculated, it has to be obtained from measurements using of the Fermi constant G_F

$$v = \frac{1}{\sqrt[4]{2} \cdot \sqrt{G_F}} \approx 246 \text{ GeV} \tag{1.45}$$

Symmetry breaking also involves another effect, the so-called Goldstone-Theorem [Gol62]. If one breaks a continuous global gauge invariance, one gets according to Goldstone one or more scalar and massless bosons, the so-called Goldstone bosons. If one breaks a local gauge invariance, the Goldstone boson disappears, because it can be eliminated by the proper choice of the gauge. This becomes clear, if one looks at the degrees of freedom before and after breaking the symmetry. Before breaking the symmetry one has the following degrees of freedom:

- 4 massless vector fields $(W^{i\mu}, B^\mu)$ with two degrees of freedom each.
- 2 complex Higgs fields (Φ^+, Φ^0) with two degrees of freedom.

So one obtains 12 degrees of freedom altogether. After symmetry breaking this has changed due to the massive vector fields.

- 3 massive vector fields $(W^{\mu\pm}, Z^\mu)$ with three degrees of freedom each.
- 1 massless vector field $A^\mu$with two degrees of freedom each.
- 1 scalar Higgs field with one degree of freedom.

One gets 12 degrees of freedom again, as before the symmetry breaking. The massive gauge bosons obtained the third degree of freedom by eliminating the three Goldstone bosons.

The masses of the fermions

Till now, only the gauge bosons have obtained mass via the Higgs mechanism, the fermions are still massless. In order to give mass to the fermions, one introduces the Yukawa couplings [dB94]. The Yukawa part of the Lagrangian for the leptons is:

$$\mathcal{L}_{Yukawa} = -\tilde{g}_l \left(\bar{L}\Phi l_R + \bar{l}_R \Phi^\dagger L\right) \tag{1.46}$$

Putting in the vacuum expectation value of Φ, the lepton doublets and singlets, one obtains:

$$\mathcal{L}_{Yukawa} = -\frac{\tilde{g}_l v}{\sqrt{2}}\bar{e}e \tag{1.47}$$

which corresponds to a leptons mass:

$$M_l = \tilde{g}_l \frac{v}{\sqrt{2}} \tag{1.48}$$

The charged lepton are now massive, while the neutrinos are still massless[2]. For the quarks the procedure is quite similar, but one has to consider additionally that all quarks are massive and that the quarks are mixed. The weak eigenstates of the down-type quarks (d, s, b) are not the same as the mass eigenstates. This is, because the weak interaction only conserves flavour in neutral weak processes. For charged weak currents this does not apply. Otherwise bound states consisting of members of the second or third family would have an extremely long lifetime. The eigenstates of the weak interactions are connected with the mass eigenstates via the Cabbibo-Kobayashi-Maskawa (CKM) matrix [Kob73].

$$\begin{pmatrix} d' \\ s' \\ b' \end{pmatrix}_L = \begin{pmatrix} V_{ud} & V_{us} & V_{ub} \\ V_{cd} & V_{cs} & V_{cb} \\ V_{td} & V_{ts} & V_{tb} \end{pmatrix} \cdot \begin{pmatrix} d \\ s \\ b \end{pmatrix}_L \tag{1.49}$$

The matrix elements of the CKM matrix can not be calculated from the Standard Model, they have to be measured by experiments. This is one of the reasons, why one is looking for extensions of the Standard Model. An interesting consequence from the Higgs mechanism and the fermion mass generation is, that the Yukawa couplings of the fermions to the Higgs boson depend on the fermion mass, so the Higgs bosons then also decays preferably in the heaviest fermions (see chapter 3.1).

The mass of the Higgs boson

The mass of the Higgs boson in the Standard Model is given as:

$$M_H = \sqrt{2}\mu \tag{1.50}$$

The parameter μ cannot be calculated in the Standard Model framework, which is the reason, why the Higgs mass is unknown in the Standard Model. The mass can only be constrained by theoretical assumptions. One of these assumptions is the unitarity limit in the process $e^+e^- \rightarrow W^+W^-$. The cross-section for this process diverges at high energies, if one does not add a graph with a Higgs boson exchange. Using this, one can give an upper limit on M_H:

$$M_H \leq \frac{8\pi\sqrt{2}}{3G_F} \approx 1 \text{ TeV} \tag{1.51}$$

If M_H is lighter than this limit, then the behaviour of the weak interaction is independent of the energy scale. If not, then the gauge bosons of the weak interaction show a similar behaviour like the strong interaction at the 1 TeV

[2] Although there is experimental evidence for neutrino masses today, the neutrinos are considered massless in the SM.

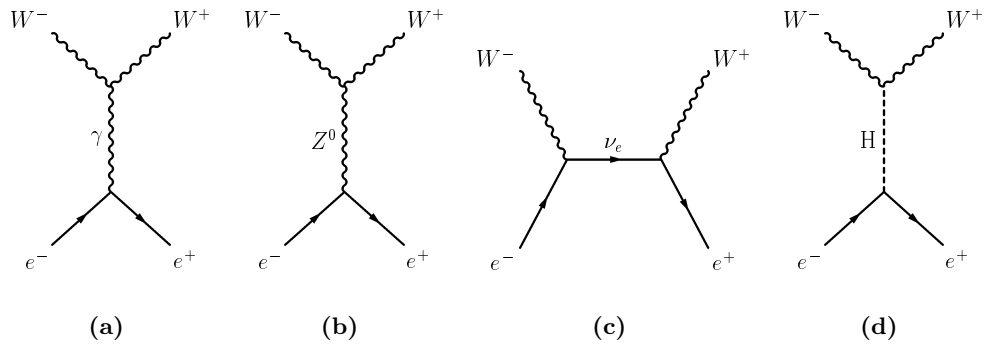

Figure 1.3: The 4 processes, contributing to $e^+e^- \rightarrow W^+W^-$.

scale [Qui99]. The Higgs mass is further constrained, if one also considers higher order corrections [Spi97].

The energy dependence of the Yukawa coupling of the top quark and the coupling[3] λ gives the following limit on the Higgs mass:

$$M_H^2 \leq \frac{8\pi^2 v^2}{3 \log \frac{\Lambda^2}{v^2}} \tag{1.52}$$

This limit depends on the cut-off parameter[4] Λ. With the known top quark mass of about 175 GeV, the following limits are obtained for different cut-off parameters:

$$55 \text{ GeV} \leq \quad M_H \quad \leq 700 \text{ GeV} \quad (\Lambda = 10^3 \text{ GeV}) \tag{1.53}$$
$$130 \text{ GeV} \leq \quad M_H \quad \leq 190 \text{ GeV} \quad (\Lambda = 10^{19} \text{ GeV}) \tag{1.54}$$

Another constraint originates from the fits of the LEP Electroweak Working Group [LEP02]. The free parameters of the Standard Model are fitted here to electroweak precision data. The result from the preliminary fit (see Fig. 1.4) gives an upper exclusion limit with 95% CL[5]

$$M_H \leq 193 \text{ GeV} \tag{1.55}$$

and as most probable Higgs mass

$$M_H = 81^{+52}_{-33} \text{ GeV} \tag{1.56}$$

[3] $\lambda = \mu/v$

[4] In order to avoid divergences a cut-off parameter is introduced in the calculation of the higher order corrections

[5] CL: Confidence Level

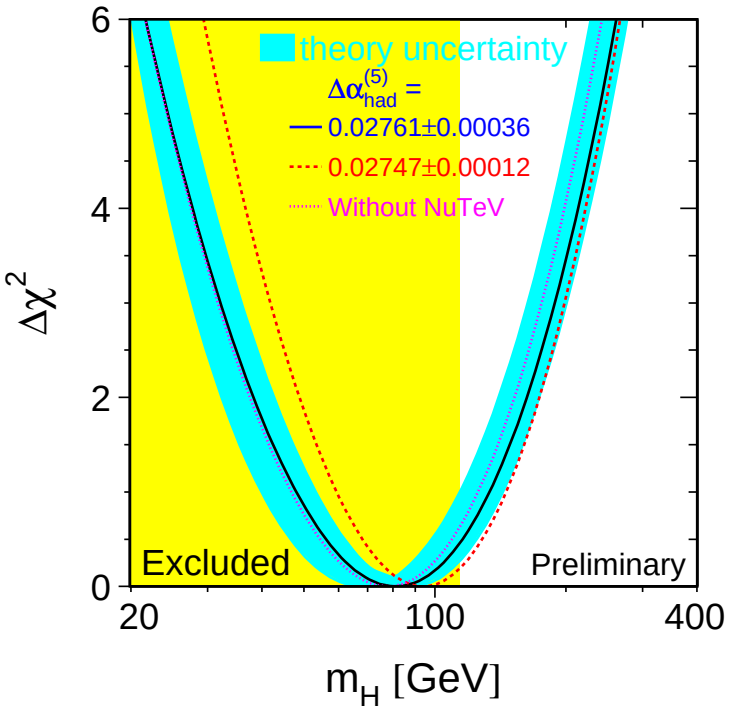

Figure 1.4: The $\Delta\chi^2(M_H)$ Fit [LEP02]. The two lines show the Higgs mass fit using all SM Data as inputs. The dark gray band shows the theoretical uncertainty due to the error on higher order correction, the light grey band shows the 95% CL exclusion with direct searches at LEP2.

1.2.4 Running coupling constants

In a quantum field theory the coupling constant is not constant for all energies, but it depends strongly on the momentum transfer Q^2. This behaviour has its origin in vacuum polarisation. The vacuum is filled with virtual particle pairs, which orient themselves in the field and either decrease ("Screening") or increase the bare charge ("Anti-Screening"). This behaviour is theoretically described by the help of loop corrections to the original value, the so-called radiative corrections. These corrections are divergent, so one has to find a way to keep the result finite. This is done using the renormalisation procedure. This procedure tries to isolate the divergent part of the radiative corrections and to renormalise the physical quantities like charge afterwards. Those quantities then absorb the divergences. This leads to a difference between the bare charge, the charge one would measure directly at the particle, and the effective charge, which depends on Q^2. Renormalisation therefore yields that the coupling[6] α

[6] One uses either α or g, with $g = \sqrt{4\pi\alpha}$.

is a function of Q^2. This behaviour is called running coupling constant. QED shows only the Screening, since only the charged fermions contribute and there is no self interaction between the gauge bosons. Applying the renormalisation procedure to QED yields for the running coupling constant:

$$\alpha_e(Q^2) = \frac{\alpha_e}{1 - \frac{\alpha_e}{3\pi} \ln \frac{Q^2}{m_e^2}} \tag{1.57}$$

This effect can not be neglected at high energies, at centre-of-mass energies of 90 GeV α_e is increased by roughly 6%. For QCD as a nonabelian gauge theory, the situation is more complex. In QCD there is both Screening and Anti-Screening, because both quarks and gluons carry colour charge. This behaviour is the origin of the effects of confinement and asymptotic freedom, as already mentioned in 1.2.1. The coupling constant α_s only shows this expected feature, if $N_f \leq 16$, the number of quark flavours, is limited to 16. Another difficulty one has to keep in mind is, that $\alpha_s(Q^2)$ diverges for $Q^2 \to 0$. In order to do renormalisation, one has to define a confinement scale Λ with $\alpha_s \to \infty$ for $Q^2 \to \Lambda$. The actual choice of Λ depends on the renormalisation scheme. For the Q^2 dependence of α_s one obtains:

$$\alpha_s(Q^2) = \frac{4\pi}{(11 - \frac{2N_f}{3}) \ln \frac{Q^2}{\Lambda^2}} \tag{1.58}$$

Another effect of renormalisation is the running quark mass, which means, that

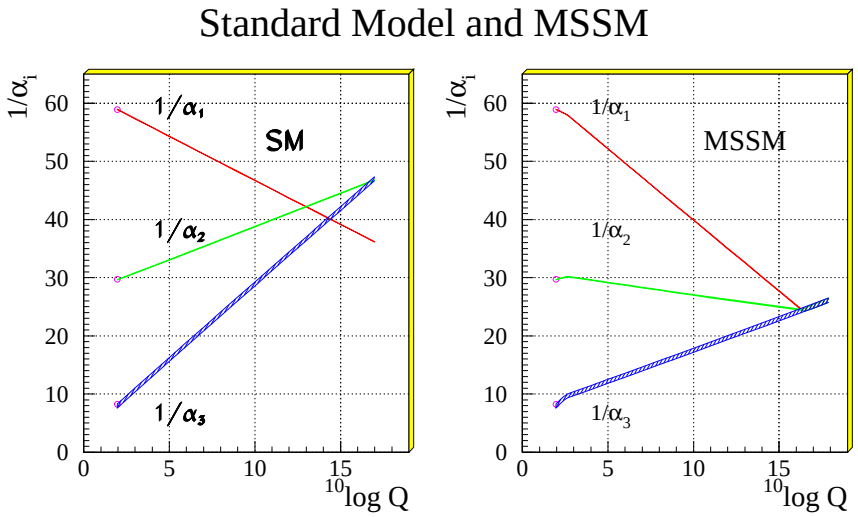

Figure 1.5: The Q^2 dependence of the coupling constants in the Standard Model (SM) (left) and the Minimal Supersymmetric Standard Model (MSSM) (right) [Ama91].

there is no fixed quark mass. In QCD the quark mass is defined $m = m(Q^2)$,

so it depends on Q^2. As the physical mass one usually refers to the pole mass, the mass at the pole of the quark propagator. The running quark mass $m(Q^2)$ decreases with increasing Q^2. If one plots also the three coupling constants of the Standard Model over Q^2, one sees, that there is no unification of the couplings at high Q^2 (see Fig 1.5). A unification of strong and electroweak interaction is therefore not possible within the Standard Model.

Chapter 2

Extensions to the Standard Model

2.1 Motivation

The Standard Model provides a good description of the data up to the electroweak scale ($\approx$ 100 GeV). But many questions are still left open in the Standard Model, coming from both theoretical and experimental arguments.

- The amount of free parameters in the Standard Model is large. The values of the Yukawa couplings, the Weinberg angle and the elements of the CKM- matrix cannot be predicted by the Standard Model. The same argument applies for the mass of the Higgs boson. Also the generation of fermion masses via the Yukawa couplings is a pretty ad-hoc procedure.
- The fine tuning problem: Radiative corrections for the masses of gauge and Higgs bosons lead to quadratic divergences. In order to avoid this, one has to do an extremely fine tuning of the Higgs potential during renormalisation. This fine tuning has to be introduced "by hand"in the Standard Model.
- The hierarchy problem: Why is there such a large difference between the electroweak scale $\mathcal{O}(10^2$ GeV) and the Planck scale $\mathcal{O}(10^{18}$ GeV)?
- Why are there three generations of fermions in the Standard Model?
- The charge of the quarks: Why is the charge of the up-type quarks $+\frac{2}{3}$ and the one of the down-type quarks $-\frac{1}{3}$ of the lepton charge?
- The quark mass: Why are the up-type quarks always heavier than the down-type quarks, e.g top ($\approx$ 175 GeV) and bottom ($\approx$ 5 GeV)?
- Neutrinos are considered massless in the Standard Model, this contradicts the latest experimental results from Superkamiokande [Sup98, Fuk01] and SNO[1] [SNO01].

[1] **S**udbury **N**eutrino **O**bservatory

- The mass of the W boson: Why is there a disagreement of direct measurement of m_W and the mass predicted from the Z mass measurements (see Fig. 2.1)?

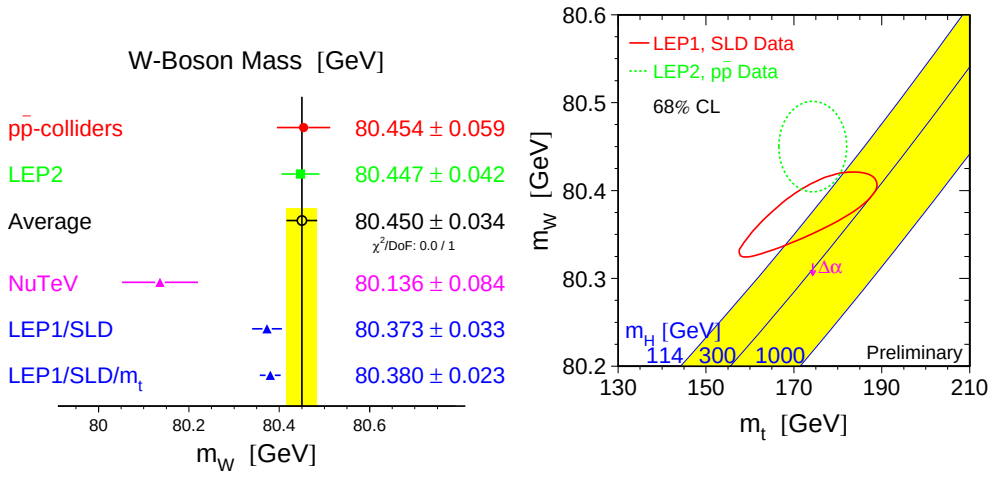

Figure 2.1: The W mass measurements [LEP02]: The direct measurements of LEP2 and the $p\bar{p}$ colliders deviate from indirect measurements done with LEP1 and SLD (left plot). This can also be seen plotting the results of the direct measurements of m_W (LEP2 , $p\bar{p}$ colliders) and m_{top} (CDF, D0) (dotted curve) and the indirect measurements from LEP1 and SLD in the m_W-m_{top} plane. The yellow band indicates the Higgs mass ranging from 114 GeV to 1 TeV (right plot).

Furthermore it is not possible to have a unification for the three interactions in the Standard Model (see e.g. Fig. 1.5). An obvious first approach of extending the Standard Model is to unify the three symmetry groups of the Standard Model in the framework of a Grand Unified Theory (GUT). The lowest order group that yields the desired unification is a $SU(5)$ group. But the $SU(5)$ approach does not unify the couplings, another desired feature of an extended model and the $SU(5)$ introduces new gauge bosons X and Y, which violate baryon number conservation. The violation of baryon number conservation leads to rapid proton decay rate, giving a half-life period of $\approx 10^{30}$ years. This is in obvious contradiction to the experimental results [Hag02], which set a limit to proton half-life period two orders of magnitude higher. Since this very obvious way of extending the Standard Model is excluded, other approaches have been proposed, like supersymmetric models, a Standard Model with two Higgs doublets and Majoron models. In this chapter, these extended models are briefly introduced, their phenomenological consequences for production and decay of Higgs bosons are discussed in chapter 3.

2.2 Supersymmetry

Supersymmetry nowadays is one of the most favoured extensions to the Standard Model since it provides a very elegant way to solve many problems of the Standard Model. Supersymmetry introduces a new symmetry between fermions and bosons. Using the SUSY[2] generators one can transform a fermion into a boson.

$$Q_{SUSY}|Boson> = |Fermion> \tag{2.1}$$
$$Q_{SUSY}|Fermion> = |Boson> \tag{2.2}$$

The SUSY generators change the spin of the particles, therefore supersymmetry is also referred to as a spin symmetry. Such a kind of symmetry has never been observed before in nature and is a purely theoretical idea up to now. The SUSY generators fulfil the following conditions [Kaz96]:

$$\{Q_\alpha, Q_\beta\} = 0 \tag{2.3}$$

The fact that they are anticommutating and fermionic can be easily shown [Kaz96]. In general, an infinitesimal transformation ϵ between bosons (B) and fermions (f) can be written as

$$\delta B = \epsilon \cdot f \tag{2.4}$$

Applying the commutators and anticommutators

$$[B, B] = 0 \text{ and } \{f, f\} = 0 \tag{2.5}$$

it immediately follows for the SUSY generators:

$$\{\epsilon, \epsilon\} = 0 \tag{2.6}$$

So it is clear, that these are odd (fermionic) generators that change the spin by a factor $\frac{1}{2}$ and change the particle statistics. One gets the following hierarchy of spins:

$$\text{Spin } 2 \Rightarrow \text{Spin } \frac{3}{2} \Rightarrow \text{Spin } 1 \Rightarrow \text{Spin } \frac{1}{2} \Rightarrow \text{Spin } 0 \tag{2.7}$$

A unique feature of SUSY and its algebra is, that it is the only possible algebra containing fermionic and bosonic operators within a relativistic field theory. Considering the anticommutator of two SUSY generators

$$\{Q_\alpha, \bar{Q}_{\dot{\alpha}}\} = 2\sigma^\mu_{(\alpha\dot{\alpha})} P_\mu \tag{2.8}$$

one obtains, that this is a local coordinate transformation [Kaz01]. Another theory, that is invariant under local coordinate transformations is general relativity. So by using local spacetime dependence in SUSY, one obtains a theory of gravity or supergravity. A very interesting question is, how many SUSY

[2]Supersymmetry is usually abbreviated as SUSY.

generators are possible in a supersymmetric theory. One obtains the following limits [Kaz96]:

$$N \leq 4J \tag{2.9}$$

J is the largest spin of a particle here. Applying this equation yields:

$$\begin{aligned} N &\leq 4 \quad \text{for renormalisable theories} \\ N &\leq 8 \qquad \text{for (super}-\text{)gravity} \end{aligned} \tag{2.10}$$

This is because the maximum spin of a particle in a renormalisable Yang-Mills theory is 1. Since renormalisation is a desired feature for an extension of the Standard Model, this puts a stringent limit on the number of SUSY generators. Depending on the number of SUSY generators, one refers to a $N = 1$ theory as a Minimal Supersymmetric Model and to $N > 1$ theory as an Extended Supersymmetric Model. More details on the mathematical calculus of supersymmetry are described in [Kaz96, Kaz01, Kal97, Wes83].

Due to the symmetry between fermions and bosons, every Standard Model

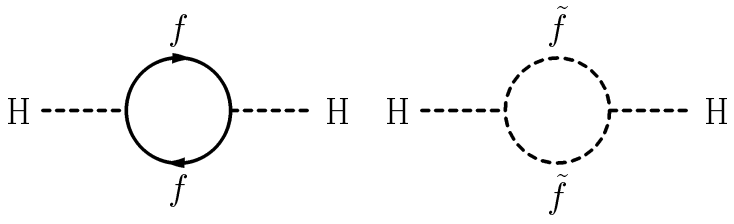

Figure 2.2: The fermionic one loop corrections to the Higgs mass in the Standard Model (a) and the additional loop with the bosonic superpartner of the fermions, the sfermions (b).

fermion has a bosonic superpartner and every Standard Model boson has a fermionic superpartner. So the number of particles is doubled in a supersymmetric model. The naming convention of the superpartner is summarised in Tab. 2.1.

With the additional particles, a supersymmetric theory solves the fine tuning problem in an elegant way, by adding sfermionic loop corrections to the fermionic loop corrections of the Standard Model (see Fig. 2.2). The additional loops cancel the divergences, since the sfermionic corrections have the opposite sign.

All these arguments apply only if we have an exact supersymmetry, meaning that all superpartners have the same properties like the Standard Model

Transformation	SM particle	Superpartner
Fermion → Boson	quark lepton	squark slepton
Boson → Fermion	Gauge boson Higgs boson	gaugino Higgsino

Table 2.1: The naming convention of the superpartners in a supersymmetric theory. The superpartners are also often called sparticles.

particles besides their spin. This obviously contradicts the experimental results, since the superpartners have not been found yet. If supersymmetry is realised in nature, it has to be broken. There are several ways of breaking supersymmetry, common for all is their use of a "hidden"sector to break supersymmetry [Kaz01]. According to this formalism, all the particles are in the visible sector, while the SUSY-breaking fields are in the so-called hidden sector. These two sectors interact with each other using messenger particles, that mediate the SUSY-breaking to the visible sector. There are three common mediation processes, gravity mediated, also called MSUGRA [Arn76, Bar82], gauge mediated (GMSB) [Din93, Din95, Din96] and anomaly mediated (AMSB) [Ran99, Giu98, Ghe99, Fen00]. All these theories have to use "soft-breaking"terms for the SUSY breaking in order to avoid introducing quadratic divergences again. The breaking mechanism leads to the fact that the mass spectrum of the superpartners is different from the Standard Model particles. After SUSY breaking, the quarks and leptons are still massless, $SU(2)$ still has to be broken. In supersymmetry this has not to be introduced by hand, it is the result of radiative corrections [Kaz01]. Since those radiative corrections are logarithmic in energy, this automatically leads to a large difference between the electroweak and the SUSY scale [dB94]. Another important definition in supersymmetric models is the R-parity, which is obtained from baryon number (B), lepton number (L) and the spin of the particle (S):

$$R = (-1)^{3(B-L)+2S} \tag{2.11}$$

Like parity this is a multiplicative quantum number, it has the value +1 for particles and -1 for the sparticles. R-parity is mainly motivated by experiment. Violation of R-parity would lead to violation of baryon and lepton number conservation, leading to higher proton decay rates. From the experimental results, one either assumes, that the R-parity violating terms are very small or that there is no R-parity violation. The first version is the more favoured nowadays. R-parity conservation leads to the following consequences for a supersymmetric model:

- There are fewer free parameters due to the lack of R-parity violating terms.
- Supersymmetric particles can only be produced in pairs.

- The lightest supersymmetric particle (LSP) is stable. If it is sufficiently heavy, it could contribute to the dark matter in the universe. Because of the dark matter R-parity conservation is preferred in cosmology.
- The interactions of the sparticles are basically the same as for the particles.

The main goal of any extension to the Standard Model is the unification of the three couplings in the Standard Model. Supersymmetry provides this unification at the right scale (see Fig. 1.5) without introducing more fine-tuning problems. Supersymmetry can be considered as a pretty successful approach. Till now, supersymmetry has been described in a very general way, to have real prediction of the properties, one has to use a certain theoretical framework.

2.2.1 The Minimal Supersymmetric Standard Model (MSSM)

The MSSM is a N=1 supersymmetric model, so there is only one SUSY generator. In the MSSM model considered here, it is assumed that R-parity is conserved and Supersymmetry is broken by supergravity (MSUGRA). The conservation of R-parity leads to the fact that the LSP is stable, as mentioned before. The particle content resulting out of this is listed in Tab. 2.2.

SM particle		Supersymmetric particle					
		Superpartner			Mass eigenstate		
Symbol	N[3]	Symbol	Name	N	Symbol	Name	N
g	8	$\tilde{g}$	Gluino	8	$\tilde{g}$	Gluino	8
$W^{\pm}$	2	$\tilde{W}^{\pm}$	Wino	2			
H_1^+	1	$\tilde{H}_1^+$	Higgsino	1	$\tilde{\chi}_{1,2}^{\pm}$	Chargino	4
H_2^-	1	$\tilde{H}_2^-$	Higgsino	1			
W^3	1	$\tilde{W}^3$	Wino	1			
B	1	$\tilde{B}$	Bino	1			
H_1^0	1	$\tilde{H}_1^0$	Higgsino	1	$\tilde{\chi}_{1..4}^0$	Neutralino	4
H_2^0	1	$\tilde{H}_2^0$	Higgsino	1			
q_L	6	$\tilde{q}_L$	Squark	6			
$u_R(u,c,t)$	3	$\tilde{u}_R$	Squark	3	$\tilde{q}_1, \tilde{q}_2$	Squark	12
$d_R(d,s,b)$	3	$\tilde{d}_R$	Squark	3			
$l_L(e,\mu,\tau)$	3	$\tilde{l}_L$	Slepton	3	$\tilde{l}_1, \tilde{l}_2$	Slepton	6
$l_R(e,\mu,\tau)$	3	$\tilde{l}_R$	Slepton	3			
ν	3	$\tilde{\nu}$	Sneutrino	3	$\tilde{\nu}$	Sneutrino	3

Table 2.2: The particles of the Standard Model (SM) and their superpartners in the MSSM.

The choice of supergravity as the mechanism for breaking supersymmetry leads to some additional parameters, most important are the common mass of

[3] N denotes the number of particles.

the scalar particles at the GUT scale m_0 and the common mass of the Spin $\frac{1}{2}$ particles (Gauginos) at the GUT scale $m_{1/2}$.

2.2.2 The Higgs sector of the MSSM

The Higgs sector of the MSSM is more complicated than in the Standard Model. In the MSSM 2 Higgs doublets are required:

$$H_1 = \begin{pmatrix} H_1^0 \\ H_1^- \end{pmatrix} \quad H_2 = \begin{pmatrix} H_2^+ \\ H_2^0 \end{pmatrix} \tag{2.12}$$

Two Higgs doublets are necessary because of the chirality of the supersymmetric fields. In the Standard Model the mass of the down-type quarks[4] is generated using H and the mass of the up-type quarks[5] is generated by the charge-conjugated field $\tilde{H}$. In the MSSM it is not possible to use the charge conjugated field in order to generate mass. This is due to the fact that in theories with chiral superfields each type needs a Higgs doublet. Furthermore two Higgs doublets are required to avoid chiral anomalies. These anomalies do not occur in the Standard Model, because they cancel in each generation of quarks and leptons. If one adds chiral superfields, they include fermionic Higgsinos that contribute to the anomalies. The Higgs potential of the MSSM is fixed by the structure of the superfields and the soft-breaking terms of the MSSM [Gun90].

$$\begin{aligned} V(H_1, H_2) = m_1^2|H_1|^2 + m_2^2|H_2|^2 - m_3^2(H_1 H_2 + H_2^\dagger H_1^\dagger) + \\ \frac{g^2 + g'^2}{8}(|H_1|^2 - |H_2|^2)^2 + \frac{g^2}{2}|H_1^\dagger H_2|^2 \end{aligned} \tag{2.13}$$

with $m_1^2 = m_{H_1}^2 + \mu^2$ and $m_2^2 = m_{H_2}^2 + \mu^2$. At the GUT scale using the bilinear coupling B, one obtains the relation: $m_1^2 = m_2^2 = m_0^2 + \mu_0^2$, $m_3^2 = -B\mu_0$. Requiring a nontrivial minimum for both Higgs doublets H_1 and H_2

$$H_1 = \begin{pmatrix} v_1 + \frac{1}{\sqrt{2}}(\eta_1 + i\xi_1) \\ H_1^- \end{pmatrix} \quad H_2 = \begin{pmatrix} H_2^+ \\ v_2 + \frac{1}{\sqrt{2}}(\eta_2 + i\xi_2) \end{pmatrix} \tag{2.14}$$

yields the following relations:

$$\begin{array}{cc} < H_1 > \equiv v_1 = v\cos\beta & < H_2 > \equiv v_2 = v\sin\beta \\ v^2 = v_1^2 + v_2^2 & \tan\beta = \frac{v_2}{v_1} \end{array} \tag{2.15}$$

Furthermore

$$m_1^2 + m_2^2 > 2m_3^2 \quad m_1^2 \cdot m_2^2 < m_3^4 \tag{2.16}$$

has to be fulfilled, in order to get positive real solutions. From the eight degrees of freedom five physical Higgs bosons remain after the radiative symmetry breaking (three degrees of freedom are absorbed by the massive gauge bosons

[4] down, strange and bottom quark
[5] up, charm and top quark

like in the Standard Model). One obtains one neutral pseudoscalar Higgs boson A ($CP = -1$), two charged Higgs bosons $H^{\pm}$ and two neutral scalar Higgs bosons h, H ($CP = 1$). The h Higgs boson is the most similar one to the Higgs boson in the Standard Model. After diagonalisation of the mass matrices of the Higgs fields, the following masses for the Higgs bosons are derived [Gun90]:

$$m_A^2 = m_1^2 + m_2^2 \tag{2.17}$$

$$m_{H^{\pm}}^2 = m_A^2 + M_W^2 \tag{2.18}$$

$$m_{H,h}^2 = \frac{1}{2}\left[m_A^2 + M_Z^2 \pm \sqrt{(m_A^2 + M_Z^2)^2 - 4m_A^2 M_Z^2 \cos^2 2\beta}\right] \tag{2.19}$$

with M_Z defined as:

$$M_Z^2 = \frac{g^2 + g'^2}{2} v^2 \tag{2.20}$$

At tree level, this leads to the MSSM relations for the Higgs boson masses:

$$m_{H^{\pm}} \geq M_W \tag{2.21}$$

$$m_h \leq m_A \leq m_H \tag{2.22}$$

$$m_h \leq M_Z \cos 2\beta \tag{2.23}$$

A Higgs mass significantly lower than the mass of the Z boson has already been excluded by direct searches. Including higher order loop corrections, the mass of the lightest Higgs boson is significantly shifted towards higher values, an upper limit $m_h \leq 135$ GeV/c^2 [Hei99] has been calculated. For the parametrisation of the Higgs sector in the MSSM only few parameters are necessary, usually chosen are $\tan\beta$ and m_A. Also important is the mixing angle α, which is defined as:

$$\tan 2\alpha = -\tan 2\beta \frac{m_A^2 + M_Z^2}{m_A^2 - M_Z^2} \tag{2.24}$$

This angle influences mainly the Higgs production cross-sections in the MSSM (see section 3.2).

2.2.3 The mass eigenstates of the MSSM

The superpartners of the Standard Model particles are not automatically the mass eigenstates (see table 2.2). In order to obtain the mass eigenstates, one has to distinguish between the gauginos and Higgsinos on one side and the sfermions on the other side.

Gauginos and Higgsinos

For the gauginos and Higgsinos the mass mixing term results from the fact, that the mass matrix is not diagonal. The mass terms is:

$$\mathcal{L}_{Gaugino-Higgsino} = -\underbrace{\frac{1}{2}\bar{\chi} M^{(0)} \chi}_{\text{Neutralino mass term}} - \underbrace{(\bar{\psi} M^{(c)} \psi + h.c.)}_{\text{Chargino mass term}} \tag{2.25}$$

with

$$\chi = \begin{pmatrix} \tilde{W}^3 \\ \tilde{B} \\ \tilde{H}_1^0 \\ \tilde{H}_2^0 \end{pmatrix} \quad \text{and} \quad \psi = \begin{pmatrix} \tilde{W}^+ \\ \tilde{H}^+ \end{pmatrix} \tag{2.26}$$

For the neutral superpartners ($\tilde{W}^3$, $\tilde{B}$, $\tilde{H}^0_{1,2}$), the neutralino mass matrix $M^{(0)}$ can be written as:

$$\begin{pmatrix} M_1 & 0 & -M_Z \cos\beta \sin\theta_W & M_Z \sin\beta \sin\theta_W \\ 0 & M_2 & M_Z \cos\beta \cos\theta_W & -M_Z \sin\beta \cos\theta_W \\ -M_Z \cos\beta \sin\theta_W & M_Z \cos\beta \cos\theta_W & 0 & -\mu \\ M_Z \sin\beta \sin\theta_W & -M_Z \sin\beta \cos\theta_W & -\mu & 0 \end{pmatrix} \tag{2.27}$$

M_1 and M_2 are the gaugino masses at the GUT-scale. In this SUGRA inspired model, one has the additional relation [Hab85] between M_1 and M_2:

$$M_1 = \frac{5}{3} \tan^2 \theta_W M_2 \tag{2.28}$$

The masses of the four neutralinos are the eigenvalues of this matrix. These eigenvalues are explicitly given in [EK92].
For the charginos, one only has a 2×2 matrix:

$$M^{(c)} = \begin{pmatrix} M_2 & \sqrt{2} M_W \sin\beta \\ \sqrt{2} M_W \cos\beta & \mu \end{pmatrix} \tag{2.29}$$

The chargino masses are the eigenvalues of the matrix:

$$\begin{aligned} M^2_{\tilde{\chi}_{1,2}} \;=\; & \frac{1}{2}\Big[M_2^2 + \mu^2 + 2M_W^2 \mp \\ & \sqrt{(M_2^2 - \mu^2)^2 + 4M_W^4 \cos^2 2\beta + 4M_W^2 (M_2^2 + \mu^2 + 2M_2 \mu \sin 2\beta)}\Big] \end{aligned} \tag{2.30}$$

Squarks and sleptons

For the sfermions the mechanism that leads to mass mixing is different. It is generated by non-negligible Yukawa-couplings between the sfermions. This is mainly true for the mass eigenstates of the third generation, since the Yukawa couplings are negligible for the first two generations. One obtains the following matrix for the mixing

$$\begin{pmatrix} \tilde{m}^2_{X_L} & m_X (A_X - \mu \cot\beta) \\ m_X (A_X - \mu \cot\beta) & \tilde{m}^2_{X_R} \end{pmatrix} \tag{2.31}$$

with $X = t$, b, τ and the mixing term A_X.

2.2.4 AMSB inspired model

Another interesting mechanism for supersymmetry breaking is the Anomaly-Mediated Supersymmetry Breaking (AMSB) model. It assumes a general hidden sector model and points out, that one has loop contributions to the gaugino and scalar masses as a consequence of the Super-Weyl anomaly [Ran99]. This is true for all hidden sector models, which use supergravity for communicating supersymmetry breaking. Even more, this mechanism holds for any hidden sector, although the AMSB is usually embedded in brane-inspired models [Ran99]. In the AMSB a sequestered sector is introduced, which means that the hidden sector is *truly hidden* [Ran99]. Contrary to the usual models, where the leading term contributions to the masses are dominant, in this model they are suppressed and the anomaly contributions dominate. One obtains then one-loop contributions to the gaugino masses and degenerate two-loop contributions for the scalar masses. One drawback is that with pure anomaly generated masses, the slepton masses are negative, yielding tachyonic particles. This features can be avoided by allowing additional contributions to scalar masses, which are not anomaly induced. These contributions are usually motivated by radiative corrections coming from bulk fields. The predicted mass spectrum is very different from SUGRA or GMSB scenarios. First a fixed ratio for the gaugino masses is predicted [Ran99].

$$m_3 : m_2 : m_1 = 3.0 : 0.3 : 1.0 \tag{2.32}$$

The LSP is a gaugino and can be nearly degenerate between wino and zino. The squarks and gluinos are quite heavy. Usually there is one order of magnitude between them and the gauginos. The gauginos are put far away to the TeV scale.

The lightest Higgs boson is the h, which is Standard Model like, but the mass is constraint between 92 and 118 GeV/c^2 [Su00]. The A is much heavier than the Z, so only the h is kinematically accessible at LEP.

2.3 General Two Higgs Doublet Model (2HDM)

The general two Higgs doublet model is a general extension to the Standard Model, without imposing supersymmetry. In the Standard Model only one Higgs doublet is used, this minimal choice is somehow arbitrary, since there is no information about the Higgs sector at all. If one is going to extend the Standard Model with more doublets and singlets one has only to respect some experimental constraints. The first experimental constraint comes from the so-called ρ-parameter.

$$\rho = \frac{m_W^2}{m_Z^2 \cos^2 \theta_W} \tag{2.33}$$

This parameter is measured to be very close to 1 [LEP02]. The tree value of the Standard Model for ρ is 1. This however is automatically true for all models consisting only of Higgs doublets and singlets (see [Lee72, Ros75]). Considering one-loop correction to the ρ parameter and using experimental results

from neutral current experiments, this already constrains the number of possible Higgs singlets [Hol86, Hol88]. A study of the allowed vacuum expectation values also disfavours models with Higgs triplets. Another constraint comes from the stringent limits on flavour-changing neutral currents (FCNC). Tree level FCNC's are automatically absent in the Standard Model, since the diagonalisation operation for the mass matrix is the same as for the Higgs-fermion couplings [Gun90]. In a theorem proposed by Glashow and Weinberg [Gla77], there are no tree-level FCNC's mediated by Higgs bosons, if all fermions of a given charge do not couple to more than one Higgs doublets. With this theorem there are basically two possibilities to realise a model with two Higgs doublets. The first one would be, as for example realised in the MSSM, that one doublet only couples to up-type fermions and the other one couples only to down-type fermions. In the MSSM this comes out of the model directly, in a 2HDM this is just a choice respecting the Glashow-Weinberg theorem. Models of that kind are referred to as Type II models. Another choice would be that one doublet couples to the fermions, while the other does not couple to fermions at all. This is called a Type I model and the Higgs phenomenology of such a model can be quite different from the Standard Model. Finally the extended models have to fulfil the unitarity conditions for $e^+e^- \to W^+W^-$ (see chapter 1.2.3). Detailed analyses lead to the constraint, that at least one neutral scalar has to have a mass of less than 1 TeV [Gun90].

2.3.1 The Higgs sector of the 2HDM

After putting these severe constraints to the form of an 2HDM, one can write the Higgs potential of a general 2HDM as follows [Geo78]:

$$\begin{aligned} V(H_1,H_2) &= \lambda_1(H_1^\dagger H_1 - v_1^2)^2 + \lambda_2(H_2^\dagger H_2 - v_2^2)^2 \\ &\quad +\lambda_3\left[((H_1^\dagger H_1 - v_1^2) + (H_2^\dagger H_2 - v_2^2)\right]^2 \\ &\quad +\lambda_4\left[(H_1^\dagger H_1)(H_2^\dagger H_2) - (H_1^\dagger H_2)(H_2^\dagger H_1)\right] \\ &\quad +\lambda_5\left[Re(H_1^\dagger H_2) - v_1 v_2\right]^2 \\ &\quad +\lambda_6\left[Im(H_1^\dagger H_2)\right]^2 \end{aligned} \tag{2.34}$$

We can define again the ratio of the vacuum expectation values

$$\tan\beta = \frac{v_2}{v_1} \tag{2.35}$$

The Higgs particle spectrum is analogous to the one in the MSSM, in the charged sector one has two charged Higgs bosons with a mass:

$$m_H^\pm = \sqrt{\lambda_4(v_1^2 + v_2^2)} \tag{2.36}$$

The three neutral Higgs bosons, one pseudoscalar Higgs bosons A with a mass:

$$m_A = \sqrt{\lambda_6(v_1^2 + v_2^2)} \tag{2.37}$$

and two neutral scalars h and H. Their mixing is described with a mass matrix:

$$\mathcal{M} = \begin{pmatrix} 4v_1^2(\lambda_1+\lambda_3)+v_2^2\lambda_5 & (4\lambda_3+\lambda_5)v_1v_2 \\ (4\lambda_3+\lambda_5)v_1v_2 & 4v_2^2(\lambda_2+\lambda_3)+v_1^2\lambda_5 \end{pmatrix} = \begin{pmatrix} M_{11}\, M_{12} \\ M_{21}\, M_{22} \end{pmatrix} \tag{2.38}$$

The physical mass eigenstates then are:

$$m_{H,h} = \sqrt{\frac{1}{2}\left(M_{11}+M_{22} \pm \sqrt{(M_{11}-M_{22})^2+4M_{12}^2}\right)} \tag{2.39}$$

The 2HDM has six free parameters: the masses of the Higgs bosons $(h, H, A, H^{\pm})$, $\tan\beta$ and a Higgs mixing angle α, which is defined as

$$\sin 2\alpha = \frac{2M_{12}}{\sqrt{(M_{11}-M_{22})^2+4M_{12}^2}} \tag{2.40}$$

$$\cos 2\alpha = \frac{M_{11}-M_{22}}{\sqrt{(M_{11}-M_{22})^2+4M_{12}^2}} \tag{2.41}$$

It is important to note, that there are no relations between the Higgs boson masses as in the MSSM, in a 2HDM the Higgs boson masses are the input parameters and they are defining the model.

2.4 Majoron models

Another interesting approach is the combination of Higgs doublets and singlets, which can lead to a new class of models containing Goldstone bosons, usually named Majorons. As has been mentioned before, there are no strong constraints against adding an additional singlet to the Standard Model. The strong motivation for this class of models comes from neutrino physics in order to explain the very small neutrino masses [Chi81, Zee80]. There are two choices for neutrinos, either being Dirac or Majorana particles. The first possibility conserves lepton number, the second one does not. In the Majoron models, the second possibility is chosen. So a $SU(2) \times U(1)$ singlet field η and right-handed neutrinos are introduced. The lepton number conservation, associated with the global $U(1)$ symmetry is then broken explicitly, leading to a Goldstone boson. The Higgs fields can be written as

$$\begin{pmatrix} \phi^+ \\ \phi^0 \end{pmatrix} + \eta \tag{2.42}$$

Since it is assumed, that the Higgs doublet ϕ is neutral under global $U(1)$ transformation, the Goldstone field can be simply identified with Im η [Jos92]. Since the η field is a singlet, the Majoron does only couple to right-handed neutrinos, so it would not couple to quarks, leptons and gauge bosons, which would render it basically invisible. This behaviour however, is not true for the Higgs sector. The Higgs potential in such a model is independent of the neutrino mass nature and can be written as

$$V(\phi,\eta) = \mu_\phi^2(\phi^\dagger\phi) + \mu_\eta^2(\eta^\dagger\eta) + \lambda_1(\phi^\dagger\phi)^2 + \lambda_2(\eta^\dagger\eta)^2 + \delta(\phi^\dagger\phi)(\eta^\dagger\eta) \tag{2.43}$$

with

$$\phi_0 = \frac{v_1}{\sqrt{2}} + \frac{\phi_R + i\phi_L}{\sqrt{2}} \tag{2.44}$$

$$\eta = \frac{v_2}{\sqrt{2}} + \frac{\eta_R + i\eta_L}{\sqrt{2}} \tag{2.45}$$

and

$$< \phi_0 >= \frac{v_1}{\sqrt{2}} \tag{2.46}$$

$$< \eta >= \frac{v_2}{\sqrt{2}} \tag{2.47}$$

This leads to an already mentioned physical massive Goldstone boson, the Majoron, and two massive neutral scalars H and S, which can be written as [Jos92]:

$$H = \cos\theta\phi_R - \sin\theta\eta_R \tag{2.48}$$

$$S = \sin\theta\phi_R + \cos\theta\eta_R \tag{2.49}$$

where θ is the mixing angle of the two Higgs bosons. The whole Higgs sector in a Majoron model can be described by the masses of the two Higgs bosons m_H and m_S, the ratio of the vacuum expectation values $\tan\beta = \frac{v_1}{v_2}$ and the mixing angle θ.

There are also models with two doublets and a singlet [dC97] or with triplets [Gun90], which add more complexity to the model, but still contain Majorons.

Chapter 3

Higgs production and decay at LEP

This chapter gives an overview of the phenomenological properties like production and decay rates of Higgs bosons both in the Standard Model (SM) and in the extended models described before. This information is essential for the Higgs searches conducted at LEP. Since LEP is an e^+e^- collider, only the production in electron-positron collisions is described here with a special focus on the production of a Higgs boson accompanied by a Z boson, the so-called Higgs-Strahlung. This mechanism is the favoured production channel in the framework of this thesis. The decay properties of a Higgs boson are however independent of the production and do also apply to searches at hadron colliders like the Tevatron. First the properties of a Standard Model Higgs boson are described in detail. Later on, the Standard Model properties are compared with the properties obtained in the extended models like new production or decay channels.

3.1 Higgs production and decay in the SM

For Higgs production in e^+e^- collisions at LEP2 energies (161 - 209 GeV), Higgs bosons are mainly produced via the so-called Higgs-Strahlung process (see Fig. 3.1a). The Higgs-Strahlung is dominating as long as the Higgs and the Z bosons are not virtual, this is usually referred as the kinematical limit. Putting it the other way round, the maximum Higgs boson mass, that is accessible, is given as $m_H \leq \sqrt{s} - m_Z$. If this requirement is not fulfilled anymore, the cross-section for Higgs Strahlung rapidly goes to zero. The Higgs-Strahlung cross-section is given as [Kil96]:

$$\sigma(e^+e^- \to ZH) = \frac{G_F m_Z^4}{96\pi s}(v_e^2 + 1)\sqrt{\lambda}\frac{\lambda + 12m_Z^2/s}{(1 - m_Z^2/s)^2} \tag{3.1}$$

using $\lambda = (1 - (m_H + m_Z)^2/s)(1 - (m_H - m_Z)^2/s)$ and $v_e = -1 + 4\sin^2\theta_W$.

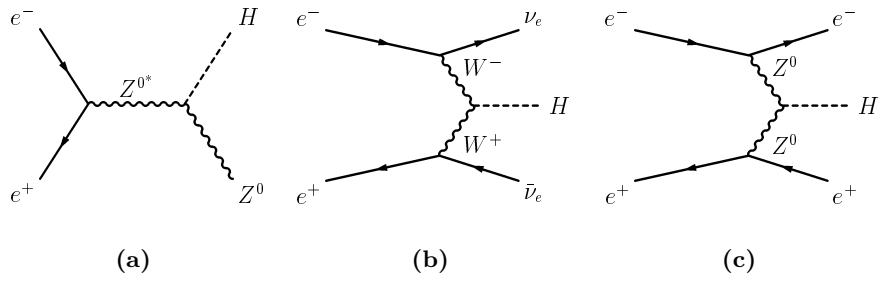

Figure 3.1: Higgs production in the SM: Higgs-Strahlung (a), WW fusion (b) and ZZ fusion (c).

Further Higgs production processes in e^+e^- collisions are the WW fusion and the ZZ fusion. Both are t-channel processes, that do not suffer from a kinematical limit, like the Higgs-Strahlung does. However, the cross-sections are very small below the kinematical limit. The WW fusion cross-section, for example, is comparable with the Higgs-Strahlung cross-section only at Higgs masses around or above the kinematical limit. The cross-section for ZZ fusion is always one order of magnitude lower than the WW fusion, this is due to the vertex factors. What makes especially WW fusion interesting for the searches is the interference of Higgs-Strahlung and WW fusion in the final state $e^+e^- \rightarrow HZ \rightarrow H\nu_e\bar{\nu}_e$. This interference term has the same order of magnitude as the fusion process itself for Higgs masses between 80 and 120 GeV/c^2 and LEP2 centre-of-mass energies. The total cross section for $e^+e^- \rightarrow ZH \rightarrow H\nu\bar{\nu}$ is given as

$$\sigma_{H\nu\nu} = 3 \cdot \sigma_{Higgs-Strahlung} + \sigma_{WW-Fusion} + \sigma_{Interference} \tag{3.2}$$

and is shown in Fig. 3.2. All terms are given explicitly in [Kil96].

The same arguments basically also apply to ZZ fusion in the channel $e^+e^- \rightarrow ZH \rightarrow He^+e^-$, but the effect is very small and basically not visible at LEP.

As already mentioned, the Higgs bosons always decays in the heaviest particles possible, which also means, that the branching ratio depends on the Higgs mass considered. There are three possible classes of decays: decays into fermions, decays into massive bosons and the decays into massless bosons via loop diagrammes. All possible decay graphs are shown in Fig. 3.3. The fermionic decay width is given as [Gun90]:

$$\Gamma(H \rightarrow f\bar{f}) = \frac{N_c g^2 m_f^2}{32\pi m_W^2} \cdot \beta^3 m_H \tag{3.3}$$

with N_C as the number of colours [1] and $\beta = 1 - 4m_f^2/m_H^2$. For the decays into quarks, QCD corrections for the quarks masses have to be considered. Since the

[1] N_C=1 for the colourless leptons and N_C=3 for the quarks

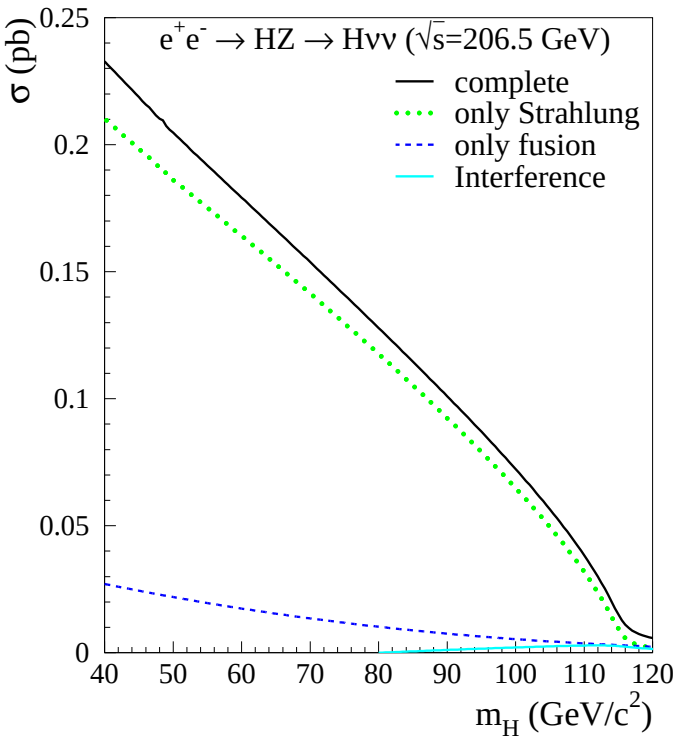

Figure 3.2: The cross-section for $e^+e^- \to HZ \to H\nu\bar{\nu}$ at a $\sqrt{s}$=206.5 GeV for Higgs-Strahlung, WW fusion and the interference term. Since the neutrinos are indistinguishable in the detector, all three neutrino flavours are considered. The cross-sections have been calculated using HZHA [Jan96].

energy scale of a Higgs decay is much higher than the quark pole masses, the running quark masses have to be used. These corrections lead to a decrease of the decays into b quarks and to an increase for the decay into τ leptons [Sak80].

For the decay into massive gauge bosons, one has to keep in mind, that for LEP2 energies, one massive gauge boson has to be offshell. Therefore the following formulas [Mar88] for the decay width apply:

$$\Gamma(H \to WW^*) = \frac{3g^4 m_H}{512\pi^3} \cdot F(\frac{m_W}{m_H}) \tag{3.4}$$

$$\Gamma(H \to ZZ^*) = \frac{g^4 m_H}{2048\pi^3} \frac{7 - \frac{40}{3}\sin^2\theta_W + \frac{160}{9}\sin^4\theta_W}{\cos^4\theta_W} \cdot F(\frac{m_Z}{m_H}) \tag{3.5}$$

The function F(x) is a very complex phasespace factor and is not given explicitly. It can be found in [Mar88, Gun90]. As already mentioned, both expressions are only valid if

$$m_W < m_H < 2m_W \tag{3.6}$$

$$m_Z < m_H < 2m_Z \tag{3.7}$$

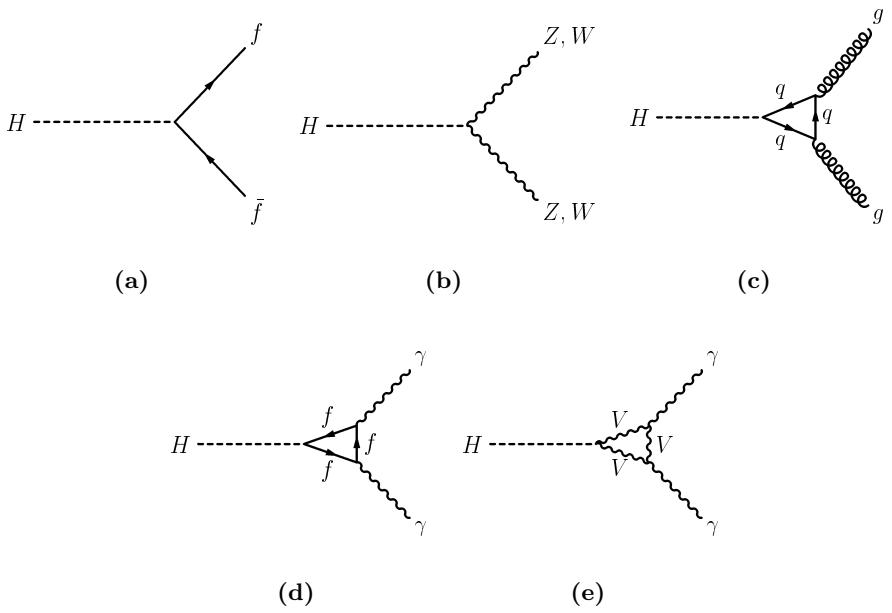

Figure 3.3: Feynman graphs for the Higgs decays in the SM : The decay in a fermion-antifermion pair (a), the decay in a W or Z boson pair (b), the decay into 2 gluons via a quark triangle (c) and the decay into 2 photons via a W or Z boson (V=Z,W) or fermionic triangles (d, e).

and no decays of the massive gauge bosons into top quarks occur. The decays into gluons or photons are more complicated, since they are mediated via loop diagrammes. The gluonic decay width is given as [Ell76]:

$$\Gamma(H \to gg) = \frac{G_F \alpha_s^2 m_H^3}{36\sqrt{2}\pi^3} \left| \sum_{t,b} A_H(\tau_q) \right|^2 \tag{3.8}$$

with the form factor $A_H(\tau_q)$, which is explicitely written in [Ell76]. The most dominant contribution in the loop comes from the top quark. Additionally, there are radiative corrections to this decay due to virtual gluon exchange and gluon splitting. This corrections then almost double the branching ratio into gluons [Djo91]. The decay width into two photons is the smallest one in the Standard Model, in the mass range accessible to LEP, it is always of the order of 0.1%.

The total decay width of the Standard Model Higgs boson is given as

$$\Gamma_H = \Gamma_{Fermion} + \Gamma_{W,Z} + \Gamma_{Gluon} + \Gamma_{\gamma\gamma} \tag{3.9}$$

and its dependence on the Higgs mass can be seen in 3.4. It is clearly visible, that the Higgs is a very narrow object for the mass range accessible at LEP2.

The Higgs boson branching ratios in the Standard Model for a mass range between 20 and 200 GeV are shown in Fig. 3.5. Only decay modes with a

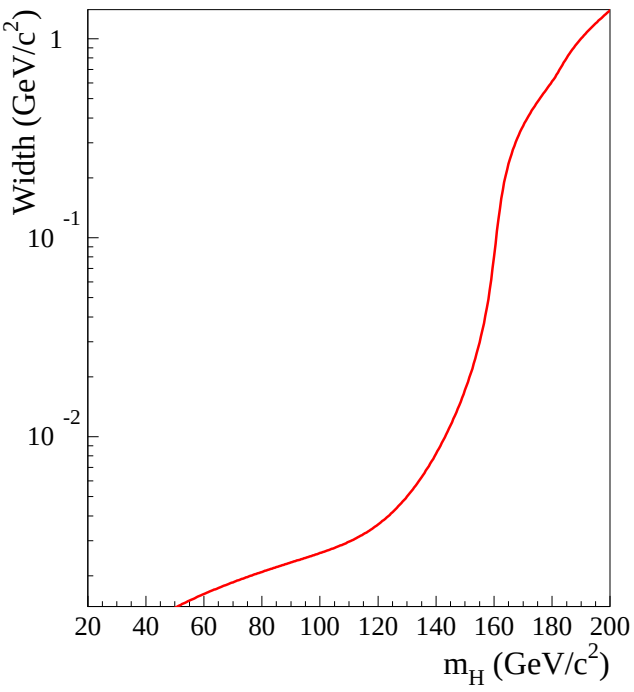

Figure 3.4: The total Higgs decay width in the SM calculated using HZHA [Jan96].

branching ratio greater than 1% are included in this plot. One clearly sees, that the decay into b quarks is dominating over the whole mass range accessible at LEP and the decay into τ leptons is the second most important. Decays into WW pairs only become important at higher Higgs masses, for Higgs masses of 150 GeV/c^2 or more they are the dominant decay channels.

$H \rightarrow$	$Z \rightarrow$	Signature	BR
$b\bar{b}$	$q\bar{q}$	4 jets	57.1%
$b\bar{b}$	$\nu\bar{\nu}$	2 jets + missing energy	17.2%
$b\bar{b}$	$\mu^+\mu^-$	2 jets + 2 muons	2.5%
$b\bar{b}$	e^+e^-	2 jets + 2 electrons	2.5%
$b\bar{b}$	$\tau^+\tau^-$	2 jets + 2 taus	2.5%
$\tau^+\tau^-$	$q\bar{q}$	2 jets + 2 taus	5.5%

Table 3.1: The Higgs signatures in the SM for a Higgs boson with a mass of 100 GeV/c^2. These signatures cover almost 90% of the possible HZ final states.

For the Higgs boson signatures one searches for at LEP2, one has to take also the decays of the accompanying Z boson into account. The most common signatures are listed in Tab. 3.1. One should keep in mind that in all cases, where the Higgs decays into a $b\bar{b}$ pair, one also requires in the analyses that two

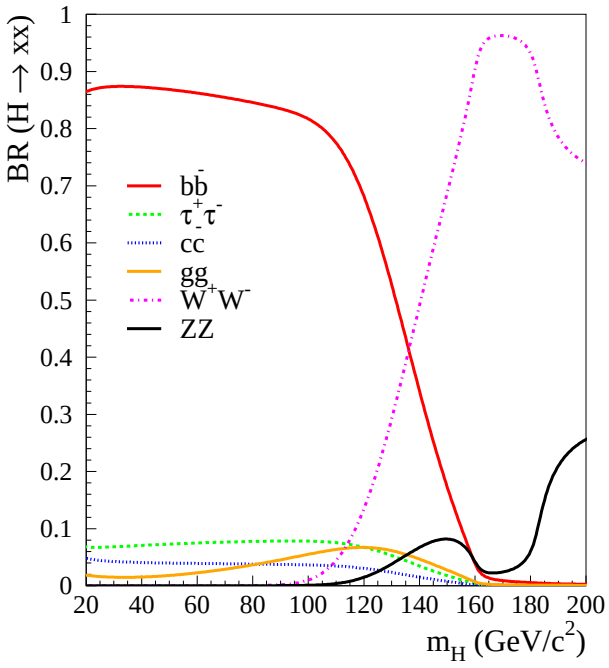

Figure 3.5: The branching ratios for the different Higgs decay channels in the SM. They have been calculated using HZHA [Jan96].

jets have a high probability to originate from a b quark (so-called b-tag).

3.2 Higgs production and decay in the MSSM

The MSSM has 5 physical Higgs bosons states after electroweak symmetry breaking, which leads to many more possible production channels. For the two neutral scalars h and H, there is also pair production together with the pseudoscalar A (see Fig. 3.6). Since the H is usually[2] much heavier than the mass range accessible at LEP2, only the h is considered here in detail. Also there is pair production of charged Higgs boson pairs and Higgs decay cascades from the heavier to lighter states like $h, H \to AA$. These production mechanisms are not considered here.

The cross-sections for the h production are suppressed by a α, β dependent factor in the MSSM [Spi97], compared to one in the Standard Model.

$$\sigma(e^+e^- \to Zh) = \sin^2(\beta-\alpha)\sigma_{SM} \quad (3.10)$$

$$\sigma(e^+e^- \to Ah) = \cos^2(\beta-\alpha)\bar{\lambda}\sigma_{SM} \quad (3.11)$$

with the Standard Model cross-section σ_{SM} and $\bar{\lambda}$, which is an additional coefficient to suppress the p-wave cross-section of Ah close to the production

[2] There are a few points in the MSSM parameter space, where one obtains $m_h = m_A =$ 90 GeV/c^2 and m_H =115 GeV/c^2

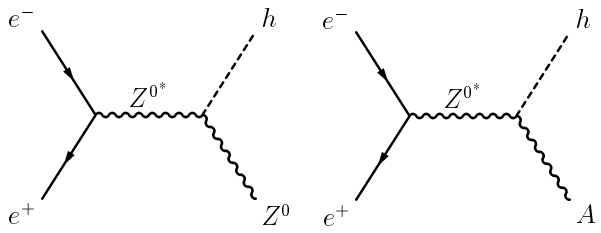

(a) **(b)**

Figure 3.6: Higgs-Strahlung (a) and the hA-pair production (b) in the MSSM.

threshold. Since the mass of the light Higgs boson h is not a free parameter anymore, one has to evaluate the dependence on parameters like m_A,μ and $\tan\beta$. For $\tan\beta$ one usually picks the values 3 and 36 as a kind of lower and upper bound in order to illustrate the different behaviour of the MSSM Higgs sector. The behaviour of the hZ and hA cross-sections is shown in Fig. 3.7. It is clearly visible, that for small $\tan\beta$, the hZ production is the dominant channel, while for large $\tan\beta$, hA dominates, if it is kinematically accessible[3].

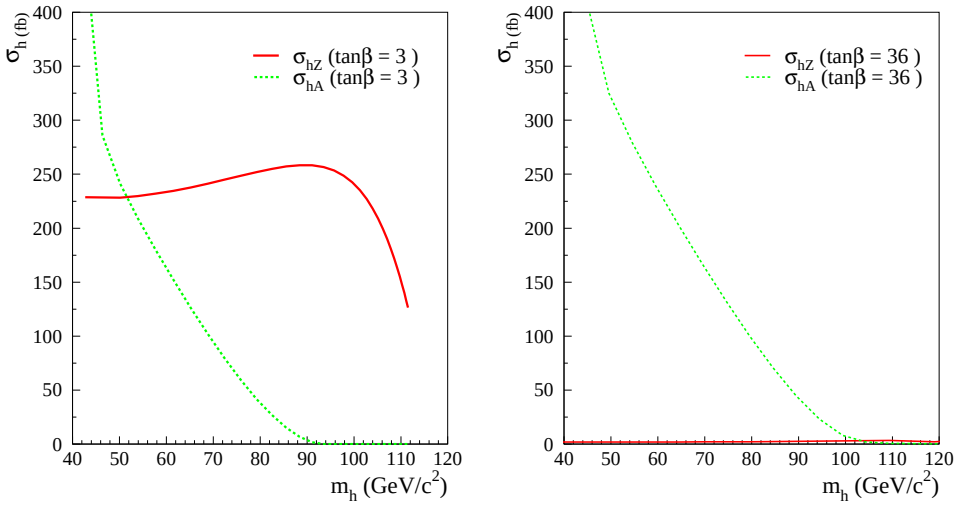

(a) **(b)**

Figure 3.7: The cross-sections for hZ and hA production at $\sqrt{s} = 206.8$ GeV. In (a) the behaviour is shown for a $\tan\beta$ of 3, in (b) for $\tan\beta$ of 36. The other parameters used were $m_A \leq 200$ GeV/c^2, $M_2 = 200$ GeV/c^2 and μ=-200 GeV.

Due to the different parametrisations of the corrections to the Higgs masses

[3]The kinematical limit is given as $\sqrt{s} = m_h + m_A$

[Car00], there are different parameter sets to describe the MSSM Higgs sector. The four LEP experiments use the following parameters (see Tab. 3.2). These parameters are also used in the HZHA [Jan96] package, which was used for calculating MSSM Higgs cross-sections and branching ratios in this thesis.

Parameter	Description
m_A	Mass of pseudoscalar Higgs boson A
$\tan\beta$	Mixing angle of the Higgs doublets
μ	Higgs mixing term
M_2	Common gaugino mass at the GUT scale
X_t	Mixing in the $\tilde{t}$ sector
M_{SUSY}	Common sfermion mass at the GUT scale
m_{top}	Mass of the top quark

Table 3.2: The MSSM parameters used by the LEP experiments in order to describe the Higgs sector.

In Fig. 3.8a the dependence on the μ parameter is shown, varying m_A from 20 to 1000 GeV/c^2. It is clearly visible, that for higher masses of m_A one reaches a decoupling limit, where the mass of m_h remains constant. In this region, the h is very Standard Model like. The effect of varying μ between -500 and 500 GeV leads to a very small effect, in the order of 1 GeV/c^2. Another general feature is, that one obtains higher Higgs masses for larger values of $\tan\beta$. As a next step the mass of the top quark was varied by the experimental error of 5.1 GeV/c^2 [CDF01, D0 99, Dem99] around the central value of 174.3 GeV/c^2 (see Fig. 3.8b) The general behaviour of m_h is the same as in Fig. 3.8a, but the effect of the top quark mass is much larger than the effect of the μ parameter. A more precise measurement of the top quark mass would put strong constraints on any supersymmetric model. The choice of the mixing in the stop sector also leads to different m_h and the highest possible m_h is reached for the maximal mixing in the stop sector. Since there are many possible parameter combinations, it is quite difficult to exclude parameter ranges in the MSSM.

For the Higgs decays in the MSSM the couplings of the Standard Model particles are modified by an α, β dependent factor like for the cross-sections. (see Tab. 3.3). This can strongly alter the branching ratios of the Higgs bosons compared to the ones in the Standard Model.

Φ		g^{ϕ}_{up}	g^{ϕ}_{down}	$g^{\phi}_{W,Z}$
SM	H	1	1	1
MSSM	h	$\cos\alpha/\sin\beta$	$-\sin\alpha/\cos\beta$	$\sin(\beta-\alpha)$
	H	$\sin\alpha/\sin\beta$	$\cos\alpha/\cos\beta$	$\cos(\beta-\alpha)$
	A	$1/\tan\beta$	$\tan\beta$	0

Table 3.3: The Higgs couplings to fermions and W, Z bosons in the Standard Model and the MSSM [Spi97]

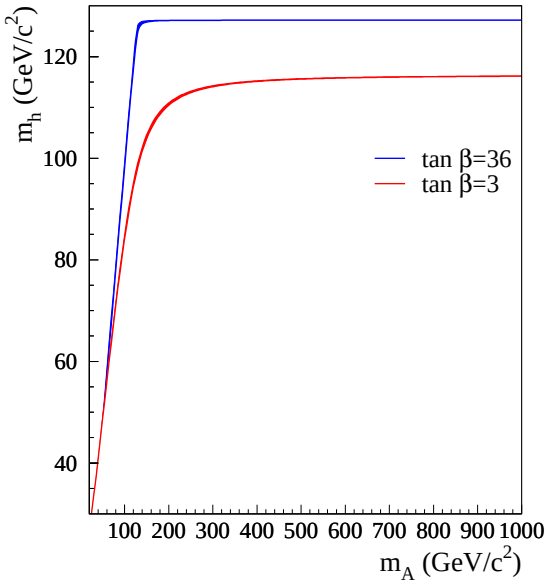

(a)

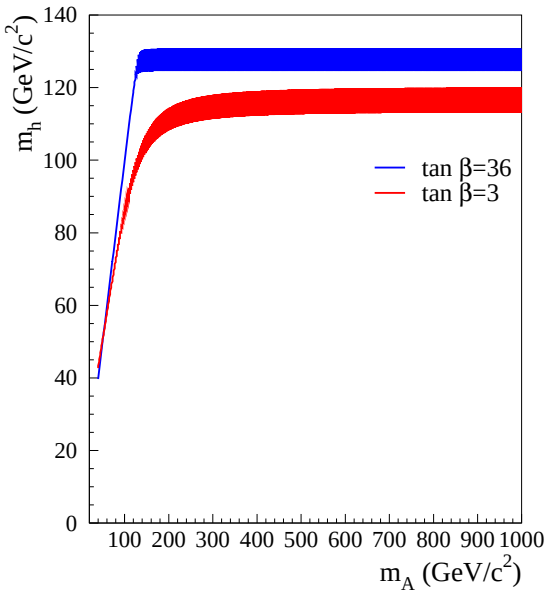

(b)

Figure 3.8: The dependence of $m_h(m_A)$ on μ (a) and m_{top} (b) for two values of $\tan\beta$. μ has been varied between -500 and —-500 GeV and m_{top} has been varied by the experimental errors. For both plots M_{SUSY} has been fixed to 1 TeV, M_2 to 200 GeV/c^2 and X_t to 2439. m_{top} was set to 175 GeV/c^2 in (a) and μ was set to 150 GeV in (b).

In addition to the modifications to the branching ratios into Standard Model fermions and bosons, completely new decay channels may be opened up for a Higgs decay, like the decay into squarks, sleptons or neutralinos and charginos. This may lead to striking new signatures for Higgs decays in the MSSM. In general, one can divide the decays of the light neutral Higgs h in the MSSM in three cases.

Standard Model like case: This is certainly the most familiar one, b quark decays are the dominant decays and the decay into τ leptons is the second most important one, like in the Standard Model.

Couplings to down-type fermions suppressed: This is quite an interesting scenario, usually referred to as the large-μ scenario [Car99]. By choosing the MSSM parameters in a way that the coupling to the down-type fermions, disappear, one obtains regions of the parameter space in which decays into gluons (via top quark loops) or into c quarks dominate. Although these decays are rather uncommon in the Standard Model, these decays are not MSSM specific.

Supersymmetric decays are dominant: These decays can only occur in the MSSM and add a lot of new signatures for the Higgs searches like 2 jets plus missing energy for the process $h \rightarrow \tilde{q}\tilde{q}$ $(\tilde{q} \rightarrow q + \tilde{\chi}_1^0)$ or 2 leptons and missing energy for the process $h \rightarrow \tilde{l}\tilde{l}$ $(\tilde{l} \rightarrow l + \tilde{\chi}_1^0)$. But since one usually assumes, that squarks and sleptons are beyond the LEP2 kinematical range, only the decays into neutralinos or charginos remain interesting. Chargino decays are strongly constrained from the direct searches for chargino production ($e^+e^- \rightarrow \tilde{\chi}_1^+\tilde{\chi}_1^-$), so the most promising decay mode remains the decay to the lightest neutralino. The lightest neutralino is the LSP and therefore stable. It interacts very weakly in the detector. Such a decay would be invisible.

3.2.1 Standard Model decays

For a large part of the MSSM parameter space, the decays into b quarks dominate like in the Standard Model. They are even a bit more dominant, because the coupling to the up-type particles like c quarks or to the bosons are more suppressed. This can be shown for a SM like point in the MSSM for a Higgs mass of 100 GeV/c^2 (see Tab. 3.4).

3.2.2 Decays into gluons or c quarks

For certain points in the MSSM the coupling to the down-type particles can be strongly suppressed. This happens directly via the couplings given in Tab. 3.3. This effect however, can be enhanced by radiative corrections like gluino exchange, that even further suppress the couplings especially to b quarks. In general those points are considered pathological within the MSSM framework, since the theoretical calculations of the radiative corrections in this region are

Channel	SM	MSSM ($\tan\beta$=3)	MSSM ($\tan\beta$=36)
$b\bar{b}$	81.7%	90.8%	88.9%
$\tau^+\tau^-$	7.8%	8.4%	10.9%
$c\bar{c}$	4.6%	0.3%	0.0%
W^+W^-	1.0%	0.1%	0.0%
gg	5.5%	0.4%	0.1%

Table 3.4: Branching ratios for h with a mass of 100 GeV/c^2 in a Standard Model like parameter region of the MSSM.

very difficult [Car99]. The parameter set for one region, including this kind of

Parameter	Value
μ	1000 GeV
M_2	400 GeV/c^2
X_t	-300
M_{SUSY}	400 GeV

Table 3.5: The parameters in the MSSM used to obtain points with suppresses couplings to down-type particles in the large-μ scenario.

points is given in Tab. 3.5. For this parameter set the hotspots are illustrated in the m_A-$\tan\beta$ plane, showing the region where the down-type couplings break down rapidly (see Fig. 3.9). The behaviour of couplings for down-type, up-type and W, Z particles can be seen in more detail in Fig. 3.10a for three values of $\tan\beta$ illustrating again also the dependence on $\tan\beta$. A general comment is, that these points only show up for small m_A (less than 200 GeV/c^2). In the high mass region, the behaviour of the couplings becomes Standard Model like again.

Although the Higgs may be in the kinematical range of LEP2, it may not be visible for the Standard Model like searches, because these searches usually rely strongly on the Higgs decay into b quarks. In the mass range accessible by LEP2, one would then not see an excess in events containing b quarks, but notice a general access coming from hadronic events. This can originate from decays into c quarks or into gluons, which would lead to slightly different topologies, since the jets coming from gluons tend to be broader and contain more particles. The branching ratios for the different decay channels are shown in Fig. 3.10b, showing also that this behaviour is always limited to a small region of m_h.

3.2.3 Invisible decays

As already mentioned, the MSSM also includes completely new decay channels for the Higgs bosons. Besides scenarios with decays in squarks, sleptons or charginos, which are usually disfavoured, the decay of a Higgs in a pair of the lightest neutralinos $\tilde{\chi}_1^0$ is the most attractive scenario. Since the $\tilde{\chi}_1^0$ is

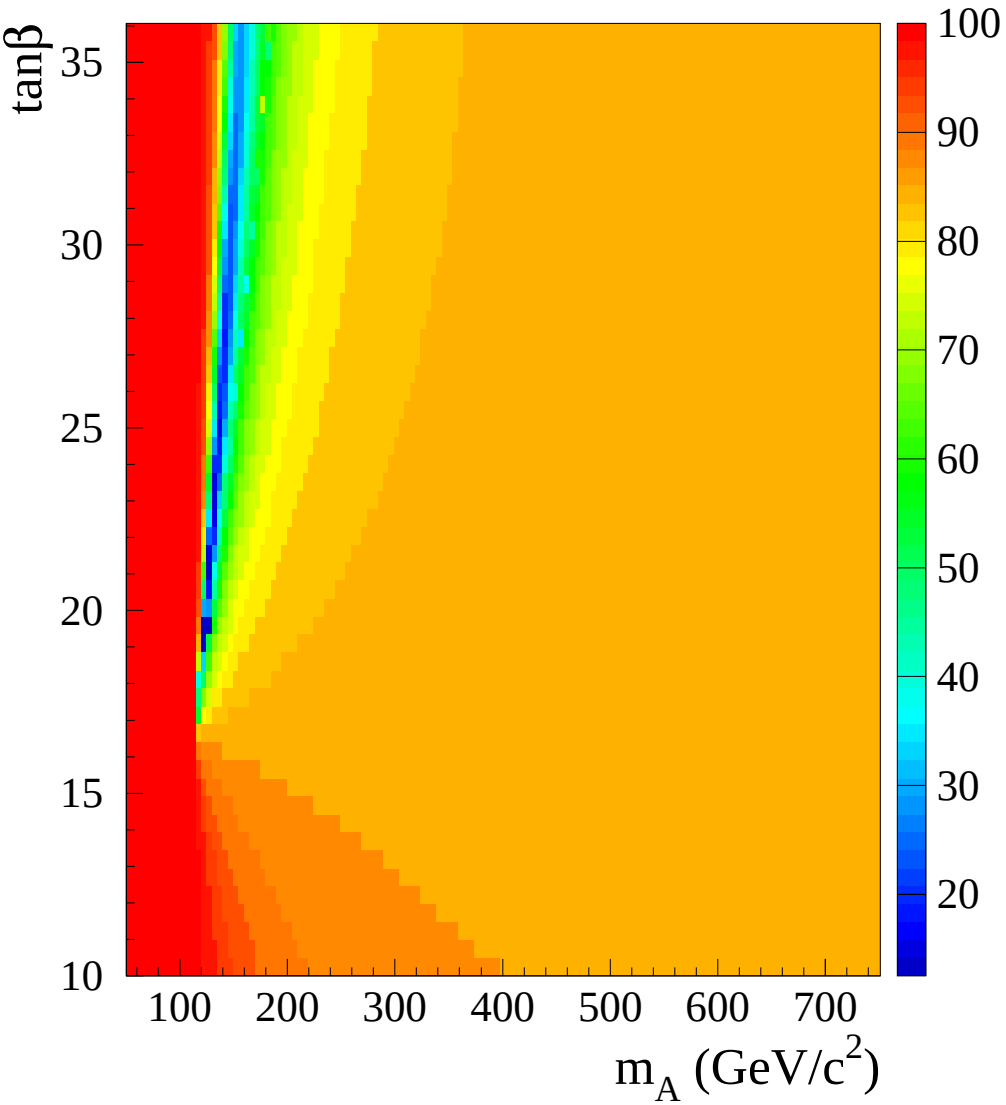

Figure 3.9: MSSM large-μ scenario: The branching ratio of h into down-type particles in the m_A-tan β plane. Clearly visible is the black region, where the branching ratio into down-type particles approaches the 10% level.

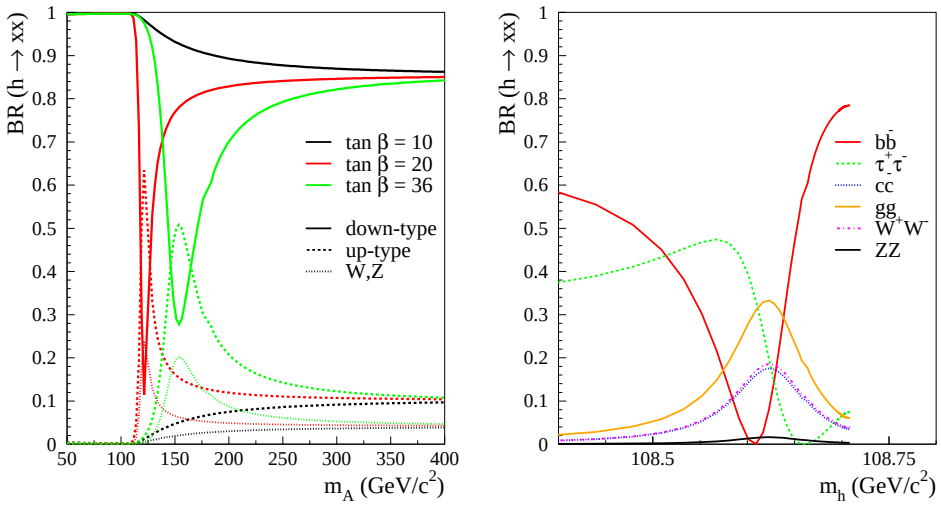

(a) **(b)**

Figure 3.10: MSSM large-μ scenario: In (a) the behaviour for the h couplings to down-type, up-type and W, Z bosons is shown for three values of $\tan\beta$ depending on m_A. In (b) the branching ratios of h are shown for a fixed value of $\tan\beta = 36$.

usually assumed to be the LSP, the $\tilde{\chi}_1^0$ would be stable and due to the very weak interaction with ordinary matter, such a decay would be invisible in the detector. An invisible decay would lead to a completely new signature, and by focusing on Standard Model like Higgs decays, a Higgs decaying invisibly could easily be missed. The branching ratio of the Higgs into neutralinos has been

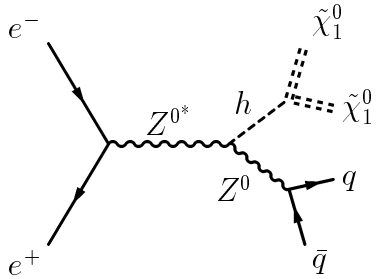

Figure 3.11: The decay of the Higgs boson h into two neutralinos $\tilde{\chi}_1^0$. Since the neutralino is the LSP, this decay is invisible.

calculated as [Djo96]:

$$\Gamma(h \to \tilde{\chi}_1^0 \tilde{\chi}_1^0) = \frac{G_F m_W^2}{\sqrt{8}\pi} m_h \left[1 - \frac{4m_{\tilde{\chi}_1^0}^2}{m_h^2}\right]^3 \kappa_h^2 \tag{3.12}$$

with κ_h^2 being a coefficient depending on the diagonalising matrix Z [Khe92]:

$$\kappa_h^2 = (Z_{12} - \tan\theta_W Z_{11})(\sin\alpha Z_{13} + \cos\alpha Z_{14}) \tag{3.13}$$

The neutralino is a mixture of gaugino and Higgsino states:

$$\tilde{\chi}_1^0 = Z_{11}|\tilde{B}\rangle + Z_{12}|\tilde{W}_3\rangle + Z_{21}|\tilde{H}_1^0\rangle + Z_{22}|\tilde{H}_2^0\rangle \tag{3.14}$$

Therefore the decay of the Higgs into neutralinos is only possible, if the neutralino is not a pure gaugino or Higgsino state. This can be seen from eq. 3.13, where one term of κ_h^2 would disappear for a pure gaugino or Higgsino state. As one can see from the neutralino mass matrix (see chapter 2.2.3), such pure states are only obtained for large values of $|\mu|$ or M_2. This dependence is due to the off-diagonal elements of the diagonalising matrix Z. The decay into neutralinos is also only possible, if the neutralinos are kinematically accessible, which already puts strong constraints on the possible MSSM points. As the kinematical reach for a Higgs at LEP2 is around 115 GeV/c^2, the maximal neutralino mass is around 57.5 GeV/c^2 ($2 \times m_{\tilde{\chi}_1^0} = m_h$).

The dependence of the branching ratio into neutralinos on the μ and M_2 parameters is shown in Fig. 3.12 for two values of m_A (200 and 500 GeV/c^2) and $\tan\beta$ (3 and 36). One can clearly see that small $\tan\beta$ values are favoured and the value of m_A has only a minor impact on the coupling. As one can see from the plots, such decays are only occurring on some points in the parameter space, but then cover a sizeable part of it. The region with large branchings into neutralinos found for negative μ values at a large $\tan\beta$ is kinematically not accessible at LEP2 due to the mass of the Higgs boson h. The possible parameter space at LEP2 for invisible decays is therefore well constrained, the preferred parameters of such decays are shown in Tab. 3.6. As the Higgs may be too light to decay into neutralinos in the no-mixing scenario, the region with a maximal mixing in the stop sector is preferred.

Parameter	Value
M_2	$100 \leq M_2 \leq 300$ GeV/c^2
μ	$100 \leq \mu \leq 200$ GeV
$\tan\beta$	$0.5 \leq \tan\beta \leq 3$

Table 3.6: MSSM parameter set for the invisible Higgs decays, in these regions, invisible decays into neutralinos are the dominant decay modes.

For this selected region in the MSSM parameter space, the decay of h into neutralinos is usually the dominant one, as soon as it is kinematically possible ($m_h = 2 \times m_{\tilde{\chi}_1^0}$). This is shown in Fig. 3.13 for one point in the region. The kinematical threshold is clearly visible here.

In the MSSM there are also other decays, that could lead to invisible final states (see Fig. 3.14). The first one is the decay into two stau sleptons $\tilde{\tau}$ with the $\tilde{\tau}$ being almost degenerate with the neutralino $\tilde{\chi}_1^0$. The mass relation between stau and neutralino is then $m_{\tilde{\tau}} \approx m_{\tilde{\chi}_1^0} + m_\tau$. The $\tilde{\tau}$ subsequently

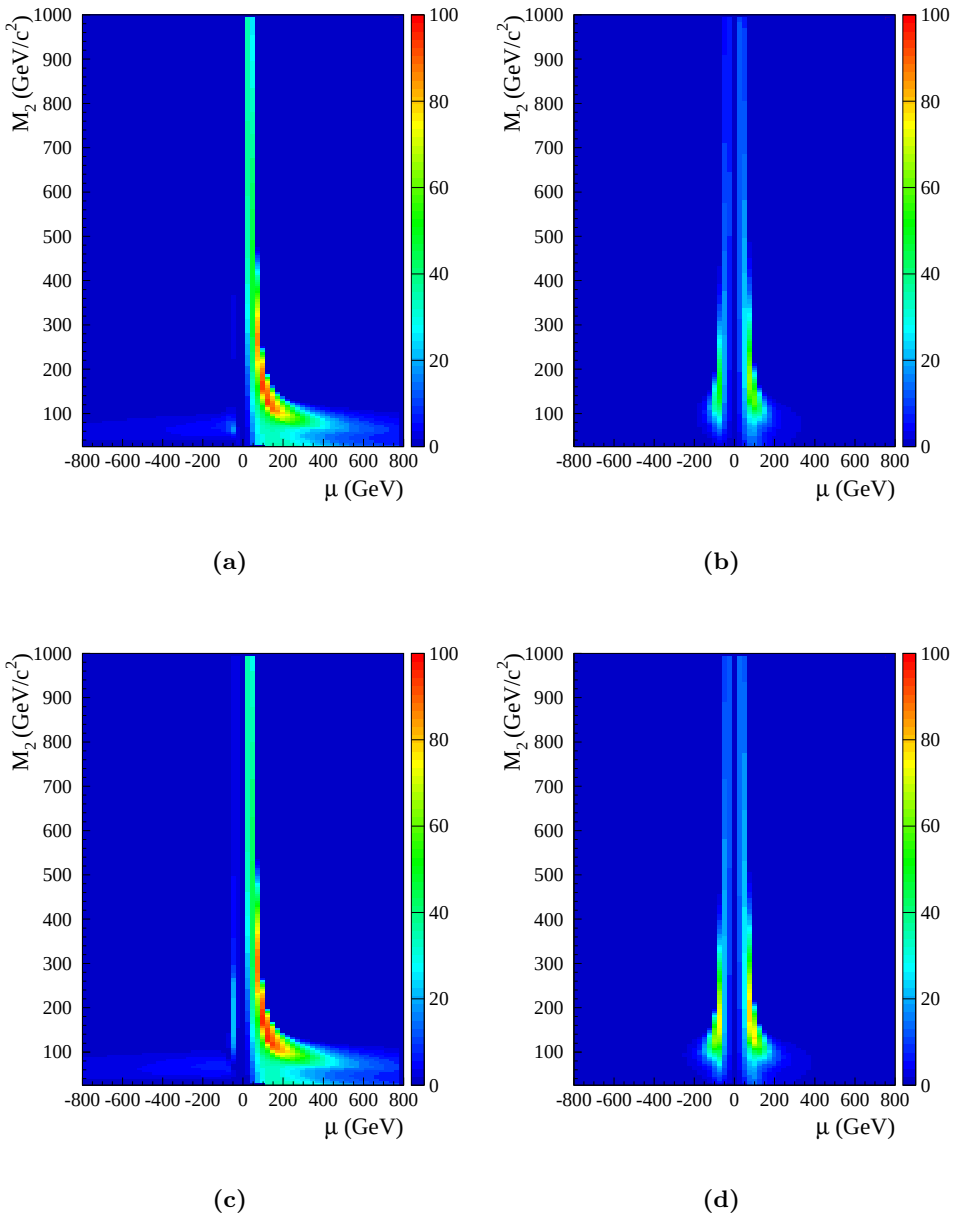

Figure 3.12: The dependence of the branching ratios into neutralinos for different m_A in the μ-M_2 plane. For a light m_A (200 GeV/c^2) this is shown in (a) for $\tan\beta = 3$ and in (b) $\tan\beta = 36$. For a heavy m_A (500 GeV/c^2) this is shown in (c) for $\tan\beta = 3$ and in (d) $\tan\beta = 36$. The mixing in the stop sector was set to the maximum value.

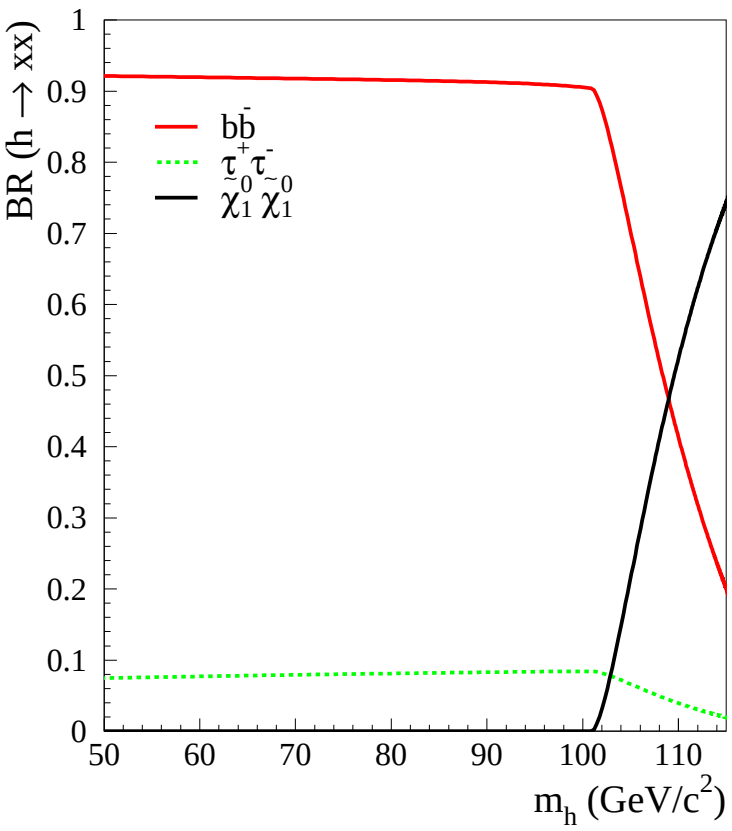

Figure 3.13: The branching ratio of h, if decays into neutralinos are possible. The parameter set used is $\mu = 150$ GeV, $M_2 = 200$ GeV/c^2 and $\tan\beta = 3$.

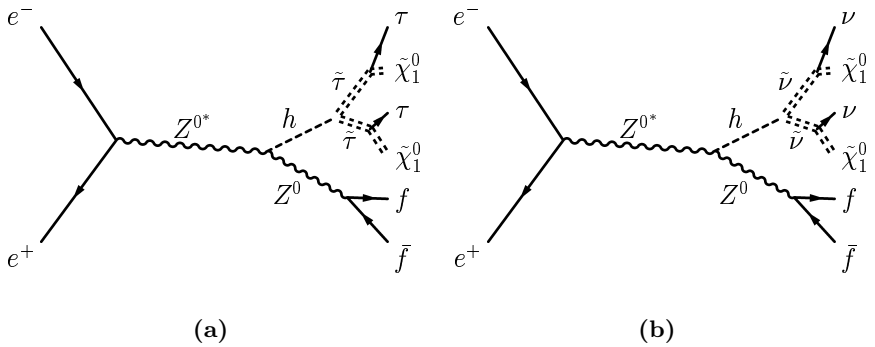

(a) **(b)**

Figure 3.14: The decay of the Higgs boson h into two staus $\tilde{\tau}$ (a) or into two sneutrinos $\tilde{\nu}$ (b). In order to have an invisible decay, the $\tilde{\tau}$ has to be almost degenerate with the $\tilde{\chi}_1^0$ in (a) and the chargino $\tilde{\chi}_1^+$ has to be heavier than the $\tilde{\nu}$ (b).

Parameter	$h \to \tilde{\tau}_1\tilde{\tau}_1$	$h \to \tilde{\nu}\tilde{\nu}$
$\tan\beta$	19.5	10
M_2	85.0 GeV/c^2	70 GeV/c^2
M_0 (common scalar mass)	85.0 GeV/c^2	45 GeV/c^2
μ	-300 GeV	200 GeV
A_t	200 GeV	110 GeV

Table 3.7: Parameter sets for Higgs decays into $\tilde{\tau}$ or $\tilde{\nu}$ using a common scalar mass in the SUSYGEN3 [Gho99] parameter set, which is slightly different to the one from HZHA.

decays into a τ lepton and a neutralino $\tilde{\chi}_1^0$. This decay mode leads to a Higgs signature with two τ produced basically at rest and large missing energy from the neutralinos. The τ's are not detected in this case, or at most seen as very low energetic tracks, that are most likely not fully reconstructed at all. There is however one complication to this, the $\tilde{\tau}$ mixes and one has then two $\tilde{\tau}$ final states, $\tilde{\tau}_1$ and $\tilde{\tau}_2$ with the following relation

$$\tilde{\tau}_1 = \tilde{\tau}_L \cos\theta + \tilde{\tau}_R \sin\theta \tag{3.15}$$

$$\tilde{\tau}_2 = \tilde{\tau}_L \sin\theta + \tilde{\tau}_R \cos\theta \tag{3.16}$$

This decay considered here only assumes the decay into light $\tilde{\tau}_1$. The decay width into two $\tilde{\tau}_1$ can then be written as

$$\Gamma(H \to \tilde{\tau}_1\tilde{\tau}_1) = \frac{G_F}{2\sqrt{2}\pi m_h}\left(1 - 4\frac{m_{\tilde{\tau}_1}^2}{m_h^2}\right)^{\frac{1}{2}} g_{h\tilde{\tau}_1\tilde{\tau}_1}^2 \tag{3.17}$$

The coupling $g_{h\tilde{\tau}_1\tilde{\tau}_1}$ is more complicated than the Standard Model coupling due to the presence of mixing. It is given explicitly in [Djo97]. As one can see in Fig. 3.15, this decay can become dominant, as soon as it is kinematically allowed. A parameter set calculated using SUSYGEN3[4] [Gho99] is given in Tab. 3.7. In order to obtain very low neutralino and stau masses, very low values of M_0 and M_2 have to be used, since it is now required to have both light neutralinos and staus and a sufficiently heavy h, because the decays has also to be kinematically possible. The branching ratios of h for the point given in Tab. 3.7 are shown in Fig. 3.15a, for a mass difference between $\tilde{\tau}$ and $\tilde{\chi}_1^0$ of 2 GeV/c^2. As can be seen in this plot, the decays into $\tilde{\tau}$'s becomes dominant only, if the Higgs is approaching its maximal mass at this parameter point. A general comment is, that the parameters in the MSSM have to be extremely fine tuned to open this decay mode, since the sleptons are usually heavier, so this is a kind of very exotic MSSM scenario.

The other interesting possibility is the decay of the Higgs into two sneutrinos $\tilde{\nu}$ [Djo99]. The masses of the $\tilde{\nu}$ and the slepton masses are related, so in

[4]SUSYGEN had to be used instead of HZHA, because HZHA does not include decays into squarks or sleptons.

order to have light sneutrinos masses and sufficiently heavy slepton[5] masses, the following mass relations apply, using a common scalar mass $\tilde{m}$ [Djo99]:

$$m^2_{\tilde{\nu}} \approx \tilde{m}^2 + \frac{1}{2} M_Z^2 \cos 2\beta \tag{3.18}$$

$$m^2_{\tilde{l}_L} \approx \tilde{m}^2 - 0.27 M_Z^2 \cos 2\beta \tag{3.19}$$

$$\tag{3.20}$$

For large $\tan\beta$ $\cos(2\beta)$ approaches -1 and the required mass splitting is achieved, however with a very large $\tan\beta$, one gets strongly mixed sleptons, which then makes one slepton lighter than the sneutrino again. The decay width summing over all three $\tilde{\nu}$ is [Djo99]:

$$\Gamma(h \to \tilde{\nu}\tilde{\nu}) == \frac{3 G_F M_Z^4}{8\sqrt{2}\pi m_h} \left(1 - 4\frac{m^2_{\tilde{\nu}}}{m^2_h}\right)^{\frac{1}{2}} \tag{3.21}$$

If the decay is kinematically possible, it will be the dominant decay channel. This decay will be invisible as long as the chargino $\tilde{\chi}_1^+$ is heavier than the sneutrino and only the decay $\tilde{\nu} \to \nu\tilde{\chi}_1^0$ is possible. A point where one can have such decays can be found in Tab. 3.7 and the branching ratios are shown in Fig. 3.15b. The same comment as for the $\tilde{\tau}$ decay applies also here; these are very exotic points in the MSSM parameter space and such points can be strongly constrained by direct searches for sparticle production.

3.3 Higgs production and decay in the 2HDM

The 2HDM contains, like the MSSM, 5 physical Higgs bosons. The masses of these bosons are free parameters in the 2HDM and not constrained like in the MSSM. Compared to the MSSM, no new decay channels are introduced, only the branching ratios may be different. As has been already mentioned, there are two types of 2HDM's of interest, the Type-I and Type-II scenarios. Since the Type-II scenario is more closely related to the MSSM, it is described in detail first. Actually, the MSSM is a Type-II 2HDM with a supersymmetric extension.

3.3.1 Type-II scenarios

The Higgs boson properties in the Type-II 2HDM are very similar to the ones in the MSSM, but there are no constraints on the values of the angles β and α, since those angles are free parameters. The couplings to up-type, down-type and vector bosons are the same as in the MSSM (see Tab. 3.3). By the choice of β and α, one can then modify the couplings to up-type or down-type quarks and in an extreme case switch one coupling off completely and set the other to maximum. For searches in the Type-II 2HDM framework one can use the

[5] Otherwise sleptons may have been directly produced in $e^+e^- \to Z \to \tilde{l}^+\tilde{l}^-$ at LEP

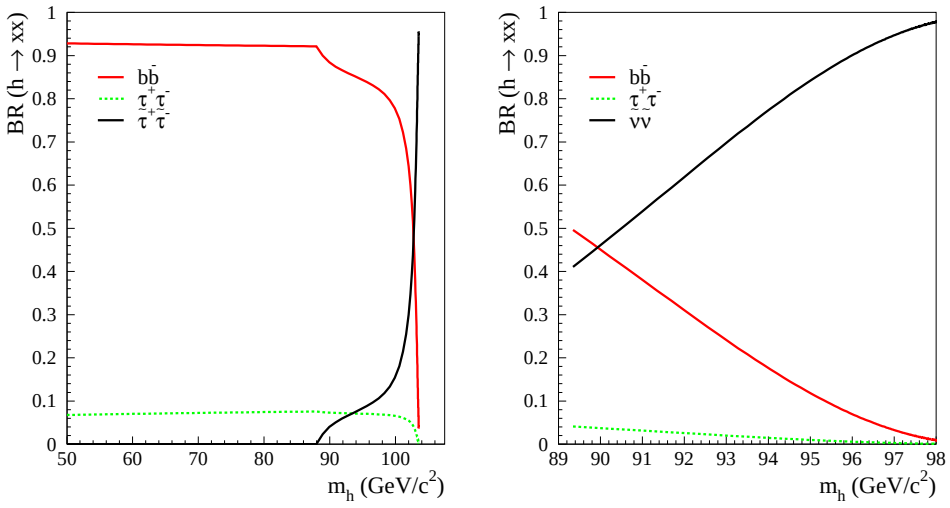

(a) **(b)**

Figure 3.15: In (a) the branching ratio for h is shown, if one has a very light $\tilde{\tau}$, which is almost degenerated with the $\tilde{\chi}_1^0$. In (b) the case with light sneutrinos and the decay $\tilde{\nu} \to \nu\tilde{\chi}_1^0$ being the only possible decay mode.

Standard Model like searches or the down-type dominated regions or use the same searches developed for MSSM large-μ scenarios for the up-type dominated regions. The behaviour for different values of $\tan\beta$ and α is illustrated in Fig. 3.16.

For a fixed value of $\tan\beta = 2$ the branching ratios of the light Higgs boson h is shown in Fig. 3.17 for two values of α (0.035, 0.96), clearly illustrating the dependence of the couplings on α (see Fig. 3.17). Since the coupling of the vector bosons depend on $\beta - \alpha$, their behaviour is slightly different, which could also lead to regions where the decay into bosons is enhanced compared to the Standard Model.

3.3.2 Type-I scenarios

The phenomenology of a Type-I model is completely different compared to the one of a Type-II 2HDM. Since the fermions only couple to one of the doublets, and keeping in mind the possibility to switch off the coupling to one doublet completely, one can easily get fermiophobic scenarios, where the Higgs does not couple to fermions at all. The effect on the branching ratios for this case is illustrated in Fig. 3.18. This effect can also be seen in the behaviour of the couplings, which are listed in Tab. 3.8. As one can see, the fermiophobic limit can be reached for $\alpha \to \frac{\pi}{2}$. The decay into fermions may still be possible via first order loops, but this effect is usually small and only of some importance

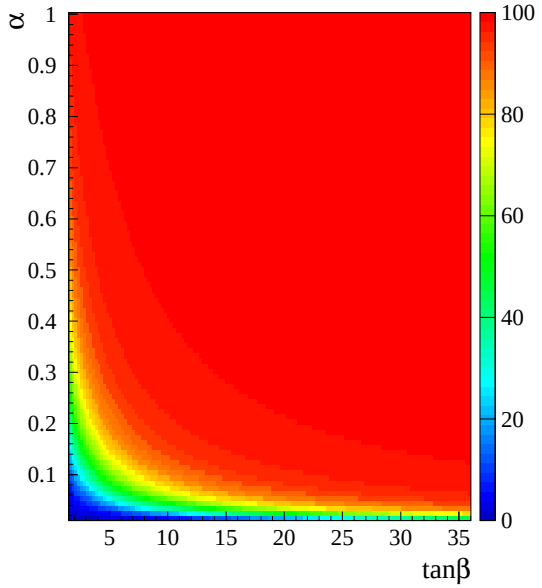

Figure 3.16: The branching ratios of h with a mass of 90 GeV/c^2 in down-type quarks depending on α and $\tan\beta$. For $\alpha \to 0$ the effect of the suppression can be clearly seen. The other 2HDM values were fixed to $\tan\beta$=2, m_A=140 GeV/c^2, m_H=200 GeV/c^2 and $m_{H^\pm}$=135 GeV/c^2.

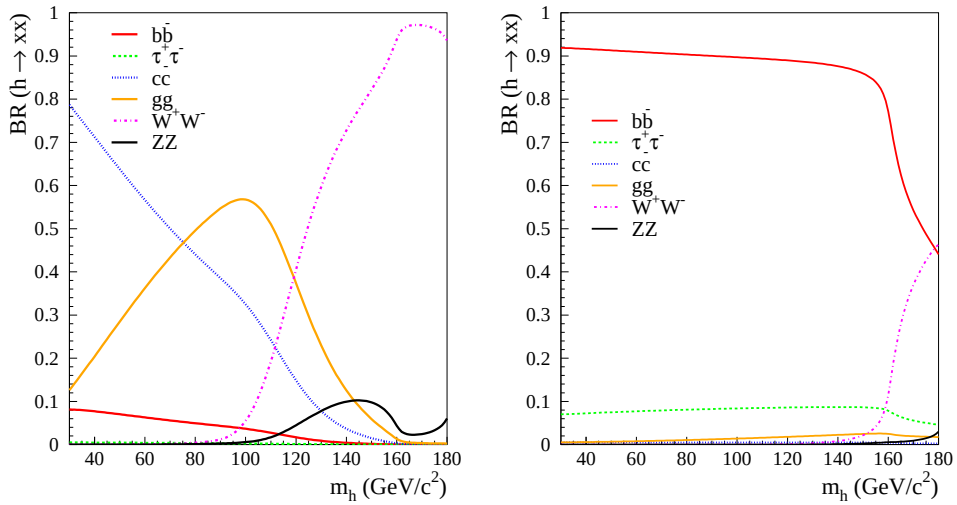

Figure 3.17: The branching ratios of h for two values of α : 0.035 showing clearly the dominance of the up-type decays in that region (a) and 0.96 showing the dominance of down-type decays (b). The other 2HDM values were fixed to m_A=140 GeV/c^2, m_H=200 GeV/c^2 and $m_{H^\pm}$=135 GeV/c^2.

at large values of $\delta = \alpha - \beta$. So only the decays in the W and Z bosons at tree level and the decay into photons at one-loop level give a sizeable contribution. The decay into photons is dominant below a Higgs mass of 100 GeV/c^2, the decay into W bosons dominates above this mass (see Fig. 3.18).

Φ		$g^{\phi}_{f\bar{f}}$	$g^{\phi}_{W,Z}$
SM	H	1	1
2HDM	h	$\cos\alpha$	$\sin(\beta-\alpha)$
	H	$\sin\alpha$	$\cos(\beta-\alpha)$
	A	$1/\tan\beta$	0

Table 3.8: The Higgs couplings to fermions and W, Z bosons in the Standard Model and a Type-I 2HDM [Bar99, Bru00].

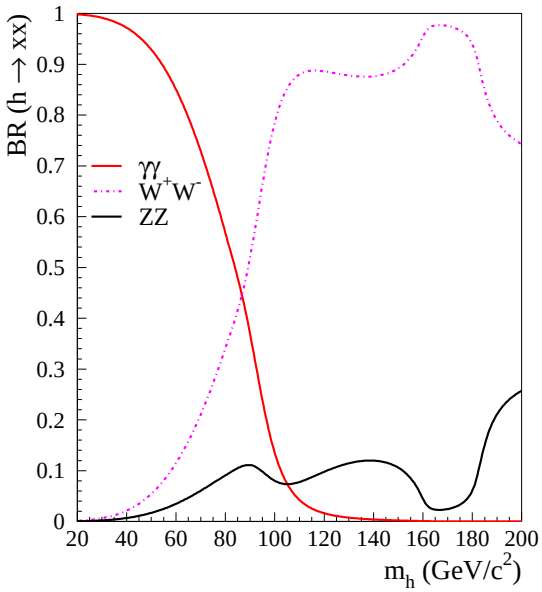

Figure 3.18: The branching ratios of h in the fermiophobic limit of a Type-I 2HDM for a small value of δ.

3.4 Higgs production and decay in a Majoron Model

The most appealing decay mode in this kind of models (see chapter 2.4) is of course the decay in Majorons, because this leads again to invisible final states, since the Majorons are stable and do not interact with ordinary matter. The decay width of the Higgs bosons H,S into two Majorons J is [Jos92]:

$$\Gamma(H \to JJ) = \frac{\sqrt{2}G_F}{32\pi} M_H^3 \tan^2\beta \sin^2\theta \tag{3.22}$$

$$\Gamma(S \to JJ) = \frac{\sqrt{2}G_F}{32\pi} M_H^3 \tan^2\beta \cos^2\theta \tag{3.23}$$

However the decay into quarks is still possible, the Standard Model formula is only slightly modified to take account for the mixing.

$$\Gamma(H \to q\bar{q}) \frac{3\sqrt{2}G_F}{8\pi} M_H m_q^2 \left(1 - \frac{4m_q^2}{M_H^2}\right)^{\frac{3}{2}} \cos^2\theta \tag{3.24}$$

$$\Gamma(S \to q\bar{q}) \frac{3\sqrt{2}G_F}{8\pi} M_S m_q^2 \left(1 - \frac{4m_q^2}{M_H^2}\right)^{\frac{3}{2}} \sin^2\theta \tag{3.25}$$

The decay into Majorons can be dominant, if $\tan\beta$ is large and $\tan\theta$ is of the order of 1. The production behaviour is more difficult, due to the mixing. The H and S bosons are only produced in Higgs-Strahlung, if the doublet component of the Higgs is dominating, since only this component couples to the Z.

Chapter 4

LEP and DELPHI

The data set used in the analyses presented in this thesis, was taken with the DELPHI detector at the Large Electron Positron collider LEP. In this chapter a short overview about the LEP accelerator, the preaccelaration and the LEP performance concerning centre-of-mass energy and luminosity is given. After this summary, the DELPHI detector and its components relevant for the analyses are shortly described and the DELPHI data acquisition chain is sketched.

4.1 The LEP collider

LEP is the world largest e^+e^- collider[1] and has a circumference of 26.8 km. The construction at the CERN site near Geneva started in 1983 and was finished in 1989. The costs for the tunnel and the accelerator complex accumulated to 1.3 billion Swiss Francs, paid by the CERN member states over a time period of 10 years. The tunnel is located between Meyrin (CH), Ferney-Voltaire (F) and the Jura mountains (see Fig. 4.1). In order to shield LEP from cosmic rays the whole site was put about 100 metres below the surface. To save money during tunnel construction close to the Jura mountains, the whole tunnel was inclined by 1.4 degrees towards the Lake Geneva. The tunnel itself consists of 8 straight tubes with a length of 500 metres and eight ring segments with a length of 2800 metres each. The diameter of the tunnel varies from 3.8 to 5.5 metres. The control of LEP takes place at both CERN sites in Meyrin (CH) and Prevessin (F).

Since LEP is a e^+e^- collider, it is possible to accelerate both types of particles in one single beam pipe. For the guidance of the beams 3368 dipole magnets are used, for the focusing of the beams 816 quadrupole-, 504 sextupole- and 700 correction magnets are used [Sch99]. To control the position of the beams, 504 beam position monitors are installed. In the middle of the straight tubes eight caverns have been excavated, 4 small ones for LEP infrastructure and 4 large

[1] also known as a synchrotron, since it is a circular collider

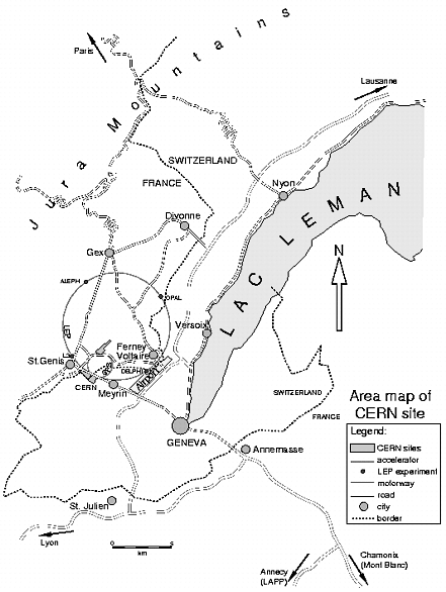

Figure 4.1: The LEP collider at CERN in the Geneva area.

ones to host the 4 LEP experiments: ALEPH[2], DELPHI, L3[3], OPAL[4]. At these points also the four interaction points are located, where the beam collisions take place.

4.1.1 Particle production and acceleration

For the production of electrons and positrons and their preacceleration some additional accelerators are used. Some of these were already present at CERN like the PS (**P**roton **S**ynchrotron) and the SPS (**S**uper **P**roton **S**ynchrotron), others were specially built for the operation of LEP, a sketch of the CERN accelerator infrastructure is shown in Fig. 4.2. At the beginning of the acceleration procedure, the electrons are accelerated in a linear accelerator LIL (**L**EP **i**njector **L**inac) to 200 MeV. These electrons are then converted into positrons via pair production in a material with a high atomic number, for LEP lead is used. The positrons and electrons emerging directly from LIL are then accelerated to 600 MeV and are injected to the EPA (**E**lectron **P**ositron **A**ccumulator), a storage ring with a circumference of 126 metres. In the EPA, the electrons and positrons are stacked to 4 bunches and are then injected into the PS (circumference of 630 metres). There they are accelerated again up to 3.5 GeV and are injected with this energy in the SPS (circumference of 6.9 km). Here the bunches are accelerated one last time up to 22 GeV and are then injected into LEP. The acceleration to the final energy (up to 104 GeV) takes then place

[2] **A**pparatus for **LE**P **PH**ysics
[3] **L**etter of intend no. **3**
[4] **O**mni**P**urpose **A**pparatus for **L**EP

in LEP. For the acceleration in LEP, superconducting cavities were used and the necessary energy is provided by klystrons and lead into the cavities using waveguides.

One weakness of circular storage rings is, that electrons and positrons tend to radiate off photons on their trajectory. This effect is called synchrotron radiation. The loss of energy via synchrotron radiation depends on the centre-of-mass energy (2 times beam energy). For a centre-of-mass energy of 91.2 GeV, it is 1.2 MW, for 200 GeV, it is already 30 MW. So even without acceleration, this amount of energy has to be used, to maintain the energy reached. The energy loss due to synchrotron radiation is given as:

$$\Delta E = 8.85 \cdot 10^{-5} \cdot \frac{E^4}{r} \frac{\mathrm{m}}{\mathrm{GeV}^3} \tag{4.1}$$

with E being the beam energy and r the curvature radius. This leads to the result, that it is very difficult to built e^+e^- synchrotrons with a higher centre-of-mass energy without building very large tunnels, so the future of e^+e^- physics will certainly be in linear accelerators.

4.1.2 The LEP programme

The LEP program can be divided into 2 phases, LEP1 lasting from 1989-1995 and LEP2 lasting from 1995 to 2000. During the LEP1 phase LEP was running on the Z-pole at a centre-of-mass energy of 91.2 GeV producing millions of Z bosons. The main goals of LEP1 were precision measurements of the Z and its properties and the studies of the Z decay products like b-hadrons or τ leptons. For LEP2 the centre-of-mass energy was increased in several steps up to 208 GeV using additional new superconducting cavities. The physics goals for LEP2 were different, besides the measurements of WW and ZZ pair production, a strong focus was set on the searches for new particles, especially Higgs bosons and SUSY particles.

Another very important quantity of a collider is its luminosity, which gives a measure of the expected data rate. Is is defined as:

$$n = \sigma \cdot \mathcal{L} \tag{4.2}$$

with n being the number of events for a certain process and σ being the corresponding cross-section. The luminosity depends on the following parameters of the collider:

$$\mathcal{L} = \frac{N^- N^+ k f}{4\pi\sigma_x\sigma_y} \tag{4.3}$$

$N^{\pm}$ is the number of particles in one bunch, k is the number of bunches (at LEP2 4), f is the frequency and σ_x, σ_y are the widths of the beam at the interaction point assuming a gaussian distribution of particle density orthogonal to the beam direction. At colliders very often the integrated luminosity is quoted, the LEP integrated luminosity from 1990 to 2000 is shown in Fig. 4.3. One also distinguishes between the luminosity delivered to the experiment, and the

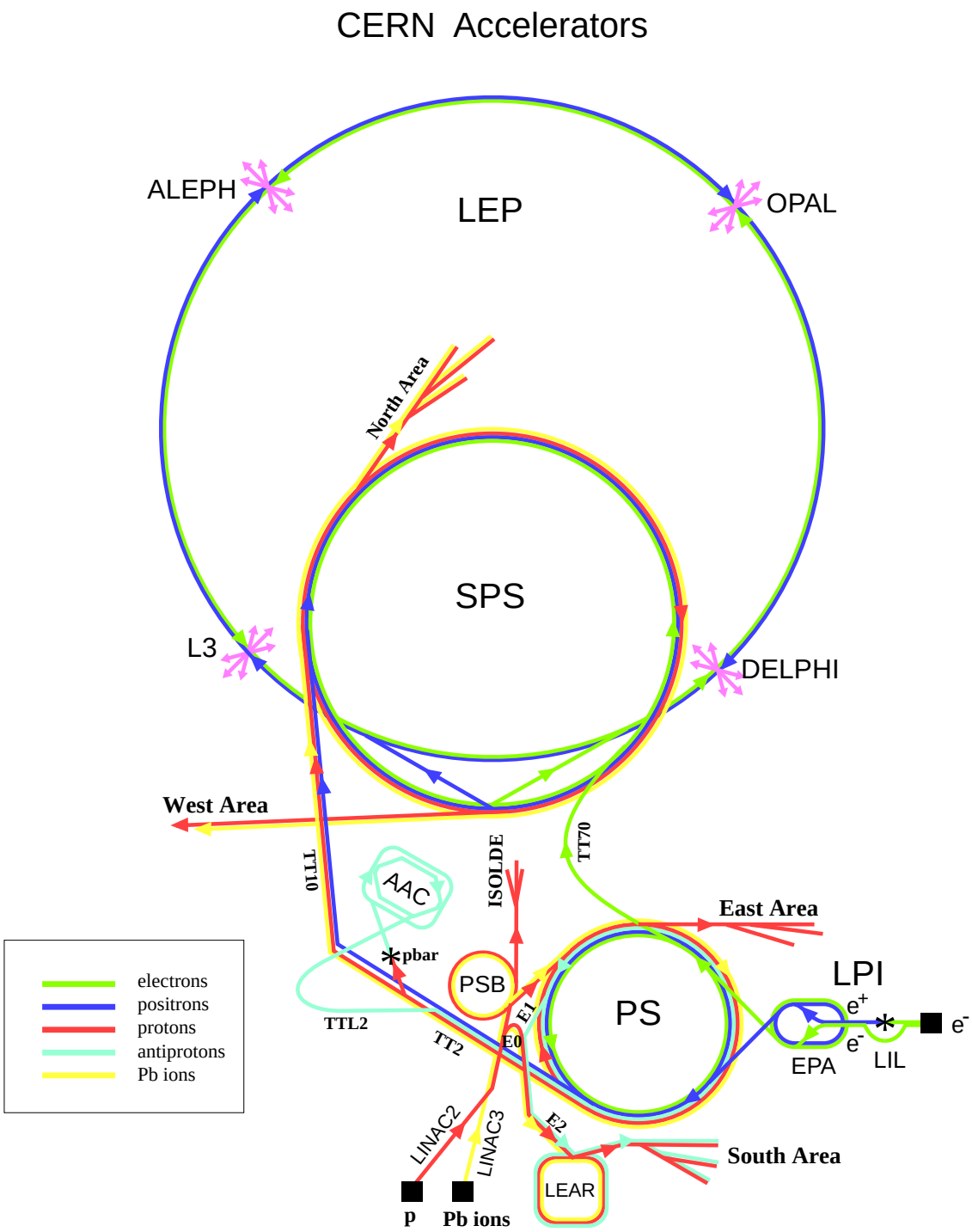

LEP: Large Electron Positron collider
SPS: Super Proton Synchrotron
AAC: Antiproton Accumulator Complex
ISOLDE: Isotope Separator OnLine DEvice
PSB: Proton Synchrotron Booster
PS: Proton Synchrotron
LPI: Lep Pre-Injector
EPA: Electron Positron Accumulator
LIL: Lep Injector Linac
LINAC: LINear ACcelerator
LEAR: Low Energy Antiproton Ring

Figure 4.2: The different accelerators at CERN.

luminosity actually recorded by the experiment, which is usually a bit lower due to the data taking efficiency of the experiment (For DELPHI the average data taking efficiency for 2000 was about 95%). For LEP2, the following centre-of-

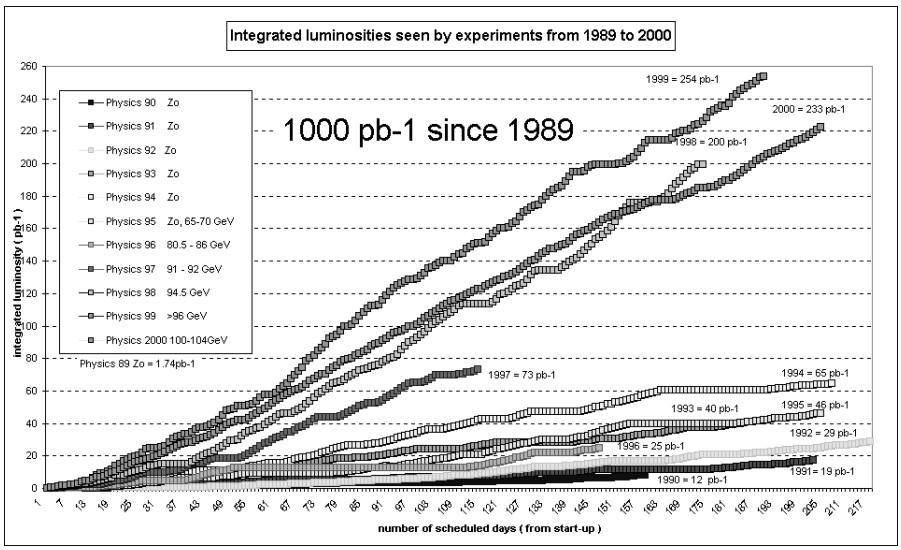

Figure 4.3: The integrated delivered luminosity of LEP between 1990 and 2000 averaged over ALEPH, DELPHI, OPAL and L3.

mass energies and integrated recorded luminosities were obtained from DELPHI (see Tab. 4.1). For the data taking period of 2000, one should keep in mind, that the machine was not operated at a fixed centre-of-mass energy but used the technique of miniramps during a fill. The data taking started e.g. at 205.5 GeV, the centre-of-mass energy was then increased to 206.5 GeV and finally to 208.0 GeV during data taking. This leads to spectrum of centre-of-mass energies as shown in Fig. 4.4.

Year	Centre-of-mass energy (in GeV)	Luminosity (in pb^{-1})
1995	130-136	6
1996	161	10
	172	10
1997	183	54
1998	189	158
1999	192	26
	196	77
	200	84
	202	41
2000	200-209	225

Table 4.1: The centre-of-mass energies of LEP2 and the integrated luminosities recorded by DELPHI from 1995 to 2000.

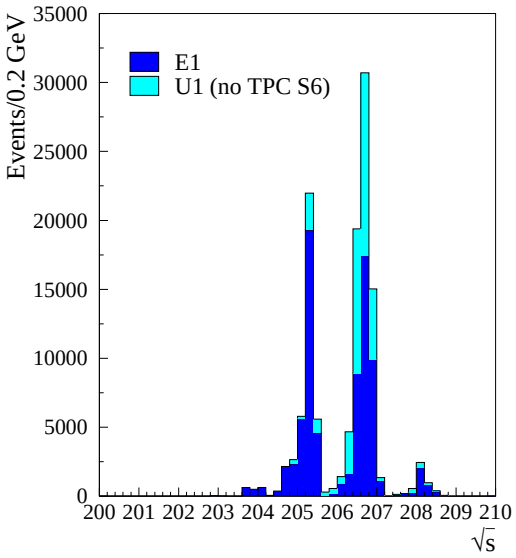

Figure 4.4: The centre-of-mass spectrum of LEP in the year 2000. The U1 data set refers to the period of data taking, where one sector of the TPC (S6) was offline, while E1 refers to the rest of the data recorded.

4.2 The DELPHI detector

DELPHI is one of the four LEP detectors and is operated by the DELPHI collaboration, which has about 550 members from 56 institutes in 22 countries. DELPHI is a general purpose detector, which has an almost optimal coverage of the solid angle of 4 π. The detector diameter is 10 metres and its weight is 3500 tons. DELPHI consist of a central part, the barrel and two endcaps, the forward regions A and C. Only a short overview of the DELPHI subdetectors is given in this thesis, for detailed information see [DEL91, DEL96b]. DELPHI and its subdetectors are shown schematically in Fig. 4.5. The subdetectors of DELPHI can be divided in four categories: luminosity measurement, tracking, calorimetry and particle identification.

4.2.1 The Coordinate system of DELPHI

Since DELPHI has a cylindrical shape, it is convenient to use cylindrical coordinates as DELPHI coordinate system. The origin is put at the interaction point. The z-axis is then defined along the beam pipe, with positive z in the direction of the electrons. The radius R is given as $R = \sqrt{x^2 + y^2}$ and the angle ϕ defines the azimuth angle in the xy-plane. Additionally the angle θ is defined as the polar angle with respect to the z-axis.

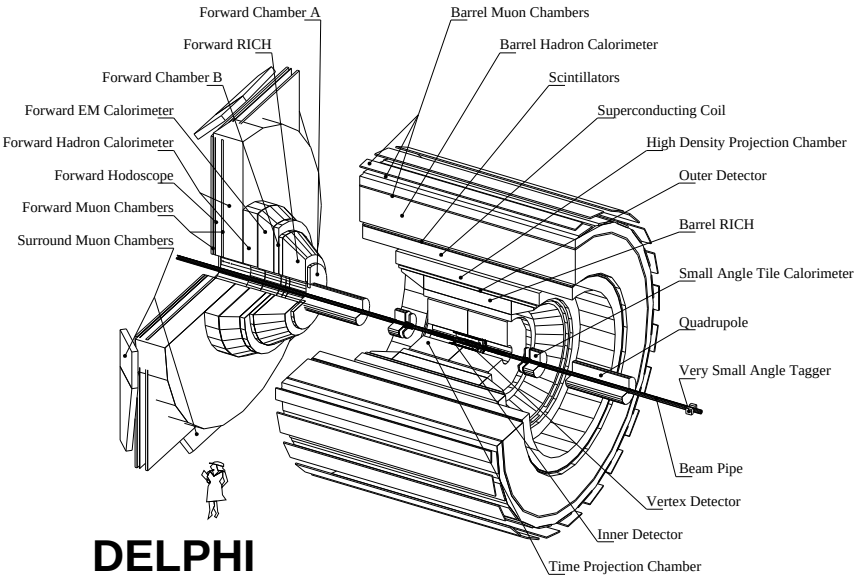

Figure 4.5: Schematic view of the DELPHI Detector.

4.2.2 Luminosity measurement with the STIC

Measuring the luminosity online during data acquisition is very important for a collider experiment. In e^+e^- collisions the luminosity is usually measured using the Bhabha scattering process $e^+e^- \rightarrow e^+e^-$ at small angles of θ. The cross section of this process has been calculated to a very high precision, so theoretical errors can be neglected. The luminosity is then calculated online by counting Bhabha events.

DELPHI uses two detectors to measure the luminosity online, the STIC (**S**mall angle **TI**le **C**alorimeter) and the VSAT (**V**ery **S**mall **A**ngle **T**agger). DELPHI has one STIC for each forward region and the two STIC detectors have a distance of 220 cm each from the interaction point. The polar angle coverage ranges from 1.7° up to 10.6°. The STIC [Alv99] consists of 47 layers of lead and scintillators (see Fig. 4.6) and it has silicon strip detectors after the seventh and thirteenth layer. Every scintillator layer is divided in 10 rings with 16 sectors each.

This form of calorimeter is usually referred to as chachlik calorimeter. The STIC works as follows: A particle hitting the detector generates a shower in the lead layers and this shower generates a blue light in the scintillators. This light is brought to the photomultipliers by wavelength shifting fibres. The spatial resolution in ϕ is 3°, the one in R is about 0.3 - 1 mm. The energy resolution of the STIC can be parametrised as [Alv99]:

$$\frac{\sigma_E}{E} = \frac{0.141 \pm 0.004}{\sqrt{E}} \oplus (6.8 \pm 0.9) \times 10^{-3} \tag{4.4}$$

In order to count Bhabha events online, one requires an energetic cluster in

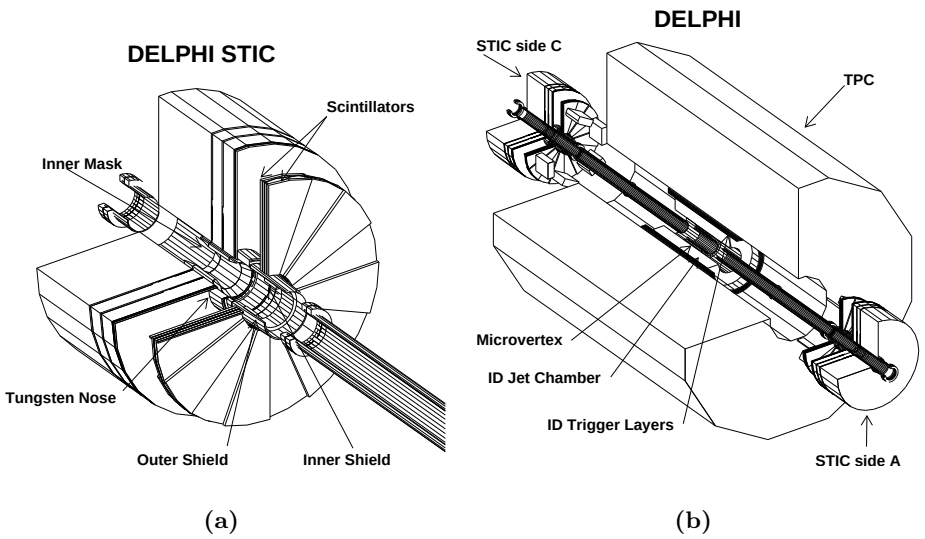

Figure 4.6: Schematic view of the STIC's (a) and their positions. (b)

both STIC's. The accuracy obtained with this method is at the level of 0.2%. The STIC is additionally used to measure the energy of particles at low angles and to increase the hermeticity of the detector.

4.2.3 The tracking system of DELPHI

The tracking system measures the momentum of charged particles. This is done by the curvature of the tracks in a magnetic field. In order to obtain an optimal tracking performance, several tracking systems have to be used and a very homogeneous magnetic field is required.

The superconducting coil

All the tracking detectors besides the muon chambers[5] are located within the superconducting coil of DELPHI. The coil itself has a diameter of 5.2 metres and a length of 7.4 metres. During operation, the temperature of the coil is 4.5 Kelvin and the current is 5000 A, generating a field of 1.23 T. An additional wire layer is located at the end of the coil in order to increase the homogeneity of the field. The coil of DELPHI is still the largest superconducting coil in the world.

[5]Only L3 had also the muon chambers within the coil.

The silicon Vertex Detector (VD)

The VD is the detector which is closest to the beam pipe. Its high resolution combined with the small distance to the interaction point allows a very precise measurement of the particle tracks. The vertex detector has been improved sev-

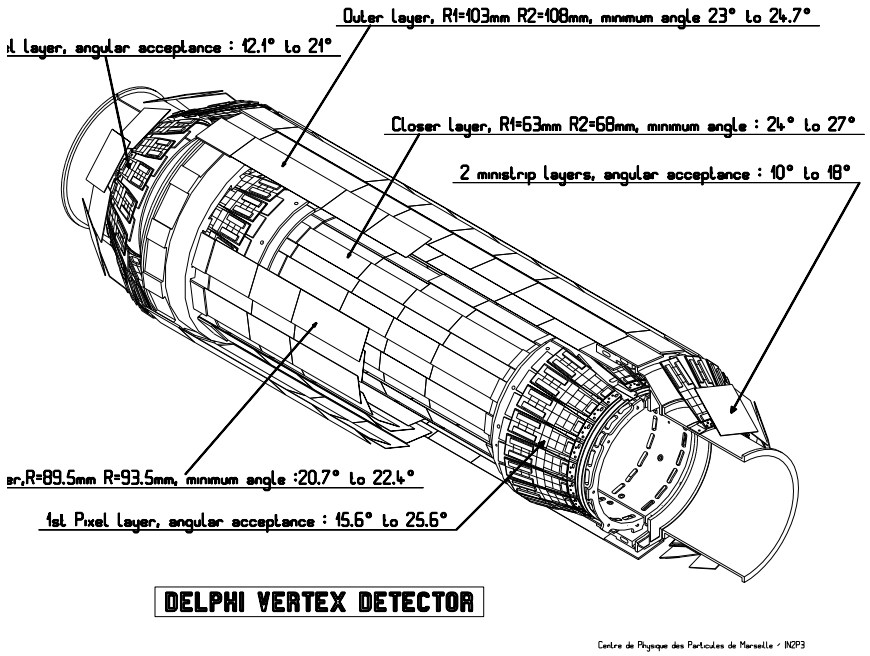

Figure 4.7: The silicon vertex detector of DELPHI as it was used during LEP2.

eral times [Cho98] and consists of a central barrel and the VFT (**V**ery **F**orward **T**racker). The central barrel consists of three layers of silicon strip detectors, called closer, inner and outer layer. The distances of the three layers from the beam pipe are 63, 90 and 109 mm. All three layers have silicon strips in the direction of the z-axis, which leads to a good resolution in $R\phi$. The closer and the outer layer have additional strips orthogonal to the other strips and these strips are used to measure the Rz position. The coverage of the central barrel in θ starts at 23°. The resolution in $R\phi$ is 7.6 μm and the resolution in Rz is 9 μm assuming, the particles pass orthogonally. In order to cover angles below 23°, the VFT was constructed. It consists of 2 layers of silicon microstrip and silicon pixel detectors (see Fig. 4.7) and its resolution is comparable to the one in the central barrel and the ministrips cover an angle between 10°-18°. The two pixel layers consist of 2 x 38 modules with 8064 pixels each The size of one pixel is 330 x 330 μm and its resolution is at the same level. The pixel coverage ranges from 12.1°-25.6°.

The Inner Detector (ID)

The inner detector is the next to innermost detector and it consists of two parts, one JET chamber and a trigger layer. The JET chamber is a drift chamber consisting of 24 segments (see Fig. 4.8). The JET chamber measures up to 24 points for one track, depending on the track energy (for tracks with E $>$ 1 GeV). The trigger layer consists of five cylindrical layers with 192 straw tubes with 8 mm diameter. The straw tubes are very thin proportional counter tubes and measure drift time and the signal peak height of the drift electrons. The

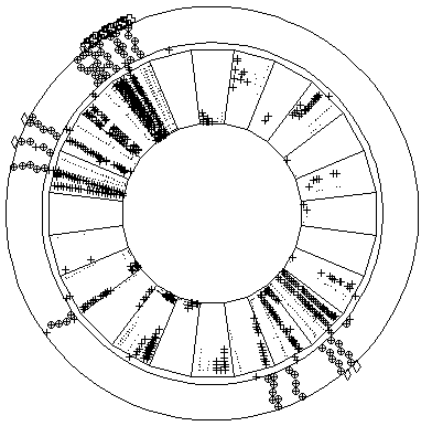

Figure 4.8: The DELPHI inner detector with tracks from a Z event. Inside is the JET-Chamber with its 24 segments and the 5 straw tube layers are visible outside.

inner detector covers angles down to 15°, its resolution in the JET chamber is 40 μm in Rϕ and 1.2 mrad in θ. The straw tube layer has only a resolution of approximately 150 μm in Rϕ and is also used to resolve track ambiguities in the JET chamber. Since the ID is a very fast detector, it has a very important function in the DELPHI trigger.

The Time Projection Chamber (TPC)

The TPC is the main tracking detector of DELPHI, it measures the longest linked parts of a track. A schematic view of the TPC is shown in Fig. 4.9. The TPC consists of two 1.3 metres long cylinders with an inner radius of 29 cm and an outer radius of 122 cm. As filling gas a 4:1 mixture of argon and methane is used. In both halves an electrical field of 150 V/cm oriented towards the endcaps is used as drift field. Each endcap is divided in 6 sectors, each sector contains 1680 cathode strips and 192 signal wires an for one track up to 16 points can be measured. The TPC covers polar angles from 39° onwards and the active volume ranges from 40-110 cm. The resolution is 250 μm in $R\phi$ and 900 μm in z. Since the TPC also measures the signal height, one can obtain

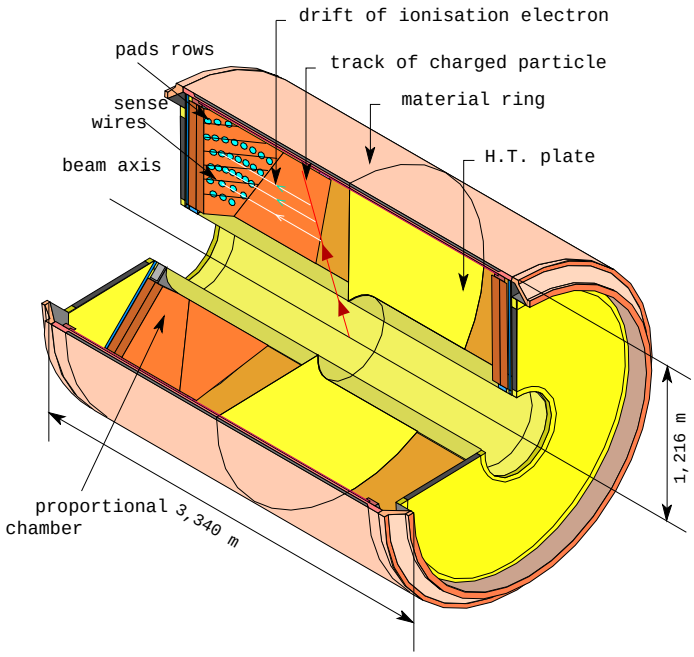

Figure 4.9: The time projection chamber (TPC) of DELPHI.

the specific energy loss dE/dx of a track and use this information for particle identification.

The Outer Detector (OD)

The outer detector is the last tracking detector inside the coil and is necessary because of the RICH (see chapter 4.2.6). One needs to have tracking information before and after the passage of the particles through the RICH in order to resolve ambiguities. The OD covers polar angles from 42° onward and radii from 197 to 206 cm and it consists of 24 modules with 5 layers containing 32 drift tubes each. The OD reaction time is only about 3 ns, which makes it very important for triggering. Its track resolution is 100 μm in $R\phi$ and 44 mm in z.

The endcap tracking chambers (FCA and FCB)

For the tracking in the forward direction, DELPHI has two tracking chambers called FCA[6] and FCB[7]. The FCA is mounted on the endcap of the TPC and is 160 cm away from the interaction point. The coverage in θ ranges from 11° up to 33°. The FCA consists of three drift tube layers, which are rotated by 120° with respect to each other. The FCB is the equivalent to the OD in forward region, since the forward RICH is located between FCA and FCB and it covers

[6] **F**orward **C**hamber **A**
[7] **F**orward **C**hamber **B**

angles between 11° up to 36°. The resolutions in xy are 200 μm (FCA) and 150 μm (FCB). Both chambers are also used in the DELPHI trigger.

The muon chambers

Muons are the only charged particles, that penetrate the inner tracking system and the calorimeters almost unaffected. The muon chambers of DELPHI are therefore the outermost detectors, any particle coming from the interaction point and making a hit in a muon chamber is then considered to be a muon. This information in also used in the particle information process. DELPHI has three muon chambers, the MUB[8] in the barrel region, the MUF[9] in the endcaps and the MUS[10] between the endcaps and the barrel. The MUB uses drift chambers in 24 sectors, each consisting of 3 layers shifted with respect to each other in order to obtain the best possible muon coverage. The MUB covers polar angels from 53.0° up to 88.5°. The resolution is 2 mm in $R\phi$ and 80 mm in z. The two MUF chambers consist of 2 layers, each layer divided in four quadrants (4.5 x 4.5 m). Each quadrant consists again of two drift chamber layers, rotated by 90° with respect to each other. The polar angle coverage ranges from 20° to 42°, its resolution in xy is 5mm. The MUS has been installed in 1994 in order to close a gap in the coverage of the muon system (see Fig. 4.5) the resolution of the MUS is similar to the one mentioned before.

The resolution of the tracking system

The TPC is the main tracking device of DELPHI and measures the most hits per track. This information is then combined with the information coming from the VD, ID and OD. The resolution obtained with the tracking system was measured with LEP1 $Z \rightarrow \mu^+\mu^-$ events and the resolution for tracks in the barrel is [DEL91, DEL96b]:

$$\sigma(1/p) = 0.57 \times 10^{-3} \frac{1}{\text{GeV}} \tag{4.5}$$

The resolution in the forward region between 20° and 35° is

$$\sigma(1/p) = 1.31 \times 10^{-3} \frac{1}{\text{GeV}} \tag{4.6}$$

using the information from VD, FCA and FCB [DEL91, DEL96b]. Important for a good detector resolution is the alignment of the different detector components. The alignment is also done with $Z \rightarrow \mu^+\mu^-$ events at 91.2 GeV, this is one of the reasons why also every LEP2 data taking period contains one or more runs at 91.2 GeV.

[8] **MU**on chamber **B**arrel
[9] **MU**on chamber **F**orward
[10] **MU**on chamber **S**urround

4.2.4 The calorimeters

The calorimeters are used to measure the energy depositions in an event. A precise measurement of the energy is especially useful for searches with a large amount of missing energy, where one is relying on a precise measurement of the visible energy. DELPHI has two types of calorimeters, the electromagnetic calorimeters for electrons and photons and the hadronic calorimeters for charged and neutral hadrons.

The High density Projection Chamber (HPC)

The HPC is the electromagnetic calorimeter in the barrel and is the last detector inside the coil. It consists of 144 modules, which are arranged in rings of 24 modules. The HPC covers the space between 2.08 - 2.6 m and polar angles from 41.5° onwards. A disadvantage of the HPC is the existence of gaps every 15 degrees due to the modular structure of the HPC. The same gap also exists between the six rings. A module consists of 41 3 mm thick lead layers as conversion material, the space between them (8 mm) is filled with an gas mixture of 80% argon and 20% methane. The HPC works the following way: A charged particle produces a shower in a lead layer and the ionised particles then drift in the electric field along the z-axis towards the module endcaps, where they are read out via multiwire proportional chambers like in a TPC, a schematic view of one HPC module is shown in Fig. 4.10. Additionally there is one layer of plastic scintillators, that provides fast trigger signals (<1 μs), as the readout of the complete chamber takes about 17 μs. Due to the readout in 256 channels, the z resolution obtained is quite high, after calibration, it ranges from 2.3 to 4.5 mm. The resolution in θ is about 1.2 mrad, the one in ϕ is about 3.1 mrad. The energy resolution is given as:

$$\frac{\sigma_E}{E} = \frac{0.44}{\left(\frac{E}{GeV}\right)^{0.6}} \oplus 0.0042 \tag{4.7}$$

This value has been obtained from the calibration with Compton and Bhabha events.

The Forward ElectroMagnetic Calorimeter (FEMC)

The FEMC is based on another principle than the HPC, it uses lead glass detectors. Each FEMC is a disc of 5 metres diameter and has 4532 detectors with 32 cm^2 each. Particles that pass through the lead glass generate Cherenkov light which is read out with photomultipliers. The coverage in θ ranges from 8° up to 35°and the energy resolution of the FEMC is

$$\frac{\sigma_E}{E} = 0.03 \oplus \frac{0.12}{\sqrt{\left(\frac{E}{GeV}\right)}} \oplus \frac{0.11}{\left(\frac{E}{GeV}\right)} \tag{4.8}$$

The spatial resolution in the xy plane is 0.5 cm for showers larger than 2 GeV.

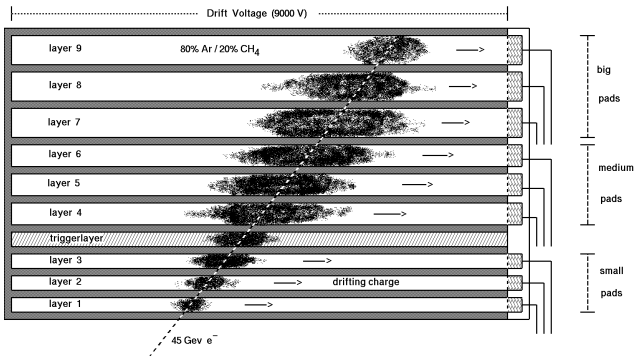

Figure 4.10: One module of the High density Projection Chamber (HPC) of DELPHI. Shown is the passage of one electron through the modules and an artistic view of the shower profile.

The HAdron Calorimeters (HAC)

DELPHI has hadron calorimeters both in the barrel and in the endcaps. The HAC in the barrel is installed in the magnetic joke of the coil and covers polar angles from 42.6° onwards and it consists of 24 sectors with 20 layers of gas detectors each. These gas detectors are installed in between 5 cm thick iron plates and are filled with a mixture of argon, CO_2 and iso-butane. The two hadron calorimeters in the forward region cover polar angles between 11.2° and 48.5°, they are constructed in the same way than the one in the barrel. The resolution of the hadron calorimeter is 3.75° in ϕ and 2.96° in θ, the energy resolution is

$$\frac{\sigma}{E} = 0.21 \oplus \frac{1.12}{\sqrt{\left(\frac{E}{GeV}\right)}} \tag{4.9}$$

The resolution in the endcaps is approximately the same.

4.2.5 The hermeticity counters

One goal for a detector is to obtain an almost perfect hermeticity, meaning, that no particle, that could interact with the detector matter, can escape undetected. This is even more important, if you are looking for events with missing energy. In reality, there are always gaps in a detector, due to construction constraints, like detector coverage but also cables, gas lines or mounting structures. Particles that pass through such regions remain undetected. At DELPHI there are two regions, which have gaps, the first one is the region between barrel and endcaps, because in this place there are a lot of cables and other supply lines. So a region with a θ between 36° and 42° (40° region) is not covered by calorimeters. The other region is the region between a θ of 89.5° and 91.5° (90° region), because of the separation plate in the center of the TPC. In order

to detect especially photons escaping in those gaps, special hermeticity counter have been installed from 1993 to 1995 in the 40° region [DEL92, Bam94] and later also in the 90° region. The so-called 40° taggers consist of three rings of lead and scintillator plates. The light from the scintillators is brought to the photomultipliers with wavelength shifting fibres. With this setup, no direct energy measurement is possible, but the passage of photons can be detected and a so-called hermeticity veto is then given. The gaps in the HPC are also closed with such lead+scintillator plates (ϕ taggers). In order to improve the hermeticity even more, two other systems mainly used for triggering, the TOF and the HOF are used. The TOF[11] is a scintillator layer in the barrel outside of the HPC and the HOF[12] is a scintillator layer in the MUF. The detection efficiency is around 90-95% for the 40, 90° taggers and almost 100% for the ϕ taggers.

4.2.6 Identification of charged particles with the RICH

A unique component of DELPHI is the RICH[13]. It does particle identification using the Cherenkov effect. The opening angle of the Cherenkov cone is given as:

$$\cos\theta_c = \frac{\sqrt{1+m^2/p^2}}{n} \tag{4.10}$$

with m being the mass of the particle, p its momentum and n being the ratio of the speed of light in the vacuum and in the medium. Measuring this angle and the momentum of the particle allows to measure its mass precisely and with this information identify the particle. DELPHI was constructed to provide 4π particle identification and therefore has a RICH in the barrel and in the endcaps. The capability of particle identification is however not very often used in searches for new physics, but more in analyses of b decays.

4.3 The online system of DELPHI

4.3.1 The triggers

The readout time of the different subdetectors are quite different, the typical readout time is about 3 ms. During detector readout, the detector is not capable to record another event and is blind. With 4 bunches in LEP a BCO[14] takes place every 22 μs. The triggers must therefore separate events from background and decide when to readout the complete detector in order to minimise the deadtime. DELPHI has a four level trigger system, with two hardware triggers (T1 and T2) and 2 software triggers (T3 and T4). They are described in detail in [DEL02c]. T1 and T2 run synchronous with the BCO signal provided

[11] **T**ime **O**f **F**light counters
[12] Forward scintillator **HO**doscope**F**orward
[13] **R**ing **I**maging **CH**erenkov detector
[14] **B**eam **C**ross **O**ver

by LEP. T1 triggers after 3.9 μs using the informations from the fast subdetectors (ID, OD, TPC, FCA, FCB), from TOF, HOF, MUB, FEMC, HAC and the scintillator layer in the HPC. It requires either a track segment in one of the tracking chambers, or an energy deposition in one of the calorimeters. Alternatively a back-to-back coincidence in the scintillators (TOF,HOF) is also possible. T2 then uses additionally the other detectors and makes a trigger decision after 39 μs after the BCO. The T2 trigger can be divided into a single track trigger, a single photon trigger, a multi photon trigger and a two track trigger. Already with these two triggers, the downtime is reduced to about 2%. T3 and T4 are software filters on top after the hardware trigger. The efficiency for hadronic events, which is the important one in the context of this theses, is almost 100%.

4.3.2 Data Acquisition

During data taking all events that have passed the T2 trigger are written on tape. All raw data of every event are stored in ZEBRA banks [CER93], which allows dynamical access to all data. The data taking is controlled with the DAS[15] system. Every event gets a unique identifier with a number of the LEP fill, the run number, a consecutive number of data taking periods and the event number within a run. A typical hadronic event has an event size of 150 kBytes on tape.

4.4 The Offline system

After writing the data on tape, the so-called offline process starts. The data are then analysed using DELANA [DEL89a], which analyses and calibrates the informations of the subdetectors. Then DELANA does the track reconstruction and tries to fit the tracks to energy deposits in the calorimeter. All calorimeter deposits that have no track pointing to them are then identified as neutral particles. Furthermore the primary vertex is reconstructed and a first particle identification is done. This is then written out as FullDST[16]. It contains all detector informations, the four vectors of the reconstructed particles and the particle identification results. To reduce the data size further, a so-called XSHORT[17] DST is produced. This package removes some of the raw detector information and adds the results of additional software packages for particle identification, like the recognition of b hadron decays. As a last step, the events are then classified using DAFNE[18][Nav96], to simplify the analyses later. The classifications are:

- Events with a signature for new physics (Higgs, SUSY). This is used primarily for fast scanning interesting events during data taking.

[15] **D**ata **A**cquisition **S**ystem
[16] **D**ata **S**ummary **T**ape
[17] e**X**tended **SHORT**
[18] **D**ELPHI **A**nalysis to **F**lag **N**ew **E**vents

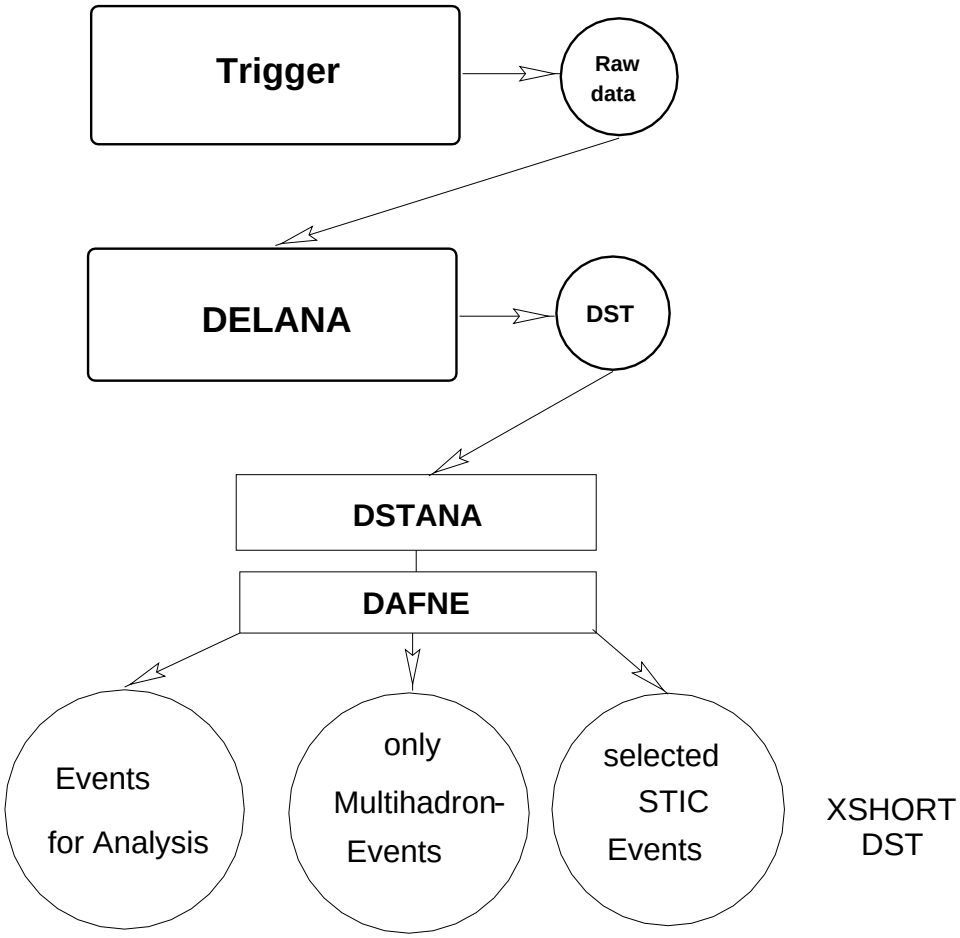

Figure 4.11: The offline data stream of DELPHI.

- All events that are relevant for analysis.
- All hadronic events.
- Events with activity in the STIC.

After converting the event into the XSHORT format, the event size for a hadronic Z event is reduced to 20 kBytes. These final data sets are then uniquely identified with a label including the year of data taking and the DELANA version. 2000E1 e.g, is the 2000 data set, processed with DELANA version E1 for the corresponding year. Note, that the raw data are kept and are processed several times in order to obtain the best possible quality of reconstructed data. The offline data stream is shown in Fig. 4.11.

Chapter 5

Analysis tools for Higgs searches

In this chapter various important tools used in the searches for Higgs bosons are introduced. The searches for Higgs bosons depend on a very good description of the Standard Model backgrounds, since a possible signal would show up as a tiny deviation in the Standard Model background. Furthermore the searches conducted in the context of this thesis, which rely on a good reconstruction of the jets, originating from the Higgs decays. Therefore an introduction to the jet reconstruction algorithms used in the analyses is given. Another important task is to ensure a reliable energy flow, which done using a hermeticity veto procedure. Since the expected signal is usual very small, it is not sufficient to use sequential cut analyses to get a reasonable signal efficiency. More sophisticated methods like neural networks or Iterated Discriminant Analyses (IDA) have been used in the framework of this thesis. The advantage of these methods is, that they take correlations between the variables into account, which allow a more efficient separation between signal and background. If no evidence for a Higgs bosons has been found, one would like to set an exclusion limit on masses or cross-sections. This can be done using statistical methods like the modified frequentist likelihood ratio approach.

5.1 Event simulation

As has already been mentioned, the quality of the simulation for the Standard Model background processes is essential for searches for new physics. For LEP2 one has quite a variety of Standard Model backgrounds to simulate, as can be seen in Fig. 5.1.

In general, one can distinguish between final states containing leptons and final states containing jets. In the searches conducted in this thesis, only final states containing jets are interesting, so the simulation of this class of final states will be described in more detail.

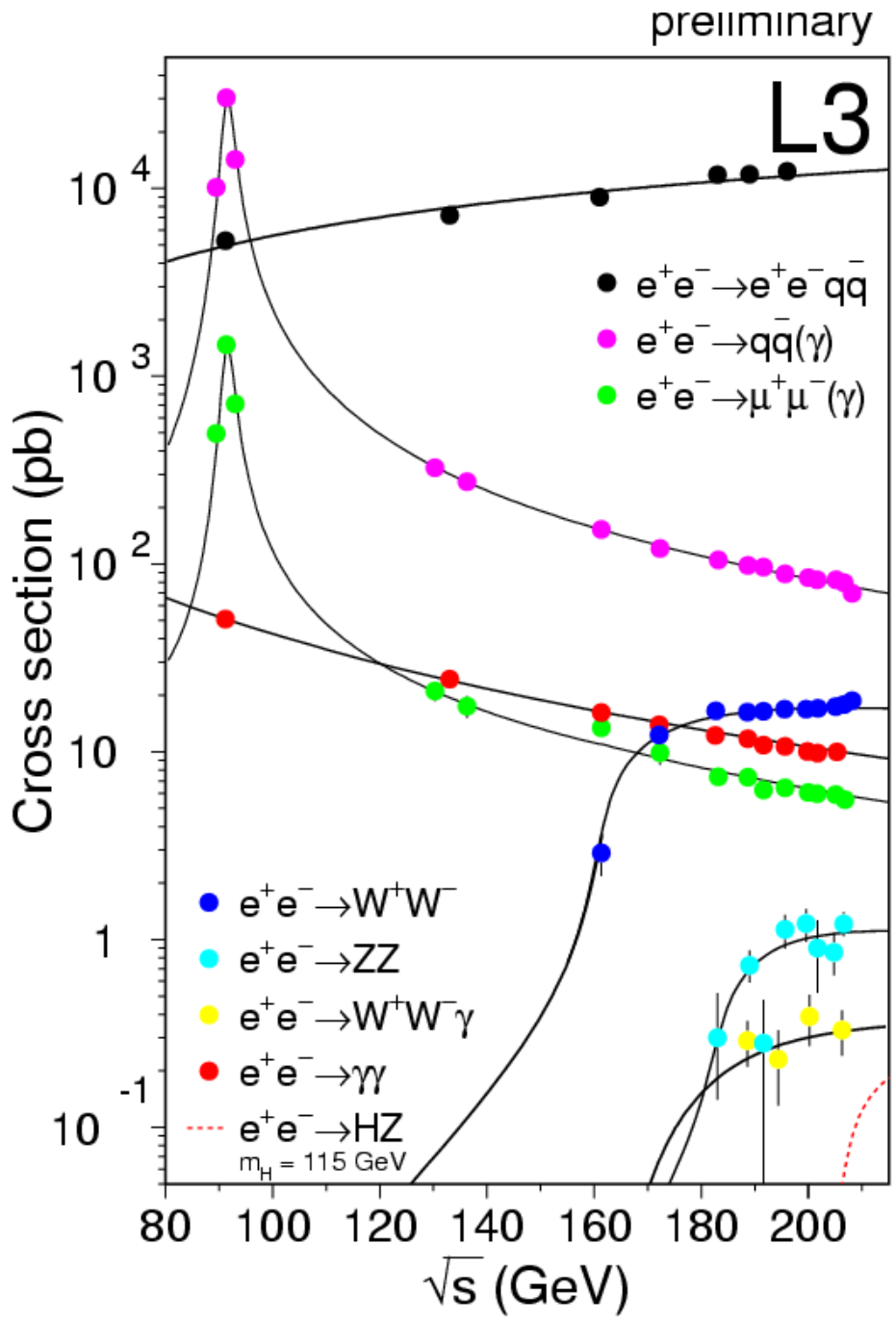

Figure 5.1: The Standard Model background processes at LEP showing the production cross-sections depending on the centre-of-mass energies for selected two fermion ($q\bar{q}\gamma$, $\mu^+\mu^-\gamma$), 4 fermion (WW,ZZ) and photon-photon ($q\bar{q}$,$\gamma\gamma$) processes. Additionally, a possible SM Higgs signal is shown.

5.1.1 Simulation with jets in the final state

The process $e^+e^- \rightarrow Z \rightarrow q\bar{q}\gamma$ is taken as an example for a final state containing jets, since this process is certainly one of the best known processes at LEP and it is the simplest final state containing jets. The formation of the jets out of the primary quarks can be divided in four phases.

- The electroweak phase
- The parton generation phase
- The hadronisation phase
- The decay of all unstable particles

Since all four phases are quite different from the interactions that take place there, they will be described separately. These phases are illustrated in Fig. 5.2.

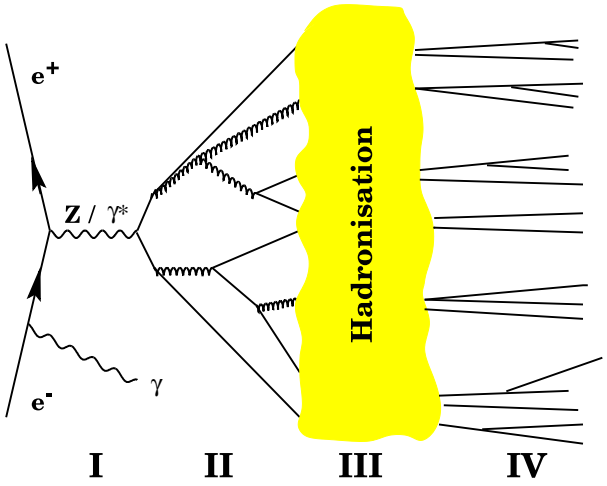

Figure 5.2: The four phases exemplary for the process $e^+e^- \rightarrow Z \rightarrow \bar{q}q\gamma \rightarrow$ *hadrons*. The phases are: the electroweak phase (I), the parton generation due to QCD processes (II), the hadronisation of the partons (III) and the decay of the hadrons to stable final states (IV) [Vol99].

The electroweak phase

This phase involves the formation of virtual Z bosons in a e^+e^- collision and the Initial State Radiation (ISR) of the electrons and positrons. The formation of a Z is a normal electroweak interaction, that is theoretically well understood. At an e^+e^- collider, one has also the ISR effect: One or more photons are radiated of the incoming electrons or positrons before the collision takes place. This reduces the centre-of-mass energy by the amount of the energy carried

away by the photons. Since many analyses rely on the precise knowledge of the centre-of-mass energy, the ISR has to be also precisely simulated. In the case of the example process $e^+e^- \to Z$, this effect can be pretty strong, leading to so-called radiative returns to the Z pole. In this case, a hard photon is radiated of, and the centre-of-mass energy is reduced to the Z-pole energy, which strongly effects the event topology.

The parton generation phase

The Z boson decays into two primary quarks, also called partons. These partons then radiate off gluons, that again split up into gluons or quarks. Since this all takes place at high energies, this can be calculated using perturbation theory. The problem however is the large amount of partons, so that several approaches are used in the description of the parton phase, like the exact matrix elements from perturbation theory, parton shower models and colour dipole models.

The exact matrix elements are only available for up to four final particles ($q\bar{q}, q\bar{q}g, q\bar{q}q\bar{q}$ and $q\bar{q}gg$). The implementation of these elements are usually limited, when it comes to 4 partons, like e.g. in the PYTHIA generator [Sjö01].

A method used very often is the parton shower approach. In this method only leading log approximations are taken into account. The three processes

- $q \to qg$: Gluon radiation
- $g \to gg$: Gluon splitting to gluons
- $g \to q\bar{q}$: Gluon splitting to quarks

are used iteratively as long as the energy scale allows the application of perturbation theory. This cut-off is usually at 1 GeV. In order to include higher order interferences, the radiated gluons are ordered according to their angles.

A third approach for the parton phase is the usage of colour dipole models. In these models it is assumed, that one treated the radiated gluon as radiation between a colour dipole between the $q\bar{q}$ pair. This is also true for a second less energetic gluon. This second gluon is then treated as radiation between two independent dipoles qg_1 and $g_1\bar{q}$. In the colour dipole model, this approach is generalised for many partons. One uses then three kinds of dipoles, $q\bar{q}$, qg and gg, for the parton generation. One interesting point is, that this description tends to have a higher rate of gluon splittings than parton shower models. The only generator, which has a colour dipole approach implemented is ARIADNE [Lon92].

The generation of the partons in Phase II is shown in Fig. 5.2.

The hadronisation phase

After the generation of all partons, the energy scale is so low, that perturbative QCD cannot be used anymore. Therefore phenomenological approaches

have to be used. The most successful model for the description of the hadronisation is the string fragmentation or Lund model [Sjö94, Sjö01]. In order to generate hadrons, the string fragmentation model uses the colour potential and fragmentation functions. The colour potential can be written as:

$$V(r) = -\frac{4}{3}\alpha_s \frac{1}{r} + \sigma r \tag{5.1}$$

If the distance between the two quarks is small, the σr disappears and the quarks are asymptotically free. If the distance is increased, the potential grows proportional to r. Due to the self interaction in the QCD, the field lines between the two quarks have a string like shape. As soon as the energy is sufficient, a new $q\bar{q}$ pair is created out of the string (see also Fig. 5.3). This process is repeated as long till only colourless hadrons remain. The quark flavour produced in the

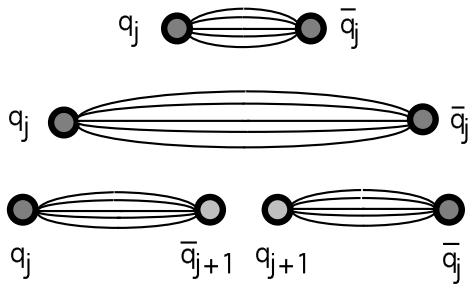

Figure 5.3: The string fragmentation between two quarks. If one tries to separate the two quarks, the energies increases drastically. If the distance approaches a certain level, the generation of another quark pair is energetically preferred [Vol99].

string fragmentation depends quite strongly on the mass of the different quarks. The probability depending on the mass is [Sjö94, Sjö01]:

$$P \propto e^{-\frac{\pi m^2}{\kappa}} e^{-\frac{\pi p_\perp^2}{\kappa}} \tag{5.2}$$

with $\kappa \approx 1$ GeV/fm being the energy density of the colour field. The ratio obtained for the different quarks flavours in fragmentation is:

$$u : d : s : c : b = 1 : 1 : 0.3 : 10^{-11} : 10^{-100}$$

So mostly the light quarks (u, d, s) are produced in fragmentation. In order to describe the momenta of the daughter particles from fragmentation, one use the following assumptions. The transverse momentum is gaussian distributed and has to be estimated from data. The longitudinal momenta z depend on the quarks mass, and are parametrised using the symmetric Lund function [Sjö94, Sjö01] for light quarks.

$$f(z) = \frac{1}{z}(1-z)^A \cdot e^{\frac{Bm_\perp^2}{z}} \tag{5.3}$$

with the parameters A and B. For the heavy quarks (c, b) the Peterson [Sjö94, Sjö01] function

$$f(z) = \frac{1}{z\left(1 - \frac{1}{z} - \frac{\epsilon_q}{1-z}\right)^2} \tag{5.4}$$

with the parameters ϵ_q $q = b, c$ is used. All theses parameters have to be derived from data. The fragmentation functions for the different quarks flavours are shown in Fig. 5.4. The heavy quark, especially the b quarks tend to fragment

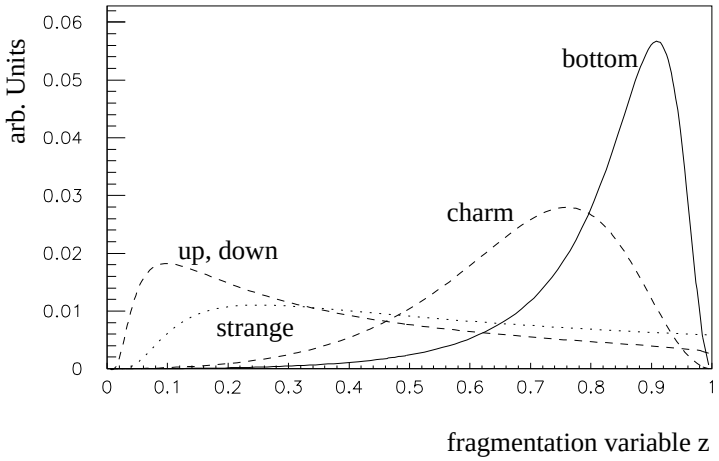

Figure 5.4: The Lund and the Peterson function for the different quark flavours.

hard, meaning, that the b hadron takes most of the energy of the primary quark.

The decay of all unstable particles

After fragmentation, one has only mesons and baryons left from the primary quarks. These are in most cases not stable yet, so as a last step they have to decay into the stable final states. These decay rates and branching ratios are again taken both from theory and from data. After this step one has all kind of particles emerging from the interaction point.

All the particles are stored in so-called LUND commons, that contain the four vectors, the flavour codes, information about parent or daughter particles and many more informations. For a detailed description of the LUND common refer to the PYTHIA manual [Sjö01].

In order to simulate not always the same event, one has to use Monte Carlo methods to generate random events. This is done using the known branching ratios and momentum and energy distributions as input probabilities for the event generation. A problem is to have unique random seeds for the random generator in order to prevent the generation of the same events. In DELPHI,

this is solved using a LABO-ID for each institute[1] and a run number like for the data. In order not to mix up data and Monte Carlo run numbers, the latter ones are negative.

5.1.2 Detector simulation

After the steps described before, the simulated events do not include the information, how they would interact with the detector. The part of the so-called detector simulation is done by a separate program, called DELSIM [DEL89b, DEL89c], that reads the Lund commons generated by the event simulation and simulates the detector response. The output of DELSIM is then stored as raw DST like the real data. After that the simulated events are parsed through the same offline chain as the data (see Fig. 4.4) and stored also as XSHORT DST's.

5.1.3 Simulation of two fermion background processes

This is a very dominant class of processes, which can be separated into hadronic two fermion final states and leptonic two fermion final states. The corresponding Feynman diagrammes are shown in Fig. 5.5. The generation of $q\bar{q}\gamma$ has been described in detail in section 5.1.1. This backgrounds have been generated using

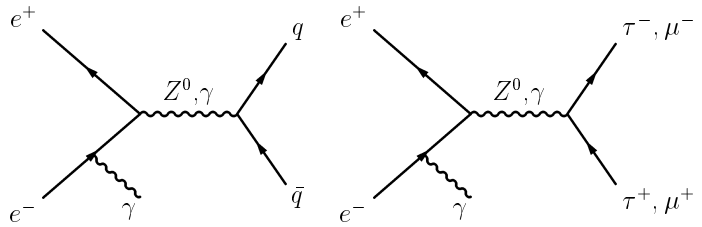

Figure 5.5: The two fermion background processes at LEP. The $q\bar{q}\gamma$ process is shown in (a), the $l^+l^-\gamma$ is shown in (b).

the KK2F 4.14 [Jad00] event generator. The parton generation and hadronisation of the generated events were done using PYTHIA 6.156 [Sjö01]. This was done because the description of ISR is better in KK2F than in PYTHIA, but KK2F does not include code to do the parton generation and hadronisation, it stops after the electroweak phase. The description of ISR is especially important for searches in missing energy channels, since this class of events can be quite similar to the expected signature, especially if the radiated photon is lost either in the cracks of the detector or in the beam pipe. The lepton samples

[1] The one for Karlsruhe is KARL.

were separated into $\mu^+\mu^-\gamma$ and $\tau^+\tau^-\gamma$ samples due to their quite different behaviour. The muons just travel through the detector without decaying, while the τ leptons do decay within the detector, which means that the decays have to be treated also. These events contain very few charged tracks, so these channels are not very important for the searches conducted in this thesis.

5.1.4 Simulation of four-fermion background processes

Four-fermion processes are all kind of processes with four fermions in the final state, excluding processes like final state radiation. The most common processes

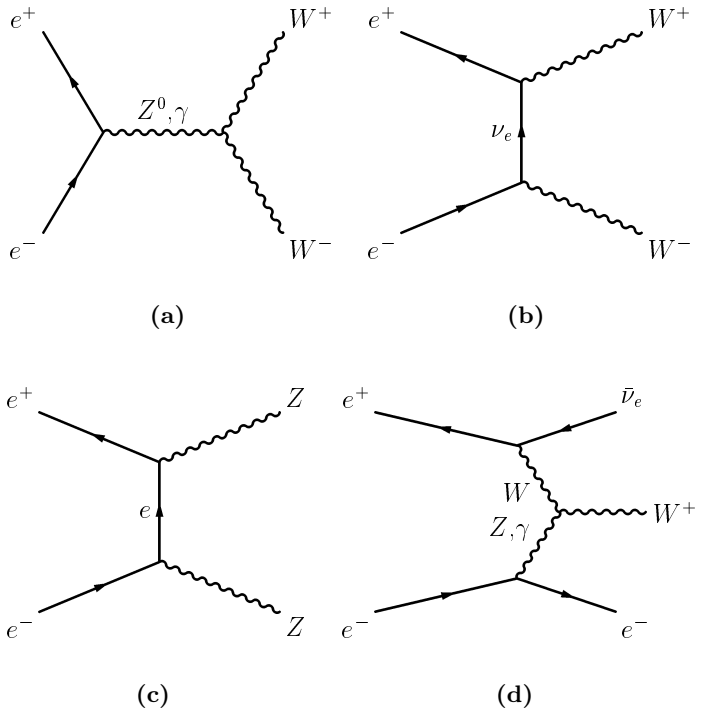

Figure 5.6: The four-fermion background processes at LEP. The WW pair production is shown (a) and (b), the ZZ pair production is shown in (c) and the $We\nu_e$ t-channel process is shown in (d).

in this class of backgrounds are the pair production of W or Z bosons, but there are many other interesting processes like $We\nu_e$ or Zee t-channel processes or the $Z\gamma^*$ channels. The production cross-section of most of those channels is however much smaller than the one of WW or ZZ pair production. The Feynman graphs of some of the processes are shown in Fig. 5.6. For an accurate simulation of the four-fermion background, one has to take into account all four-fermion diagrammes. This results in the following number of diagrammes [Ber94] for the three main classes of final states: fully leptonic (431), semileptonic[2] (222)

[2]One pair of fermions is leptonic, the other one hadronic.

and fully hadronic (210). Compared to the two-fermion backgrounds this is a huge number, which makes simulation much more challenging.

The production of these final states is done using the WPHACT 2 generator [Acc02]. The parton generation and hadronisation is again performed with the PYTHIA 6.156 generator [Sjö01]. All four-fermion background processes are put into two classes of simulation samples, the 4f-CC[3] and 4f-NC[4] samples. In the 4f-CC samples, the WW pair production processes and all kind of processes with similar final states are included. For example, these samples include the $We\nu_e$ t-channel process and also some NC final states, which have similar final states like WW pair production, e.g. $ZZ, Z\gamma^* \rightarrow q\bar{q}q\bar{q}$. This can also be seen in Fig. 5.7a. The reason for putting all those kinds into one sample are the interference terms between these final states.

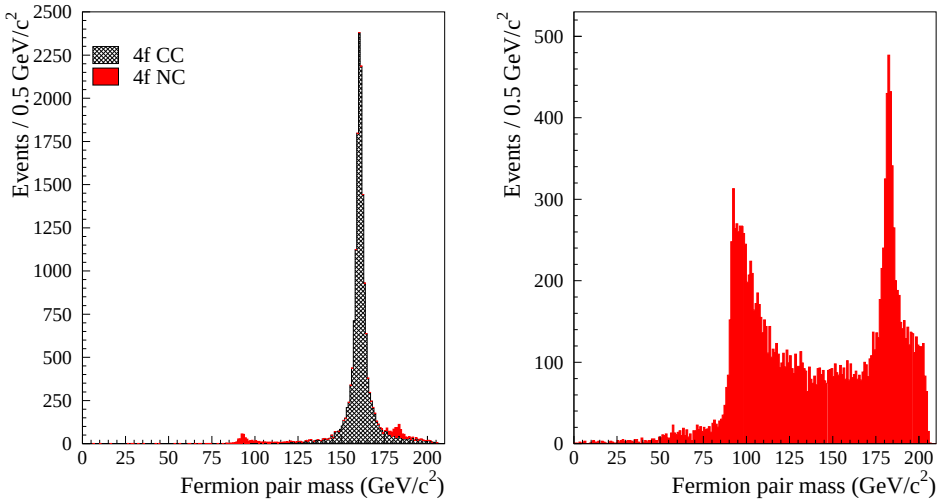

Figure 5.7: The 4f-CC and 4f-NC mass spectra. In (a) one can clearly see the contribution of NC processes in this sample, especially around 91 GeV/c^2 ($Z\gamma^*$) and 182 GeV/c^2 (ZZ), however this sample is dominated by the WW pair production peak at 161 GeV/c^2. In (b) the mass spectrum for remaining NC processes is shown: the expected peaks at 91 GeV/c^2 from $Z\gamma^*$ and 182 GeV/c^2 from ZZ are clearly visible. The spectra have been generated using WPHACT 2.

In the 4f-NC samples all the other NC samples, that are not WW like, are included, e.g. $ZZ, Z\gamma^* \rightarrow q\bar{q}\nu\bar{\nu}$ or $ZZ, Z\gamma^* \rightarrow q\bar{q}l^+l^-$. The mass spectrum is shown in 5.7b. The four-fermion background is one of the dominating backgrounds for all kinds of searches for Higgs bosons, so their accurate simulation

[3] **C**harged **C**urrent
[4] **N**eutral **C**urrent

is very important.

5.1.5 Two photon background

The last class of backgrounds arises from so-called $\gamma\gamma$ interactions leading to $e^+e^-f\bar{f}$ final states. Concerning the cross-section, they are the largest class of backgrounds. The process itself seems to be easy at first glance. Each incoming electron/positron radiates off a photon. These photons collide and generate hadrons or leptons. The theoretical treatment is not so easy, since one has to account for the properties of the incoming photons, which can be either point-like or have a structure. One can separate three classes of events:

- Point-like interactions of the photons (QPM).
- Hard processes, one of the photons fluctuates into a $q\bar{q}$ pair
- Soft hadronic processes. The photons takes vector meson like properties, that interact very softly. This is described by the VDM[5].

The situation is even more complicated due to the fact that these processes tend to be very forward boosted, so one might miss one or all of the incoming particles. The divergencies at these low angles can lead to numerical problems. An event generator has to take into account all these possibilities to simulate the $\gamma\gamma$ background accurately. For the generation of those final states, the PYTHIA 6.143[6] [Sjö01] generator is used, which provides the best description of this background. Another technical problem is that there is an overlap with four-fermion final states, which has to be taken into account. The $\gamma\gamma$ sample is therefore split, between the "pure"$\gamma\gamma$ sample, which is generated using PYTHIA, and a $\gamma\gamma$ sample with NC component, simulated using WPHACT. Concerning cross-sections, the first one is by far dominating. By using this splitting, one avoids double counting between $\gamma\gamma$ and four-fermion generators. Although the $\gamma\gamma$ interactions provides a large number of events, their importance is not that large for the analyses conducted in this thesis.

5.1.6 Simulation of Higgs signals

In order to search for Higgs bosons, it is important to have a theoretically accurate simulation how the signal could look like. This becomes especially important if one likes to use more sophisticated methods like Iterated Discriminant Analyses or neural networks. The simulation is in many points quite similar to the generation of the four fermion final states, since in the (h,H)Z channel one also has at least four fermions. The simulation of Higgs signal Monte Carlo is done using the HZHA 3.0 generator [Jan96]. As in WPHACT, this generator only provides the initial four fermions, that are then processed

[5] **V**ector **D**ominance **M**odel

[6] The choice for this version of PYTHIA was due to its better description of the $\gamma\gamma$ interactions.

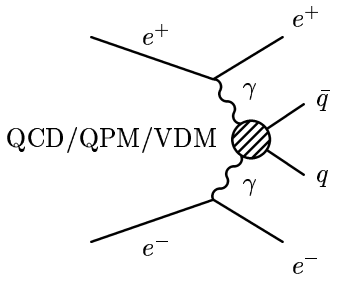

Figure 5.8: Photon Photon interactions for the process $e^+e \to e^+eq\bar{q}$ [Vol99].

in PYTHIA 6.156. HZHA does also include six fermion final states originating from Higgs decays into W or Z bosons.

5.2 Jet clustering

Hadronic jets are the result of the fragmentation process. In the example process $e^+e^- \to Z \to q\bar{q}$, one produces two primary quarks, that are then fragmented. Instead of two particles, one ends up with a whole bunch of charged and neutral particles flying roughly in the same direction as the primary quark. This object is then called a jet. In order to obtain the jet four vector, one has to use special clustering algorithms, since only in rare cases, one can estimate the four vector "by eye". Several algorithms are available, like DURHAM [Dok91], LUCLUS [Sjö94, Sjö01], or JADE [JAD86]. In this thesis the DURHAM algorithm is used.

The algorithm takes each particle as a jet in the beginning. Then it calculates a distance measure, in the case of DURHAM, the scaled transverse momentum

$$y_{kl} = 2(1 - \cos\theta_{kl}) \cdot \frac{min(E_k^2, E_l^2)}{s} \tag{5.5}$$

between two particles k and l is used. If this distance measure is smaller than a certain cut value, referred to as y_{cut}, then the four vectors of the two jets are added up and form a new jet. This procedure is then continued until no jet pair has a smaller distance than y_{cut}. The procedure is similar for LUCLUS or JADE, only the distance measure is different.

In some cases, one is looking for a certain event topology, like two jets or four jets. In this case, one can force the event in the desired configuration. The y_{cut} then is not longer fixed, but contains the information, at which cut value the event would change to the desired configuration: y_{23}, for example, is the cut value, at which the event changes from a three jet configuration to a two jet configuration.

5.3 Hermeticity veto

This veto is a technical procedure to ensure the hermeticity of the detector. If the veto is set, there is the possibility that some energy has escaped in the insensitive regions of the detector. The hermeticity of the detector is especially important for searches with a lot of energy escaping undetected, like invisible Higgs decays or a Z decaying into neutrinos. The hermeticity veto uses mainly the taggers installed in DELPHI, in order to estimate if energy might have escaped undetected. Two separate kind of vetoes are used, both for the 40° and the 90° taggers. For the 40° veto, the angle between a tagger fired and the nearest jet, and the ϕ and θ angle between the missing momentum and the active tagger is calculated. This helps to estimate if either a part of the jet is lost, or if the missing momentum is coming from e.g. a photon lost in the cracks. These informations are then combined with the number of taggers fired into a discriminant variable. For the 90° veto, a similar approach is used, but the combination is not done using a likelihood but a simple counting of required conditions is done. If more than five conditions are fulfilled, the veto is set. The usage of this veto does suppress the number of fake signals due to energy loss dramatically, but leaves the signal almost unaffected.

5.4 Iterated discriminant analysis

As has already been mentioned, the separation of a possible signal and background processes is one of the main difficulties for searches at LEP2. One of the methods used is the **I**terated **D**iscriminant **A**nalysis (IDA), which is a nonlinear variant of the Fisher discriminant analysis [Fis36]. Before the Iterated Discriminant Analysis will be described in detail, a short introduction to discriminant analyses in general is given.

5.4.1 Fisher discriminant analysis

The goal of a linear or Fisher discriminant analysis is to find a function that separates between signal and background in an optimal way. In the linear discriminant analysis one tries to separate k classes with straight lines g_i. This takes place in an N-dimensional space, with N meaning the number of variables used to characterise the classes. The variables i from a class k form a vector $\vec{X}_{ki} = (X_1, X_2, ...X_N)$. In order to evaluate to which class an event belongs, the euclidian distance measure is used. In the case considered here, one has only two classes, signal and background, which simplifies the problem. The estimated mean value for a test sample with n_k elements is given as

$$\vec{m}_k = \frac{1}{n_k} \sum_{i=1}^{n_k} \vec{X}_{ki} \tag{5.6}$$

and the covariance matrix as

$$\mathbf{T} = \frac{1}{n_1 + n_2} \sum_{k=1}^{2} \sum_{i=1}^{n_k} (\vec{X}_{ki} - \vec{m}_k)(\vec{X}_{ki} - \vec{m}_k)^T \tag{5.7}$$

The desired function can be written as

$$D(\vec{X}) = \vec{a} \cdot \vec{X} \tag{5.8}$$

with $\vec{a}$ being the coefficient vector. This function attributes each point a value D, so one separates between signal and background with a single cut in D. This is a projection of the two classes, maximising the distance between the class centres and minimising the distances within the classes. One introduces a Matrix M

$$\mathbf{M} = (\vec{m}_1 - \vec{m}_2)(\vec{m}_1 - \vec{m}_2)^T \tag{5.9}$$

which describes quadratic distances of class centres. This leads to the problem of maximising the following equation:

$$J(\vec{a}) = \frac{\vec{a}^T \mathbf{M} \vec{a}}{\vec{a}^T \mathbf{T} \vec{a}} \tag{5.10}$$

It can be solved using the variation principle. It leads to an eigenvalue problem, the eigenvector with the largest eigenvalue is the solution of the problem:

$$\vec{a} = \mathbf{T}^{-1}(\vec{m}_1 - \vec{m}_2) \tag{5.11}$$

The desired cut a_0 is then

$$a_0 = \frac{1}{2}(\vec{m}_1 - \vec{m}_2)^T \mathbf{T}^{-1}(\vec{m}_1 - \vec{m}_2) \tag{5.12}$$

If $D(\vec{X}) < a_0$, it belongs to class 1, if $D(\vec{X}) > a_0$, it belongs to class 2. An interesting point is that the Fisher discriminant analysis is the optimal way to combine variables, if they are gaussian distributed. More details on Fisher discriminant analyses can be found in [Cow98].

5.4.2 Nonlinear discriminant analyses

The Fisher discriminant analysis works very nice, if the problem can be separated by a straight line in the N-dimensional space. This is not true, if the two classes partially overlap or have shapes that can not be separated by straight lines. One can replace the linear cut by a nonlinear cut, using a nonlinear discriminant function. This behaviour is shown in Fig. 5.9.

A quadratic function has been applied in the discriminant analyses used in this thesis:

$$D(\vec{X}) = \vec{X} \cdot (\vec{a} + \mathbf{B}\vec{X}) \tag{5.13}$$

One can perform a linearisation of this term

$$\vec{X}' = (X_1, X_2, ...X_N, X_1X_1, X_1X_2, X_1X_N, ..., X_NX_N)^T \tag{5.14}$$

$$\vec{a}' = (a_1, a_2, ..., a_N, B_{11}, B_{12}, B_{1N}..., B_{NN})^T \tag{5.15}$$

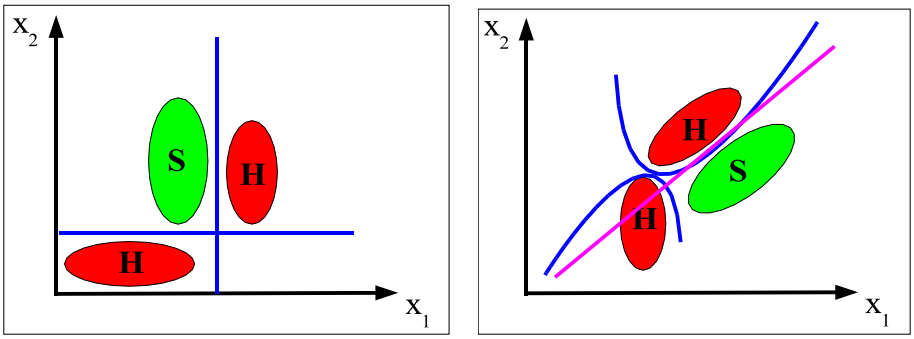

(a) (b)

Figure 5.9: The separation of signal (S) and background (H) for a well separatable problem (a). Here the linear cuts (the two lines) of the linear discriminant analysis are sufficient. In (b), the problem is not so easy to be solved by a linear cut (light straight line), the nonlinear discriminant analysis achieves a better separation here using hyperbolas [Reh03].

The resulting function describes hyperplanes in the N-dimensional space of the characteristics. Due to their curvature, they can separate much better between signal and background in the more difficult cases. The number of degrees of freedom for a quadratic polynomial with N variables is:

$$N_F = \frac{1}{2}(N^2 + 3N) \tag{5.16}$$

As an example imagine a problem in 3 dimensional space, which means 9 degrees of freedom. The vector $\vec{X}'$ can then be written as:

$$\vec{X}' = (X_1, X_2, X_3, X_1X_1, X_1X_2, X_1X_3, X_2X_2, X_2X_3, X_3X_3)^T$$

5.4.3 Iterated discriminant analyses

In order to improve the separation power even more, the nonlinear discriminant analysis is iterated twice. All events that have been classified to be signal-like in the first step are the inputs for the second discriminant function. This procedure is illustrated in Fig. 5.10.

5.4.4 Implementation

As already has been mentioned, a two step IDA with a quadratic polynomial has been used in this thesis. The problem of particle physics analyses is, that one usually does not have a uniform signal and background class, but that both classes k consist of a number of channels C_k with an estimated mean value $\vec{m}_c$ and a covariance matrix $\mathbf{T}_c$. If one is going to combine the channels and

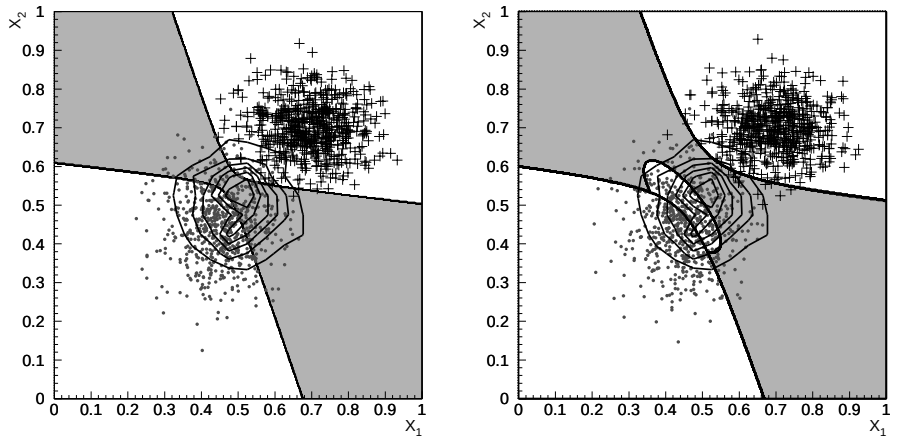

(a) **(b)**

Figure 5.10: Example for a two step IDA using two variables. The dots and crosses represent the background, the contour lines the signal. In (a) the first step is shown, the grey area represents the selected part of the space of characteristics at 52% signal efficiency. In (b) additionally the second step is shown, one can clearly see, that the second iteration improves the separation power in the area, were signal and background overlap. Again the grey area represents the selected part of the space of characteristics at 52% signal efficiency [Vol99].

calculates the IDA function, one would weight the channels according to the number of events simulated, which is of course unphysical. So every channel is weighted antiproportional to the number of simulated events in order not to favour the samples with the largest amount of simulated events. In the case of a background channel the channel is additionally weighted with the number of expected events in this channel, σ^k. This procedure weights the channels according to their contribution to the data. For the signal, all channels get the same weight, in order not to prefer a single channel. For the $\vec{m}_k$ and $\mathbf{T}_k$, the following formulae are used:

$$\vec{m}_k = \frac{1}{w_k} \sum_{c=1}^{C_k} \frac{\sigma^{k,c}}{N_{MC}^{k,c}} \vec{m}_c \tag{5.17}$$

$$\mathbf{T}_k = \frac{1}{w_k} \sum_{c=1}^{C_k} \frac{\sigma^{k,c}}{N_{MC}^{k,c}} \mathbf{T}_c \tag{5.18}$$

$$w_k = \sum_{c=1}^{C_k} \frac{\sigma^{k,c}}{N_{MC}^{k,c}} \qquad \sigma^{Signal,c} = 1 \tag{5.19}$$

In order to have no correlations between the calculation of the IDA function and the determination of the signal efficiencies, both quantities have been cal-

culated separately, in order to avoid those effects. Therefore the whole Monte Carlo sample has been split into two parts, one for training the IDA and the second to calculate signal efficiencies. Another problem is overtraining. This happens, if the IDA has been calculated with too few events. The IDA then memorates every single event instead of using the distributions. It has been shown in [Mal96, Mal97, Mal98], that the number of events in order to calculate the IDA should always be at least a factor 10 higher than the number of degrees of freedom N_F as defined in eq. 5.16.

5.5 Neural networks

Another method for signal and background separation are the so-called artificial neural networks. The approach used here is different from the one used in the IDA before. In this section, only a short overview about the ideas are given, for more detailed information we refer to e.g. [Her98].

The development of neural networks started in 1960 in the Artifical Intelligence (AI) research. The goal was to develop methods that could learn to classify patterns. However, it took about 20 years until an usable tool for science had evolved [McC81, Rum86]. The basic idea was to mimic the neuron structure of the human brain, having numerous neurons, that are all connected with each other. In order to implement this in an algorithm, several approaches have been suggested, a very common one is the Feed-Forward network, which is shown in Fig. 5.11. It has been found, that Multilayer-Feed-Forward networks [Her98] are superior to a simple Feed-Forward networks like in Fig. 5.11a. The Multilayer-Feed-Forward networks introduce a hidden layer, which allows to make nonlinear transformations. The network architecture is shown in Fig. 5.11b.

The input layer nodes are connected with the hidden layer nodes using the following function:

$$H_j = g(h_j) = g\left(\sum_i W_{ij} I_i\right) \tag{5.20}$$

g is the so-called activation function, which is usually a sigmoid function, which has the form:

$$g(h) = \frac{1}{1 + e^{-ch}} \tag{5.21}$$

where c is the so-called temperature parameter, which is put to a fixed value. The output node is connected with the hidden layer nodes using the following function:

$$O = g\left(\sum_j w_j H_j\right) = g\left(\sum_j w_j \left(\sum_i W_{ij} I_i\right)\right) \tag{5.22}$$

An error measure can be obtained by comparing the output node O with the desired output Ω_i:

$$E(\omega) = \frac{1}{2}\sum_i (\Omega_i - O_i)^2 \tag{5.23}$$

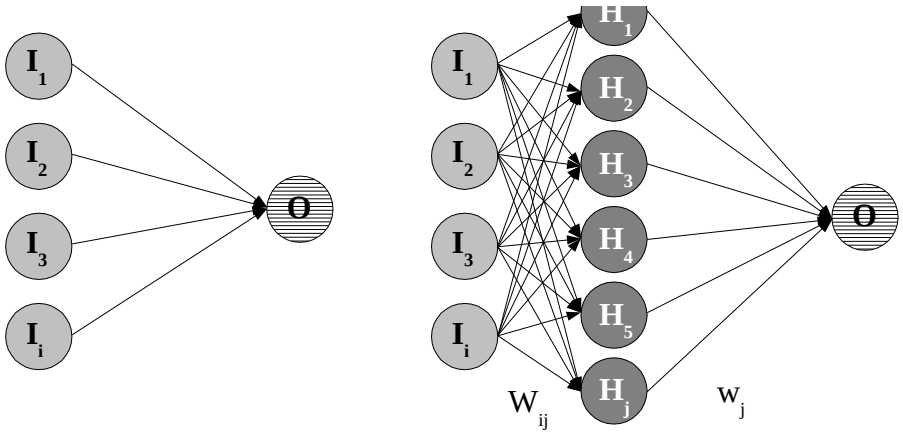

Figure 5.11: Feed-Forward Networks with several input nodes I_i and one output node O. A network with no hidden layer is shown in (a) and one hidden layer of nodes H_j in (b).

The training has been a problem for Feed-Forward networks for a long time. The introduction of the backward error propagation procedure solved this problem. The training is done in the following way: For each node, one tries to minimise the errors of the weights:

$$\Delta w_j = -\eta \frac{\partial E}{\partial w_j} \quad \Delta W_{ij} = -\eta \frac{\partial E}{\partial W_{ij}} \tag{5.24}$$

The errors are then propagated backwards form the output node to the input nodes. Therefore the procedure is called backward error propagation. The minimisation is done using a separate training sample. This ensures that doing the minimisation and determining the signal efficiencies are uncorrelated.

5.5.1 The NeuroBayes network

The NeuroBayes network has been developed by M. Feindt and is described in details in [Fei01]. It uses a Bayesian estimator:

$$P(H|D) = \frac{P(D|H)P(H)}{P(D)} \tag{5.25}$$

in order to estimate the full probability density function on an event per event basis. For the analyses in this thesis, this capability has not been fully exploited, NeuroBayes was used for classification only. The Bayesian approach in statistics makes use of a prior before doing the actual experiment. In the estimator used

here, the prior probabilities $P(H)$ for the hypothesis being true and $P(D)$ for obtaining the measured data are used. The likelihood $P(D|H)$ gives the probability to obtain the measured data under the assumed hypothesis. One can then calculate the posterior probability $P(H|D)$ for the hypothesis being correct after the measurement has been made. A more detailed introduction to Bayesian statistics is given e.g. in [Cow98].

Some of the nice benefits NeuroBayes offers compared to other Network packages is that it can do normalisation, decorrelation and pruning. All input variables are normalised in a way, that the mean is zero and transformed into gaussian distributed variables. After that all variables are decorrelated. This decorrelation can be done using a linear transformation for each variable x_j:

$$y_i = \sum_{j=1}^{n} A_{ij} x_j \tag{5.26}$$

with A being the transformation matrix. The new diagonal covariance matrix U_{ij} can be calculated from the original covariance matrix V_{kl}. This leads to an eigenvalue problem:

$$U = AVA^T \tag{5.27}$$

which is in principle easily solvable but can get numerically complicated especially with large matrices. After this step, all input variables are uncorrelated gaussian distributed variables, which increases the training speed quite dramatically. Note, that higher order correlations are not decorrelated in this procedure.

In NeuroBayes only one hidden layer is used, but NeuroBayes has the capability of pruning: one can start with a large number of nodes in the hidden layer and NeuroBayes can remove those nodes that do not affect the result. This leads to almost optimal networks for the problem they are trained for.

5.6 Calculating a 95% Confidence Level limit

The most interesting question after an analysis, if no signal has been found, is which mass or cross-section can be excluded with a certain level of confidence. Although the question is pretty easy, it is not easy to answer it. The calculation of confidence level limits remains one of the most disputed topics in particle physics.

In order to get a limit, one has to give a hypothesis first:

Production of Higgs boson of a mass m.

In the case of hypothesis testing one has two kinds of error one can make. The error of the first kind is accepting the hypothesis, although it is wrong, the error of the second kind is to reject the hypothesis, although it is correct. For setting limits, one would of course like to minimise the error of the first kind, since otherwise the results would be too optimistic. This leads to the definition

of a Confidence Level (CL), which is defined as $1-\alpha$. Setting α to 0.05, means, that in 5% of the cases one would reject the hypothesis, although it is correct. These definitions are common for all limit calculation methods. Important is also that for all the limits set for LEP2 one always has to take the background into account. The background is obtained from Monte Carlo simulation, so setting a limit strongly depends also on the quality of the background Monte Carlo.

5.6.1 The event counting method

This method takes into account the number of expected events n_B and the observed events n_{obs} in the data in order to set a limit. In general, one only knows that the number of signal events n_S has to be larger than 0 and contributes to the number of observed events (see e.g. [Cow98]).

$$n_{obs} = n_B + n_S \tag{5.28}$$

If one assumes that both variables are poissonial distributed with mean values ν_S and ν_B, the sum of ν_S and ν_B is again a poissonial distributed variable [Cow98]:

$$f(n, \nu_S, \nu_B) = \frac{(\nu_S + \nu_B)^n}{n!} e^{-(\nu_S+\nu_B)} \tag{5.29}$$

The value of ν_B is obtained from Monte Carlo simulations, assuming, that their statistical error is negligible. It can be shown that using the classical approach, one may get difficulties with a small n_{obs} and a large ν_B, so one has to use a Bayesian approach, which yields the following equation for an upper limit on ν_S [Cow98]:

$$\alpha = \frac{e^{-(\nu_S+\nu_B)} \sum_{n=0}^{n_{obs}} \frac{(\nu_S+\nu_B)^n}{n!}}{e^{-\nu_B} \sum_{n=0}^{n_{obs}} \frac{\nu_B^n}{n!}} \tag{5.30}$$

This can be solved numerically in order to obtain ν_S for a given number of α. In order to obtain a limit on a cross-section one has to use the relation

$$\sigma_{excluded} = \frac{\nu_S}{\mathcal{L}} = \sigma_{theory} \cdot \epsilon_{exp} \tag{5.31}$$

with $\mathcal{L}$ being the luminosity. In order to get a theoretical predicted cross-section σ_{theory}, one has to take the experimental efficiency ϵ_{exp} for the desired process into account. However, this efficiency has to be determined either from Monte Carlo simulation or from the data directly. From this cross-section, one can obtain a mass limit using the mass dependence of the cross-section. This mass limit is then model dependent, since $\sigma(m)$ is model dependent. The limit on the cross-section on the other hand is more model independent, it only depends on the background description by the Monte Carlo simulations.

There is also one large drawback of the event counting method: it only uses the total event numbers for the limit. This effect can be reduced by using the method bin by bin of a chosen distribution, but it is still far from being optimal. A typical problem is illustrated in Fig. 5.12. Both have an excess

from data, but in Fig. 5.12a the excess is clearly signal-like, as one expected from Monte Carlo simulation. In Fig. 5.12b it looks more like a fluctuation in the background. In both cases, the limit is affected, giving a hint for a signal. This is the drawback of the method, so in order to give more stable limits, one

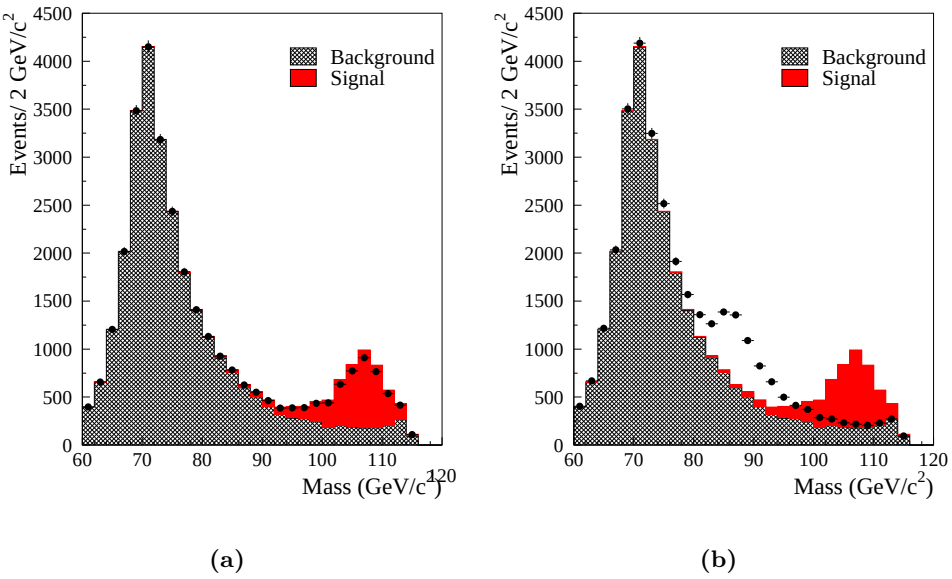

Figure 5.12: The problems of setting a limit using event counting. The excess in (a) is clearly signal-like, so a weaker limit is correct. However in (b) the limit is also lower, but there is no evidence for signal at all, but just a fluctuation in the background.

should consider using a better method.

5.6.2 The Modified Frequentist Likelihood Ratio method

Since the event counting method has been proven to be not the optimal solution, better methods have been developed for the Higgs searches at LEP2. The method used by DELPHI and the LEP Higgs Working Group is the **M**odified **F**requentist **L**ikelihood **R**atio (MFLR) approach in the implementation of ALRMC [Rea97]. The main advantage of this method is that it can take into account the distributions of background and signal. This can avoid the situation sketched in Fig.5.12b. This method is now shortly described.

As a first step a test statistics X is constructed, which increases monotonically for increasingly signal-like (decreasingly background-like) experiments, so that the confidence for the *Signal + Background* hypothesis is given by

$$CL_{S+B} = P_{S+B}(X \leq X_{obs}) \tag{5.32}$$

with

$$P_{S+B}(X \leq X_{obs}) = \int_0^{X_{obs}} \frac{dP_{S+B}}{dX} dX \tag{5.33}$$

In this case $\frac{dP_{S+B}}{dX}$ is the probability density function of the test statistics X. The same definitions are made for the *Background only* hypothesis:

$$CL_B = P_B(X \leq X_{obs}) \tag{5.34}$$

with

$$P_B(X \leq X_{obs}) = \int_0^{X_{obs}} \frac{dP_B}{dX} dX \tag{5.35}$$

In order to become less sensitive to fluctuations of the background, the CL_{S+B} is normalised:

$$CL_S = \frac{CL_{S+B}}{CL_B} \tag{5.36}$$

This is called the modified frequentist procedure. Although the CL_S is not exactly a confidence limit (it is a ratio), it can be shown that the choice does not overestimate the limits, but leads to slightly more conservative limits instead [Rea97].

In order to construct the test statistics, a likelihood ratio Q is introduced:

$$Q = \frac{\mathcal{L}_{\mathcal{S}+\mathcal{B}}}{\mathcal{L}_{\mathcal{B}}} \tag{5.37}$$

This is ratio of the two hypotheses (*Signal+Background* and *Background only*) introduced before. It can be shown, that Q minimises the probability of the error of the first kind [Rea97]. Furthermore this can be extended very easily to several independent channels by just multiplying the likelihood ratios. For one channel, Q can be written as:

$$Q(m_H) = e^{-s(m_H)} \prod_{j=1}^{n_{obs}} \left(1 + \frac{s(m_H)S(m_H, m_j)}{bB(m_j)}\right) \tag{5.38}$$

with $s(m_H)$ being the total number of events expected for a Higgs mass[7] with a mass m_H, b is the total background rate and S and B are the probability density functions for signal and background for the different candidates n_{obs}. This definition gives one the complete freedom what to use as the probability density function (pdf), it can be the mass spectra, the output of an IDA or a neural network, basically every variable one would consider to have some discrimination between signal and background. As has already been mentioned, the extension to several channels $N_{Channel}$ is straight forward:

$$Q(m_H) = \prod_{i=1}^{N_{Channel}} Q_i \tag{5.39}$$

[7]The Higgs bosons is chosen as an example here, of course any other process can be used.

The test statistics X is then constructed as

$$X = -2 \ln Q \tag{5.40}$$

The cut value X_{obs} is obtained from the data, and in order to solve the integrals 5.33 and 5.35, one has to rely on Monte Carlo methods. For the number of events, one uses Poisson-distributed numbers n_B and n_S and generates their spectra using the pdfs of signal and background. From these Monte Carlo candidates X is calculated. Then one tests if $X \leq X_{obs}$. The CL_S is then easily calculated. This methods derives the so-called observed limit, meaning the limit derived from data. Usually, one is also interested in getting an expected limit, which gives a measure of the analysis sensitivity. It can be calculated using the same methods, but instead of data to calculate X_{obs}, one also has to use simulated events. It has to be mentioned that this method of calculating limits is rather CPU intensive, since for each point one has to use several ten thousand Monte Carlo events.

A benefit of this method is that systematic errors can be easily included. They are used to smear the pdfs for signal and background accordingly. A problem is that not for every Higgs boson mass a pdf is available, so e.g. the pdf of a Higgs boson 82.5 GeV/c^2 has to be interpolated between the pdfs of 80 and 85 GeV/c^2. The interpolations put a strong limit of the width of the simulated Higgs mass grid, where a distance of 2.5 to 5 GeV/c^2 is preferable in order to minimise the effects of the interpolation. This interpolation has also to be done for the signal efficiencies, because for every test mass the signal efficiency has to be known.

For several analyses it has been found that one-dimensional pdfs are not optimal, so two-dimensional pdfs were introduced. But the usage of two-dimensional pdfs leads to a higher sensitivity to the Monte Carlo statistics and the necessity of sophisticated smoothing algorithms to avoid empty bins in the distributions. For the analyses in this thesis, one-dimensional pdfs were used, since it has been found that the gain in sensitivity using two-dimensional pdfs was too small to justify the huge technical effort.

5.6.3 Interpreting the CL limits

After running ALRMC one obtains the 95% CL limits for e.g the Higgs mass, both for the observed and the expected case. The expected limit gives information about the expected sensitivity of the analysis/analyses, meaning which Higgs mass can be excluded. This value is determined from the simulated Monte Carlo signal and background samples, so a good description of the background is essential. If one is going to compare several analyses in one search topology concerning their sensitivity, this is always done using the expected limits. If one compares the expected with the observed mass limits, this gives a measure, whether for this signal mass there is a deficit or an excess in the data. If the observed limit is lower than the expected limit, then there is an excess in data in this region. If the observed limit is larger than the expected one, then there

is a deficit in the data. ALRMC also calculates the value of the expected and the observed CL_B. The observed CL_B gives a measure of the background compatibility of the data for the tested Higgs mass. The expected CL_B derived from the simulated background distributions is by definition exactly 0.5. If the observed CL_B is larger than 0.5, then the data favour the *Signal+Background* hypothesis, if is less than 0.5 there is even a deficit in the data compared to background expectation. The 1σ bands are at 0.159 and 0.842 respectively, which also shows, that the fluctuations in CL_B have to be rather larger in order to be statistically significant.

Chapter 6

Searches for invisible Higgs decays

In this chapter, searches for invisibly decaying Higgs bosons are presented. Such decays can for example occur in the MSSM or in Majoron models, as has been pointed out in chapter 3. However the searches aim to be as model independent as possible, so the only assumption made is that the Higgs is produced via Higgs-Strahlung and decays invisibly and that the Z decays into two quarks. The signature searched for in this analysis is 2 jets compatible with a Z boson and a large amount of missing energy, as sketched in Fig. 6.1 This final state

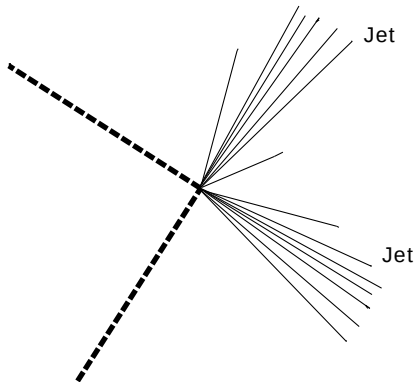

Figure 6.1: The topology searched for in the reaction $e^+e^- \rightarrow HZ$ $(H \rightarrow inv)(Z \rightarrow q\bar{q})$. The dotted lines indicate the particles leaving the detector undetected.

represents about 70% of all possible HZ final states. The dominant background for these searches originates from $e^+e^- \rightarrow ZZ \rightarrow q\bar{q}\nu\bar{\nu}$ or the $We\nu$ t-channel $e^+e^- \rightarrow We\nu_e(W \rightarrow q\bar{q}')$.

Searches using the $Z \rightarrow l^+l^-$ decays are also possible and have been con-

ducted in DELPHI as well, they account for 9% of the final states. The results of these searches were combined with the results from $Z \to q\bar{q}$[1] in order to increase sensitivity for an invisibly decaying Higgs boson.

The searches were designed to cover a mass range for invisibly decaying Higgs bosons from 40 GeV/c^2 to 120 GeV/c^2. The data sets used are described first, then some signal-specific details are explained. After that the preselection of the events is described followed by the final selection using an IDA. The mass reconstruction is then shortly explained, before the systematic errors and the results are presented.

6.1 The data set

The data from 1998 to 2000 have been used in the analysis. The centre-of-mass energies range from 188.6 to 208.8 GeV and the total luminosity is about 590 pb^{-1}. For the data sample of 2000, there is a spectrum of centre-of-mass energies (see Fig. 4.4). So for the E1 processing, the data sample was divided in two parts cutting at $\sqrt{s} = 205.8$ GeV. This leads to two samples clustered around 205.0 and 206.5 GeV. For the two other years, the corresponding energies (188.6, 191.6, 195.5, 199.5 and 201.6) were used. The background samples used are listed in appendix A. For the signal, the following masses have been simulated using HZHA:

- 40 to 90 GeV/c^2 in 5 GeV/c^2 steps,
- 90 to 115.0 GeV/c^2 in 2.5 GeV/c^2 steps and
- 120 GeV/c^2.

6.1.1 The track selection

In order to use only well reconstructed charged and neutral tracks in the whole data set, a common track selection was applied, based on the standard DELPHI track selection as defined in the SKELANA [Spa97, Spa99] analysis package:

- Charged track momentum greater than 400 MeV/c.
- Charged tracks have to originate within 4 cm in the transverse plane and within 4 cm/$\sin\theta$ along the beam axis, depending on the polar angle θ.
- Neutral clusters with more than 300 MeV in the HPC and the STIC or with more than 400 MeV deposited in the FEMC.

For the neutral clusters in the HAC, no fixed cut, but a more sophisticated noise suppression algorithm [Spa97, Spa99] was used.

[1] Usually referred to as hadronic channel

Year	Low mass (GeV/c^2)	High mass (GeV/c^2)
1998	40-90	75-120
1999	40-100	75-120
2000	40-105	95-120

Table 6.1: Low and high Higgs boson mass ranges for three years of data-taking.

6.2 Dependence on m_H and $\sqrt{s}$

Since the analysis covers a large range both in the mass of the Higgs boson and also in the centre-of-mass energies, some things have to be considered to optimise the analyses.

The mass range of 80 GeV has been split in two parts, since one can clearly see in Fig. 6.2, that the events are pretty different for low and high masses. This can be seen for the visible energy distribution in Fig. 6.2a and the transverse momentum distribution in Fig. 6.2b. Also for the acollinearity and the $\sqrt{s'}$ distributions, one clearly sees a difference. The acollinearity is defined as 180° minus the angle between the two jet axes and $\sqrt{s'}$ [DEL96a] is the centre-of-mass energy after the radiation of the first ISR photon[2]. This quantity is evaluated using a kinematic fit, taking the di-jet system and assuming the photon is being lost in the beam pipe. This leads to a large amount of missing energy. The hypothesis of a lost photon applies for the $q\bar{q}\gamma$ background, but an invisible Higgs decay has also a large amount of missing energy, which leads to a similar signature, although no photon is lost. However due to the $\sqrt{s}$ dependence of the variables, one has to take into account the different centre-of-mass energies. The distribution also depend on $\sqrt{s}$ because of two facts. First the visible energy and the transverse momentum tend to be larger, because there is more energy available for the same process. The same is true for $\sqrt{s'}$. The acollinearity on the other hand illustrates the dependence of the event shape. At the kinematic limit for HZ, the Higgs and the Z decay almost at rest, leading to a very small acollinearity. If one increases the centre-of-mass energy, but still looks at the same Higgs mass, the Z gets more and more boosted, leading to a larger acollinearity. For an 100 GeV/c^2 Higgs, this is shown in Fig. 6.3 for the same variables like above, but this time for three different centre-of-mass energies (206.5, 199.5 and 188.6 GeV). For a 50 GeV/c^2 Higgs the behaviour is much less significant, because one is far away from the kinematic limit, this can be seen in Fig. 6.4. All this information has been used for the choice of the mass ranges shown in Tab. 6.1. Important is also the handling of the cuts in the preselection, since they have to be similar for all centre-of-mass energies. This has been obtained by normalising the variables to the centre-of-mass energies or having more loose cuts in order not to cut away the signal at some energy.

[2]Or the photon with the largest energy, if there is one than one photon.

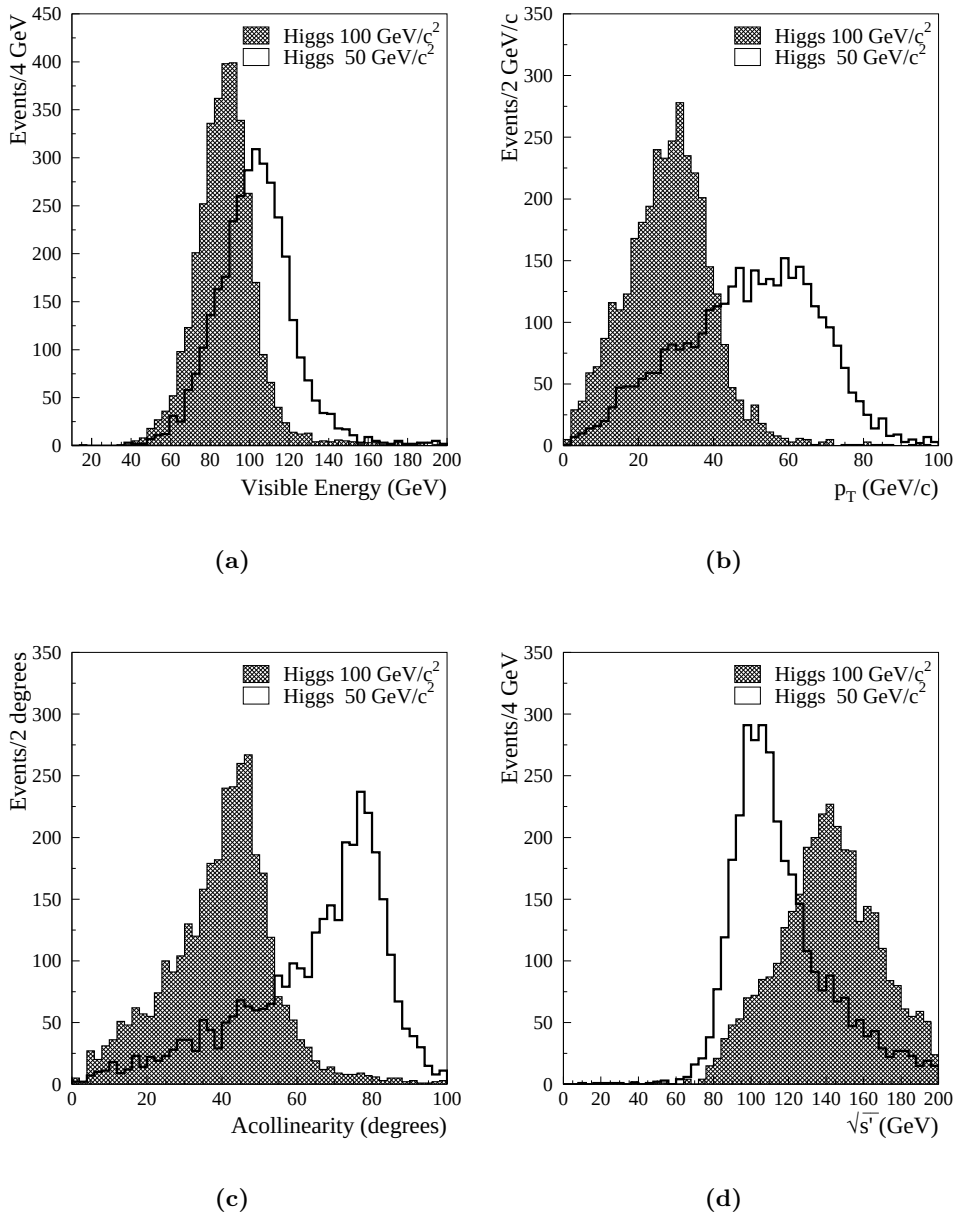

Figure 6.2: The mass dependence of some event variables at a $\sqrt{s}$=206.5 GeV for m_H=100 GeV/c^2 (hatched) and 50 GeV/c^2 (white). Shown are the visible energy (a), the transverse momentum (b), the acollinearity (c) and the $\sqrt{s'}$ (d).

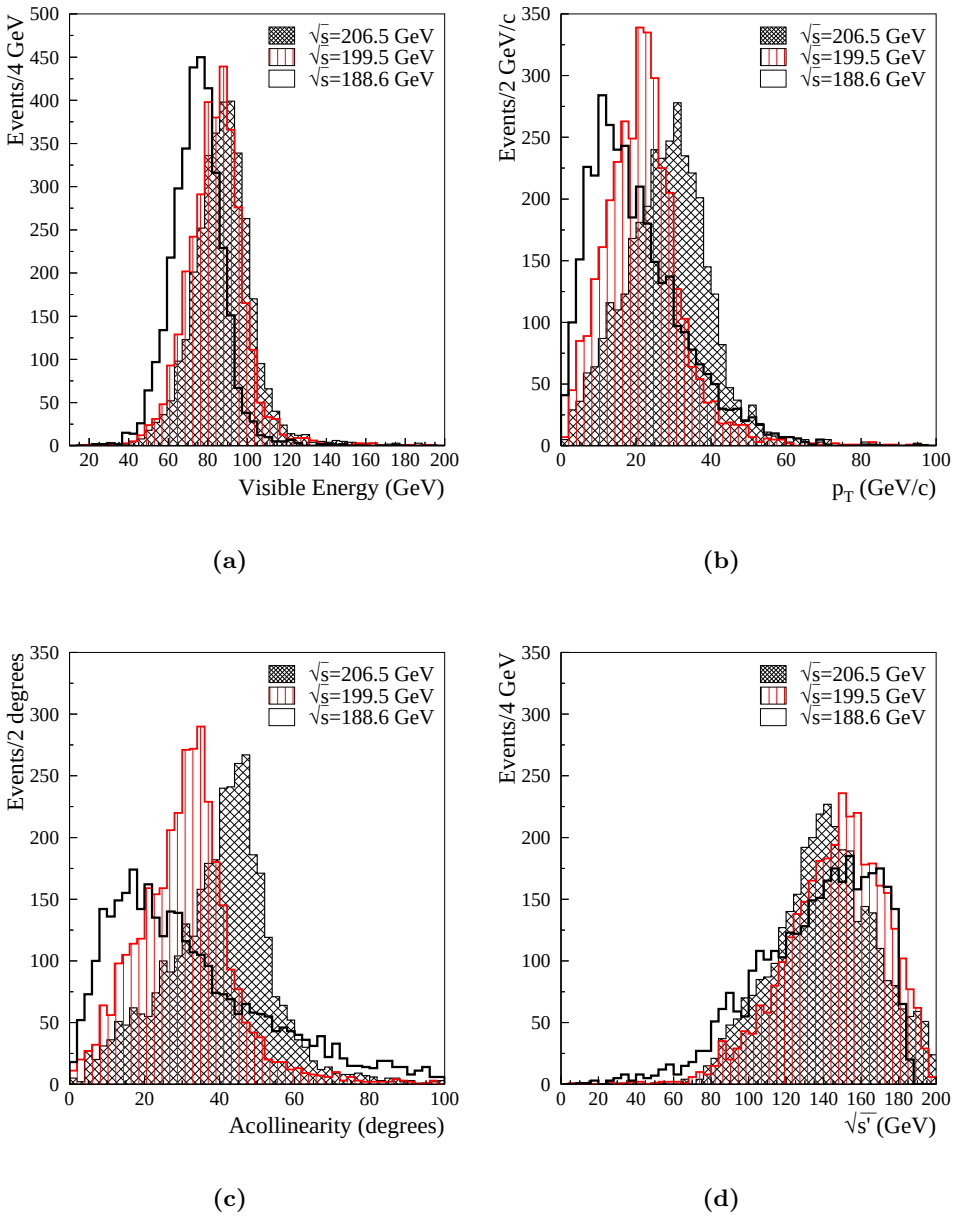

Figure 6.3: The $\sqrt{s}$ dependence of the event signatures for m_H=100 GeV/c^2 for three different centre-of-mass energies: 206.5 GeV (hatched), 199.5 GeV (lines) and 188.6 GeV (white). The distributions shown are the same as in Fig. 6.2.

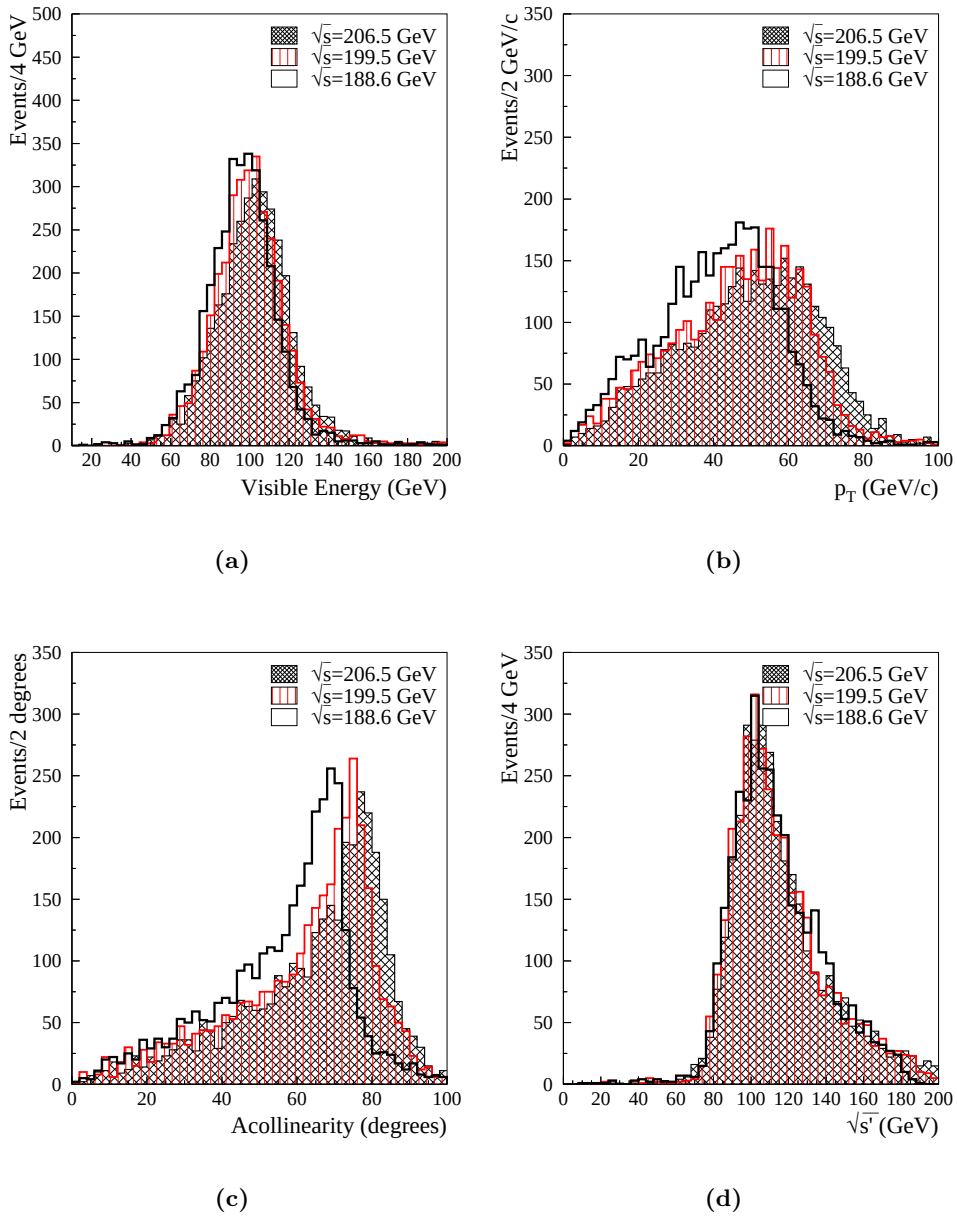

Figure 6.4: The $\sqrt{s}$ dependence of the event signatures for m_H=50 GeV/c^2 for three different centre-of-mass energies: 206.5 GeV (hatched), 199.5 GeV (lines) and 188.6 GeV (white). The distributions shown are the same as in Fig. 6.2.

$\sqrt{s}$(GeV)	$\mathcal{L}$ (pb^{-1})
188.6	152.4
191.6	24.7
195.5	74.3
199.5	82.2
201.6	40.0
205.0	74.3
206.5	82.8
206.5U	58.0

Table 6.2: The luminosities for the analyses after the data quality veto .The label 206.5U refers to the period of data taking, where one sector of the TPC was not working (S6). This has been fully taken into account in the event simulation.

6.3 Preselection

The goal of the preselection is to cut away events which are clearly not signal-like and only enrich events with the desired topology. In this analysis, the preselection can be split into four parts:

- Data quality veto
- Anti-$\gamma\gamma$ selection
- Anti-radiative $q\bar{q}\gamma$ and anti-WW selection
- Tail cuts

The four steps will be described in detail, also concerning the Standard Model backgrounds they cut away. First the preselection for high mass range analyses is described, for the low mass range analyses only the differences compared to the high mass range analyses are given. For reconstructing the jets in the event, the DURHAM jet clustering algorithm has been used (see chapter 5.2).

6.3.1 High mass analyses

Data quality veto

A detector quality selection was used, rejecting events where either the calorimeters or the tracking system were offline. This was introduced in order to kill fake signal events due to parts of the detector being offline. On average about 3-4% of the events in the data were vetoed by this procedure. Since this is not simulated in Monte Carlo, the luminosities had to be adjusted. The corrected luminosities used are shown in Tab. 6.2.

Anti-$\gamma\gamma$

This selection suppressed most of the background due to two-photon interactions. Most of this kind of background events have a low charged multiplicity[3] and are usually concentrated in the forward region. Each event was required to have at least 9 charged particle tracks, two of them with transverse momentum greater than 2 GeV/c and impact parameters less than 1 mm in the transverse plane and less than 3 mm along the beam axis. It was also required that the charged energy be greater than $0.16\sqrt{s}$, there be no electromagnetic shower with more than $0.45\sqrt{s}$, the transverse energy be greater than $0.15\sqrt{s}$ and the sum of the longitudinal momenta be greater than $0.25\sqrt{s}$.

Anti-$q\bar{q}(n\gamma)$ and anti-WW

This selection was applied to suppress most of the $q\bar{q}(n\gamma)$ background events resulting from radiative return to the Z-pole and some part of the WW events as well. A two-dimensional cut in the $\theta_{\mathrm{p_{mis}}}$ versus $\sqrt{s'}$ plane was applied, requiring

$\theta_{\mathrm{p_{mis}}} \geq 40^\circ$ and $\sqrt{s'} \geq 115$ GeV,

$\theta_{\mathrm{p_{mis}}} \leq 140^\circ$ and $\sqrt{s'} \geq 115$ GeV,

where $\sqrt{s'}$ stands for the effective centre-of-mass energy after the initial state radiation of one or more photons and $\theta_{\mathrm{p_{mis}}}$ is the polar angle of the missing momentum. In addition, it was required that less than $0.08\sqrt{s}$ was deposited in the STIC, $\sqrt{s'}/\sqrt{s}$ was less than 0.96 in order to reject events with $E_{vis} \approx \sqrt{s}$ and that the total electromagnetic energy below 30° was less than $0.16\sqrt{s}$. These cuts were used to suppress the bulk of the radiative return events. In order to suppress badly reconstructed events, candidates in which a jet pointed to the insensitive region between barrel and endcap detectors or where both jet axes were below 12° were rejected. A hermeticity veto algorithm (see chapter 5.3) using the scintillator counters was applied to ensure that no photon escaped in the insensitive region of the electromagnetic calorimeter at polar angles near 40°, 90° and 140°. To suppress background from WW pair production, the energy of the most energetic particle was required to be less than $0.2\sqrt{s}$ and the transverse momentum of any particle in the jet with respect to its jet axis (forcing the event into a two-jet configuration) to be less than $0.05\sqrt{s}$. Finally, it was required that upon forcing the event into a three-jet configuration, every jet had at least one charged particle in order to suppress $q\bar{q}(n\gamma)$ events.

Tail cuts and IDA

Twelve variables were used to construct an effective tagging variable in the framework of the IDA. In order to calculate these variables, the event was forced into two jets, using the DURHAM algorithm. The variables were:

[3] Number of charged tracks

- $E_\gamma/E_\gamma^{\mathrm{Z}}$: The normalised energy of a photon assumed to be escaped in the beam direction, deduced from the polar angles of the two jet directions in the event. The photon energy was normalised to the energy expected for a photon recoiling against an on-shell Z.

- $\ln(p_{\mathrm{T}})$: Logarithm of the transverse momentum of the event.

- $E_{\mathrm{vis}}/\sqrt{s}$: Visible energy of the event, normalised to the centre-of-mass energy. This variable, as the following one, exploits the fact, that one expects a large amount of missing energy due to the invisible Higgs decay.

- $E_{\mathrm{T}}/\sqrt{s}$: Transverse energy of the event, normalised to the centre-of-mass energy.

- θ_{cone}: The minimum polar angle defining a cone in the positive and negative beam directions containing 6% of the total visible energy.

- $|\cos\theta_{\vec{p}_{\mathrm{mis}}}|$: Cosine of the polar angle of the missing momentum.

- $E_{\mathrm{isol}}/\sqrt{s}$: Energy sum between the two cones, defined by half opening angles 5° and α_{max} around the most isolated particle. The most isolated particle is defined as the particle with momentum above 2 GeV/c with the smallest energy sum in the double cone. In the momentum interval from 2 to 5 GeV/c, α_{max} is set to 60° in order to maximise the sensitivity to isolated particles from tau decays in $\mathrm{WW} \to \mathrm{q\bar{q}}'\tau\nu$ events, while an opening angle of 25° is used for particles with higher momenta. This variable is illustrated in Fig. 6.5. The energy sum is then normalised by the centre-of-mass energy.

- $p_{\mathrm{isol}}/\sqrt{s}$: Momentum of the most isolated particle, as defined above and normalised by the centre-of-mass energy.

- $\log_{10}$(scaled acoplanarity): $\log_{10}$ of the scaled acoplanarity. The acoplanarity is defined as $180° - \Delta\phi$, where $\Delta\phi$ is the difference in azimuthal angle (in the plane perpendicular to the beam axis) between the two jets. In order to compensate for the geometrical instability of the acoplanarity for jets at low angles it was scaled with the angle between the 2 jets.

  The acoplanarity like the acollinearity contains information about the boost of the two-jet system. If one produces a Higgs together with a Z at the kinematic limit, the jets are almost back to back, which can then discriminate against most of the more boosted 2 fermion and 4 fermion background.

- Thrust: Thrust value of the event, computed in the rest frame of the visible system. The thrust of an event is defined as [Sjö01]:

$$T_{RS} = \max_{|\vec{n}|=1} \frac{\sum_i |\vec{n} \cdot \vec{p}_i|}{\sum_i |\vec{p}_i|} \tag{6.1}$$

  The so-called thrust-axis is given by the vector $\vec{n}$. The thrust gives information about the event shape, for perfect two jets events, the thrust is close to 1, for spherical events (multi-jets), the thrust is about 0.5.

Variable	lower cut	upper cut
E_γ/E_γ^Z	0.0	0.90
$\ln(p_T)$	1.75	4.5
$E_T/\sqrt{s}$	0.15	0.6
$p_{isol}/\sqrt{s}$	0.008	0.18
$\log_{10}$(scaled acoplanarity)	0.3	2.5
Thrust	0.65	1.0
ln(acollinearity)	2.0	4.5
$\ln(\max(p_T)_{jet})$	-0.5	2.50

Table 6.3: Tail cuts used in the high mass analyses.

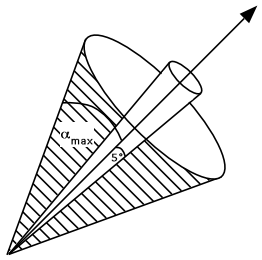

Figure 6.5: The double cone used in order to estimate the energy of the isolated particle E_{isol} [Vol99].

- ln(acollinearity): Logarithm of the acollinearity of the two-jet system.
- $\ln(\max(p_T)_{jet})$: The logarithm of the highest transverse momentum of the jet-particles, defined by the transverse momentum of any particle in the jet with respect to the nearest jet axis. This variable is useful to suppress events with high energetic particles like e.g. semileptonic WW events.

The cuts listed in Tab. 6.3 were applied in the tails of these variable distributions in order to concentrate on the signal region and to obtain gaussian-like distributions as input for the IDA. In addition to the cuts listed in Tab. 6.3, the number of identified electrons or muons was required to be less than three.

The simulation is in good agreement with the data as shown in Tab. 6.4. The distributions for some of the preselection variables are shown in appendix B.

The IDA was then calculated using the twelve variables described above. The cut on the number of events, with which the second step is calculated, was set in that way, that 90% of the signal efficiency was kept. The IDA was not trained on only one mass but on a mass range as has been mentioned before. The cut on the second IDA step was done using the WPOINT program [Ada00], which calculates the optimal working point concerning the expected sensitivity of the analysis. This was done separately for each centre-of-mass energy, optimising the analysis for a 85 GeV/c^2 Higgs boson at 188.6 GeV, for a

$\sqrt{s}$	Anti-$\gamma\gamma$		Anti-q$\bar{q}(n\gamma)$ & anti-WW		Tail cuts	
(GeV)	Data	MC	Data	MC	Data	MC
188.6	15115	14967.0 ± 8.1	1578	1565.2 ± 6.0	494	485.9 ± 3.2
191.6	2394	2351.8 ± 1.3	258	249.9 ± 0.9	88	79.0 ± 0.5
195.5	7040	6782.4 ± 3.7	739	734.9 ± 2.8	242	242.0 ± 1.4
199.5	7296	7168.9 ± 3.9	784	795.4 ± 2.8	295	264.4 ± 1.6
201.6	3557	3407.8 ± 1.9	396	382.9 ± 1.3	152	130.6 ± 0.7
205.0	6272	6011.6 ± 3.7	678	686.2 ± 2.4	240	239.2 ± 1.3
206.5	6772	6697.0 ± 4.5	798	768.5 ± 2.9	283	268.2 ± 1.6
206.5U	4472	4560.4 ± 3.9	534	541.5 ± 2.6	202	190.7 ± 1.5

Table 6.4: Comparison of simulation and data after the different steps of the preselection in the high-mass hadronic analyses. The listed errors are from Monte Carlo statistics only. The last line (206.5U) refers to the data taken with one TPC sector inoperative, which has been fully taken into account in the event simulations.

Variable	lower cut	upper cut
E_γ/E_γ^Z	0.0	1.20
$E_T/\sqrt{s}$	0.0	0.6
$p_{isol}/\sqrt{s}$	0.0	0.18
$\log_{10}$(scaled acoplanarity)	1.0	2.5
ln(acollinearity)	2.25	4.5

Table 6.5: Tail cuts used in the low mass analyses.

95 GeV/c^2 Higgs boson at 191.6 and 195.6 GeV, for a 100 GeV/c^2 Higgs at 199.5 and 201.6 GeV and for a 105 GeV/c^2 Higgs for 205.0 and 206.5 GeV assuming SM production cross section and a branching ratio of 100% into invisible final states. The separation power of the IDA method is shown in Fig. 6.6. The observed and expected rates at $\sqrt{s}$=206.5 GeV are shown in Fig. 6.7a as a function of the efficiency to detect a Higgs boson when varying the cut on the second IDA variable. The working point calculated before is indicated as the vertical dashed line.

6.3.2 Low mass analyses

For the low mass analyses the first two steps of the preselection have been kept unchanged. In the anti-q$\bar{q}(n\gamma)$ and anti-WW selection, the two-dimensional cut in the $\theta_{p_{mis}}$ versus $\sqrt{s'}$ plane and the cut on $\sqrt{s'}/\sqrt{s}$ were removed in order to increase the signal efficiency. This was due to the fact, that the signal events have a much smaller amount of missing energy than the events in the high mass range. The tail cuts were also slightly modified as can be seen in in Tab. 6.5 and a cut requiring the visible mass to be at least 20% of $\sqrt{s}$ was added. The simulation is in good agreement with the data as shown in Tab. 6.6. The

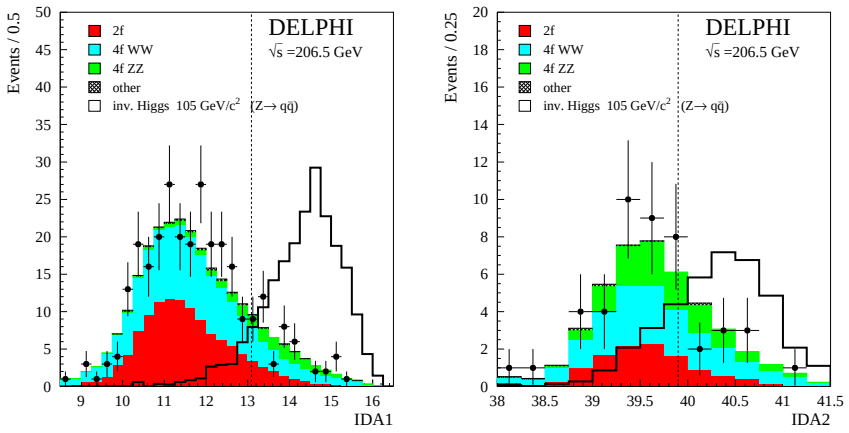

(a) **(b)**

Figure 6.6: Distributions for the IDA variables after first (a) and second IDA step (b) at $\sqrt{s}$=206.5 GeV. The dashed line indicates the calculated cut on the IDA variable. The white histogram shows the expectation of a 105 GeV/c^2 Higgs signal with an arbitrary scale.

distributions for some of the preselection variables are also shown in appendix B.

The low mass analyses also used two IDA steps in order to obtain optimal signal to background discrimination. The observed and expected rates at $\sqrt{s}$=195.5 GeV are shown in Fig. 6.7b as a function of the Higgs efficiency. The cut on the second IDA variable was again determined separately for each centre-of-mass energy as described above. It was optimised for a 60 GeV/c^2 Higgs boson mass at all energies.

6.4 Mass reconstruction

In order to reconstruct the mass of the invisibly decaying Higgs boson one uses measured quantities like the visible mass m_{vis}, the visible energy E_{vis}, the centre-of-mass energy $\sqrt{s}$ and the missing momentum p_{mis}.

$$m_{inv} = \sqrt{(\sqrt{s} - E_{vis})^2 - |\vec{p}_{mis}|^2} \tag{6.2}$$

The mass resolution is limited by energy and momentum resolution of the DELPHI detector. However, one can exploit the information, that the di-jet[4] has the mass of a Z boson m_Z.

$$E^2 \quad = (\alpha E_1 + \alpha E_2)^2 = \alpha^2 E_{vis}^2 \tag{6.3}$$

[4]pair of two jets

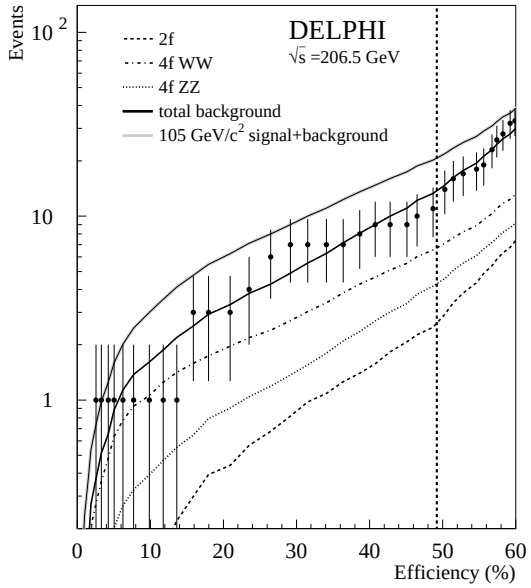

(a)

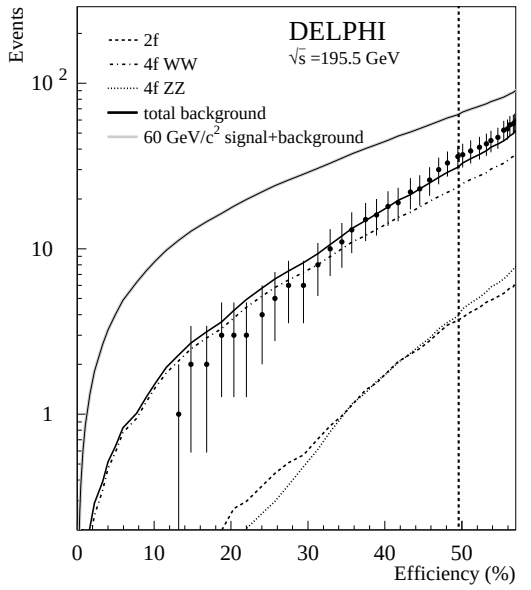

(b)

Figure 6.7: Data and expected background rates as a function of the efficiency for a Higgs signal of 105 GeV/c^2 Higgs in the high-mass analyses at 206.5 GeV (a) and a 60 GeV/c^2 Higgs (b) in the low mass analysis . The indicated lines show number of events from the most important background reactions and the solid black line shows the sum of all the background processes. In addition the grey line shows the expectation for a 105 (a) or 60 GeV/c^2 Higgs (b) signal added on top of the background. The vertical dashed lines indicate the final cut on the IDA chosen to maximise the sensitivity.

$\sqrt{s}$	Anti-$\gamma\gamma$		Anti-$q\bar{q}(n\gamma)$ & anti-WW		Tail cuts	
(GeV)	Data	MC	Data	MC	Data	MC
188.6	15115	14967.0 ± 8.1	6604	6735.2 ± 11.0	622	652.0 ± 3.9
191.6	2394	2351.8 ± 1.3	1013	1051.2 ± 1.7	112	103.0 ± 0.6
195.5	7040	6782.4 ± 3.7	2939	3003.0 ± 4.8	322	301.3 ± 1.8
199.5	7296	7168.9 ± 3.9	3122	3117.7 ± 5.0	338	315.1 ± 1.8
201.6	3557	3407.8 ± 1.9	1551	1495.9 ± 2.4	168	152.1 ± 0.8
205.0	6272	6011.6 ± 3.7	2617	2614.9 ± 4.3	344	307.3 ± 1.6
206.5	6772	6697.0 ± 4.5	2885	2909.0 ± 5.2	305	293.6 ± 1.7
206.5U	4472	4560.4 ± 3.9	1878	1982.5 ± 4.7	257	237.5 ± 1.7

Table 6.6: Comparison of simulation and data after the different steps of the preselection in the low-mass analyses. The errors given are from Monte Carlo statistics only. The last line (206.5U) refers to the data taken with one TPC sector inoperative, which has been fully taken into account in the event simulations.

$$p^2 = (\alpha p_1 + \alpha p_2)^2 = \alpha^2 p_{vis}^2 \tag{6.4}$$

$$E^2 - p^2 = m_Z^2 = \alpha^2 (E_{vis}^2 - p_{vis}^2) \tag{6.5}$$

$$\Rightarrow$$

$$\alpha = \frac{m_Z}{M_{vis}} \tag{6.6}$$

Using this and putting it into eq. 6.2, the mass of the invisible Higgs boson is then given as

$$m_{\mathrm{inv}} = \sqrt{\left(\sqrt{s} - \frac{m_Z E_{vis}}{m_{vis}}\right)^2 - \left(\frac{m_Z p_{\mathrm{mis}}}{m_{vis}}\right)^2}, \tag{6.7}$$

The gain in resolution is illustrated in Fig. 6.8. For the low mass analyses, it can happen, that the constrained mass becomes negative, in those cases, the standard missing mass calculation (see eq. 6.2) was used.

6.5 Systematic errors

The estimation of systematic errors is quite difficult in this channel at a first glance. Since these analyses rely mainly on the description of the data by Monte Carlo simulation, the quality of these simulations is the dominant source of systematic errors. One should also keep in mind, that all these searches are operating with a small number of events and are therefore statistically limited. Several sources of systematics have been investigated:

- Choice of the Monte Carlo generator for the $q\bar{q}\gamma$ background.
- Error on the luminosity.
- Influence of the jet clustering.

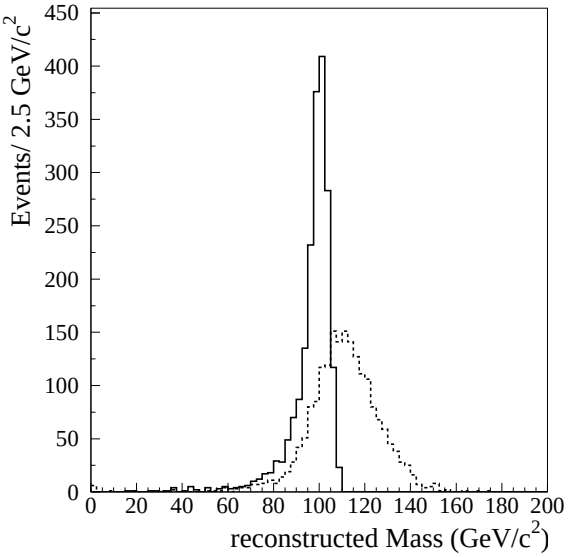

Figure 6.8: The mass of the invisible Higgs boson (dotted line) and the constrained mass of the invisible Higgs boson (continuous line). The constrained mass gives a greatly improved mass resolution for the case of invisibly decaying Higgs boson with a mass of 100 GeV/c^2.

- Uncertainties in the $We\nu$ cross-section.
- The Monte Carlo description in general.

The effect of modelling the $q\bar{q}\gamma$ background has been studied by changing the fragmentation model in KK2F from PYTHIA model (parton shower) to ARIADNE (colour dipoles) [Lon92] at 206.5 GeV. The results are identical within statistical errors, which is an expected behaviour, because the search is not very sensitive to the fragmentation model. The error on the luminosity is assumed to be $\pm 0.5\%$. The process $We\nu$ provides about a fifth of the background and it is known that there are uncertainties in the calculation of the cross-section. In order to estimate the effect, the signal definition of the $We\nu$ process was taken, which requires the cosine of the angle between the electron momentum and the beam axis to be

$$\cos\theta_e > 0.9999$$

This means, the electron is lost in the beam pipe. In the Monte Carlo 4f-CC sample, such events were selected. Then their IDA value has been calculated for those events, checking how many events have passed the final selection. The theoretical cross-section is known to have an error of about $\pm 5\%$ [Gru00]. Taking this into account leads to an error of $\pm 1\%$ on the background uncertainty. In order to see the influence of the jet clustering algorithm the DURHAM algorithm was replaced by the LUCLUS algorithm [Sjö01]. This results in an uncertainty on the background estimation and the signal efficiency in the order

of ±1% for the high mass regime and an error in the order of ±2.5% for the low mass regime.

The data and Monte Carlo simulation were found to be in good overall agreement. However, since we are searching for events with a large amount of missing energy, we become sensitive to the tails of the distributions from the expected Standard Model background events. It was found previously in the $ZZ \to q\bar{q}\nu\bar{\nu}$ analysis [Reh03](UPDATE), that the minor disagreement in the tails can be considerably improved, if the multiplicities of data and Monte Carlo simulation are brought into agreement. In order not to bias the present analyses, where the disagreements in the tails could come from new physics, the tuning of the multiplicities was done with $Z \to q\bar{q}$ events taken at $\sqrt{s} = 91.1$ GeV for each year of data taking. The events multiplicities were estimated separately for the barrel ($\cos\theta \leq 0.7$) and the forward region ($\cos\theta > 0.7$) and for different momentum bins. For each of these classes of multiplicities, a separate correction factor P was calculated using

$$P = \frac{< N_{\mathrm{data}} > - < N_{\mathrm{MC}} >}{< N_{\mathrm{MC}} >}.$$

These correction factors are in the order of a few percent in the barrel region, they tend to be larger in the forward region and are also larger for neutral than for charged tracks. The correction factors obtained were then applied to the high energy LEP2 Monte Carlo simulation on an event per event basis. The factor P was used as a probability whether to add or remove tracks in the Monte Carlo simulation. If P was less than zero, there were fewer tracks in data than in Monte Carlo and the tracks of the corresponding class were removed in the simulated events. For P greater than zero, tracks have to be added to the simulated events. This was performed copying another track of the same class and smearing its momentum by 2.5% in order not to affect the event topology. If there was no track of the corresponding class, a track of the neighbouring class was taken and scaled to fit into this class. Note that these modifications of the multiplicities in the Monte Carlo simulation were not used to change the analysis, but only to estimate the systematic error. The effect on the background estimation ranges from ±10.5% (1998), ±4.7% (1999) to ±10.6%(2000) for the high mass regime. For the low mass regime the effects are smaller, they range from ±6.6% (1998), ±4.3% (1999) to ±5.6% (2000). This procedure also affects the signal efficiencies leading to a reduction of the relative signal efficiency of up to ±1.5%. The impact of the shaking is shown in Fig. 6.9. Clearly visible is the increase of 2f-$q\bar{q}$ events in the simulated background, which leads to better agreement especially for the lower IDA2 values.

This so-called shaking method is described in detail in [Reh03, J.R03].

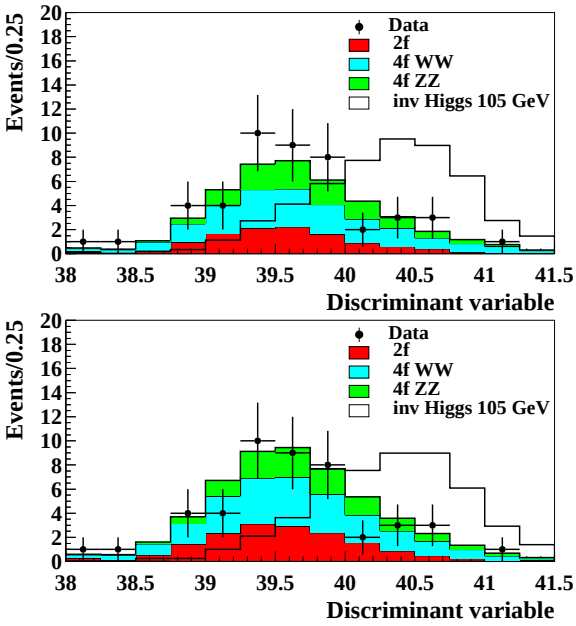

Figure 6.9: The IDA2 distribution at $\sqrt{s} = 206.5$ GeV for the unshaken expected background (upper plot) and for shaken background simulation (lower plot).

6.6 Results

At the end of the analysis, 153 events in the high mass range and 213 events in the low mass analyses were selected. The agreement of data and Monte Carlo is shown in Tab. 6.7. Also shown is the composition of the background, which varies due to different centre-of-mass energies and the choice of the final cut on the second IDA variable.

The mass plots (see Fig. 6.10) show no exccess in the signal region. The mass plots are used as input distributions for the limit calculation using the MFLR method described in chapter 5.6.2.

For the calculations of the limits, the results from the hadronic channels have been combined with the DELPHI results from the three leptonic channels [DEL03c]. These three channels also used the mass as input distributions for the MFLR method.

6.6.1 Mass Limit

In the calculation of the mass limit, all the LEP2 results were used. The results from the data taking at 161, 172 and 183 GeV are described in detail in [DEL99, DEL98]. The mass limit is derived assuming SM cross-section and a branching ratio of 100% into invisible final states. The obtained mass limits

$\sqrt{s}(GeV)$	Data	MC total	2f-$q\bar{q}$	4f-CC	4f-NC	ϵ_{Higgs}
188.6	65	71.3 ± 7.7	30.4	45.3	23.5	40.9 ± 1.9
191.6	2	5.6 ± 0.3	22.1	40.2	37.5	39.6 ± 1.7
195.5	21	18.7 ± 1.0	21.9	36.3	41.1	50.8 ± 1.7
199.5	21	20.1 ± 1.0	18.3	38.9	42.2	51.9 ± 1.7
201.6	11	10.8 ± 0.5	14.6	42.0	42.6	50.7 ± 1.7
205.0	9	12.2 ± 1.3	20.4	46.7	32.2	36.4 ± 2.1
206.5	13	13.5 ± 1.5	18.7	49.3	31.2	37.0 ± 2.1
206.5U	11	8.4 ± 0.9	19.8	46.5	32.8	31.6 ± 2.1
188.6	58	51.5 ± 3.8	17.9	76.4	5.8	49.1 ± 1.6
191.6	6	10.1 ± 0.5	13.5	75.4	10.1	50.0 ± 1.7
195.5	36	31.3 ± 1.6	11.9	75.3	12.7	49.6 ± 1.7
199.5	37	44.3 ± 2.3	6.5	88.3	5.1	50.5 ± 1.7
201.6	10	12.0 ± 0.6	8.3	77.5	14.1	44.2 ± 1.7
205.0	26	26.2 ± 1.7	8.0	71.4	20.7	47.0 ± 1.5
206.5	30	33.4 ± 2.1	6.5	69.7	23.8	48.8 ± 1.5
206.5U	10	18.0 ± 1.2	7.3	72.6	20.4	43.6 ± 1.5

Table 6.7: Number of events after the final selection for data and expected SM background. The contribution of the three main background classes are given in percent of the total background. Also given is the signal efficiency for a 100 GeV/c^2 Higgs boson (upper part) and a 60 GeV/c^2 Higgs boson (lower part).

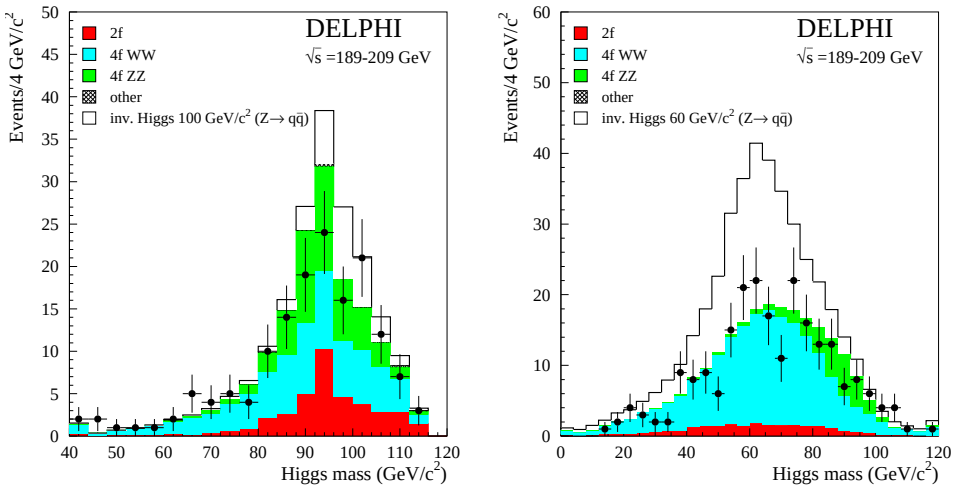

(a) **(b)**

Figure 6.10: Reconstructed Higgs boson mass for all candidates in the hadronic high mass analysis (a) and the hadronic low mass analysis (b) for 189 to 209 GeV after the final selection. The white histogram corresponds to a 100% decay into invisible modes.

are 112.1 GeV/c^2 with an expected value of 110.5 GeV/c^2. Without using the three lepton channels the results would be 111.1 GeV/c^2 with an expected value of 110.2 GeV/c^2, so the gain in combining is at the order of 1 GeV/c^2. In order to handle the overlap between low mass and high mass analyses the expected performance of the analyses were calculated for the region, where one has inputs from both analyses (see Tab. 6.1). The analysis with the better expected performance has then been used for the limit calculation. The overlap effect is not so important for the calculation of the mass limit since in this case mainly the inputs with the higher mass range and the highest centre-of-mass energy have the largest impact.

The obtained confidence level for a signal (CL_S) is shown in Fig. 6.11. Also indicated is the cut at 5% CL_S, which refers to the 95% confidence level. To test the compatibility with the background hypothesis alone, also the confidence level for the background only hypothesis in the hadronic channels has been calculated. The results obtained agree very well within 1 σ with the expected SM background from Monte Carlo simulation. The effect of the interpolation can be seen as small spikes between 90 and 95 GeV/c^2.

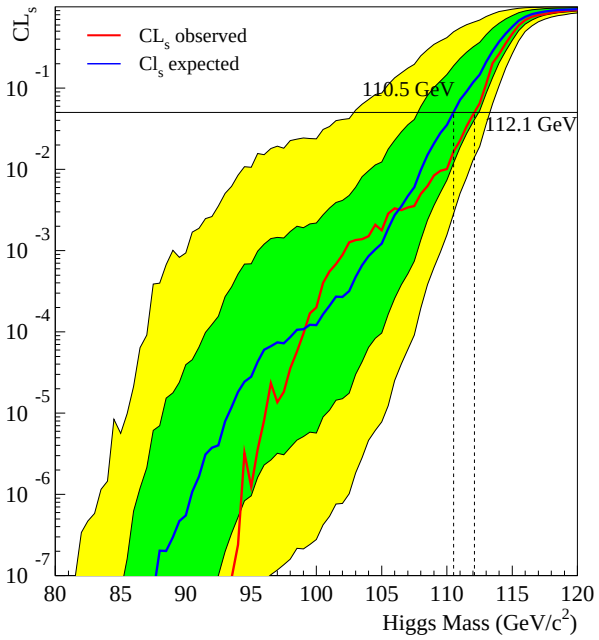

Figure 6.11: The expected and observed CL_S for $e^+e^- \rightarrow HZ(H \rightarrow$ invisible$)(Z \rightarrow q\bar{q}, l^+l^-)$ as a function of the Higgs boson mass. The dark and light bands indicate the one and two sigma bands. The cut at CL_S=0.05 is indicated by the horizontal black line.

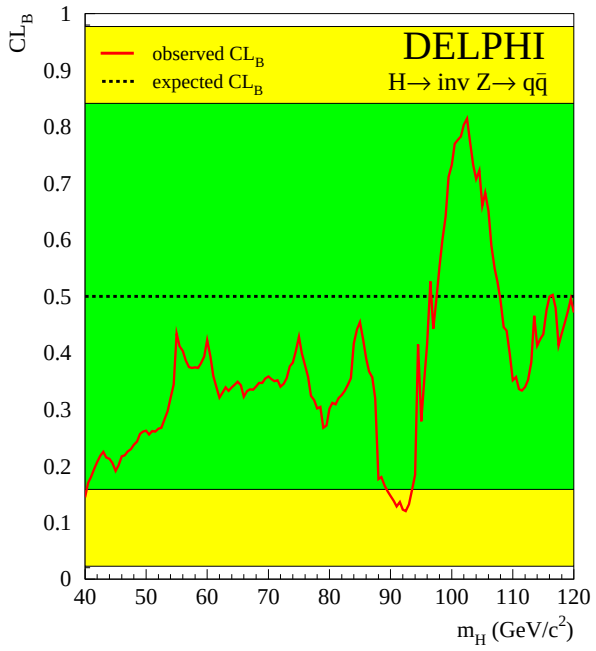

Figure 6.12: The observed CL_B for $e^+e^- \to HZ\,(H \to \text{invisible})(Z \to q\bar{q})$ as a function of the Higgs boson mass. The dark and light bands indicate the one and two sigma bands.

6.6.2 Cross-section limit

In order to get a more general exclusion, one tries not only to calculate the limit of Higgs decaying to 100% into invisible final states with a Standard Model cross-section, but would like to give an excluded cross-section for each mass. This can be useful to exclude other models with suppressed Higgs cross-sections. This cross-section limit has been calculated for the complete data set available using all the LEP2 results from 161-209 GeV. For the cross-section limit the impact of the overlap is more important since all results contribute in this case. The result from this calculation is shown in Fig. 6.13. This result can be also reformulated as suppression factor ξ compared to the Standard Model cross-section for HZ production:

$$\xi = \frac{\sigma_{excluded}}{\sigma_{SM}(e^+e^- \to HZ)}$$

The excluded range for ξ is shown in Fig. 6.14. Note that the Standard Model Higgs cross-section is used as a benchmark only, since invisible decays do not exist in the Standard Model.

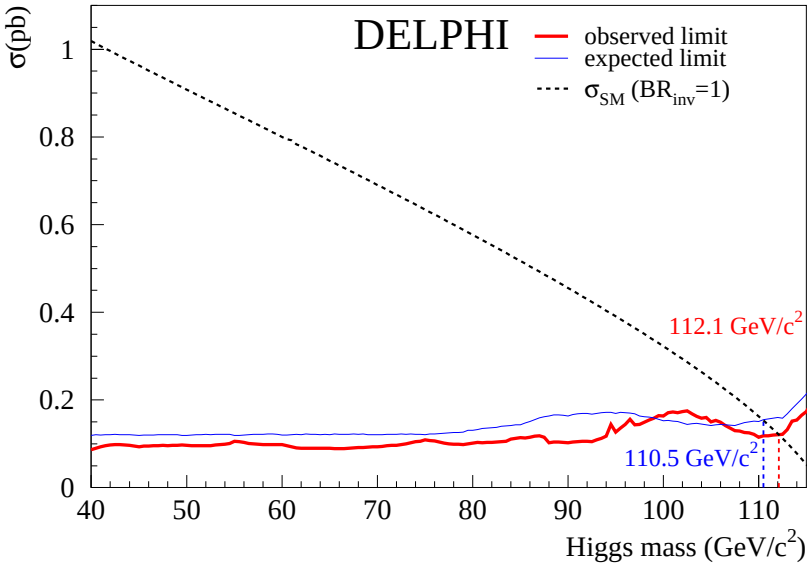

Figure 6.13: The 95% CL upper limit on the cross-section $e^+e^- \to HZ\,(H \to$ invisible$)(Z \to$ anything) as a function of the Higgs boson mass. The dashed line shows the Standard Model cross-section for the Higgs boson production with $BR_{\rm inv} = 1$.

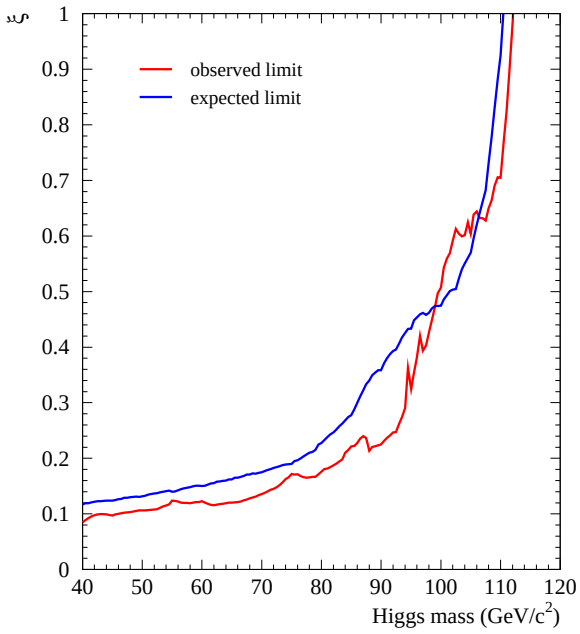

Figure 6.14: The 95% CL upper limit on the ξ factor in $e^+e^- \to HZ\,(H \to$ invisible$)(Z \to$ anything) as a function of the Higgs boson mass. The region above the line for an observed limit is excluded.

6.6.3 Branching ratio independent limit

A assumption one can make, is that the branching ratios of the Higgs boson can be written as

$$1 = \alpha \cdot BR_{invisible} + (1 - \alpha) \cdot BR_{SM-visible} \tag{6.8}$$

with the factor α between 0 and 1. Since one has the results for both invisible and visible[5] decays, it is straight forward to combine both. The visible results from DELPHI used are described in detail in [DEL98, DEL00, DEL02b, DEL03a]. The results were then combined for different values of α, so for each point of α a 95% CL limit was set, at which a Higgs can be excluded. The lowest limit was taken as a branching ratio independent limit on the Higgs boson mass. The result of this scan is shown in Fig. 6.15 and the lowest value obtained is 111.8 GeV/c^2 (109.3 GeV/c^2 expected). It can be nicely seen in this plot, that

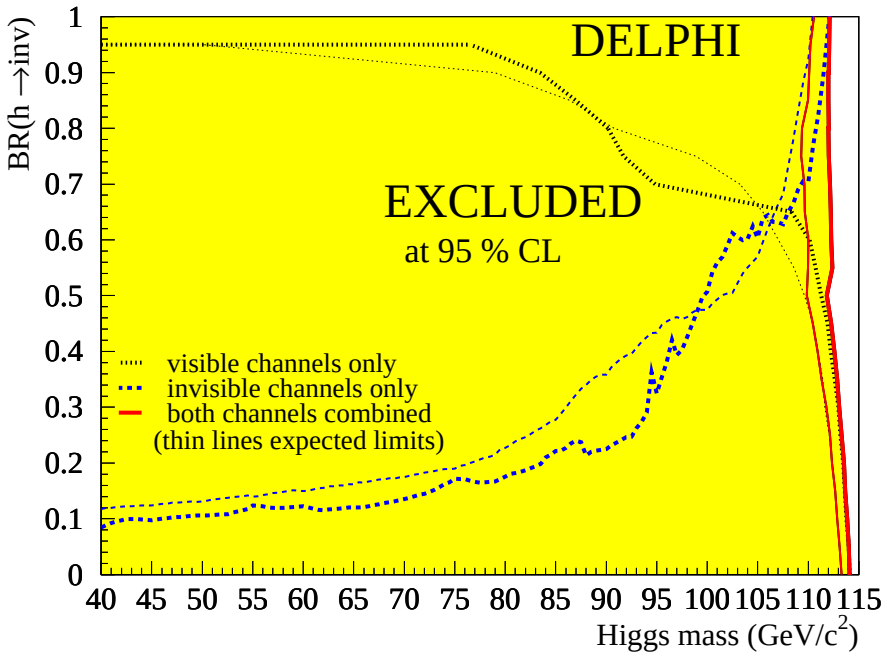

Figure 6.15: The Higgs boson mass limits as function of the branching ratio into invisible decays BR_{inv}, assuming a $1 - BR_{\text{inv}}$ branching ratio into standard visible decay modes.

a slight deficit in the results from both the visible and invisible searches leads to a larger observed limit compared to the expected limit. A difficult question in the combination of visible and invisible results was the treatment of possible overlaps. This is mainly an issue for the channels

$$e^+e^- \to HZ \quad (H \to b\bar{b}) \quad (Z \to \nu\bar{\nu})$$
$$e^+e^- \to HZ \quad (H \to inv) \quad (Z \to q\bar{q})$$

[5] visible means decays into b-quarks or τ leptons

Both channels have the signature of two jets and missing energy. The first channel only considers jets with b quarks, but the second channels includes all quarks, so especially for the region $m_H \approx m_Z$ the results from the first channel can be a subset of the second channel. In order to avoid this overlap, a cut off value was set. For a branching ratio into invisible final states greater than 50%, only the $e^+e^- \rightarrow HZ(H \rightarrow inv)(Z \rightarrow q\bar{q})$ was used, for branching ratio into invisible final less or equal than 50% only the $e^+e^- \rightarrow HZ(H \rightarrow b\bar{b})(Z \rightarrow \nu\bar{\nu})$ was used.

There are some constraints on this branching ratio independent limit. This limit only includes the case of Standard Model or invisible decays, neglecting fermiophobic decays and secondly for the visible decay modes only the Standard Model decay modes into b or τ quarks have been taken into account and the visible decay modes were weighted accordingly to their Standard Model branching ratios.

6.6.4 Limit in the MSSM

Up to now, all the results did not test any specific model, but tried to exclude a invisibly decaying Higgs boson as model independent as possible. These results can be used to test certain specific models (see chapters 2 and 3). The MSSM provides the most favoured scenario for invisible Higgs decays, so the results obtained were used to exclude some regions of the MSSM parameter space. In order to do this, a large database with cross-sections for the decay $h \rightarrow \tilde{\chi}_1^0\tilde{\chi}_1^0$ was generated using HZHA. Since the H is too heavy to be detected at LEP2 in this scenario, only the light h has been considered. The MSSM parameters varied were m_A and $\tan\beta$, while the other parameters were fixed to M_2=μ=150 GeV, the common mass M_{SUSY} was set to 1000 GeV/c^2, m_{top} has been set to 174.3 GeV/c^2 and the mixing in the stop sector has been set to the maximal value. It turned out, as expected, that the searches are only sensitive for low $\tan\beta$. The result in the $m_h - \tan\beta$ plane can be seen in 6.16. In this plot, one can see, that there are large regions (intermediate), where on has very tiny decay rates[6] into neutralinos. The white region contains points in the MSSM parameter space, where either the branching ratio into neutralinos was too small or the h is too heavy to be produced. This also shows the limitations of that kind of scan. A general exclusion of parts of the MSSM parameter space is only possible with combining all available results both from the searches for Higgs bosons (hZ,hA H^+H^-) and the direct searches for SUSY particles.

6.6.5 Limit in a Majoron Model

Another extension to the Standard Model is the so-called Majoron model (see chapters 2.4 and 3.4). It contains two Higgs bosons H and S. Their decay can be invisible, if the decay into two Majorons J is possible. This depends however on the mixing angle θ, so in Fig. 6.17 the exclusion for both H and S is shown

[6] less than 1%

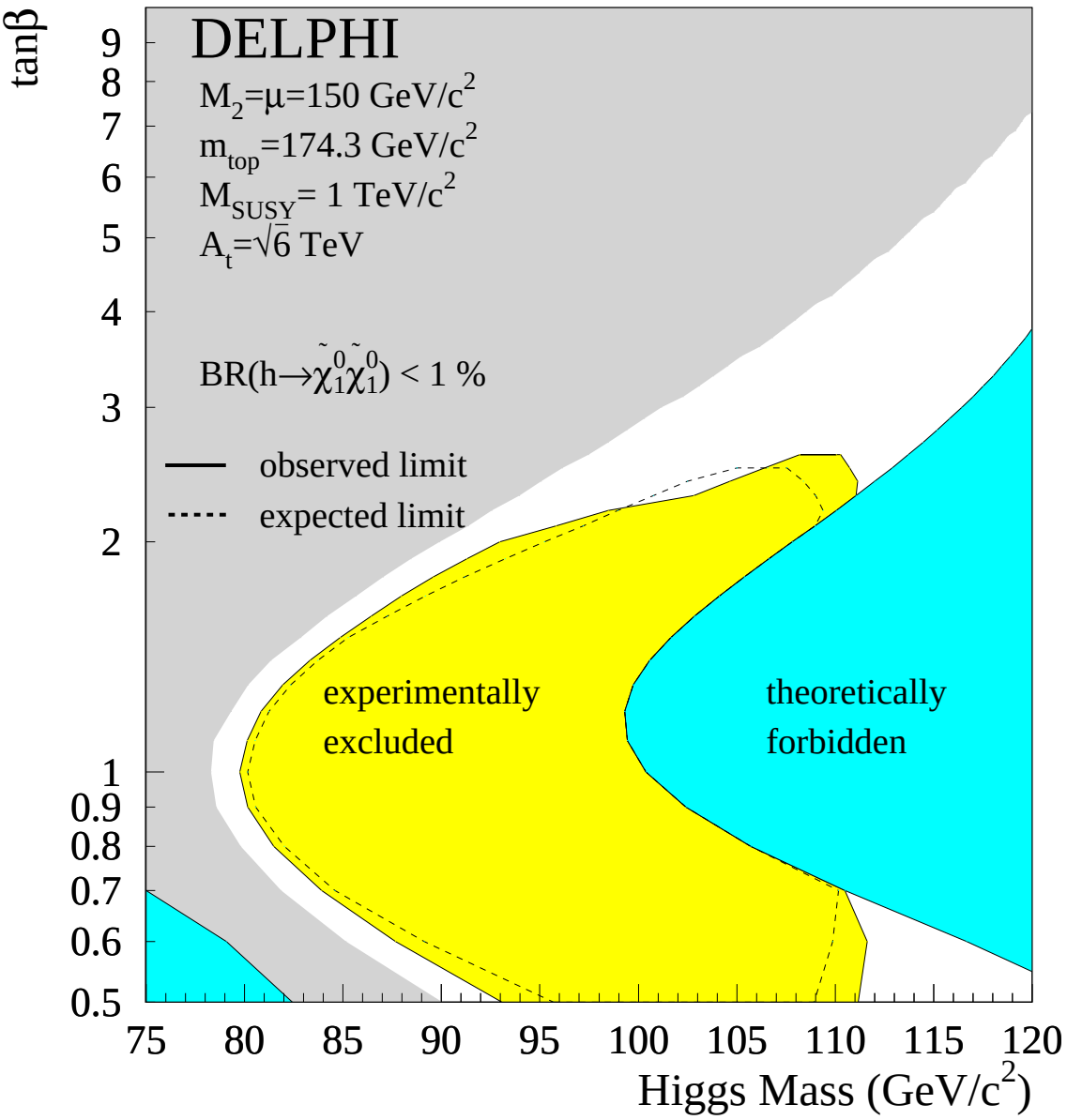

Figure 6.16: Excluded region in the MSSM from searches for Higgs boson decaying into invisible final states for maximal mixing in the stop sector. The different grey areas show the theoretically forbidden region (dark), the region where the Higgs boson does not decay into neutralinos (intermediate), the region which is excluded at 95% CL by this search for invisibly decaying Higgs bosons (light) and the unexcluded region (white).

depending on $\sin^2\theta$. The two areas (gray and hatched) show the excluded mass

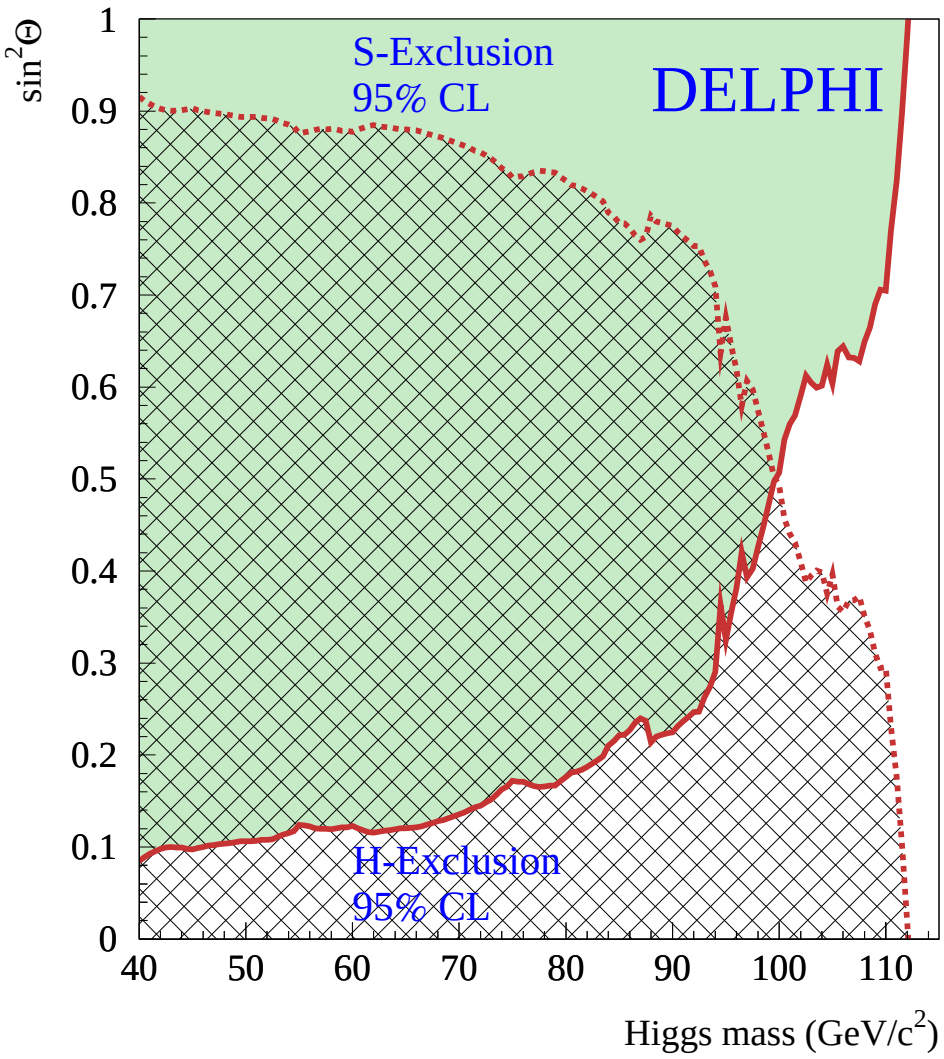

Figure 6.17: Limit on $\sin^2\theta$ as a function of the Higgs boson mass at 95% CL. S and H are the Higgs bosons in the Majoron model with the expected decay rates for large $\tan\beta$. In this case the massive Higgs bosons decay almost entirely into invisible Majoron pairs.

range for both H and S. For extreme values of $\sin^2\theta$ (0,1) the limit of one of the bosons disappears.

Chapter 7

Searches for hadronic Higgs decays

Searches for hadronically decaying Higgs bosons are presented in this chapter. The main idea for this analysis is to reduce the dependence on identifying jet with b content[1], which is one of the main ingredients for the Standard Model Higgs searches, which at LEP always assume the Higgs decaying dominantly in $b\bar{b}$ pairs. This analyses only require an object that is decaying hadronically either in quarks or gluons, which then form two jets. The results obtained are

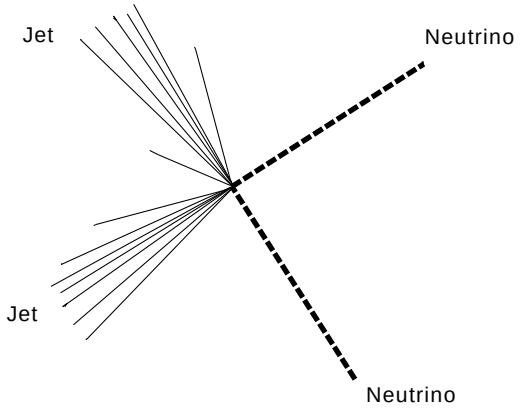

Figure 7.1: The topology searched for in the reaction $e^+e^- \rightarrow HZ\,(H \rightarrow q\bar{q}, gg)(Z \rightarrow \nu\bar{\nu})$.

by construction less dependent on b-tagging. Another strong motivation for these kind of searches is the existence of points in the MSSM or the 2HDM, at which the Higgs does not decay into b quarks but into c quarks or gluons (see chapter 3). The signature searched for is two jets and missing energy (see Fig. 7.1), a signature which is quite similar to the one of an invisible Higgs decay.

[1] b-tagging

The only difference compared to an invisible Higgs decay is that this time the Z decays into two neutrinos, which renders the Z decay invisible.

This final state represents about 21% of all final states and is the second most important decay channel, it is also referred to as neutrino channel. The other channels like the four jet ($H \to q\bar{q}, gg\ Z \to q\bar{q}$) or the leptonic channels ($H \to q\bar{q}, gg\ Z \to e^+e^-, \mu^+\mu^-$) represent about 70% or 6% respectively and have also been searched for in DELPHI. The searches for hadronically decaying Higgs bosons are also often called flavourblind Higgs searches, because they are independent of the quark flavour. The background processes are pretty similar to the one for the invisible Higgs decays, they are dominated again by $e^+e^- \to ZZ \to q\bar{q}\nu\bar{\nu}$ and $We\nu$ t-channel $e^+e^- \to We\nu_e(W \to q\bar{q}')$. The searches were again constructed to cover a large mass range between 40 and 120 GeV/c^2. The analysis is pretty similar to the one for invisible decays, but in the derivation of the limits the so-called *sliding* mass approach has been used (see chapter 7.7).

7.1 The data set

The data set and the Standard Model background Monte Carlos sample were the same ones that have been used in the search for invisible Higgs decays. However, for the signal samples, a huge effort has been made to generate a fine mass grid for different quark flavours. It was decided to generate decays in gluons, c quarks and s quarks and using the b quark samples from the Standard Model searches as well. Although there is no theoretical model predicting large decays rates into strange quarks, these samples have been generated in order to have decays into light quarks as well and to be as model independent as possible. For the set of new samples generated, the following mass grid has been used:

- 40-115 GeV/c^2 in 2.5 GeV/c^2 steps with 2000 events per Higgs mass point.

These samples have been mostly generated using the Karlsruhe EKPPLUS cluster. The total amount of samples produced was about 6 million events. The b quark samples produced contain 5000 events each, from 40 to 80 GeV/c^2 in 10 GeV/c^2 steps, and in 5 GeV/c^2 steps from 80 to 115 GeV/c^2.

7.2 Dependence on the decay flavour

The dependence on $\sqrt{s}$ is similar to the one of the invisible decays, however for this analysis, three Higgs mass windows have been defined:

Low mass range: 40-67.5 GeV/c^2

Medium mass range: 70-87.5 GeV/c^2

High mass range: 90-115 GeV/c^2

It was found, that the decays of the different flavours look pretty different. This can bee seen for different variables in Fig. 7.2 and Fig. 7.3 for two Higgs masses of 100 GeV/c^2 and 50 GeV/c^2 at $\sqrt{s}$=206.5 GeV. The first variable plotted in Fig. 7.2a and Fig. 7.3a is the charged multiplicity. One immediately sees that the gluon jets contain many more charged particles than the quark jets. Comparing the quark jets this behaviour is expected, because it is known that the jets from heavier quarks tend to have higher multiplicities. The difference of the gluon jets originates from the difference in the colour charge [Gre98]. This leads to a higher number of particles but also to broader jets. Both kinds of jets have the same average transverse momentum, so the larger number of tracks lead to wider distribution of the track transverse momentum. The distribution of the visible energy in Fig. 7.2b and Fig. 7.3b is therefore unaffected, but looking at the thrust distribution in Fig. 7.2c and Fig. 7.3c, the broadening for the gluon jets is visible, since their thrust value is smaller. The last two plots (Fig. 7.2d and Fig. 7.3d) show the largest transverse momentum of a particle with respect to the jet axis in the two jet configuration. Also here, the broadness of the gluons jets compared to the quark jets is clearly visible.

A result of these differences is, that these gluon jets would be much better to separate from background than the quark jets for the missing energy channels. This would bias the analyses towards gluon jets, so in order to avoid this, the sample composition chosen was

$$gg : s\bar{s} : c\bar{c} : b\bar{b}$$

$$1 : 1 : 1 : 2.5$$

in order to avoid any bias towards a certain flavour. At the mass points where no $b\bar{b}$ where available, the following composition was used:

$$gg : s\bar{s} : c\bar{c}$$

$$1 : 1 : 1$$

The deficit of $b\bar{b}$ samples was compensated by the fact that at the points, where $b\bar{b}$ were available, the number of events included a factor 2.5 more statistics.

7.3 Flavour-tagging

For the medium and high mass analysis a flavour tagging was used in order to use the correlations between the event shape and the decay flavour. The method used at DELPHI is mainly optimised to separate b quark decays from the other quark flavour, but can also be used as a weighting variable. The basic idea of b-tagging is to use the longer lifetime of b hadrons, which leads to secondary vertices, which are well separated from the so-called primary vertex, which is the point of the e^+e interaction. The secondary vertex from the b hadron can be reconstructed due to the high precision of the DELPHI silicon vertex detector. This secondary vertex is usually found using tracks with a high impact parameter. The impact parameter gives the minimal distance of

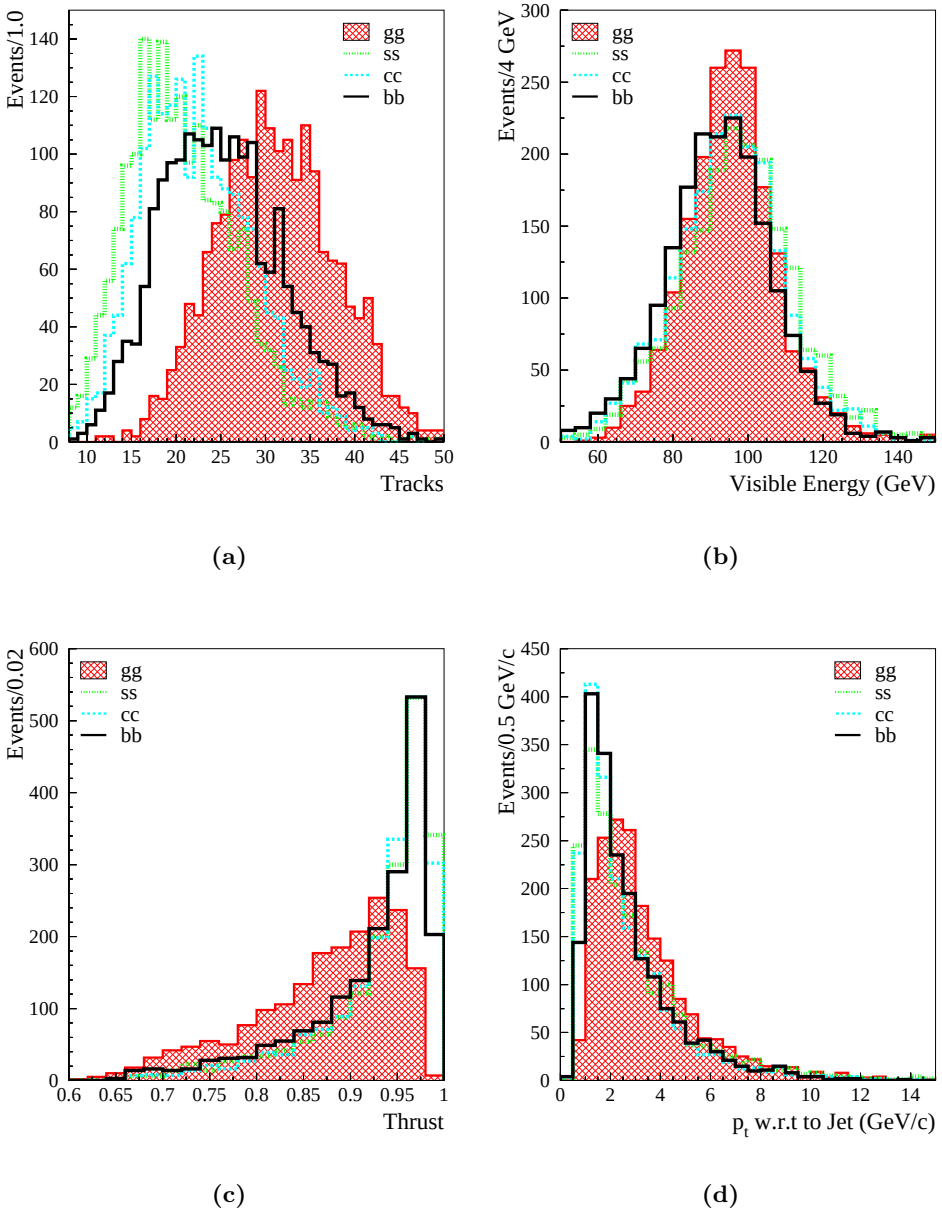

Figure 7.2: The decay flavour dependence of the event signatures for m_H=100 GeV/c^2 at a centre-of-mass energy of 206.5 GeV for the four different flavours: gluons (hatched), strange quarks (light grey dashed line), charm quarks (light grey dotted line) and bottom quarks (black solid line). Shown are the charged multiplicity (a), the visible energy (b), the thrust of the event (c) and the largest transverse momentum of a particle with respect to the jet axis (d).

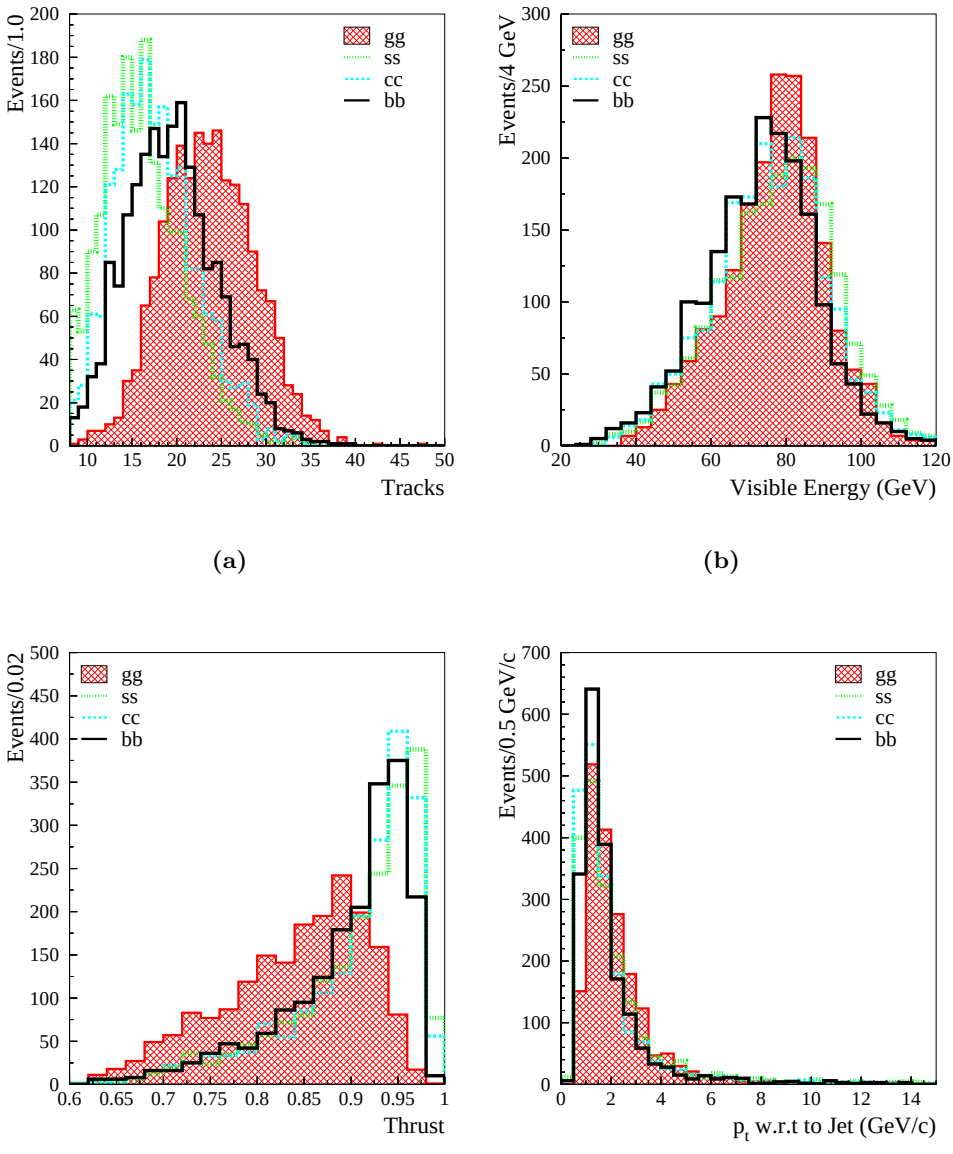

Figure 7.3: The decay flavour dependence of the event signatures for m_H=50 GeV/c^2 at a centre-of-mass energy of 206.5 GeV for the four different flavours: gluons (hatched), strange quarks (light grey dashed line), charm quarks (light grey dotted line) and bottom quarks (black solid line). The distributions shown are same as in Fig. 7.2.

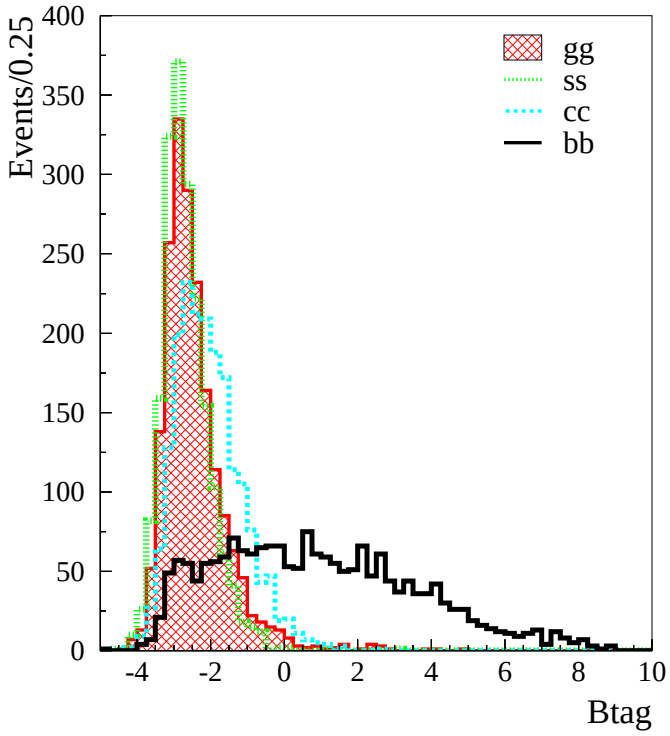

Figure 7.4: The b-tagging likelihood for the four decay flavours in HZ production. The differences between b, c, s and gluons are clearly visible.

a track to the primary vertex. This information is then combined with other informations about the event like the transverse momentum or the mass of the tracks originating from the secondary vertex into a likelihood ratio, that gives a probability, of how b-like an event is. The distributions for the different decay flavours is shown in Fig.7.4. The shift of the c quarks compared to the s quarks is due to the fact, that also c quarks have a longer lifetime compared to s quarks. This can also lead to measurable secondary vertices. One the other hand, the lifetime is still short compared to the b quarks. The tail in the gluon distribution originates from the splitting of the gluon in a $b\bar{b}$ or $c\bar{c}$ pair, which adds this small contribution.

The b tagging package used at DELPHI is described in great detail in [DEL02a].

7.4 Preselection

For all the three mass windows, the first two steps of the preselection are the same as the ones for the invisible Higgs search. The tail cuts and the variables used in the IDA have been modified for the three different mass range analyses. At the tail cut level, it was required that the event does not contain more than

two clearly identified electron or muons.

7.4.1 Low mass analyses

In the low mass analyses, twelve variables were used to construct an efficient IDA variable.

- $\ln(p_{\mathrm{T}})$: The logarithm of the transverse momentum of the event.
- $\ln(\min(\mathrm{E_{Jet}})/5$: The logarithm of the energy of the least energetic jet in the three-jet configuration, divided by 5.
- $E_{\mathrm{vis}}/\sqrt{s}$: Visible energy of the event, normalised to the centre-of-mass energy.
- $E_{\mathrm{T}}/\sqrt{s}$: Transverse energy of the event, normalised to the centre-of-mass energy.
- $H_{20} - H_{40}$: The difference between the Fox-Wolfram momenta H_2 and H_4. The Fox-Wolfram [Fox79] momenta are defined as

$$H_l = \sum_{i,j} \frac{|\vec{p}_i||\vec{p}_j|}{E_{vis}^2} P_l(\cos\theta_{ij}) \tag{7.1}$$

  with P_l being the Legendre polynomials and $\vec{p}_i, \vec{p}_j$ being the particle momenta. The Fox-Wolfram momenta are then normalised to the first momentum H_0, so H_{10} is H_1 normalised by H_0. Like the thrust, the Fox-Wolfram momenta contain information about the event shape.

- $E_{\mathrm{isol}}/\sqrt{s}$: Energy sum between the two cones, defined by half opening angles 5° and $\alpha_{\max}$ around the most isolated particle (see chapter 57).
- $p_{\mathrm{isol}}/\sqrt{s}$: Momentum of the most isolated particle, as defined above.
- $\log_{10}$(scaled acoplanarity): $\log_{10}$ of the scaled acoplanarity (see chapter 57).
- Thrust: Thrust value of the event, computed in the rest frame of the visible system.
- ln(acollinearity): Logarithm of the acollinearity of the two-jet system.
- m_{mis}: The missing mass calculated as $\sqrt{E_{mis}^2 - p_{mis}^2}$. For a possible signal, this should be compatible with the Z boson mass.
- $\ln(\max(p_{\mathrm{T}})_{\mathrm{jet}})$: The logarithm of the highest transverse momentum of the jet-particles, defined by the transverse momentum of any particle in the jet with respect to the nearest jet axis.

$\sqrt{s}$	Low mass		Medium mass		High mass	
(GeV)	Data	MC	Data	MC	Data	MC
188.6	302	318.4 ± 2.3	478	480.3 ± 3.1	517	516.6 ± 3.4
191.6	59	52.1 ± 0.3	82	77.9 ± 0.5	91	82.4 ± 0.5
195.5	163	160.8 ± 1.0	250	235.8 ± 1.4	256	247.5 ± 1.5
199.5	178	178.6 ± 1.2	281	258.5 ± 1.5	289	263.4 ± 1.6
201.6	100	87.6 ± 0.5	143	116.9 ± 0.6	150	129.1 ± 0.7
205.0	153	162.7 ± 0.9	234	230.6 ± 1.3	229	233.7 ± 1.4
206.5	179	180.3 ± 1.2	266	258.4 ± 1.5	279	259.6 ± 1.7
206.5U	133	127.0 ± 1.1	194	183.6 ± 1.4	192	184.9 ± 1.5

Table 7.1: Comparison of simulation and data after the different steps of the preselection in the three different mass ranges. The listed errors are from Monte Carlo statistics only. The last line (206.5U) refers to the data taken with one TPC sector inoperative, which has been fully taken into account in the event simulations.

Variable	lower cut	upper cut
$\ln(p_{\mathrm{T}})$	2.00	4.75
$E_{\mathrm{vis}}/\sqrt{s}$	0.0	0.8
$E_{\mathrm{T}}/\sqrt{s}$	0.1	0.7
$H_{20} - H_{40}$	-	0.38
$p_{\mathrm{isol}}/\sqrt{s}$	0.0	0.2
$\log_{10}$(acoplanarity)	0.75	2.6
Thrust	0.6	0.99
ln(acollinearity)	2.75	5.25
m_{mis}	0.15	1.0
$\ln(\max(p_{\mathrm{T}})_{\mathrm{jet}})$	-1.0	2.50

Table 7.2: Tail cuts used in the low mass analyses.

The agreement of data and Monte Carlo simulation is shown in Tab. 7.1 and in Fig. C.1, the tail cuts applied are listed in Tab. 7.2. Like for the invisible Higgs searches, a two step IDA was used to separate between signal and background, but this time no cut on the second IDA distributions was applied. A special determination of the working point of the analysis was not done due to the *sliding* method (see chapter 7.7). The IDA was also trained over the whole mass range from 40.0 to 67.5 GeV/c^2.

7.4.2 Medium mass analyses

Twelve variables were also used in the medium mass analyses. Due to a different event shape, the variable ln(min(E$_{\mathrm{Jet}}$)/5 was replaced by B_{HZ2}.

- B_{HZ2}: The probability of the event to include a b quark assuming a HZ

Variable	lower cut	upper cut
$\ln(p_{\mathrm{T}})$	1.75	4.75
$p_{\mathrm{isol}}/\sqrt{s}$	0.0	0.2
$\log_{10}$(acoplanarity)	0.5	2.75
Thrust	0.675	1.0
ln(acollinearity)	2.25	4.75
m_{mis}	0.15	0.75
$\ln(\max(p_{\mathrm{T}})_{\mathrm{jet}})$	-0.75	2.50

Table 7.3: Tail cuts used in the medium mass analyses.

Variable	lower cut	upper cut
$\ln(p_{\mathrm{T}})$	1.75	4.25
$E_{\mathrm{vis}}/\sqrt{s}$	0.0	0.7
$H_{20} - H_{40}$	-0.2	-
$p_{\mathrm{isol}}/\sqrt{s}$	0.0	0.2
$\log_{10}$(acoplanarity)	0.0	2.75
Thrust	0.7	1.0
ln(acollinearity)	2.0	4.25
$\ln(\max(p_{\mathrm{T}})_{\mathrm{jet}})$	-0.5	2.50

Table 7.4: Tail cuts used in the high mass analyses.

event with 2 jets and missing energy [Bor97, DEL02a].

The tail cuts are listed in Tab. 7.3. The agreement between data and Monte Carlo is also shown in Tab. 7.1 and in Fig. C.2. The IDA was calculated the same way as in the low mass analyses, the mass range for the IDA training ranged from 70.0 to 87.5 GeV/c^2.

7.4.3 High mass analyses

The same 12 variables like in the medium mass analyses were used in the high mass analyses, the tail cuts are listed in Tab. 7.4. The mass range for the training of the IDA was varied for the different centre-of-mass energies, it ranges from 92.5 GeV/c^2 to 97.5 GeV/c^2 for 188.6 GeV data, 92.5 GeV/c^2 to 107.5 GeV/c^2 for 191.6 to 201.6 GeV data and 92.5 GeV/c^2 to 115.0 GeV/c^2 for 205.0 to 206.5 GeV data. This was done in order to avoid training on off-shell events beyond the kinematical limit for the HZ process (see chapter 3.1). The agreement between data and Monte Carlo is also shown in Tab. 7.1 and in Fig. C.3.

7.5 Mass reconstruction

In this case again the constraint of the Z mass was used, but this time the missing mass had to be the Z mass. For the momentum and the energy of the Higgs bosons the following relations to the visible energy and momentum apply:

$$E_{Higgs} = \alpha E_{vis} \tag{7.2}$$

$$p_{Higgs} = \alpha p_{vis} \tag{7.3}$$

The factor α describes the scaling factor between the actual measured energy and momentum and the energy and momentum that would be measured in a perfect detector. The mass of the Z boson can be then calculated as:

$$\begin{aligned} m_Z^2 &= \left(\sqrt{s} - E_{Higgs}\right)^2 - p_{Higgs}^2 \\ &= \sqrt{s}^2 - 2\sqrt{s}E_{vis}\alpha + (E_{vis}^2 - p_{vis}^2)\alpha^2 \\ &= \sqrt{s}^2 - 2\sqrt{s}E_{vis}\alpha + m_{vis}^2\alpha^2 \end{aligned} \tag{7.4}$$

Solving this for α one obtains

$$\alpha_{1,2} = \frac{E_{vis}\sqrt{s} \pm \sqrt{E_{vis}^2\sqrt{s}^2 - m_{vis}^2(\sqrt{s}^2 - m_Z^2)}}{m_{vis}^2} \tag{7.5}$$

Putting this into the relation for the Higgs mass m_{Higgs}

$$m_{Higgs} = \sqrt{E_{Higgs}^2 - p_{Higgs}^2} = \alpha\sqrt{E_{vis}^2 - p_{vis}^2} = \alpha m_{vis} \tag{7.6}$$

one obtains

$$m_H = \frac{E_{vis}\sqrt{s} \pm \sqrt{\sqrt{s}^2 E_{vis}^2 - m_{vis}^2(\sqrt{s}^2 - m_Z^2)}}{m_{vis}} \tag{7.7}$$

The solution with the mass below $\sqrt{s}$ is then taken [Pio99]. The effect on the mass reconstruction is shown in Fig. 7.5.

7.6 Systematic errors

The estimation of the systematic error follows closely the study done in the search for invisible Higgs decays (see chapter 6.5). These errors include:

- Choice of the Monte Carlo generator for the $q\bar{q}\gamma$ background.
- Error on the luminosity.
- The influence of the jet clustering.
- Uncertainty for the b-tagging.

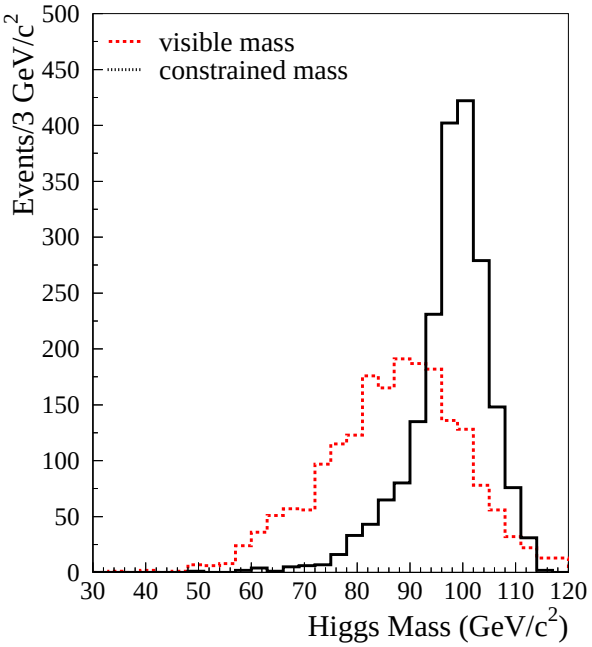

Figure 7.5: The mass reconstruction for a hadronic Higgs decay with m_H=100 GeV/c^2 using only the visible mass (hatched line) or the constrained mass (solid line).

- Uncertainties in the $We\nu$ cross-section.
- The Monte Carlo description in general (Shaking).

One difficulty for the study of the systematic errors in these analyses was the fact that three mass windows were used and in principle four different signal samples existed. The systematic errors on the signal efficiencies had been evaluated separately for all four hadronic decay modes. As for the invisible Higgs decays, the error on the luminosity was assumed to be $\pm 0.5\%$. The error on the background due to the choice of the jet clustering (replacing DURHAM by LUCLUS) was estimated to be $\pm 1.3\%$ for the high mass analyses and $\pm 1.6\%$ for the medium mass analyses. It has been found, that the error is negligible for the low mass analyses. The signal efficiency (in percent) is affected by ± 0.4 and ± 1.9 for the different flavours. Since the medium mass and high mass analyses used the b-tagging package from DELPHI, the influence of the b quark identification has also been evaluated. This was done by taking the differences in the mean between data and Monte Carlo of the b tagging distributions at the preselection level and smearing the Monte Carlo events. This smearing was done by shifting each Monte Carlo event by the mean difference and then adding a Gaussian distributed random number with mean 0 and 1 σ being the difference of data and Monte Carlo. The effect on the background was $\pm 1.0\%$ for the high mass and $\pm 1.1\%$ for the medium mass analyses. The effect on the signal was very small, in the range of ± 0.2 to $\pm 0.4\%$. As for the invisible Higgs

searches, the influences of the uncertainty on the $We\nu$ cross-section have been estimated, the effect on the background ranged from $\pm 1.3\%$ for the low mass analyses over $\pm 0.8\%$ for the medium mass analyses down to $\pm 0.5\%$ for the high mass analyses.

Analysis	Shaking			Total		
	1998	1999	2000	1998	1999	2000
Low	10.0	5.7	12.6	10.1	5.9	12.7
Medium	10.2	6.2	8.8	10.4	6.6	9.1
High	8.2	4.0	7.1	8.4	4.4	7.3

Table 7.5: Systematic errors on the background obtained by the shaking method and total error on the background in percent.

The shaking method, as described in chapter 6.5, has been also used in the analyses here. The effect on the background varies for the different years due to the usage of the different corrections. The uncertainties obtained by the shaking are listed in Tab. 7.5. A general comment is, that the influence of the systematic error due to the shaking is the highest in the medium mass range and this error source dominates the systematic error for all three mass ranges as can be also seen in Tab. 7.5. The impact on the signal efficiencies for the three different years of data-taking for the different flavours is shown together with the other sources of systematic errors in Tab. 7.6. The total systematic error is between ± 1 to $\pm 3\%$ and the errors are the largest for the low mass analysis.

7.7 Results

In order to derive the results with ALRMC, another procedure has been applied compared to the searches for invisible Higgs bosons (see chapter 6.6). In the invisible Higgs boson searches the reconstructed mass distribution has been used in order to derive the exclusion limits and for all Higgs masses tested, the same background distribution has been taken. In this analysis the IDA2 distribution itself has been taken to derive the exclusion limits and additionally, a *sliding* approach [Bam01] has been used.

The *sliding* method uses separate data and background distributions for each tested signal mass. This method is illustrated in a toy analysis shown in Figs. 7.6 and 7.7. First one picks the sliding variable which is in most cases the mass of the expected signal. Then the reconstructed mass distribution from Monte Carlo for the test mass (here 100 GeV/c^2) is plotted and the mass window for this test mass is derived. This is done by requiring that no expected signal is lost. The same mass cuts are then applied to the reconstructed mass of the background and to the selected data events. Depending on the test mass this leads to a quite visible suppression of expected background and data, which do not have a signal-like reconstructed mass. The distribution of the

Analysis	Flavour	Jets	b-tag	Shaking			Total		
				1998	1999	2000	1998	1999	2000
Low	$c\bar{c}$	0.5	-	2.4	1.0	1.0	2.5	1.1	1.1
	gg	0.5	-	2.3	1.2	1.0	2.4	1.3	1.1
	$s\bar{s}$	0.5	-	1.6	0.9	1.0	1.7	1.0	1.1
	$b\bar{b}$	0.9	-	3.5	1.3	1.2	3.6	0.0	1.5
Medium	$c\bar{c}$	0.4	0.3	0.7	0.8	1.0	0.9	0.9	1.1
	gg	0.4	0.4	1.4	1.0	1.2	1.5	1.1	1.3
	$s\bar{s}$	0.4	0.3	0.6	0.6	0.8	0.8	0.8	0.9
	$b\bar{b}$	1.9	0.1	1.1	1.4	0.8	2.2	2.4	2.1
High	$c\bar{c}$	0.4	0.2	1.0	1.0	1.1	1.1	1.1	1.2
	gg	0.4	0.2	1.0	0.5	1.3	1.1	0.7	1.4
	$s\bar{s}$	0.6	0.2	1.0	0.8	1.7	1.2	1.0	1.8
	$b\bar{b}$	1.4	0.1	2.0	0.7	1.1	2.4	1.6	1.8

Table 7.6: Summary of the systematic errors on the signal efficiencies.

discriminant variable, which is used in order to derive the exclusion limits, also shows the significant impact of this method. The same is done as an example for a test mass of 50 GeV/c^2, which leads to quite different distributions. This clearly illustrates the benefits of the *sliding* method. An issue by using the sliding method is the interpolation between different test masses which would also impose the needs for interpolation of data events. A way to avoid this is to generate very fine mass grids of simulated signal masses, which requires large amounts of CPU time.

The *sliding* method has been implemented for this analysis in order to derive the exclusion limits. The sliding cuts were made using the reconstructed Higgs mass and for each tested Higgs mass a separate IDA2 distribution for signal, expected background and selected data has been constructed. These distributions were then used as the input distributions for the ALRMC method.

An additional complication in this analysis is, since one has up to four different decay modes, for each mass up to four pairs of signal and backgrounds had to be generated. The interpolation issue in this case is not a problem, since it is known, that the mass resolution is larger than the Monte Carlo simulation grid of 2.5 GeV/c^2. The next question is to set a limit that is really flavourblind, which means not preferring one quark decay flavour. Although the training samples were constructed not to prefer any quark flavour one still obtains slightly different efficiencies as can be seen in Fig. 7.8. It is clearly visible, that the analysis is always most sensitive to gluonic Higgs decays and it is least sensitive to a decay into s quarks at low masses and into b quarks at high masses. So for each mass point, the exclusion power has been calculated for the four decay flavours and the weakest one was then chosen to calculate the limit for a hadronic Higgs decay. The combined mass distribution for all three analyses after the second IDA step is shown in Fig. 7.9 together with

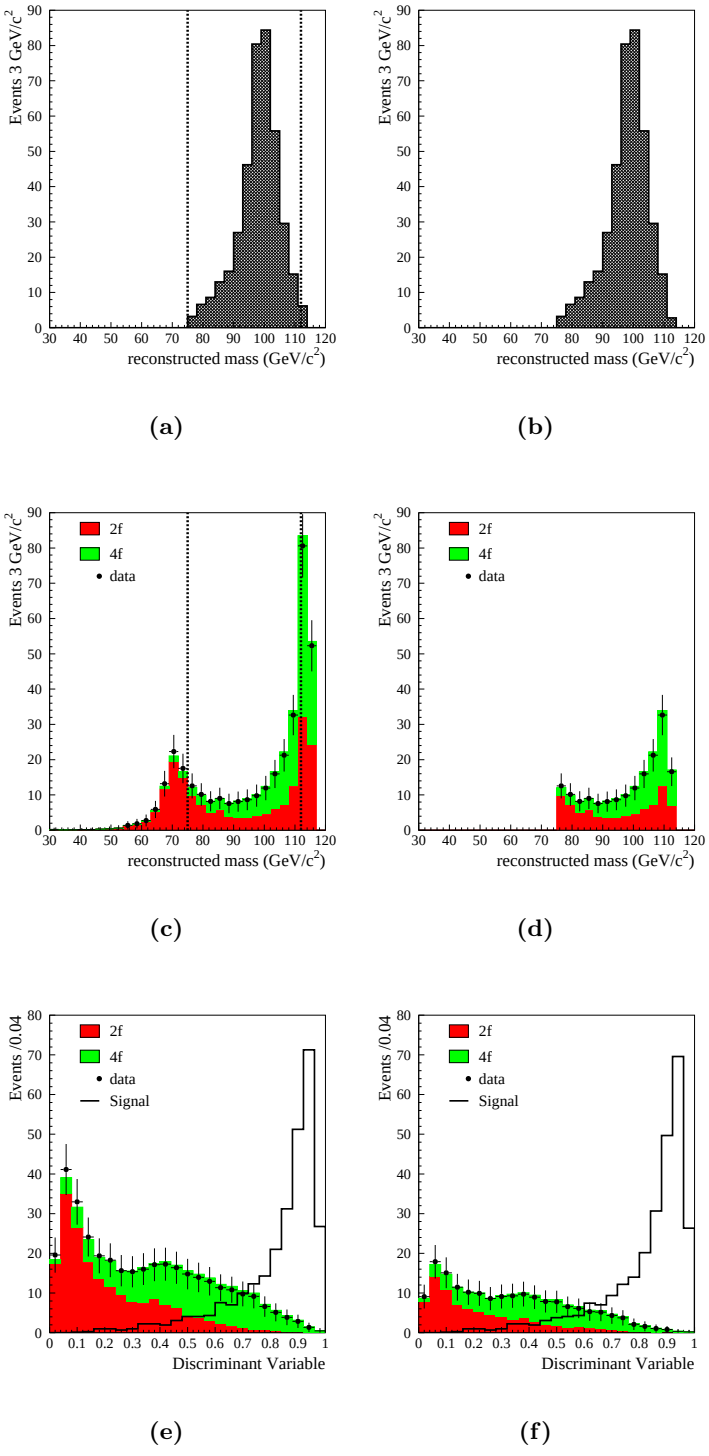

Figure 7.6: The sliding method demonstrated with a toy analysis. Shown are the reconstructed mass distributions for a 100 GeV/c^2 Higgs signal (a, b) and the data and expected background (c, d). The discriminant variable is shown in (e, f). The vertical dashed lines in (a) and (c) indicate the sliding mass cuts derived from (a). In (b) and (d) the mass distributions are shown after the cuts were applied. The impact on the discriminant variable before and after the cuts were applied is shown in (e) and (f).

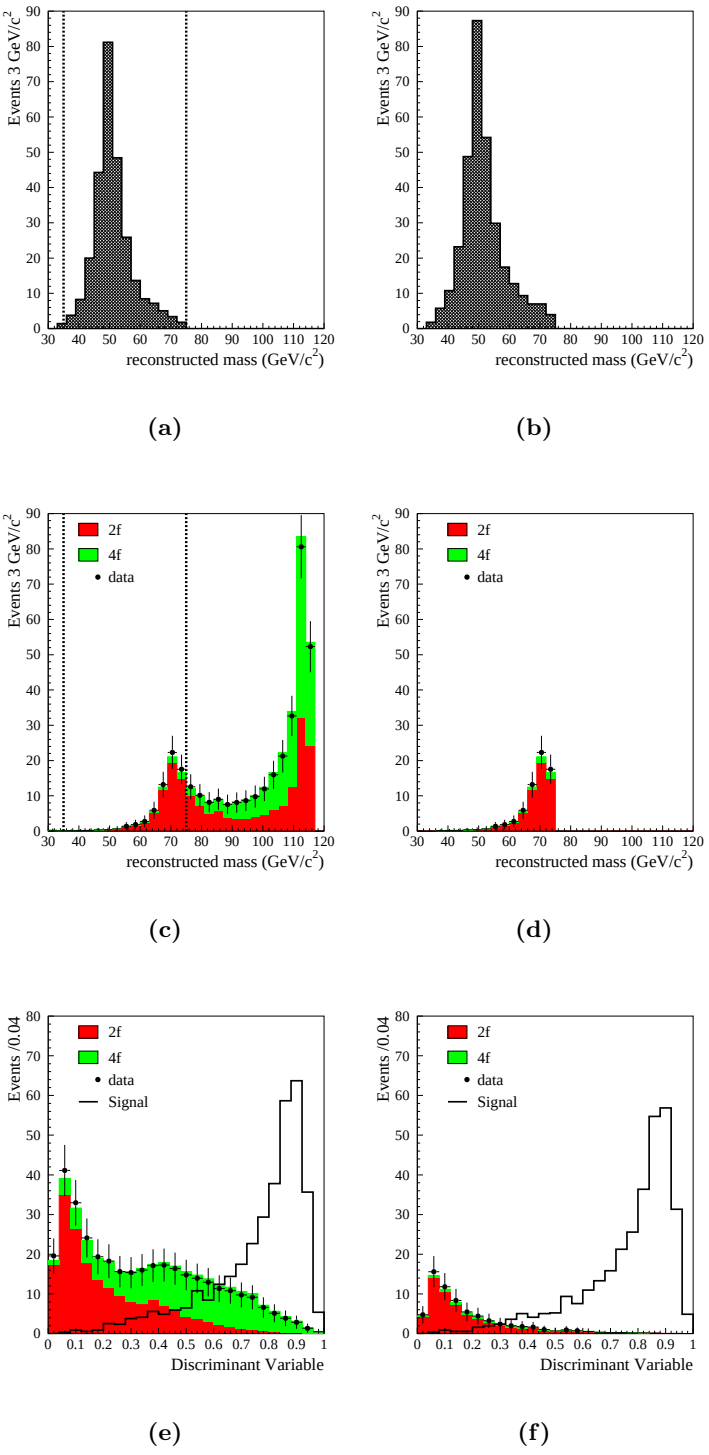

Figure 7.7: The sliding method demonstrated with a toy analysis, this time with a 50 GeV/c^2 Higgs mass. The distributions are the same as in Fig. 7.6.

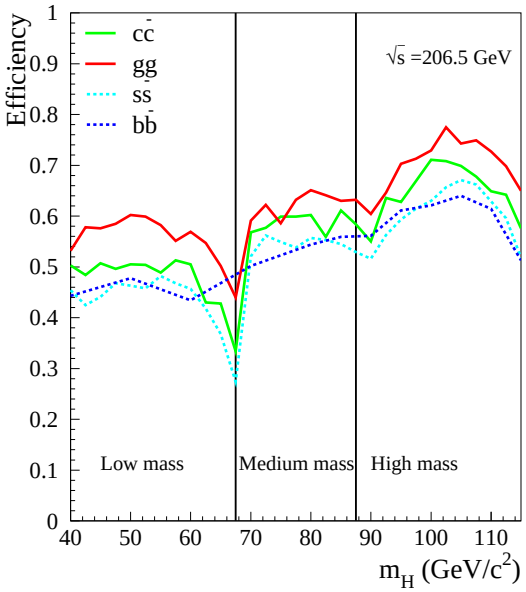

Figure 7.8: The signal efficiencies for the different decay modes in the three mass windows at $\sqrt{s}$=206.5 GeV.

three arbitrary scaled signal distributions. From this distributions, one can see again, how the *sliding* approach would select only the relevant data and Monte Carlo events for each test mass. The results from this analysis have then been combined with the results from the four jet channel and the leptonic channels (e, μ) from a $\sqrt{s}$ between 188.6 to 209 GeV [DEL03b].

7.7.1 Mass limit for a hadronic Higgs decay

The input distributions from all channels were used in order to derive a limit on the mass of a hadronically decaying Higgs bosons assuming a branching ratio of 100% into hadronic final states. The question of flavour blindness was addressed by testing it with both the four jet and the channel in this analysis, since these two channels have the biggest weight in the limit derivation. In order not to be over-conservative, it was decided, that the decay flavour is taken, where this two channels combined have the weakest performance. This avoids looking for an unphysical Higgs which decays in e.g. gluons in one search channel and decays into s-quarks in another search channel. As the flavourblind limit the case where the Higgs decays in s-quarks was taken. For the justification of this procedure one can compare the expected performance for the suppression factor ξ, which is defined as:

$$\xi = \frac{\sigma_{excluded}}{\sigma_{SM}(e^+e^- \rightarrow HZ)}$$

The results at 95% CL are shown for the neutrino and the four jet channel in Fig. 7.10. It is clearly visible that for the neutrino channel, the s-quark decay

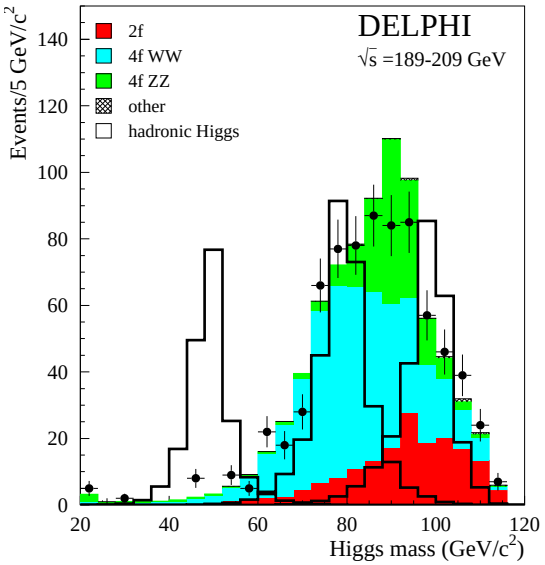

Figure 7.9: The combined mass distribution for the three hadronic Higgs analyses in the neutrino channel. Three arbitrary scaled Higgs mass distribution of 50, 80 and 100 GeV/c^2 are shown together with the data and the background from Monte Carlo simulation.

always has the worst expected performance. Also interesting to see is, that for low masses, the neutrino channel despite is factor three lower branching ratio is more performant. This effect is expected. The four jet channel relies on clear four jet events which is not the case anymore for low Higgs masses, as the jets become more and more collimated. Above 70 GeV/c^2 with well separated jets, the four jet channel begins to dominate the expected performance. For the low masses the s-quark decay is least performant, however for high masses the differences between the decay modes are marginal. So the choice of the s-quark decay as flavourblind limit is certainly justified.

The mass limit obtained in this case is 110.6 GeV/c^2 (108.0 GeV/c^2 expected) at the 95% CL. The compatibility with the background is tested using the CL_B. In Fig.7.11a the CL_B for the neutrino channel only is shown. As one can see, the CL_B is very compatible with the expectation, the observed CL_B is within one sigma for most of the mass range. The data deficit around 90 GeV/c^2 visible in Fig. 7.9 is also nicely visible as an almost two sigma deviation in the observed CL_B. In Fig. 7.11b, the CL_B after the combination is shown, which agrees again quite well with the expectation.

Comparing this obtained limit with the value obtained in the searches for Standard Model Higgs bosons (114.1 GeV/c^2), it is quite remarkable, that one is able to exclude Higgs bosons up to such a high mass without using the powerful background suppression due to b-tagging.

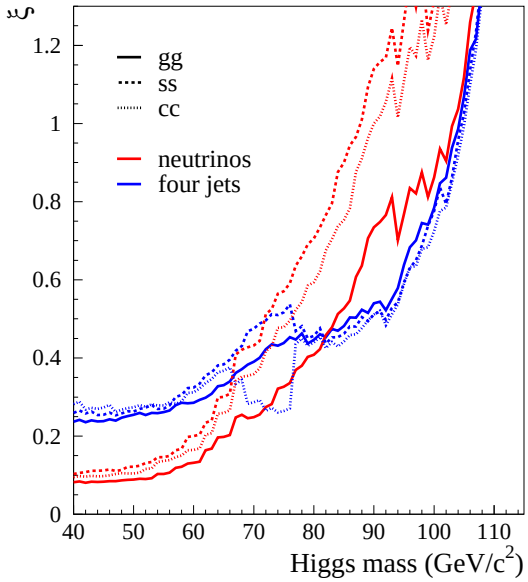

Figure 7.10: The expected performance for ξ for the different flavours in the neutrino and four jet channels.

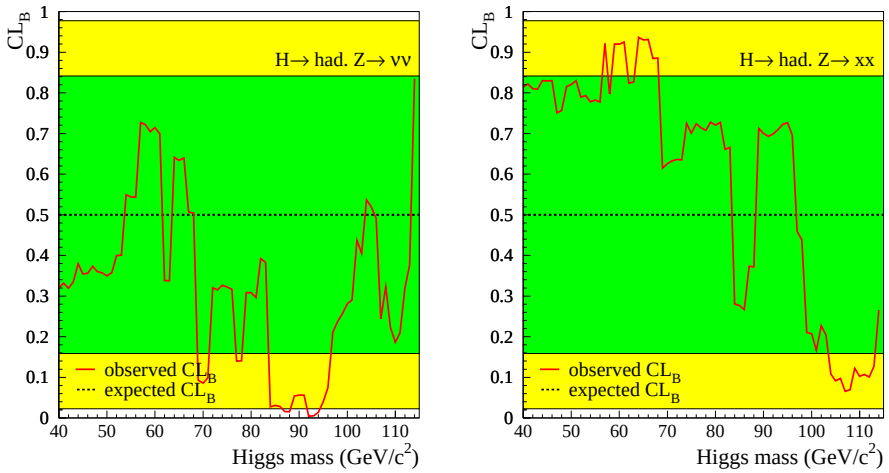

(a) **(b)**

Figure 7.11: . The compatibility of the data with the background hypothesis(CL_B). Shown are in (a) the CL_B for the $e^+e^- \rightarrow HZ(H \rightarrow had(Z \rightarrow \nu\bar{\nu})$ channel alone and in (b) the CL_B for the combination of all channels.

7.7.2 Excluded cross-section limits and excluded couplings

Additionally, one would also like to exclude the cross-section for the process $e^+e^- \rightarrow HZ \rightarrow (H \rightarrow \text{hadrons})(Z \rightarrow \text{anything})$ and additionally to exclude cross-sections for the different decay modes like $c\bar{c}$ and gg. The results for the flavourblind case were derived in the same way as for the mass limit. Like for the invisible Higgs decays, a limit on the suppression factor ξ was calculated. The results obtained for the cross-section are shown in Fig. 7.12a and the result for suppression is shown in Fig. 7.12b. As is visible in this plot, the exclusion power of the combined analysis is quite strong and there is no evidence for Higgs production between 40 and 115 GeV/c^2. The small dip in the Standard Model cross-section originates from the inclusion of the vector boson fusion processes (see chapter 3.1), which leads to increase in the cross-section. These processes are not included at low masses due to uncertainties in the Monte Carlo description. Note, that for the ξ plot shown in Fig. 7.12b, all ξ values larger than the observed limit are excluded.

After running the whole limit procedure one additionally has information about the exclusion power concerning gg or $c\bar{c}$ final states. For both cases, the excluded cross-section and the excluded suppression factor ξ are given at 95% CL. The results are shown in Fig. 7.13 and Fig. 7.14. In the case of the gluons, the obtained 95% CL limit for Higgs decay only into gluons is 111.0 GeV/c^2 (109.2 GeV/c^2 expected). The analyses are obviously more sensitive to a gluonic decay than to an decay into s-quarks, as one would expect from the expected sensitivity in Fig. 7.10. Mainly the neutrino channel contributes to this effect. In Fig. 7.13b additionally the expectation for a Standard Model Higgs boson decaying into gluons is shown. One clearly sees that in the mass region considered, one never would be sensitive to such a decay.

For the c-quarks, one obtains a mass limit of 110.6 GeV/c^2 (108.3 GeV/c^2 expected) at 95% CL. As one would expect, the limit is in between the two extremes (gg and $s\bar{s}$), but of course much closer to the decay into s-quarks. In fact, the differences in the observed limit are negligible. Like for the gluons, the expectation for a Standard Model Higgs boson decaying into c-quarks is shown in Fig. 7.14. Also here the sensitivity is not sufficient to be sensitive to such a process.

From time to time questions arise, whether one could combine these searches with the searches for the Standard Model Higgs boson, since the branching ratios of gluons and c-quarks combined can be up to 10% of the total branching ratio. However, including these two channels would trigger the question on how to deal with the overlap, because the selected events are not exclusively c or g or b events. Instead each event has a certain probability to belong to each of the three classes. Conservatively one would then decide to pick the channel, which has the best performance neglecting the two other channels. Since the b decay is the most powerful one this would lead to the starting point again.

Finally, one would also like to exclude a hadronically decaying Higgs bosons from 4 GeV/c^2 up to 115 GeV/c^2. However, it has been shown, that the signal

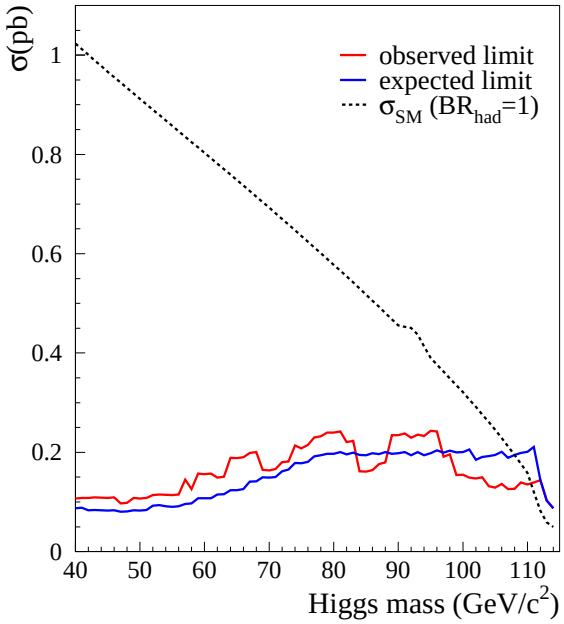

(a)

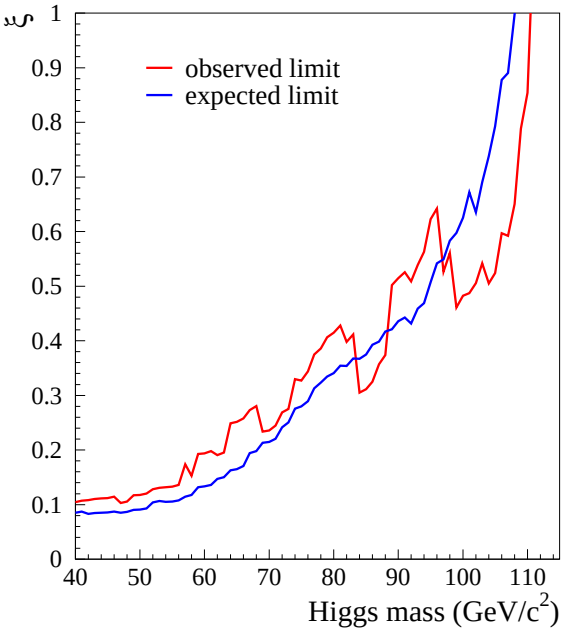

(b)

Figure 7.12: The excluded cross-section at 95% CL for the process $e^+e^- \rightarrow HZ \rightarrow (H \rightarrow \text{hadrons})(Z \rightarrow \text{anything})$ is shown in (a). The dotted line refers to Higgs boson with Standard Model production cross-section and decaying 100% hadronically. The excluded suppression factor ξ as defined in chapter 7.7.2 is shown in (b).

7.13

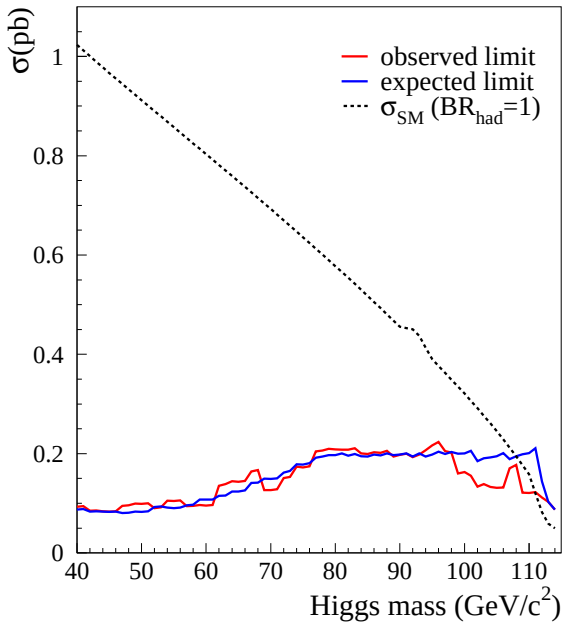

(a)

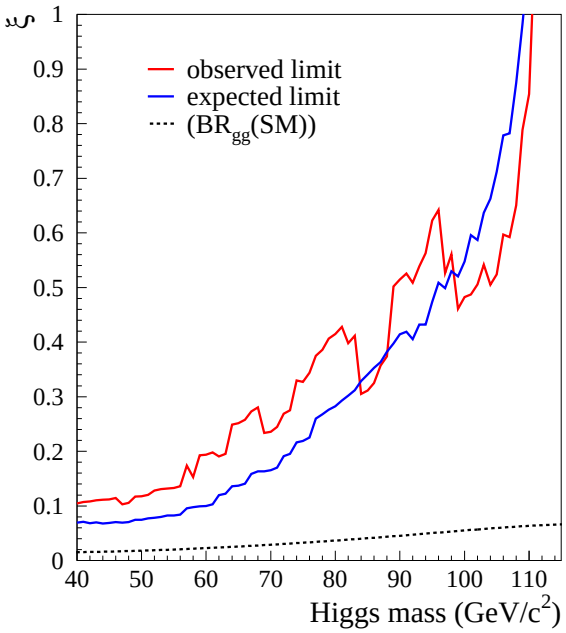

(b)

Figure 7.13: The excluded cross-section at 95% CL for the process $e^+e^- \rightarrow HZ \rightarrow (H \rightarrow gg)(Z \rightarrow \text{anything})$ is shown in (a). The dotted line refers to Higgs boson with Standard Model production cross-section and decaying 100% into gluons. The excluded suppression factor ξ as defined in chapter 7.7.2 is shown in (b).

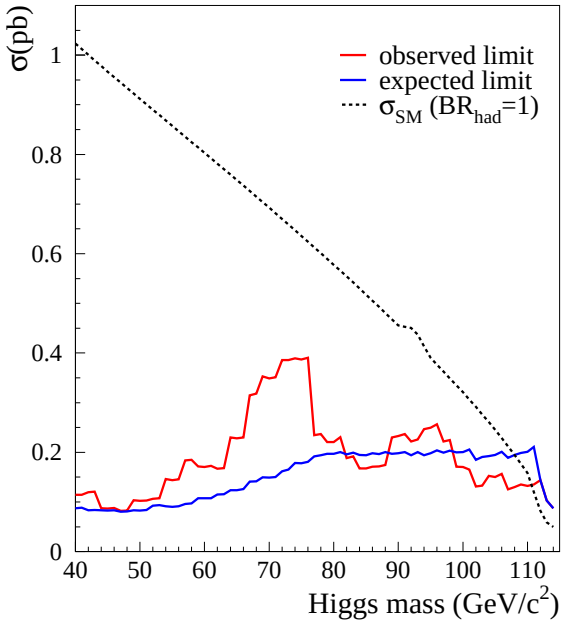

(a)

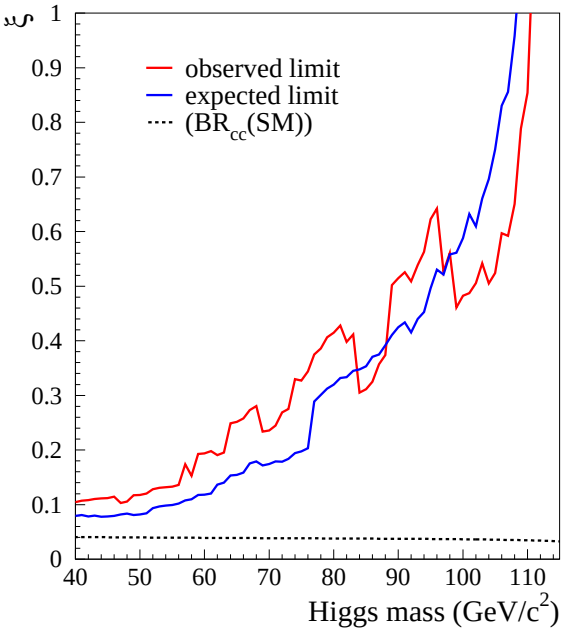

(b)

Figure 7.14: The excluded cross-section at 95% CL for the process $e^+e^- \rightarrow HZ \rightarrow (H \rightarrow c\bar{c})(Z \rightarrow \text{anything})$ is shown in (a). The dotted line refers to Higgs boson with Standard Model production cross-section and decaying 100% into charm quarks. The excluded suppression factor ξ as defined in chapter 7.7.2 is shown in (b).

efficiencies of the analyses used rapidly break down below 40 GeV/c^2, since such a low mass of the Higgs boson affects severely the event topology. The two jets from the Higgs decay become very collimated and form a mono-jet like structure. Two dedicated analyses were therefore performed in the neutrino and the four jet channel (now more a three jet channel) [DEL03b]. The results obtained were then combined with the results from the previous analyses. The excluded region concerning the suppression factor ξ is shown in Fig. 7.15 [DEL03b]. An excess of data at $m_H = 30$ GeV/c^2 is observed in both analyses below 40

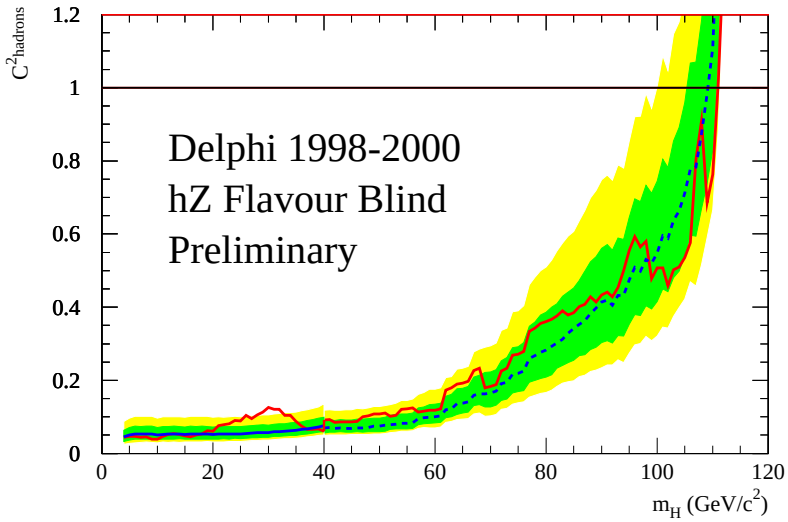

Figure 7.15: The excluded region for ξ (C^2) combining the analyses for $m_H \geq$ 40 GeV/c^2 and $m_H <$ 40 GeV/c^2. The one and two sigma bands are indicated as dark and light grey bands.

GeV/c^2. This excess is around 2.5 σ above the background expectation. It is believed to be a statistical fluctuation [DEL03b].

Chapter 8

Searches for bosonic Higgs decays

The search described in this section is quite different compared to the searches described before. This search is not a search for two jets and missing energy, but a search for six jets with a visible energy comparable to the centre-of-mass-energy. Such a signature originates from the decay of a Higgs boson in two W bosons, of which one is virtual and the accompanying Z is also decaying also hadronically (see Fig. 8.1). This decay can take place in the Standard Model, but for the Higgs masses accessible at LEP2, the branching ratio is small. A stronger motivation comes from the fermiophobic limit of the Type-I 2HDM models (see chapter 3.3.2), where decays into WW^* are dominant for Higgs masses above 90 GeV/c^2. It should be also pointed out, that the coupling HWW is much more fundamental to the understanding of the Higgs mechanism than the couplings to the fermions, since the mass generation of the massive gauge bosons is the main motivation for the Higgs mechanism. The final states

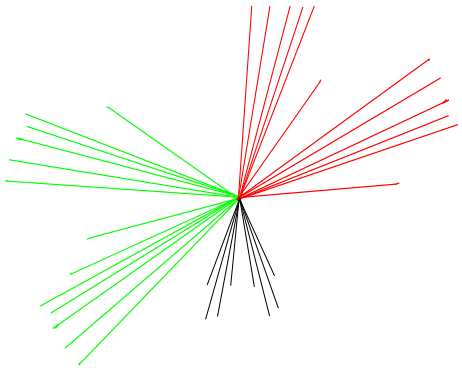

Figure 8.1: The topology searched for in the reaction $e^+e^- \rightarrow HZ$ $(H \rightarrow WW^* \rightarrow q\bar{q}'q\bar{q}')(Z \rightarrow q\bar{q})$.

$WW^* \rightarrow$	$Z \rightarrow$			
	$q\bar{q}$	$\nu\bar{\nu}$	l^+l^-	$\tau^+\tau^-$
$q\bar{q}'q\bar{q}'$	32.4%	9.9%	3.1%	1.5%
$q\bar{q}'l\nu_l$	19.9%	6.0%	1.9%	0.9%
$q\bar{q}'\tau\nu_\tau$	9.9%	3.0%	0.9%	0.5%
$l\nu_l l\nu_l$	3.0%	0.9%	0.3%	0.1%
$\tau\nu_\tau l\nu_l$	3.0%	0.9%	0.3%	0.1%
$\tau\nu_\tau\tau\nu_\tau$	0.8%	0.2%	0.1%	0.0%

Table 8.1: The branching ratios for the different final states of the process $HZ \rightarrow WW^*Z \rightarrow 6f$ assuming Standard Model branching ratios for the W. Note: l denotes electron and muon final states.

in this channel are much more complex due to the fact that the W bosons decay into fermions. All possible final states and their branching ratios are listed in Tab. 8.1. The $q\bar{q}'q\bar{q}'q\bar{q}$ channel thus represents about 32.2% of the possible final states. One can also clearly see, that although there are a lot of final states, four of them ($q\bar{q}'q\bar{q}'q\bar{q}$, $q\bar{q}'q\bar{q}'\nu\bar{\nu}$, $q\bar{q}'l\nu_l q\bar{q}$ and $q\bar{q}'l\nu_l\nu\bar{\nu}$) include about 81.2% of all possible final states.

The backgrounds in this search mainly originate from the clustering procedure. Since the events are clustered into 6 jets, one finds a small amount of fully hadronic WW or ZZ pairs, that are compatible with a 6 jet configuration. A second source of background originates from $q\bar{q}$ events with 4 or more jets, but this source of background is much smaller compared to the one before.

8.1 The data set

The data set used in this search is different from the one used in the previous searches, only the data from 195.5 GeV onwards was used. The data below was not used, because, as has been already mentioned, the branching ratio into WW^* only becomes dominant above 90 GeV/c^2 and the kinematical limit for 188.6 GeV centre-of-mass energy is around 98 GeV. Another important point is, that one would like to have also the jet originating from the W^* to have at least 15-20 GeV energy, so that the two jets from its decay are clearly separable from the other four jets. The interesting region for the search for $H \rightarrow WW^*$ starts at 100 GeV/c^2, where one has both a sizeable cross-section and a cleaner topology. Altogether about 412 pb^{-1} were analysed in the framework of the $H \rightarrow WW^*$ search.

The background MC set used corresponds to the one used in the previous searches for the corresponding centre-of-mass energies. For the signal samples, the following mass grid was chosen: 95.0, 100.0, 102.5, 105.0, 107.5, 110.0, 112.5, 115.0 and 120 GeV/c^2 with 5000 events each. The signal samples were generated using HZHA, which was slightly enhanced in order to specify the decay channels of the W bosons. The mass spectrum of the two W bosons

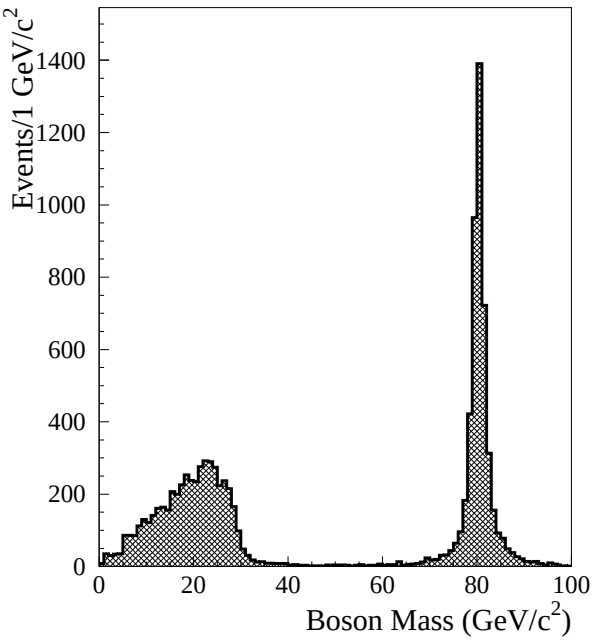

Figure 8.2: Generated mass spectrum of the $H \to WW^*$ decay using HZHA. Clearly visible is the real W at 80 GeV/c^2 and the virtual W boson around 20 GeV/c^2.

is shown in Fig. 8.2. A slight drawback is that HZHA only simulates decays into WW^*, but not into W^*W^*, but those decays are only important for a few models.

8.2 Jet clustering and constrained fits

The most important tool for this search was the clustering of events into jets. This has been done using the DURHAM algorithm (see chapter 5.2). Each event has been forced into four jets and six jets respectively. The jet four vectors obtained were used to do kinematical fits using the PUFIT [Kja91] package. Only basic features of the package will be described here, because is is described in detail in [Kja91]. A general approach for fitting multi-jet systems is the rescaling of the jet four-vectors. This is not optimal for many situations, because this method leaves the transverse momenta of the jets untouched. More desirable is a fit that can vary both jet directions and jet energies in order to obtain an optimal fit result. In the approach used in PUFIT, the χ^2 of the fitted four-vectors P is minimised using some general constraints $\vec{f}$. In PUFIT, the parameters of a jet are constrained to three, since it is assumed, that the mass scales with the energies. For an n-jet system one has $3n$ jet parameters,

which are put in a vector $\vec{y}$. The fitted parameters must then obey

$$\frac{\partial \chi^2}{\partial \vec{y}} = \vec{0} \text{ and } \vec{f}(\vec{y}) = \vec{0} \tag{8.1}$$

The χ^2 is assumed to be quadratic in the jet parameters:

$$\chi^2(\vec{y}) = (\vec{y} - \vec{y_0})^T V^{-1} (\vec{y} - \vec{y_0}) \tag{8.2}$$

with V being the error matrix and $\vec{y_0}$ being the vector containing the expectation values. The minimisation is then done in an iterative way [Kja91].

Up to now, it was assumed, that the errors are gaussian. In the usual jet parametrisation, the parameters $E_{Jet}, \theta_{Jet}, \phi_{Jet}$ tend to be non-gaussian. In PUFIT the problem is reformulated, since the jet momentum can be divided into a longitudinal and a transversal part. The skew in the energy distribution is handled by multiplying the longitudinal momentum with an exponential factor and the transverse momenta are assumed to be gaussian distributed around the measured four-vector. One picks two random vectors $\vec{p}_j^{\,b}$ and $\vec{p}_j^{\,c}$, which are orthogonal to each other and, together with the measured momentum of the jet, define a Cartesian coordinate system. The fitted momentum can be written as:

$$\vec{p}_j^{\,fitted} = e^{a_j} \vec{p}_j^{\,measured} + b_j \vec{p}_j^{\,b} + c_j \vec{p}_j^{\,c} \tag{8.3}$$

and the fitted energy is written as

$$E_j^{fitted} = E_j^{measured} \times \frac{|\vec{p}^{\,fitted}|}{|\vec{p}_j^{\,measured}|} \tag{8.4}$$

The parameters a, b, and c are obtained from Monte Carlo events where both the true[1] and the reconstructed jet four vectors are known. The expectation value $\vec{y_0}$ is also estimated from Monte Carlo events. The errors on the parameters used in V are taken to be uncorrelated. The parameters and their errors are not taken as fixed values, but are additionally evaluated depending on the polar angle of the jet, since the expected corrections in the forward region of the detector are expected to be larger than in the barrel region.

From this refitted jet four vectors, one can reconstruct the Higgs mass by paring the jets accordingly. In a 6 jet event originating from $HZ \to WW^*Z$, two jets are paired together, because they originate from the Z and the other four jets are paired together, because one assumes they originate from the WW^*.

The following constraint fits have been made in order to optimise the mass reconstruction:

4C : Calling PUFIT using the momentum (p_x, p_y and p_z) and energy conservation as the four constraints.

5C Z : Similar as the 4C fit, but additionally assigning one di-jet the mass of a Z boson.

[1] Obtained from Monte Carlo

Fit	4 Jets	6 jets
4C	1	1
5C Z	6	15
6C Z+W	not done	90
6C WW	3	not done
6C ZZ	3	note done

Table 8.2: The number of possible pairing for the different fits.

6C Z+W : Adding a 6th constraint, a second di-jet pair has the mass of a W boson.

6C WW : Done only for four jets, the first and the second di-jet pair have the mass of a W. This was done to test the event for WW pair compatibility.

6C ZZ : Done only for four jets, the first and the second di-jet pair have the mass of a Z. This was done to test the event for ZZ pair compatibility.

The problem of the fitting is the large amount of possible jet pairings one has to consider in order to constrain the Higgs mass. The number of possibilities is listed in Tab. 8.2. The difficulty is to select the right pairing in order to calculate the mass. This was done by taking the pairing which has the best χ^2-fit result. This method was tested on signal MC, whether it is able to reconstruct a given mass. The results are shown in Fig. 8.3a+b. The last two fits 6C WW/ZZ are used to suppress possible background by testing the multi jet event on its compatibility of being either a fully hadronic WW or ZZ pair. The result of this test is shown in Fig. 8.3c+d. Clearly visible is that both fits reconstruct the mass peak very well, however, in Fig. 8.3c one can also clearly see, that the method fails in the case of semileptonic decays, as expected.

8.3 Preselection

The preselection consists of three steps in order to preselect only multi-jet events:

- Data quality veto as described in chapter 6.3.1.
- General multi-jet selection.
- Six jet selection.

8.3.1 General multi-jet selection

This selection was used to enrich multi-jet events in the sample. It was required that the event had at least 20 charged tracks, that the amount of visible energy was at least 60% of centre-of-mass energy and the $\log(y_{34})$ be greater than -5.0.

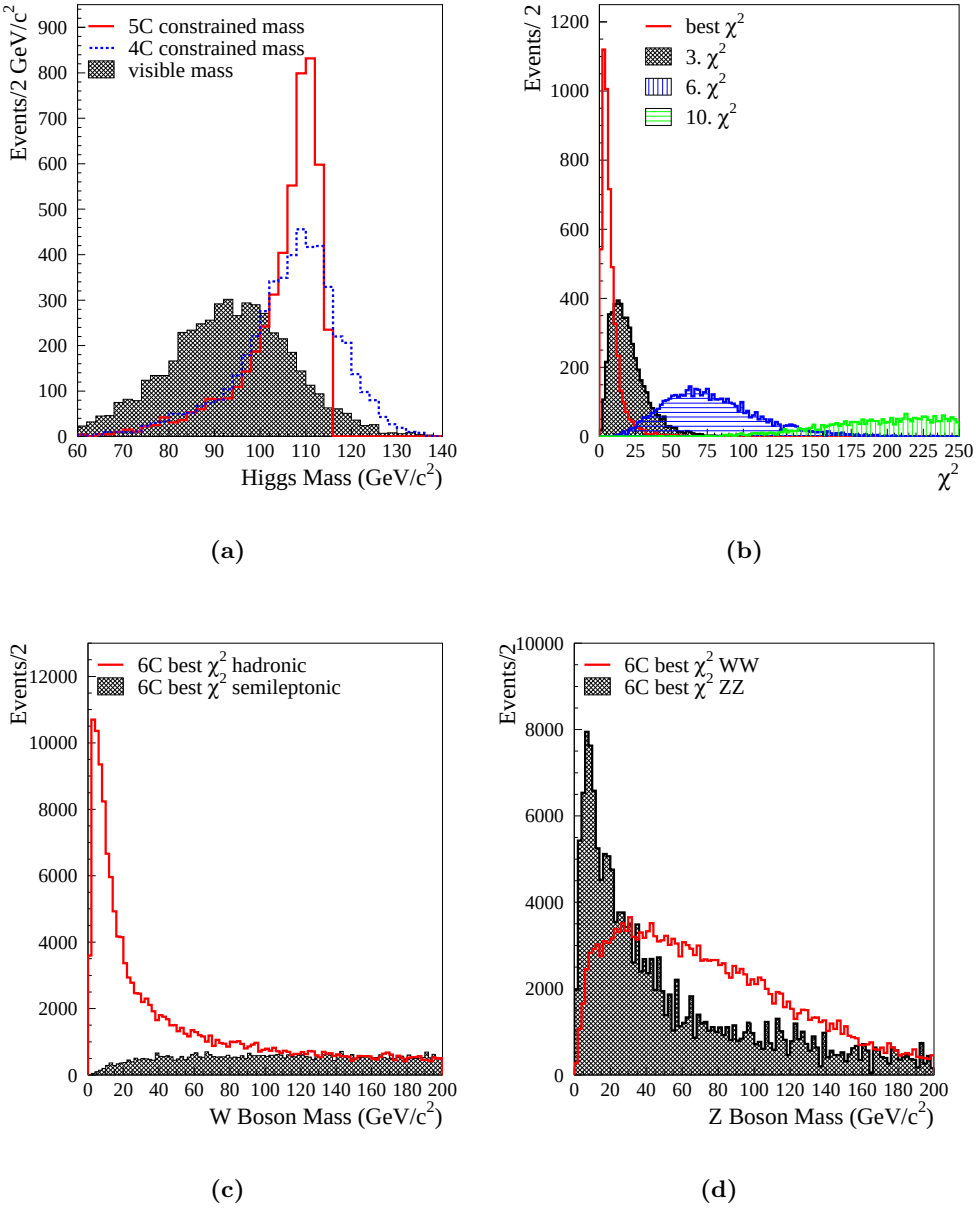

Figure 8.3: Mass reconstruction using PUFIT. First, the reconstructed mass for a Higgs boson of 110 GeV/c^2 mass decaying into WW^* using the paring with the best χ^2 is shown in (a). Plotted are the raw visible mass, the visible mass after a 4C fit and the visible mass after the 5C fit. In (b) four of the 15 χ^2 values for the 5C fit with 6 jets are shown. Second, the reconstructed masses of W and Z pairs after a 6C fit with 4 jets are shown. Plotted in (c) is the best χ^2 for the $WW \rightarrow 4$ jets hypothesis , both for the fully hadronic and semileptonic decays after a 6 C fit assuming the W mass for the two di-jet pairs. In (d), the same is shown for fully hadronic Z and W bosons after a 6 C fit assuming the Z mass for the two di-jet pairs.

$\sqrt{s}$	Fully hadronic selection		Six jet selection	
(GeV)	Data	MC	Data	MC
195.5	789	722.2±2.0	366	310.3±1.3
199.5	803	788.8±2.1	340	335.0±1.4
201.6	385	377.2±1.0	180	159.6±0.7
205.0	716	683.1±1.9	320	289.4±1.2
206.5	743	760.2±2.0	333	321.0±1.3
206.5U	472	508.7±1.4	217	216.3±0.9

Table 8.3: The agreement of data and Monte Carlo for the two preselection steps. The listed errors are from Monte Carlo statistics only. The last line (206.5U) refers to the data taken with one TPC sector inoperative, which has been fully taken into account in the event simulations.

Furthermore the $\sqrt{s'}$ was required to be higher than 0.85 $\sqrt{s}$, the event thrust to be less or equal than 0.92, the amount of charged energy to be greater than 0.5 $\sqrt{s}$ and the event to have at least two tracks with transverse momentum greater than 2 GeV/c and impact parameters less than 1 mm in the transverse plane and less than 3 mm along the beam axis. This cuts away all $\gamma\gamma$ events and most of the $q\bar{q}\gamma$ events. Also a large amount of the non fully hadronic four-fermion events like $W^+W^- \rightarrow q\bar{q}'l\bar{\nu}_l$ or $ZZ \rightarrow q\bar{q}\nu\bar{\nu}$ were eliminated by this cut.

8.3.2 Six jet selection

This selection was used to select events that have a six jet-like topology, which is close to the expected signal. The $\log(y_{56})$ was required to be larger than -7.5, the number of charged tracks in a jet in the six jet configuration had to be larger than 4 and the two combination of the Fox-Wolfram momenta $H_{30} - H_{10}$ and $H_{20}+H_{40}$, had to be less or equal than 0.25 and 0.9 respectively. Furthermore, it was required, after forcing the jet in a six jet configuration using the DURHAM algorithm, the jet with the highest charged multiplicity has at least 5 charged tracks and the jet mass of the lightest jet is at least 0.2 GeV/c^2. At the end of this selection, the signal efficiency was still at about 70-75% depending on the signal mass and the background was again reduced by a factor 3. The agreement of data and Monte Carlo simulation is shown in Tab. 8.3.

8.4 Neural network selection

The NeuroBayes neural network (see chapter 5.5.1) has been used in order to separate between signal and background events. The training has been done using the following variables:

- The $\log(y_{34})$ of the DURHAM jet clustering algorithm.

- The sum of the two Fox-Wolfram moments H_{20} and H_{40}.
- The $\sqrt{s'}$ as the energy after the radiation of the first photon (see chapter 6.2).
- The difference of the two Fox-Wolfram moments H_{30} and H_{10}.
- The event thrust as defined in chapter 57.
- The $\log(y_{56})$ of the DURHAM jet clustering algorithm.
- The best χ^2 for the 4 jet WW pair hypothesis (6C WW).
- The smallest angle between two jets in the six jet configuration.
- The best mass for the $HZ \to WW^*Z$ hypothesis forcing the event into 6 jets and assuming one jet pair is compatible with the Z mass (5CZ).
- $\min(\chi^2_{5C6J}) - \chi^2_{4C}$ The lowest χ^2 for the 5CZ fit in the six jet configuration subtracted by the χ^2 of the 4C6 fit.
- The smallest jet mass of a jet in the six jet configuration.

The network was only trained with the 4f-CC and the 2f-$q\bar{q}$ samples for the background and for signal masses between 107.5 and 112.5 GeV/c^2. In order to be statistically independent, the complete MC samples was split into two parts, one part was used to train the network, the other part was then used to derive the background and the signal efficiencies. The separation power of the neural network is shown in Fig. 8.4 and the efficiency curves are shown for two selected energies in Fig. 8.5. The final cut on the neural network was done cutting at 40% signal efficiency for a 105 GeV/c^2 Higgs boson decaying exclusively in WW^*, in order to get rid of almost all of the 4f-NC backgrounds.

8.5 Systematic errors

The systematic errors in this channel are quite different compared to the channels evaluated previously. The impact of the description of events with a large amount of missing energy is not vital for multi-jet events, since the energy of the event is expected to be fully visible. The following sources of systematic errors have been evaluated.

- Choice of the fragmentation model.
- Differences from the neural network input variable distributions.
- Error on the luminosity.
- Error on the electroweak hadronic cross-sections.

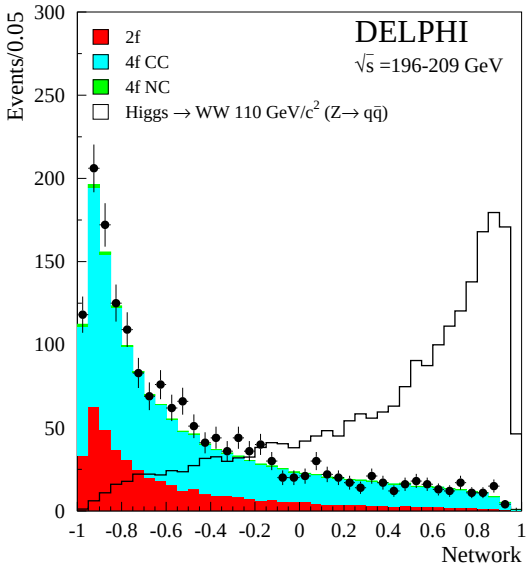

Figure 8.4: The combined neural network output from 195.5 GeV to 208 GeV. Shown are the contributions from the Standard Model background and a signal of 110 GeV at an arbitrary scale. The separation power of the network is clearly visible.

As the analysis focuses on the search for multi-jet events, the description of this kind of events in Monte Carlo simulation is essential. It has been shown previously [Reh00], that the description of multi-jet events is quite different between ARIADNE 4.1 [Lon92] and PYTHIA 6.156 [Sjö01] due to different fragmentation models for the hadronisation. In order to estimate the impact of the choice of the fragmentation model, the analysis has been applied on 2f-$q\bar{q}$ and 4f-CC samples, that used ARIADNE to do the hadronisation. The impact on the final selection was below 1% ($\pm$0.7%) for the 4f-CC background for the two years of data taking. The impact on the 2f-$q\bar{q}$ background is much larger, it is $\pm$6.4% for $\sqrt{s}$=195.5-201.6 GeV and $\pm$4.6% for 2000 data. The comparison of the different models after the general multi-jet selection is shown in Fig. 8.6. Due to limited statistics, and since there is no clear trend that one model is preferred, the difference between the models has been taken as systematic error. Especially for multi-jet QCD final states it is known that the theoretical treatment is challenging and still ongoing [Bal02]. A reliable description in Monte Carlo simulation is therefore still not available.

A second source of systematics was estimated by smearing the background distributions. This was done by taking the differences in the mean values between data and background after the preselection, where the effect of a possible signal would be still very small, and shifting the background by this difference and additionally smearing it by adding a Gauss distributed random number with mean 0 and the mean difference as its width (a similar approach has been

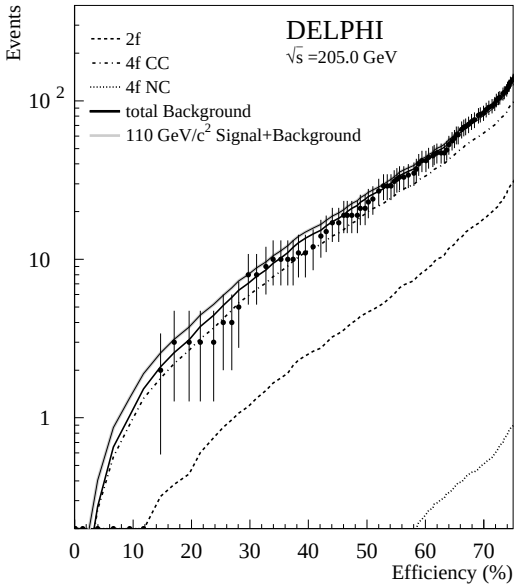

(a)

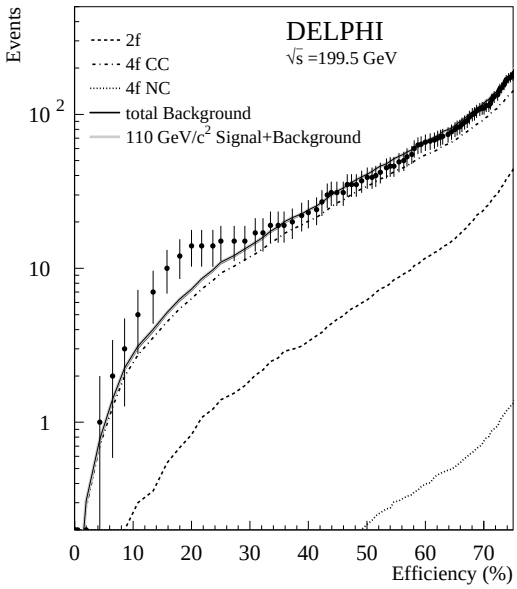

(b)

Figure 8.5: Data and expected background for the energy as a function of the efficiency for a Higgs signal of 110 GeV/c^2 Higgs at 205.0 GeV (a) and 199.5 GeV (b). The indicated lines show number of events from the most important background reactions and the solid black line shows the sum of all the background processes. In addition the grey line shows the expectation for a 105 GeV/c^2 Higgs signal added on top of the background. The vertical dashed lines indicate the final cut on the neural network chosen to maximise the sensitivity.

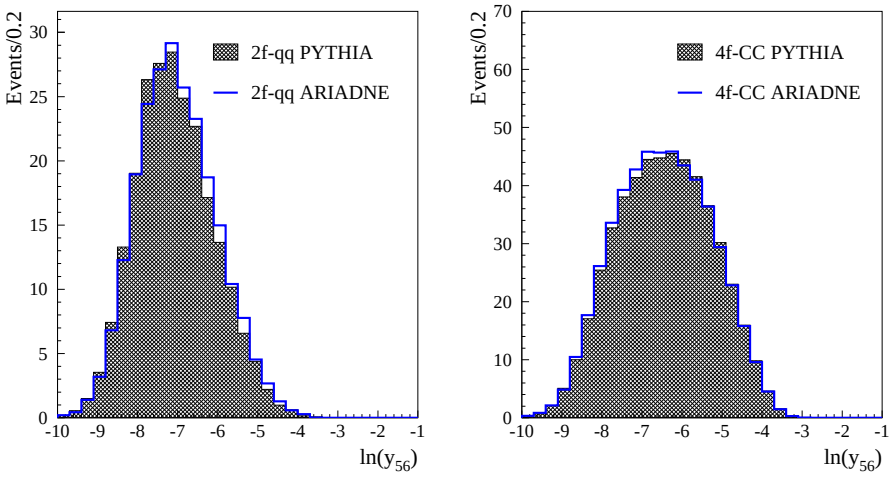

(a) **(b)**

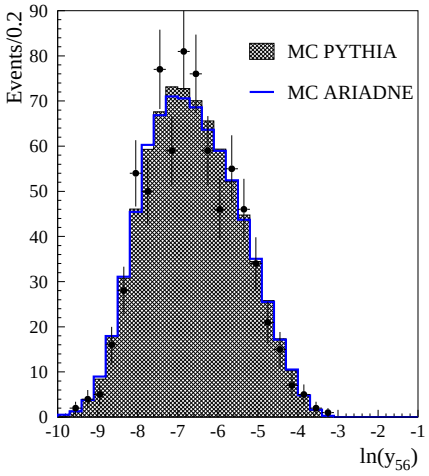

(c)

Figure 8.6: The impact of the fragmentation model (PYTHIA vs. ARIADNE) after the general multi-jet selection for the 2f-$q\bar{q}$ in (a) and 4f-CC (b). Shown are the distributions of the $\ln(y_{56})$ variable. The agreement of both models with the data at $\sqrt{s}$=206.5 GeV is show in (c).

$\sqrt{s}$ (GeV)	Data	MC total	2f-$q\bar{q}$	4f-CC	4f-NC	ϵ_{Higgs}
195.5	28	23.8±2.3	10.2	89.5	0.4	40.0±2.1
199.5	23	23.7±2.3	14.1	85.5	0.4	39.9±2.1
201.6	21	12.5±1.2	17.7	81.9	0.4	40.6±2.1
205.0	19	21.9±1.7	19.1	80.5	0.4	39.9±2.0
206.5	25	26.9±2.1	14.4	82.1	0.5	40.1±2.0
206.5U	23	21.7±1.7	20.3	79.3	0.4	40.2±2.0

Table 8.4: Number of events after the final selection for data and expected SM background. The contribution of the three main background classes are given in percent of the total background. Also given is the signal efficiency for a 105 GeV/c^2 Higgs boson.

used in chapter 7.6). This was done for each single simulated background event. In order to be less affected by statistical fluctuations, the smearing has been repeated with different random seeds and the effect has been averaged for the different centre-of-mass energies for one year of data taking. The effect on the background is ±7.1% for 1999 and ±6.1% for 2000 data. The effect on the signal efficiency was much smaller, it affects the signal efficiency by ±2%. Other sources of systematic errors were the errors on luminosity and the hadronic cross-sections. The error on the luminosity was assumed to be 0.5%. The error on hadronic cross-sections for 2f-$q\bar{q}$ and 4f-CC was estimated to be ±2%. The impact on the total background is negligible for 2f-$q\bar{q}$ (±0.2%), since the 2f-$q\bar{q}$ background is only a small part of the total background. The error from the 4f-CC background uncertainty is ±1.8%, since this is also the dominant background source.

The total systematic error combined with the error from Monte Carlo statistics is shown in Tab. 8.4.

8.6 Results

The number of selected events after the final cut on the neural network output is shown in Tab. 8.4. The mass distribution of the selected candidates is shown in Fig. 8.7 and the Higgs signal efficiencies depending on the Higgs mass are shown in Fig. 8.8. As input distribution of the ALRMC method, the output of the neural network (see Fig. 8.4) has been chosen in this channel.

Although this channel is the most important one with respect to the branching ratio, it is obvious that the combination with other channels can significantly increase the sensitivity for a possible signal. In DELPHI two other searches for $HZ \rightarrow WW^*Z$ have been conducted, looking in the decay channels $q\bar{q}'l\nu_l q\bar{q}$ [Reh03] and $q\bar{q}'q\bar{q}'\nu\bar{\nu}$ [Dal03]. The results of these two searches have then been combined with the search in this thesis.

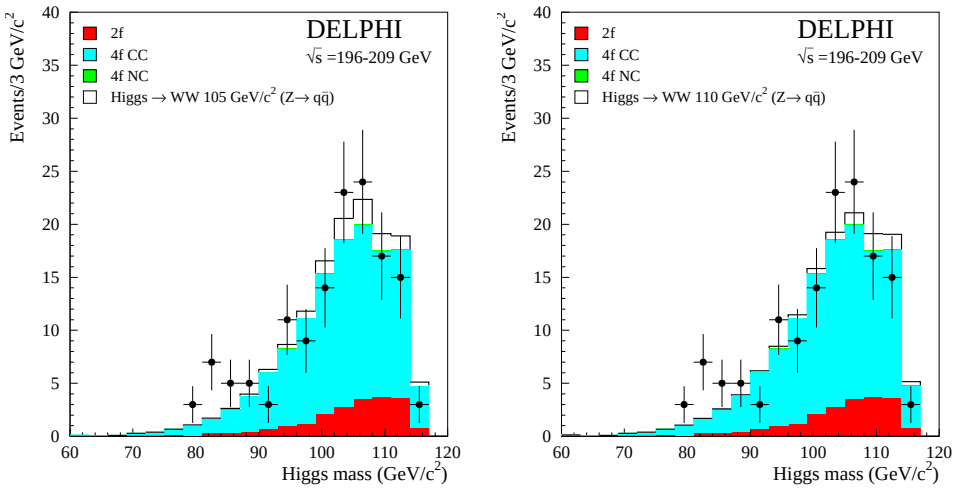

(a) **(b)**

Figure 8.7: The reconstructed mass distribution for the search $HZ \rightarrow WW^*Z \rightarrow 6q$. A 5C fit with six jets was used in order to reconstruct the mass. Two different reconstructed Higgs masses are shown: 105 GeV/c^2 (a) and 110 GeV/c^2 (b).

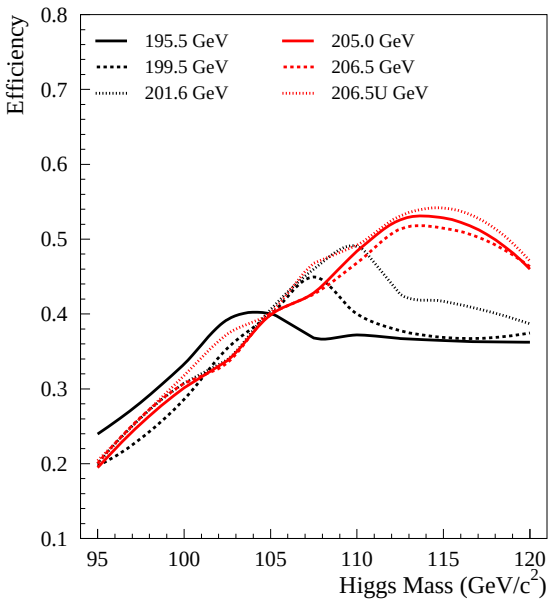

Figure 8.8: The efficiencies for $HZ \rightarrow WW^*Z \rightarrow 6q$ depending on the Higgs mass and the centre-of-mass energy. Clearly visible is the influence of the kinematic limit on the signal efficiency.

8.6.1 Mass limit

A mass limit was derived assuming a branching ratio of 100% in WW and a SM production cross-section. No observed limit was obtained and the expected limit is 101.7 GeV/c^2. The CL_S depending on the Higgs mass is shown in Fig. 8.9, the cut a $CL_S = 5\%$ is indicated by the horizontal black line. This lack

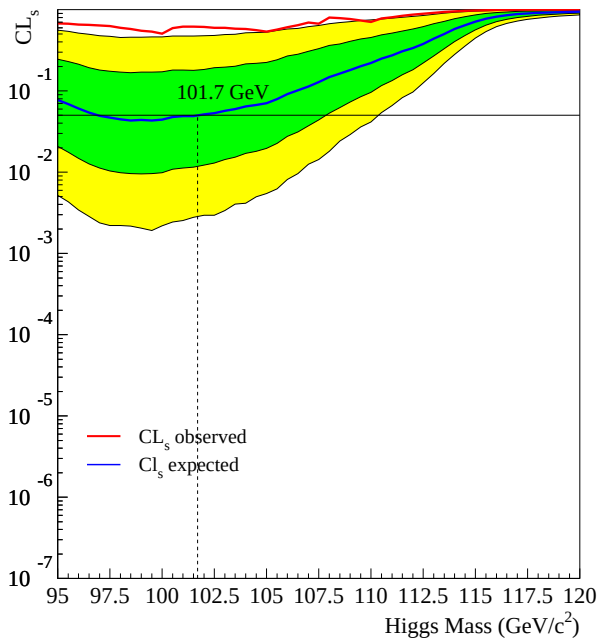

Figure 8.9: The expected and observed CL_S for $e^+e^- \to HZ\,(H \to WW^* \to q\bar{q}q\bar{q}, q\bar{q}l\nu)\,(Z \to q\bar{q}, \nu\bar{\nu})$ as a function of the Higgs boson mass. The dark and light bands indicate the one and two sigma bands. The cut at CL_S=0.05 is indicated by the horizontal black line.

of an observed limit is due to an excess in the data. To locate the origin of the excess, the compatibility with the *background only* hypothesis was plotted for all four[2] channels separately (see Fig. 8.10). The excess is mainly located in the channel $q\bar{q}'l\nu_l q\bar{q}$, where the lepton originates from the on-shell W. The excess is also mainly driven by two highly significant candidates. Since the mass resolution of the channel is rather poor due to the escaping neutrino, the excess is rather widespread over the whole mass range [Reh03]. To confirm that the excess is really caused by the on-shell lepton channel, one can additionally compare the CL_B for all channels with the CL_B with all but the on-shell lepton channel. The result is shown in Fig. 8.11. It is clearly visible that the excess in the CL_B is driven by the on-shell lepton channel. Two comments about the $q\bar{q}q\bar{q}\nu\bar{\nu}$ and the $q\bar{q}q\bar{q}q\bar{q}$ channels. The first one shows an almost 2 σ deviation for masses below 100 GeV/c^2, but then shows no significant deviations anymore.

[2]The $q\bar{q}'l\nu_l q\bar{q}$ channel has been divided into two channels, depending whether the lepton originates from the on-shell or off-shell W

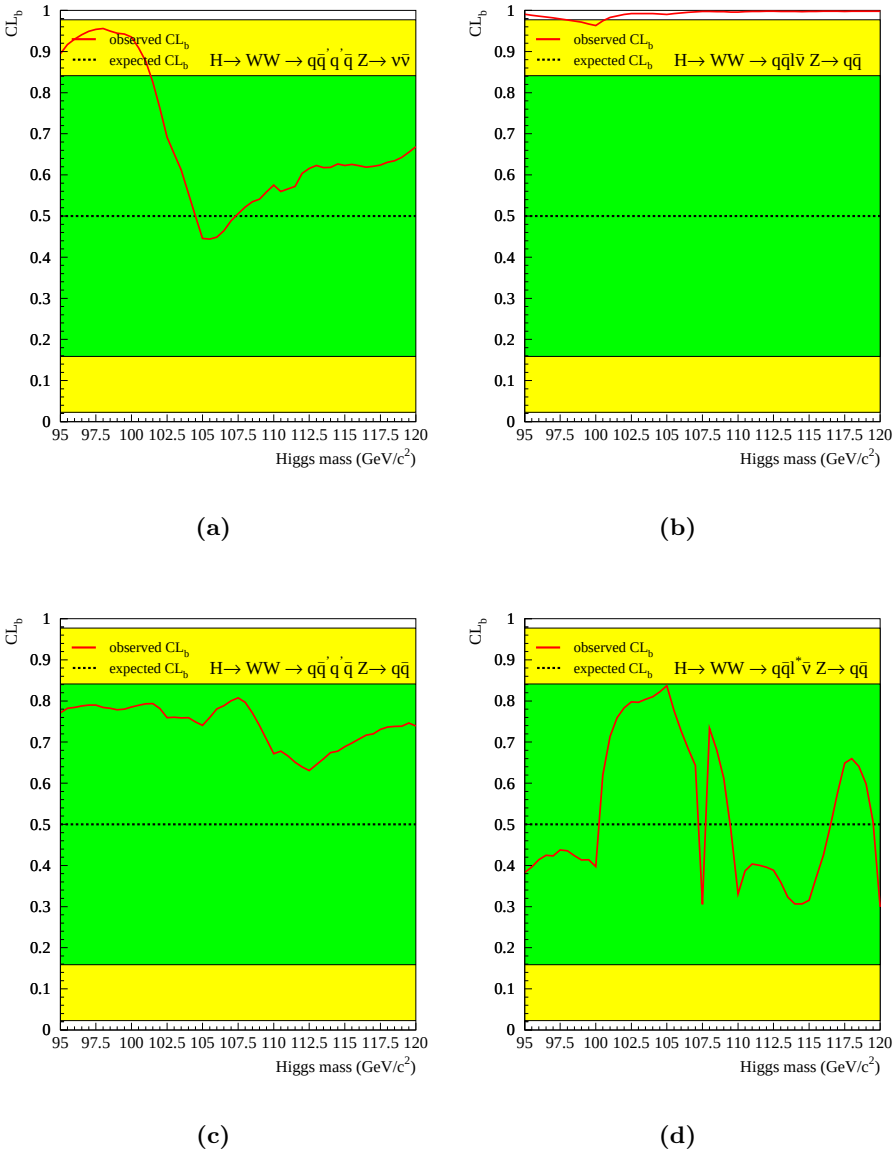

Figure 8.10: The observed CL_B for $e^+e^- \to HZ\,(H \to WW^*)(Z \to anything$ as a function of the Higgs boson mass. Shown are $q\bar{q}q\bar{q}\nu\bar{\nu}$ (a), $q\bar{q}'l\nu_l q\bar{q}$ (lepton on-shell) (b) $q\bar{q}q\bar{q}q\bar{q}$ (c) $q\bar{q}'l\nu_l q\bar{q}$ (lepton off-shell) (d). The dark and light bands indicate the one and two sigma bands.

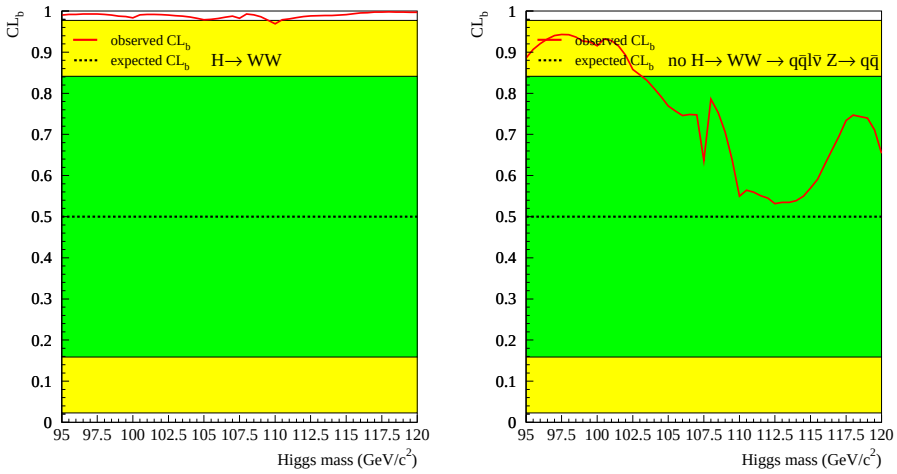

(a) **(b)**

Figure 8.11: The observed CL_B with all channels included (a) and with all but the on-shell lepton channel (b). The dark and light bands indicate the one and two sigma bands.

The second is always slightly higher than the expected CL_B, which can be understood to the underestimation of six-jet final states in the background Monte-Carlo simulation.

To understand why the on-shell lepton channel has such a large impact, it is useful to look not only at the branching ratios, but also at expected sensitivities. As can be clearly seen in Fig. 8.12, this channel is either the most or the second most sensitive one for the whole mass range, although its branching ratio is only a third compared to the 6 quark channel. So in fact the presence of highly significant candidates can certainly affect the observed limit. Probably, the observed limit would below the 95 GeV/c^2 mass bound, where one has no signal Monte-Carlo and the sensitivity of the analyses would be rather poor. This is also visible in Fig. 8.9, where the CL_S goes up again towards 95 GeV/c^2, indicating, that there sensitivity breaks down.

The interpretation of this excess as a possible signal is however disfavoured due to lack of highly significant candidates in the other channels.

8.6.2 The influence of six-fermion production

A possible explanation for the excess in the $q\bar{q}'l\nu_l q\bar{q}$ (lepton on-shell) channel can be found in the production of electroweak six-fermion final states, which would have a similar signature. Two of the Feynman graphs contributing to the six-fermion final states are shown in Fig. 8.13. The cross-section for this class of processes is small, however given the large data sample at high energies, it could

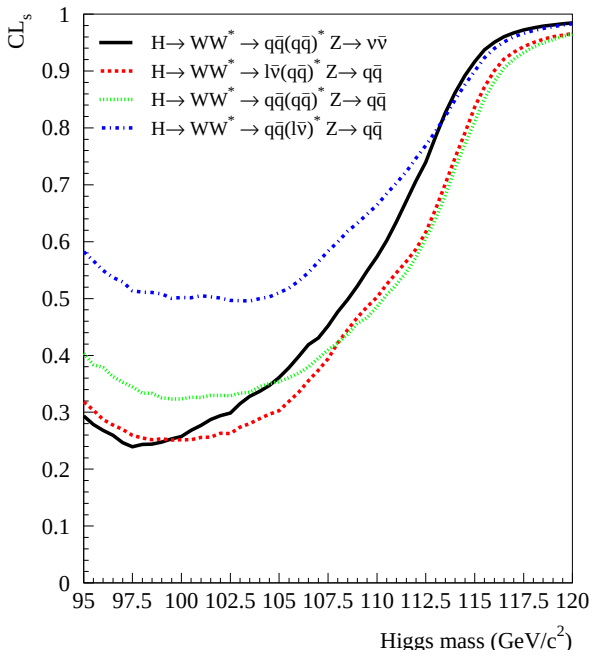

Figure 8.12: The expected CL_S for the four different channels in the $H \rightarrow WW^*$ search.

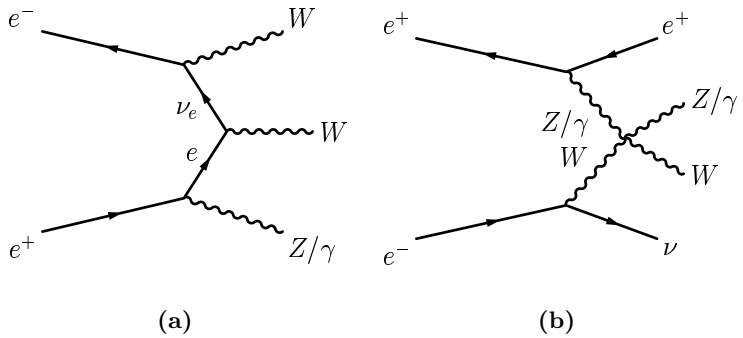

Figure 8.13: Two Feynman graphs contributing to electroweak six-fermion production at LEP: The three boson production (a) and the vector boson scattering (b).

$\sqrt{s}$	$q\bar{q}q\bar{q}q\bar{q}$		$q\bar{q}'l\nu_l q\bar{q}$		$q\bar{q}q\bar{q}\nu\bar{\nu}$	
(GeV)	σ (fb)	Events	σ (fb)	Events	σ (fb)	Events
205.0	0.47	0.04	54.55	4.05	0.74	0.06
206.7	0.50	0.07	54.83	7.72	0.73	0.10

Table 8.5: Expected events from six-fermion production at $\sqrt{s}$=205 and 206.7 GeV (using the DELPHI luminosities at these energies) from the three different topologies.

still have a sizeable contribution to the background. No six-fermion generator was available at LEP, but there exists the new LUSIFER [Dit02] six-fermion generator mainly intended for linear colliders. This generator has been used to calculate the cross-section for the interesting final states $q\bar{q}q\bar{q}q\bar{q}$, $q\bar{q}'l\nu_l q\bar{q}$ and $q\bar{q}q\bar{q}\nu\bar{\nu}$ at LEP2 energies. The results obtained are shown in Tab. 8.5.

It can be seen that the contributions are quite different in size, which is due to the fact that not for all the final states all diagrammes are possible. For the final states $q\bar{q}q\bar{q}q\bar{q}$ and $q\bar{q}q\bar{q}\nu\bar{\nu}$ the expected background contribution is marginal and will certainly not affect the total background rate. However, for the $q\bar{q}'l\nu_l q\bar{q}$ final states, the effect is larger and can affect the total background rate. More details about this issue can be found in [Reh03]. For the $q\bar{q}q\bar{q}q\bar{q}$ final state, however no QCD corrections have been taken into account, so that this cross-section is not as precisely known as the cross-sections four the final states with only four quarks. Technically the calculation of the cross-section is challenging, as for e.g. $q\bar{q}'l\nu_l q\bar{q}$ final about 5000 diagrammes have to be taken into account. So the calculation of one final state at one centre-of-mass energy can easily take 24 to 48 hours.

8.6.3 Cross-section limit

For a more general exclusion of a possible $H \to WW^*$ signal, a limit on the cross-section for the process $e^+e^- \to HZ\,(H \to WW^*)\,(Z \to \text{anything})$ is calculated (see Fig. 8.14). This result can be easily used to exclude extended models, which include decays in WW, but have non-SM production cross-section. The excess observed before is also visible here, which leads to the fact that only models with an enlarged cross-section compared to the Standard Model can be experimentally excluded here.

Like for the searches for invisible Higgs bosons, this result can be rephrased as a suppression factor ξ with respect to the SM:

$$\xi = \frac{\sigma_{excluded}}{\sigma_{SM}(e^+e^- \to HZ)}$$

The excluded range for ξ is shown in Fig. 8.15. The factor ξ can also be interpreted as the branching ratio of the Higgs into the WW^* final state. Since the decay in a W pair is also a SM process, the expected curve for the SM

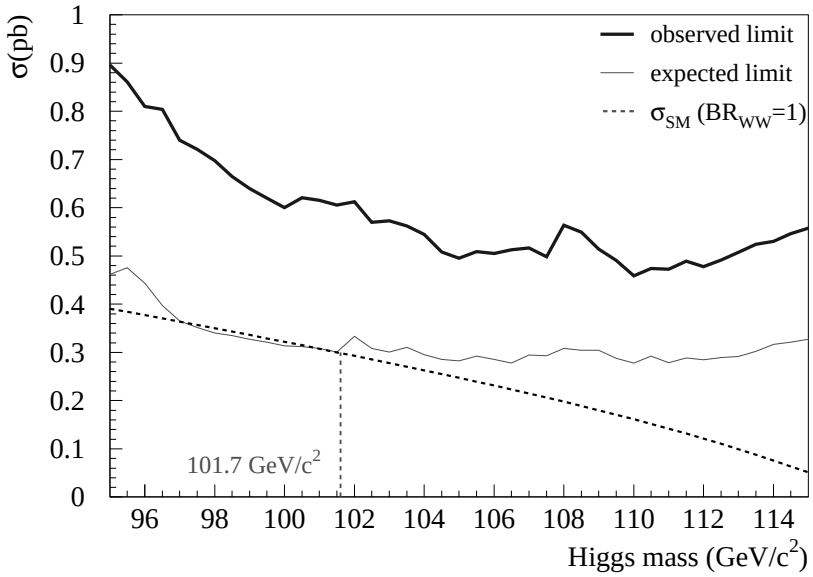

Figure 8.14: The 95% CL upper limit on the cross-section $e^+e^- \to HZ\,(H \to WW^*)\,(Z \to \text{anything})$ as a function of the Higgs boson mass. The dashed line shows the Standard Model cross-section for the Higgs boson production with $BR_{\mathrm{WW}^*} = 1$.

process is also indicated in this plot. Additionally also the expectation for a fermiophobic scenario (see chapter 3.3.2) is shown.

One can clearly see that this analysis is at the moment not sensitive to fermiophobic scenarios. To be sensitive to a Standard Model decay into WW^*, the sensitivity of the analysis has to improve by an order of magnitude, so one can safely say, that the search for such decays in the framework of the Standard Model is not possible at LEP. To exclude fermiophobic models, one could combine the searches here with the results obtained from the searches for $H \to \gamma\gamma$ at DELPHI [DEL01], which will be done in the framework of an overall fermiophobic combination.

8.6.4 Outlook

It has been shown, that searching for $H \to WW^*$ final states is in fact possible at LEP, but the sensitivity to this final state is limited. In order to have a higher coverage, one has to improve either the sensitivity of the analyses or include more channels. An improvement of sensitivity is expected from a re-analysis in the $q\bar{q}q\bar{q}\nu\bar{\nu}$ channel [Dal03]. Including more channels may prove difficult, since the present searches have focused already on the most significant channels. Other possible channels may only slightly improve the sensitivity. Another question is, how to treat the possible overlap between more and more channels.

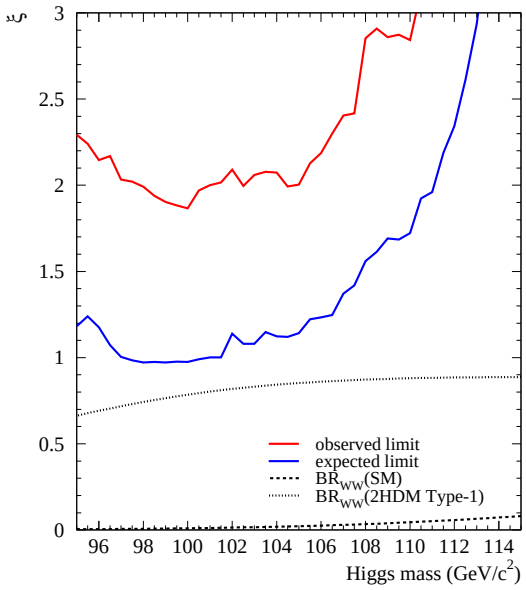

Figure 8.15: The 95% CL upper limit on the ξ factor in $e^+e^- \to HZ\,(H \to WW^*)\,(Z \to \text{anything})$ as a function of the Higgs boson mass. Additionally shown are the expectations in the SM and in a fermiophobic scenario for this process. The region above the line for the observed limit is excluded.

Thus would require detailed studies in order to really quantify this effect. The next question coming more from theoretical aspects is, if the modelling of this class of final states will be improved and will lead to a better understanding. At the moment, these searches take a look at almost unknown topologies.

Chapter 9

Conclusion

Searches for invisible, hadronic and bosonic Higgs decays have been conducted with the data recorded by the DELPHI detector between 1998 and 2000. The searches for hadronic and bosonic Higgs decays were conducted for the first time within the DELPHI collaboration, while the search for invisible final states is an continuation of previous searches [Vol99]. Since Higgs boson production in e^+e^- is a very tiny process compared to the background by Standard Model processes, very efficient statistical methods were used in order to separate a possible signal from the overwhelming background. No evidence for Higgs production was found. In order to calculate exclusion limits both on the mass of the Higgs boson and on its production cross-section, a modified frequentist likelihood ratio approach was used. This method is superior to the so-called event-counting method, since it also takes into account the distributions of the selected events.

For the invisible decay mode exclusion limits were set on a Higgs bosons decaying 100% into invisible final states. Additionally, the results were combined with the results from searches for a Standard Model Higgs boson performed within DELPHI, which allowed to set an exclusion limit on Higgs production independent of the branching ratio. Finally, a limit on the cross-section $e^+e^- \to HZ\,(H \to \text{invisible})(Z \to \text{anything})$ was calculated. The mass limits are summarised in Tab. 9.1.

Channel	95% CL limits (in GeV/c^2)	
	observed	expected
$H \to$ invisible	112.0	110.5
$H \to$ invisible+visible	111.8	109.3
$H \to$ hadrons	110.6	108.0
$H \to c\bar{c}$	110.6	108.3
$H \to gg$	111.0	109.2
$H \to WW$	-	101.7

Table 9.1: Overview of the excluded Higgs boson masses.

Also for the hadronic decay mode a mass limit was calculated. Additionally

also mass limits were set assuming different decay modes like $c\bar{c}$, $s\bar{s}$ or gg. Finally limits on the cross-sections $e^+e^- \to HZ\,(H \to \text{hadrons}, c\bar{c}, gg)(Z \to \text{anything})$ were calculated for all theses cases. The mass limits obtained are also summarised in Tab. 9.1.

For the bosonic decay of a Higgs in a pair of W bosons, again a mass limit was calculated assuming a branching ratio of 100% in W boson pairs (see Tab. 9.1). Due to an excess of signal-like events in the data, no observed limit was obtained. The excess originates dominantly from the $q\bar{q}'l\nu_l q\bar{q}$ channel [Reh03] and is most likely due to electroweak six-fermion production. As a last step, also an excluded cross-section for the process $e^+e^- \to HZ\,(H \to WW^*)(Z \to \text{anything})$ was calculated.

These results can be used to severely constrain the existence of new physics in form of models with extended Higgs sectors that include such decay modes for the Higgs bosons.

If the Higgs exists and it behaves like the Standard Model Higgs, it is likely to be found at the LHC[1], but if the Higgs does behave differently and the decay modes that have been examined in the framework of this thesis, become dominant, LHC may have difficulties to find the Higgs in some of these channels. After the Higgs boson discovery, it will be very important to measure its properties like its spin, its mass and its branching ratios. This will be however the task of a linear e^+e^- collider like TESLA[2].

[1] **L**arge **H**adron **C**ollider
[2] **T**era Electron Volt **E**nergy **S**uperconducting **L**inear **A**ccelerator

Bibliography

[Acc02] E. Accomando, A. Ballestrero and E. Maina. *WPHACT 2.0: A fully massive Monte Carlo generator for four fermion physics at e^+e^- colliders*. 2002. Hep-ph/0204052. 49

[Ada00] W. Adam, 2000. Private communication. 57

[Alv99] S. J. Alvsvaag et al. *The small angle tile calorimeter in the DELPHI experiment*. Nucl. Instrum. Meth., A425, 106, 1999. 4.2.2, 4.2.2

[Ama91] U. Amaldi, W. de Boer and H. Fürstenau. *Comparison of grand unified theories with elektroweak and strong coupling constants at LEP*. Phys. Lett., B260, 447–455, 1991. 1.5

[Arn76] R. Arnowitt and P. Nath. *Spontaneous symmetry breaking of gauge supersymmetry*. Phys. Rev. Lett., 36, 1526, 1976. 21

[Aub74] J. J. Aubert et al. *Experimental observation of a heavy particle j*. Phys. Rev. Lett., 33, 1404–1406, 1974. 1.2.1

[Bal02] A. Ballestrero, 2002. Private communication. 8.5

[Bam94] P. Bambade et al. *Test and installation of the 40 degree Counters during the 1993/94 shutdown*. DELPHI Note 94-48 HERM 1, DELPHI, 1994. 4.2.5

[Bam01] P. Bambade, 2001. Private communication. 7.7

[Bar82] R. Barbieri, S. Ferrara and C. A. Savoy. *Gauge models with spontaneously broken local supersymmetry*. Phys. Lett., B119, 343, 1982. 21

[Bar99] A. Barroso, L. Brucher and R. Santos. *Is there a light fermiophobic Higgs?*. Phys. Rev., D60, 035005, 1999. 3.8

[Ber94] F. A. Berends, R. Pittau and R. Kleiss. *All electroweak four fermion processes in electron - positron collisions*. Nucl. Phys., B424, 308–342, 1994. 5.1.4

[Bor97] G. V. Borisov. *Combined b-tagging*. DELPHI Note 97-94 PHYS 716, DELPHI, 1997. 7.4.2

[Bru00] L. Brucher and R. Santos. *Experimental signatures of fermiophobic Higgs bosons*. Eur. Phys. J., C12, 87–98, 2000. 3.8

[Car99] M. Carena, S. Heinemeyer, C. E. M. Wagner and G. Weiglein. *Suggestions for improved benchmark scenarios for Higgs- boson searches at LEP2*. 1999. Hep-ph/9912223. 27, 3.2.2

[Car00] M. Carena et al. *Reconciling the two-loop diagrammatic and effective field theory computations of the mass of the lightest CP-even Higgs boson in the MSSM*. Nucl. Phys., B580, 29–57, 2000. 27

[CDF95] CDF Collaboration. *Observation of top quark production in $\bar{p}p$ collisions with the CDF detector at Fermilab*. Phys. Rev. Lett., 74, 2626–2631, 1995. 11

[CDF01] CDF Collaboration. *Measurement of the top quark mass with the Collider Detector at Fermilab*. Phys. Rev., D63, 2001. 27

[CER93] CERN Genf. *The ZEBRA System*, 1993. CERN Program Library entries Q100 and Q101. 4.3.2

[Chi81] Y. Chikashige, R. N. Mohapatra and R. D. Peccei. *Are there real Goldstone bosons associated with broken lepton number?*. Phys. Lett., B98, 265, 1981. 2.4

[Cho98] P. Chochula et al. *The DELPHI Silicon Tracker at LEP2*. Nucl. Instrum. Meth., A412, 304, 1998. 34

[Cow98] G. Cowan. *Statistical Data Analysis*. Oxford University Press, 1998. 5.4.1, 5.5.1, 5.6.1, 5.6.1, 5.6.1

[D0 99] D0 Collaboration. *Measurement of the top quark mass in the dilepton channel*. Phys. Rev., D60, 1999. 27

[Dal03] J. Dalmau. *Search for the Neutral Higgs Boson in the bbvv final state with DELPHI at LEP*. Ph.D. thesis, Stockholm university, 2003. 5, 8.6, 8.6.4

[dB94] W. de Boer. *Grand unified theories and supersymmetry in particle physics and cosmology*. Prog. Part. Nucl. Phys., 33, 201–302, 1994. 1.2.3, 21

[dC97] F. de Campos, O. J. P. Eboli, J. Rosiek and J. W. F. Valle. *Searching for invisibly decaying Higgs bosons at LEP II*. Phys. Rev., D55, 1316–1325, 1997. 2.4

[DEL89a] DELPHI Collaboration. *DELPHI Data Analysis Program (DELANA) User's Guide*. DELPHI Note 89-44 PROG 137, DELPHI, 1989. 4.4

[DEL89b] DELPHI Collaboration. *DELSIM, DELPHI Event Generation and Detector Simulation - Reference Manual*. DELPHI Note 89-68 PROG 143, DELPHI, 1989. 5.1.2

[DEL89c] DELPHI Collaboration. *DELSIM, DELPHI Event Generation and Detector Simulation - User's Guide*. DELPHI Note 89-67 PROG 142, DELPHI, 1989. 5.1.2

[DEL91] DELPHI Collaboration. *The DELPHI detector at LEP*. Nucl. Instr. Meth., A303, 233++, 1991. 4.2, 39, 39

[DEL92] DELPHI Collaboration. *Proposal for the upgrade of DELPHI in the forward region*. DELPHI Note 92-142 GEN 135, DELPHI, 1992. 4.2.5

[DEL96a] DELPHI Collaboration. *Charged particle multiplicity in e^+e^- interactions at $\sqrt{s}$ = 130 GeV*. Phys. Lett., B372, 172–180, 1996. 6.2

[DEL96b] DELPHI Collaboration. *Performance of the DELPHI detector*. Nucl. Instr. Meth., A378, 57++, 1996. 4.2, 39, 39

[DEL98] DELPHI Collaboration. *Search for neutral and charged Higgs bosons in e^+e^- collisions at $\sqrt{s}$ = 161 GeV and 172 GeV*. Eur. Phys. J., C2, 1–37, 1998. 5, 6.6.1, 59

[DEL99] DELPHI Collaboration. *A search for invisible Higgs bosons produced in e^+e^- interactions at LEP2 energies*. Phys. Lett., B459, 367–381, 1999. 6.6.1

[DEL00] DELPHI Collaboration. *Searches for neutral Higgs bosons in e^+e^- collisions around $\sqrt{s}$ = 189 GeV*. Eur. Phys. J., C17, 187–205, 2000. 5, 59

[DEL01] DELPHI Collaboration. *Search for a fermiophobic Higgs at LEP 2*. Phys. Lett., B507, 89–103, 2001. 8.6.3

[DEL02a] DELPHI Collaboration. *B-tagging in DELPHI at LEP*. to be published in Eur. Phys. J., 2002. 7.3, 7.4.2

[DEL02b] DELPHI Collaboration. *Searches for neutral Higgs bosons in e^+e^- collisions from $\sqrt{s}$ = 191.6 GeV to 201.7 GeV*. Eur. Phys. J., C23, 409–435, 2002. 5, 59

[DEL02c] DELPHI trigger group. *The DELPHI Trigger System at LEP2 Energies*. Accepted by Nucl. Instr. and Meth. A, 2002. 43

[DEL03a] DELPHI Collaboration. *Final results from DELPHI on the searches for SM and MSSM Neutral Higgs bosons*. To be submitted to Eur.Phys.J.C, 2003. 5, 59

[DEL03b] DELPHI Collaboration. *Flavour independent Neutral Higgs Boson Searches with DELPHI at LEP-2*. To be submitted to Eur.Phys.J.C, 2003. 5, 7.7, 7.7.2, 7.7.2

[DEL03c] DELPHI Collaboration. *Searches for invisibly decaying Higgs bosons with the DELPHI detector at LEP*. To be submitted to Eur.Phys.J.C, 2003. 6.6

[Dem99] L. Demortier et al. *Combining the top quark mass results for run 1 from CDF and D0*. 1999. FERMILAB-TM-2084. 27

[Din93] M. Dine and A. E. Nelson. *Dynamical supersymmetry breaking at low-energies*. Phys. Rev., D48, 1277–1287, 1993. 21

[Din95] M. Dine, A. E. Nelson and Y. Shirman. *Low-energy dynamical supersymmetry breaking simplified*. Phys. Rev., D51, 1362–1370, 1995. 21

[Din96] M. Dine, A. E. Nelson, Y. Nir and Y. Shirman. *New tools for low-energy dynamical supersymmetry breaking*. Phys. Rev., D53, 2658–2669, 1996. 21

[Dit02] S. Dittmaier and M. Roth. *LUSIFER: A lucid approach to six fermion production*. Nucl. Phys., B642, 307–343, 2002. 8.6.2

[Djo91] A. Djouadi, M. Spira and P. M. Zerwas. *Production of Higgs bosons in proton colliders: QCD corrections*. Phys. Lett., B264, 440–446, 1991. 25

[Djo96] A. Djouadi, P. Janot, J. Kalinowski and P. M. Zerwas. *SUSY decays of Higgs particles*. Phys. Lett., B376, 220–226, 1996. 3.2.3

[Djo97] A. Djouadi, J. Kalinowski, P. Ohmann and P. M. Zerwas. *Heavy SUSY Higgs bosons at e^+e^- linear colliders*. Z. Phys., C74, 93–111, 1997. 3.2.3

[Djo99] A. Djouadi. *Impact of the SUSY decays on the search for the MSSM Higgs bosons at the LHC*. Mod. Phys. Lett., A14, 359–368, 1999. 28, 29, 29

[Dok91] S. C. Dokshitzer, L. Yu et al. *New clustering algorithm for multijet cross sections in e^+e^- Annihilation*. Phys. Lett., B269, 432–438, 1991. 5.2

[DON01] DONUT Collaboration. *Observation of tau-neutrino interactions*. Phys. Lett., B504, 218–224, 2001. 12

[EK92] M. M. El Kheishen, A. A. Aboshousha and A. A. Shafik. *Analytic formulas for the neutralino masses and the neutralino mixing matrix*. Phys. Rev., D45, 4345–4348, 1992. 2.2.3

[Ell76] J. R. Ellis, M. K. Gaillard and D. V. Nanopoulos. *A phenomenological profile of the Higgs boson*. Nucl. Phys., B106, 292, 1976. 25, 25

[Fei01] M. Feindt. *NeuroBayes - a neural Bayesian estimator for conditional probabilitiy densities*, 2001. Private Communication. 5.5.1

[Fen00] J. L. Feng and T. Moroi. *Supernatural supersymmetry: Phenomenological implications of anomaly-mediated supersymmetry breaking*. Phys. Rev., D61, 095004, 2000. 21

[Fis36] R. A. Fisher. *The use of multiple measurements in taxonomic problems*. Annals Eugen., 7, 179–188, 1936. 5.4

[Fox79] G. C. Fox and S. Wolfram. *Event shapes in e^+e^- annihilation*. Nucl. Phys., B149, 413, 1979. 7.4.1

[Fuk01] S. Fukuda et al. *Constraints on neutrino oscillations using 1258 days of Super-Kamiokande solar neutrino data*. Phys. Rev. Lett., 86, 5656–5660, 2001. 2.1

[Geo78] H. Georgi. *A model of soft CP violation*. Hadronic J., 1, 155, 1978. 2.3.1

[Ghe99] T. Gherghetta, G. F. Giudice and J. D. Wells. *Phenomenological consequences of supersymmetry with anomaly-induced masses*. Nucl. Phys., B559, 27–47, 1999. 21

[Gho99] N. Ghodbane. *SUSYGEN3: An event generator for linear colliders*. 1999. Hep-ph/9909499. 3.7, 28

[Gin50] V. L. Ginzburg and L. D. Landau. *On the theory of superconductivity*. Zh. Eksp. Teor. Fiz., 20, 1064–1082, 1950. 1.2.3

[Giu98] G. F. Giudice, M. A. Luty, H. Murayama and R. Rattazzi. *Gaugino mass without singlets*. JHEP, 12, 027, 1998. 21

[Gla61] S. Glashow. *Partial symmetries of weak interactions*. Nucl. Phys., 22, 579, 1961. 1.2.2

[Gla77] S. L. Glashow and S. Weinberg. *Natural conservation laws for neutral currents*. Phys. Rev., D15, 1958, 1977. 2.3

[GM62] M. Gell-Mann. *Symmetries of baryons and mesons*. Phys. Rev., 125, 1067–1084, 1962. 1.2.1

[GM64] M. Gell-Mann. *Nonleptonic weak decays and the eightfold way*. Phys. Rev. Lett., 12, 155–156, 1964. 1.2.1

[Gol62] J. Goldstone, A. Salam and S. Weinberg. *Broken symmetries*. Phys. Rev., 127, 965, 1962. 1.2.3

[Gre98] M. Green, S. Lloyd, P. Ratoff and D. Ward. *Electron-Positron Physics at the Z*. Institute of Physics Publishing, 1998. 7.2

[Gri87] D. J. Griffiths. *Introduction to elementary particles*. John Wiley & Sons, 1987. 1.1

[Gru00] M. W. Grunewald et al. *Four-fermion production in electron positron collisions*. 2000. Hep-ph/0005309. 6.5

[Gun90] J. F. Gunion, H. E. Haber, G. Kane and S. Dawson. *The Higgs Hunter's Guide*. Addison-Wesley publishing Company, 1990. 24, 24, 2.3, 2.4, 3.1, 25

[Hab85] H. Haber and G. Kane. *The search for supersymmetry: Probing physics beyond the Standard Model*. Phys. Rep., 117, 75, 1985. 2.2.3

[Hag02] K. Hagiwara et al. *Review of Particle Physics*. Physical Review D, 66, 010001+, 2002. 1.2, 2.1

[Hei99] S. Heinemeyer, W. Hollik and G. Weiglein. *The masses of the neutral CP-even Higgs bosons in the MSSM: Accurate analysis at the two-loop level*. Eur. Phys. J., C9, 343, 1999. 4, 24

[Her98] J. Hertz, A. Krogh and R. Palmer. *Introduction to the theory of neural computation*. Addison-Wesly Publishing, 1998. 5.5, 5.5

[Hig64] P. Higgs. *Broken symmetries, massless particles and gauge fields*. Phys. Lett., 12, 132, 1964. 1.2.3

[Hol86] W. Hollik. *Nonstandard Higgs bosons in SU(2) × U(1) radiative corrections*. Z. Phys., C32, 291, 1986. 2.3

[Hol88] W. Hollik. *Radiative corrections with two Higgs doublets at LEP / SLC and HERA*. Z. Phys., C37, 569, 1988. 2.3

[JAD86] JADE Collaboration. *Experimental studies on multi-jet production in e^+e^- annihilation at PETRA Energies*. Zeitschr. Phys., C33, 23, 1986. 5.2

[Jad00] S. Jadach, B. F. L. Ward and Z. Was. *The precision Monte Carlo event generator KK for two- fermion final states in e^+e^- collisions*. Comput. Phys. Commun., 130, 260–325, 2000. 5.1.3

[Jan96] P. Janot. *Event generators for discovery physics – HZHA*. Report 96-01, CERN, 1996. 3.2, 3.4, 3.5, 27, 5.1.6

[Jos92] A. S. Joshipura and S. D. Rindani. *Majoron models and the Higgs search*. Phys. Rev. Lett., 69, 3269–3273, 1992. 2.4, 2.4, 3.4

[J.R03] J.Rehn et al. *A technique to evaluate and propagate uncertainties in the Monte Carlo modelling of the event reconstruction*. DELPHI Note 2003-XX XXXX XX, DELPHI, 2003. 6.5

[Kal97] H. Kalka and G. Soff. *Supersymmetrie*. B. G.Teubner Verlag, 1997. 21

[Kaz96] D. Kazakov. *Minimal Supersymmetric Extension of the Standard Model*. Technical Report IEKP-KA/96-05, IEKP Karlsruhe, 1996. 21, 21, 21, 21

[Kaz99] D. Kazakov, 1999. Private Communication. 1.2.3

[Kaz01] D. Kazakov. *Beyond the Standard Model*. Technical Report IEKP-KA/2001-01, IEKP Karlsruhe, 2001. 21, 21, 21

[Khe92] M. E. Kheishen, A. Shafik and A. Aboshousha. *Analytic formulas for the neutralino masses and the neutralino mixing matrix*. Phys. Rev., D45, 4345, 1992. 3.2.3

[Kil96] W. Kilian, M. Kramer and P. M. Zerwas. *Higgs-strahlung and WW fusion in e^+e^- collisions*. Phys. Lett., B373, 135–140, 1996. 3.1, 3.1

[Kja91] N. Kjaer and R. Moeller. *Invariant mass determination in multijet events*. DELPHI Note 91-17 PHYS 88, DELPHI, 1991. 8.2, 8.2

[Kob73] M. Kobayashi and K. Maskawa. *CP Violation in the renormalizable theory of weak interaction*. Prog. Theo. Phys., 49(652), 1973. 15

[Lee72] B. W. Lee. *Perspectives on theory of weak interactions*. 1972. Report to a plenary session of 16th ICHEP, Chicago (Batavia), Sep 1972. 2.3

[LEP02] LEP Electroweak Working Group. *A combination of preliminary electroweak measurements and constraints on the Standard Model*. CERN-EP 2002-91, 2002. 4, 12, 1.2, 17, 1.4, 2.1, 2.3

[LEP03] LEP Higgs Working Group. *Search for the Standard Model Higgs Boson at LEP*. To be submitted to Physics Letters B, 2003. 4, 12

[Lon92] L. Lonnblad. *ARIADNE version 4: A program for simulation of QCD cascades implementing the color dipole model*. Comput. Phys. Commun., 71, 15, 1992. 5.1.1, 6.5, 8.5

[Mal96] T. Malmgren and K. Johansson. *Discriminant analysis for background reduction in the H^0 search at LEP2*. DELPHI Note 96-164 PHYS 653, DELPHI, 1996. 5.4.4

[Mal97] T. Malmgren and K. Johansson. *Use of discriminant analysis in search of a neutral Higgs boson*. DELPHI Note 97-59 PHYS 709, DELPHI, 1997. 5.4.4

[Mal98] T. Malmgren and K. Johansson. *An Iterative Discriminant Analysis method to search for the Higgs particle at LEP2*. Nucl. Instr. Meth., A403, 481, 1998. 5.4.4

[Mar88] W. J. Marciano and S. S. D. Willenbrock. *Radiative corrections to heavy Higgs scalar production and decay*. Phys. Rev., D37, 2509, 1988. 25, 25

[McC81] J. McClelland and D. Rumelhart. *An interactive activation model of context effects in letter perceptions*. Psychological Review, 88, 375–407, 1981. 5.5

[Nav96] S. Navas, P. Rebecchi and A. Trombini. *DAFNE program description*. DELPHI Note 96-46 PROG 215, DELPHI, 1996. 47

[Pio99] E. Piotto. *Search for neutral Higgs bosons in $e^+e^- \to H\nu\bar{\nu}$ with DELPHI at LEP2*. Ph.D. thesis, Universita degli Studi di Milano, 1999. 7.5

[Qui99] C. Quigg. *Electroweak symmetry breaking and the Higgs sector*. 1999. Presented at the XXVII International Meeting on Fundamental Physics, Sierra Nevada 1-5. Feb 1999. 1.2.3, 15

[Ran99] L. Randall and R. Sundrum. *Out of this world supersymmetry breaking*. Nucl. Phys., B557, 79–118, 1999. 21, 2.2.4

[Rea97] A. Read. *Optimal statistical analysis of search results based on the likelihood ratio and its application to the search for the MSM Higgs boson at $\sqrt{s}$=161 and 172 GeV*. DELPHI Note 97-158 PHYS 737, DELPHI, 1997. 5.6.2, 5.6.2, 5.6.2

[Reh00] J. Rehn. *Studie zum QCD-Untergrund bei der Higgs-Suche am LEP*. Master's thesis, Fakultät für Physik, Universität Karlsruhe, 2000. IEKP-KA/2000-8. 8.5

[Reh03] J. Rehn. *ZZ production and searches for bosonic Higgs decays with the DELPHI detector at LEP*. Ph.D. thesis, Universität Karlsruhe, 2003. 5, 5.9, 6.5, 6.5, 8.6, 63, 8.6.2, 9

[Ros75] D. A. Ross and M. J. G. Veltman. *Neutral currents in neutrino experiments*. Nucl. Phys., B95, 135, 1975. 2.3

[Rum86] D. Rumelhart, G. Hinton and R. Williams. *Learning representation by back propagating errors*. Nature, 323, 1986. 5.5

[Sak80] N. Sakai. *Perturbative QCD corrections to the hadronic decay width of the Higgs boson*. Phys. Rev., D22, 2220, 1980. 25

[Sch95] P. Schmüser. *Feynman-Graphen und Eichtheorien für Experimentalphysiker*. Springer, 1995. 1.1, 1.1

[Sch99] U. Schwickerath. *Suche nach Higgsbosonproduktion im Vierjetkanal mit dem DELPHI Detektor bei LEP*. Ph.D. thesis, Universität Karlsruhe, 1999. 30

[Sjö94] T. Sjöstrand. *High-energy-physics event generation with PYTHIA 5.7 and JETSET 7.4*. Comp. Phys. Comm., 82, 74, 1994. 5.1.1, 5.1.1, 5.1.1, 5.1.1, 5.2

[Sjö01] T. Sjöstrand, L. Lonnblad and S. Mrenna. *PYTHIA 6.2: Physics and manual*. 2001. Hep-ph/0108264. 5.1.1, 5.1.1, 5.1.1, 5.1.1, 5.1.1, 5.1.3, 49, 53, 5.2, 57, 6.5, 8.5

[SNO01] SNO Collaboration. *Measurement of the charged of current interactions produced by B^8 solar neutrinos at the Sudbury Neutrino Observatory*. Phys. Rev. Lett., 87, 071301, 2001. 20

[Spa97] T. Spassoff and N. Smirnov. *SKELANA - Skeleton Analysis Program*. DELPHI technical manual, 1997. 6.1.1

[Spa99] T. Spassoff et al. *Improvements to SKELANA for Version 2.0*. DELPHI Note, (99-175 PROG 239), 1999. 6.1.1

[Spi97] M. Spira and P. M. Zerwas. *Electroweak symmetry breaking and Higgs physics*. 1997. Hep-ph/9803257. 15, 26, 3.3

[Su00] S. Su. *Higgs sector in anomaly-mediated supersymmetry breaking scenario*. Nucl. Phys., B573, 87–96, 2000. 2.2.4

[Sup98] Super-Kamiokande Collaboration, Y. Fukuda et al. *Measurement of a small atmospheric neutrino ν_μ/ν_e ratio*. Phys. Lett., B433, 9–18, 1998. 2.1

[Sva68] N. Svartholm, editor. *Elementary particle theory*. 8th Nobel Symposium, Almquist and Wiskell, Stockholm, 1968. 1.2.2

[tH72] G. t Hooft and M. Veltman. *Regularization and renormalization of gauge fields*. Nucl. Phys., B44, 189–213, 1972. 1.2.2

[UA183a] UA1 Collaboration. *Experimental observation of isolated large transverse energy electrons with associated missing energy at $\sqrt{s}$ = 540 GeV*. Phys. Lett., B122, 103–116, 1983. 9

[UA183b] UA1 Collaboration. *Experimental observation of lepton pairs of invariant mass around 95 GeV/c^2 at the CERN SPS collider*. Phys. Lett., B126, 398–410, 1983. 9

[UA185] UA1 Collaboration. *Evidence for W / Z decay into jets at the CERN p anti-p collider*. 1985. In Les Arcs, Proceedings, QCD and beyond 305-310. 9

[Vol99] C. F. Vollmer. *Suche nach Higgsbosonen in unsichtbaren Zerfallskanälen am DELPHI-Detektor bei LEP2-Energien*. Diplomarbeit, Fakultät für Physik, Universität Karlsruhe, 1999. 5.2, 5.3, 5.8, 5.10, 6.5, 9

[Wei67] S. Weinberg. *A model of leptons*. Phys. Rev. Lett., 19, 1264–1266, 1967. 1.2.2

[Wes83] J. Wess and J. Bagger. *Supersymmetry and Supergravity*. Princeton University Press, 1983. 21

[Wu57] S. Wu. *Experimental test of parity conservation in beta decay*. Phys. Rev., 105, 1413, 1957. 1.2.2

[Zee80] A. Zee. *A theory of lepton number violation, neutrino majorana mass and oscillation*. Phys. Lett., B93, 389, 1980. 2.4

[Zwe64] G. Zweig. *An SU(3) model for strong interaction symmetry and its breaking*. 1964. CERN-TH-412. 1.2.1

Appendix A

SM Background Monte Carlo

Here all background samples used for analyses at different centre-of-mass energies are listed. The label 206.5U refers to the period of data taking, where one sector of the TPC (sector 6) was offline.

A.1 188.6 GeV

Generator	Type	Cross-section (pb)	Events
KK2F 4.134	2f-qq	99.70	932853
WPHACT 2.1	4f-CC	18.74	567127
WPHACT 2.1	4f-NC	8.15	443433
KK2F 4.143	2f-$\mu\mu$	8.16	50000
KORALZ	2f-$\tau\tau$	8.16	37727
WPHACT 2.1	$\gamma\gamma$-4f	58.49	794566
PYTHIA 6.143	$\gamma\gamma$	1324.00	6780003
BHWIDE	Bhabha	1205.00	139398

A.2 191.6 GeV

Generator	Type	Cross-section (pb)	Events
KK2F 4.134	2f-qq	96.06	929242
WPHACT 2.1	4f-CC	19.16	930167
WPHACT 2.1	4f-NC	8.14	463174
KK2F 4.143	2f-$\mu\mu$	8.90	100008
KORALZ	2f-$\tau\tau$	7.85	50009
WPHACT 2.1	$\gamma\gamma$-4f	55.01	755656
PYTHIA 6.143	$\gamma\gamma$	1376.00	7604342
BHWIDE	Bhabha	1008.00	32800

A.3 195.5 GeV

Generator	Type	Cross-section (pb)	Events
KK2F 4.134	2f-qq	91.30	958581
WPHACT 2.1	4f-CC	19.57	879868
WPHACT 2.1	4f-NC	8.08	525617
KK2F 4.143	2f-$\mu\mu$	8.51	100006
KORALZ	2f-$\tau\tau$	7.55	16223
WPHACT 2.1	$\gamma\gamma$-4f	55.01	755656
PYTHIA 6.143	$\gamma\gamma$	1376.000	7604342
BHWIDE	Bhabha	1008.000	928232

A.4 199.5 GeV

Generator	Type	Cross-section (pb)	Events
KK2F 4.134	2f-qq	86.72	957505
WPHACT 2.1	4f-CC	19.86	618433
WPHACT 2.1	4f-NC	8.03	436872
KK2F 4.143	2f-$\mu\mu$	8.16	99998
KORALZ	2f-$\tau\tau$	7.20	37480
WPHACT 2.1	$\gamma\gamma$-4f	55.01	755656
PYTHIA 6.143	$\gamma\gamma$	1376.00	7604342
BHWIDE	Bhabha	1008.00	928232

A.5 201.6 GeV

Generator	Type	Cross-section (pb)	Events
KK2F 4.134	2f-qq	84.56	987824
WPHACT 2.1	4f-CC	19.97	905631
WPHACT 2.1	4f-NC	8.00	488464
KK2F 4.143	2f-$\mu\mu$	7.98	110526
KORALZ	2f-$\tau\tau$	7.02	37480
WPHACT 2.1	$\gamma\gamma$-4f	55.010	755656
PYTHIA 6.143	$\gamma\gamma$	1376.00	7604342
BHWIDE	Bhabha	1008.00	928232

A.6 205.0 GeV

Generator	Type	Cross-section (pb)	Events
KK2F 4.134	2f-qq	79.78	941848
WPHACT 2.1	4f-CC	20.10	913135
WPHACT 2.1	4f-NC	7.93	499167
KK2F 4.143	2f-$\mu\mu$	7.68	99995
KORALZ	2f-$\tau\tau$	6.824	62157
WPHACT 2.1	$\gamma\gamma$-4f	55.5	176298
BHWIDE	Bhabha	1008.00	911107

A.7 206.5 GeV

Generator	Type	Cross-section (pb)	Events
KK2F 4.134	2f-qq	79.77	838526
WPHACT 2.1	4f-CC	20.14	683523
WPHACT 2.1	4f-NC	7.90	309915
KK2F 4.143	2f-$\mu\mu$	7.57	99998
KORALZ	2f-$\tau\tau$	6.70	73421
WPHACT 2.1	$\gamma\gamma$-4f	55.20	176298
PYTHIA 6.143	$\gamma\gamma$	1008.00	1494168
BHWIDE	Bhabha	1400.08	2019220

A.8 206.5U GeV

Generator	Type	Cross-section (pb)	Events
KK2F 4.134	2f-qq	79.77	468113
WPHACT 2.1	4f-CC	20.14	467923
WPHACT 2.1	4f-NC	7.90	108075
KK2F 4.143	2f-$\mu\mu$	7.57	100000
KORALZ	2f-$\tau\tau$	6.70	73421
WPHACT 2.2	$\gamma\gamma$-4f	62.56	976774
PYTHIA 6.143	$\gamma\gamma$	1008.00	1494168

Appendix B

Invisible Higgs preselection

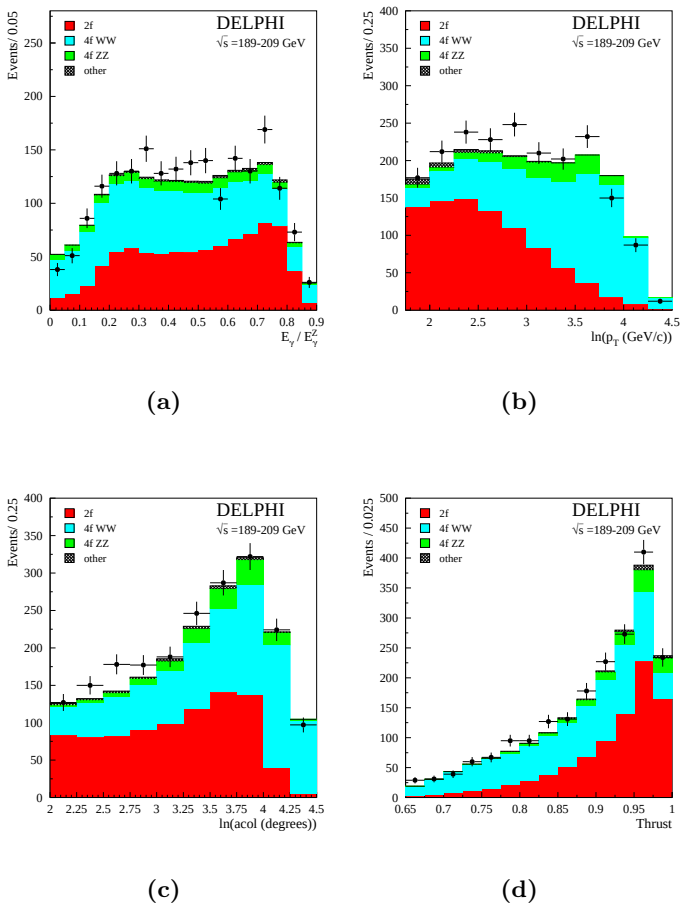

Figure B.1: Distributions for some of the preselection variables of the high mass analyses as described in chapter 57: (a) $E_\gamma/E_\gamma^{\mathrm{Z}}$ (b) $\log(p_{\mathrm{T}})$ (c) log(acol) (d) Thrust.

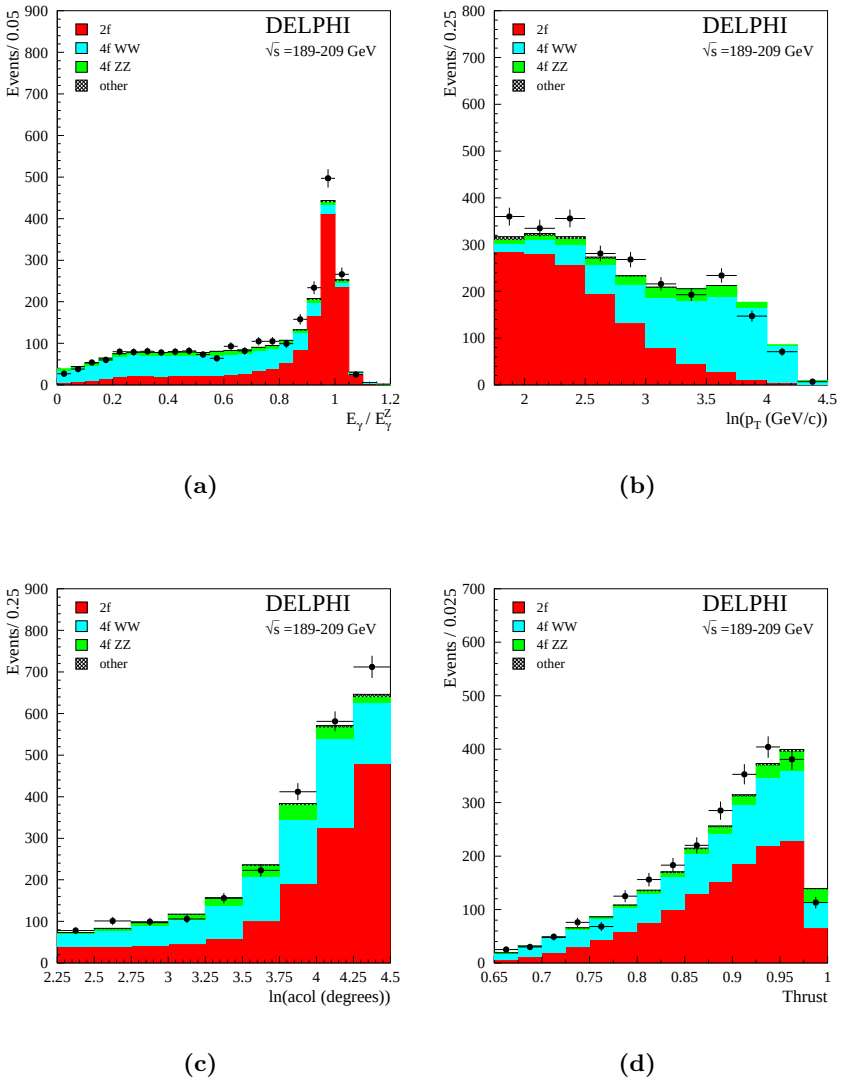

Figure B.2: Distributions for some of the preselection variables of the low mass analyses in the hadronic channel after the tail cuts as described in chapter 57: (a) E_γ/E_γ^Z (b) $\log(p_T)$ (c) log(acollinearity) (d) Thrust.

Appendix C

Hadronic Higgs preselection

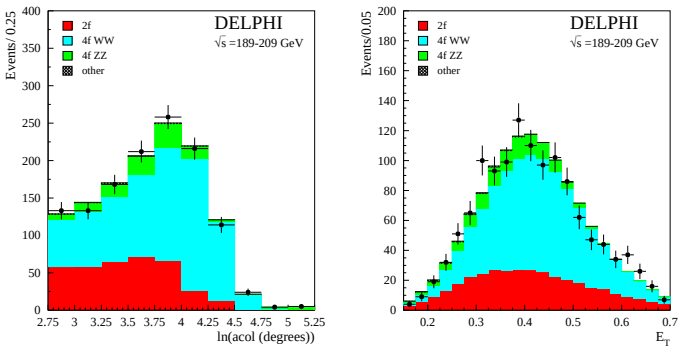

(a) **(b)**

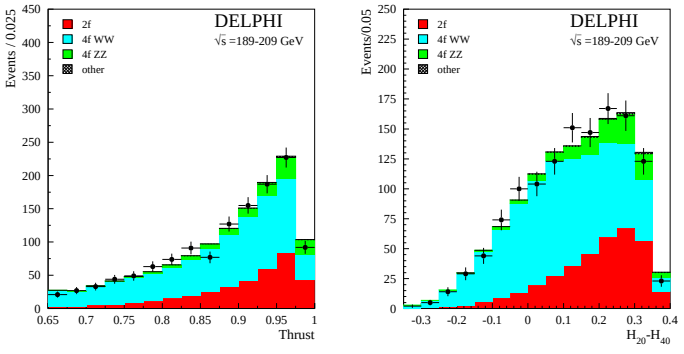

(c) **(d)**

Figure C.1: Distributions for some of the preselection variables of the low mass analyses as described in chapter 7.4.1: (a) ln(acollinearity) (b) $E_{\mathrm{T}}/\sqrt{s}$ (c) Thrust (d) Fox-Wolfram momenta $H_{20} - H_{40}$.

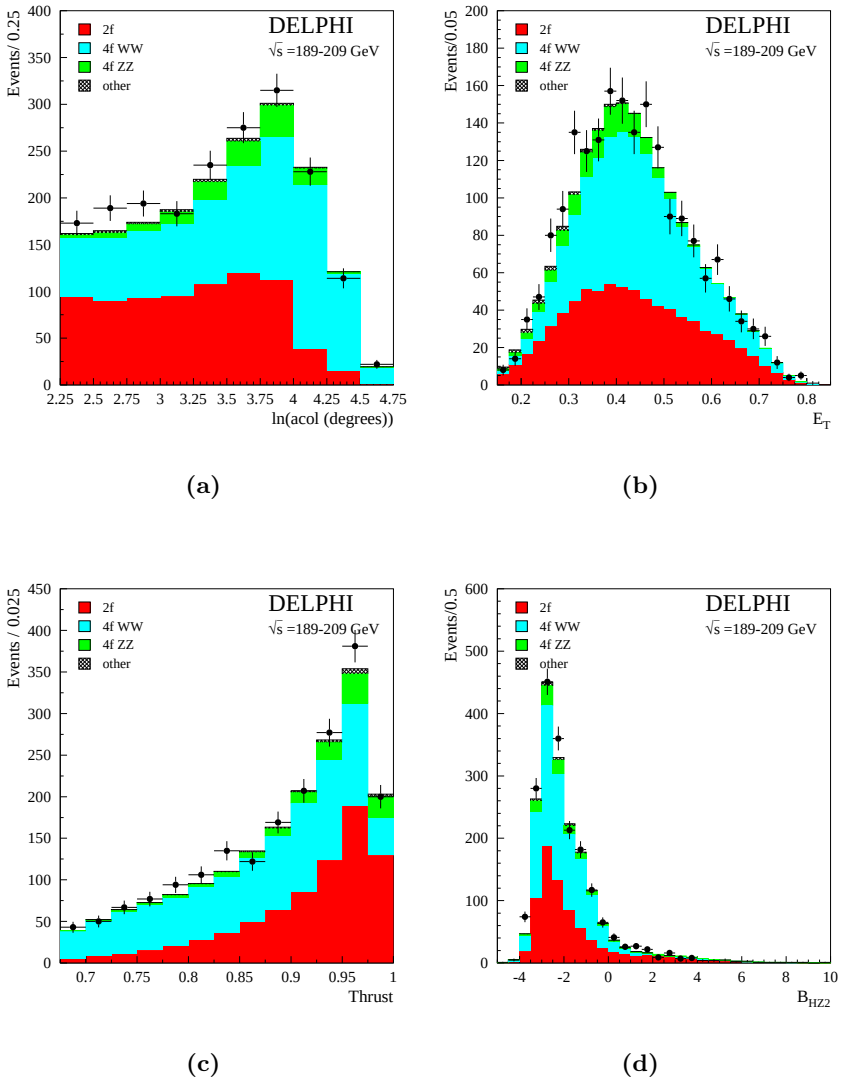

Figure C.2: Distributions for some of the preselection variables of the medium mass analyses as described in chapter 7.4.2: (a) ln(acollinearity) (b) $E_{\mathrm{T}}/\sqrt{s}$ (c) Thrust (d) B-Tagging B_{HZ2}.

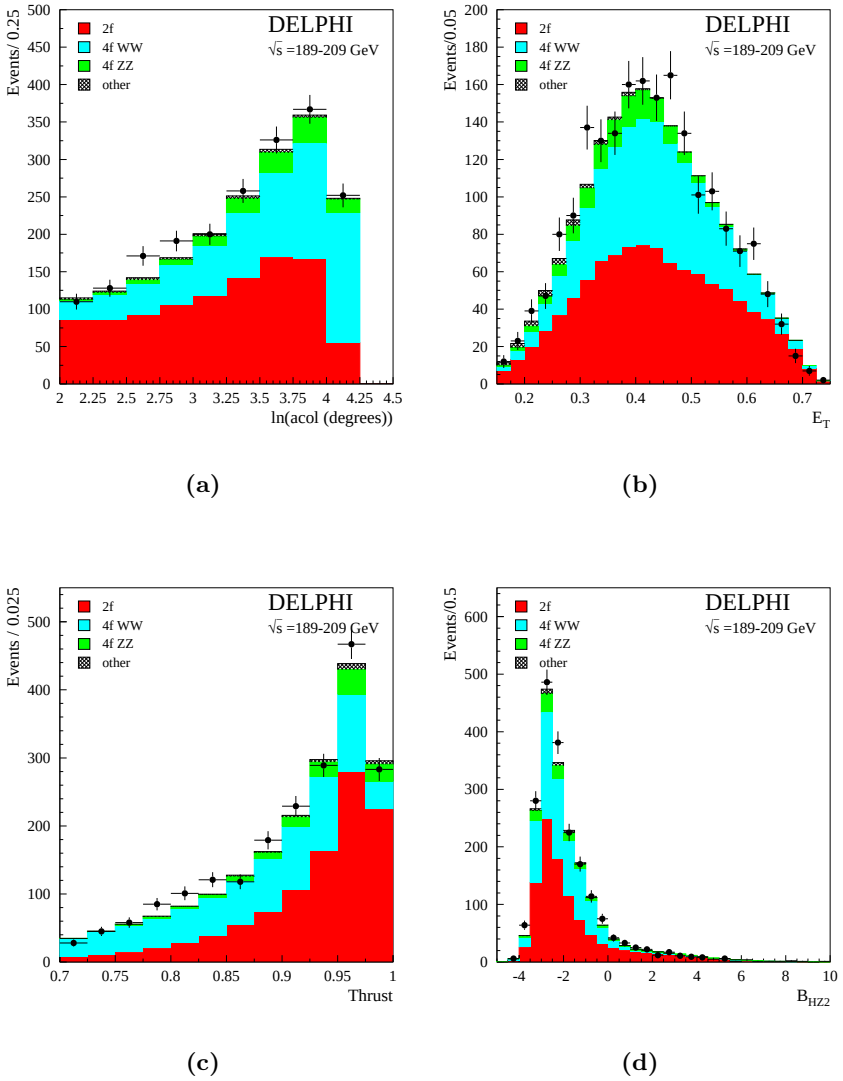

Figure C.3: Distributions for some of the preselection variables of the high mass analyses as described in chapter 7.4.3: (a) ln(acollinearity) (b) $E_{\mathrm{T}}/\sqrt{s}$ (c) Thrust (d) B-Tagging B_{HZ2}.

Appendix D

Bosonic Higgs preselection

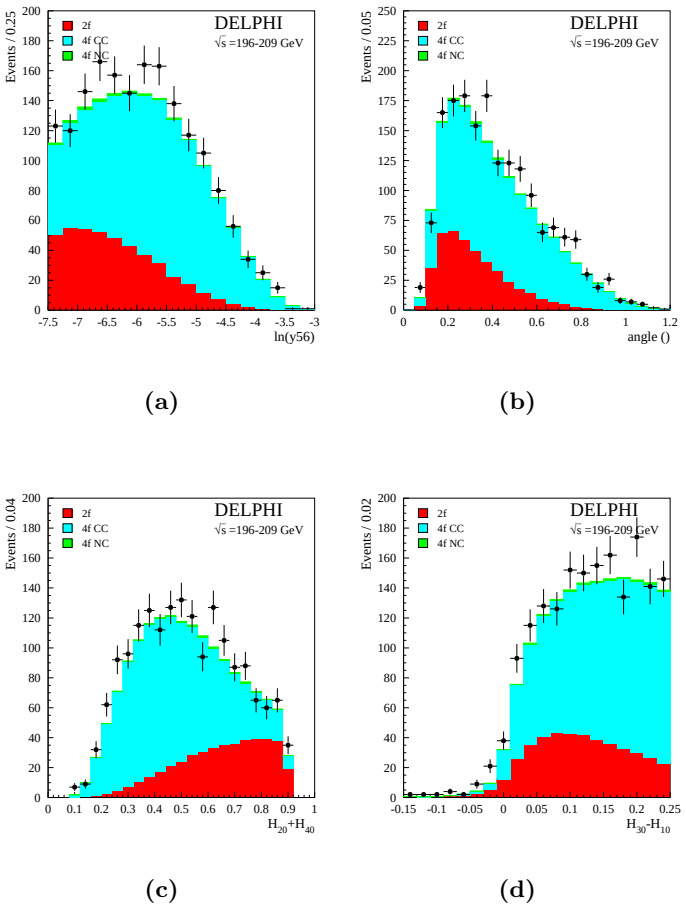

Figure D.1: The preselection for the HWW six jet final state as described in chapter 8.3 . Shown are : (a) $ln(y56)$, (b) the smallest angle between two jets $min(\alpha_{ij})$, (c) $H_{20} + H_{40}$ and (d) $H_{30} - H_{10}$.

Acknowledgements

This thesis sums up the work of three years and would not have been possible without the advice, the help and the support from many people both from Karlsruhe and from within the DELPHI collaboration. It would be impossible to name them all. Those, who are not mentioned here, are certainly not forgotten. Special thanks goes to

- Prof. Dr. Wim de Boer: for giving me the opportunity to do my Ph.D about Higgs bosons at LEP and for offering me both guidance and freedom in my research. Thanks for letting me stay half a year at CERN and giving me the possibility to present my results on international conferences.

- Prof. Dr. Günter Quast: for accepting the Korreferat, for giving me new insights into electroweak physics and sharing the difficulties with the seminars for Gewerbeschullehrer. Thanks also for compensating this by arranging the debriefing of the seminar in the *Alte Schmiede* and for our collaboration in starting to renew experiments in the physics lab.

- Philip Bambade (LAL/Orsay): for being a never ending source of new ideas and inspiration. Many things in this thesis I would not have started without the advice and the fruitful discussions with you.

- Chiara Mariotti (CERN/INFN): for always supporting and helping me at CERN and giving me the opportunities to present my results as a speaker from DELPHI. Additionally a big thanks for the best Saltimbocca in the world.

- Tiziano Camporesi (CERN): for giving me the opportunity to coordinate all the invisible and hadronic Higgs searches within DELPHI.

- Vanina Ruhlmann-Kleider (DAPNIA/Saclay): no limit or exclusion curve would have been possible without your help and support. Thanks for helping me exploring the world of ALRMC and *d_higgs.f*

- Jens Rehn: for being a good friend all the years we studied together in Karlsruhe. Thanks for your help and your ideas during our DELPHI-LEP2 analysis time.

- Jörgen Dalmau (Fysikum/Stockholm): for helping building a common analysis framework for Higgs searches and for the great time we had both at CERN, Stockholm and Karlsruhe

- Rosy Nicolaidou (DAPNIA/Saclay): for the help and cooperation in processing large amounts of ntuples and working on the *Hnn* code

- Ivo van Vulpen and Maarten Boonekamp (CERN): for the big effort putting all the flavourblind inputs into the ALRMC framework and making the machinery work.

- Ulrich Schwickerath: For the nice time we had at CERN sharing offices and for being very helpful in generating millions of Monte Carlo events at (as usual) short notice.

- Johannes Bol, Christian Haag, Levin Jungermann and Jens Rehn for the nice years we spent together studying at Karlsruhe university.

- Patrick Schemitz: For being a good officemate and the nice discussions about computers, Linux and submarines. A big thanks for your public Ph.D paperwork page, this saved a lot of time for me.

- Thomas Allmendinger: for your efforts to convice me of b-physics and for giving me all your Ph.D exam preparation papers, they really helped a lot.

- Stephanie Menzemer: For being the person to remind me, that sometimes a short break and a cup of tea can really bring you closer to the solution of a problem.

- Levin Jungermann, Stephanie Menzemer, Markus Moch and Jens Rehn: for careful reading of the manuscript and giving many hints to improve the text.

- The two Joan(n)as Joana Ferreira Montenegro and Joanna Weng: for cheering me up when everything seems to end in chaos.

- Frau Haas & Frau Weissmann: For the helping me to fight against any kind of administrational difficulties. Especially thanks to Frau Haas to take care of my large amount of travel forms.

- All the other members of the Institut für experimentelle Kernphysik for the nice atmosphere over the years, especially to the EKP AllStars.

- The members of the LEP2 physics teams from DELPHI for the nice collaboration over the years.

- To the Landesgraduiertenförderung Baden-Württemberg and to the Graduiertenkolleg *Teilchen- und Teilchenastrophysik*: for supporting my work by granting stipends.

- To my parents and my grand parents: A Big Thanks for the support (not only financial) over the longs years I studied in Karslruhe. To my grand father Karl Ulmer, who has always been a very special person in my life. Unfortunately he died before the finalisation of my Ph.D. This thesis is dedicated to him.